A Measurement of Dijet Photoproduction at HERA using the Zeus Detector

Robert L. Saunders

University College London

Submitted to the

University of London

for the degree of

Doctor of Philosophy

September 1997

Abstract

Dijet production by almost real photons has been studied at HERA using the ZEUS detector. The photoproduction of dijets can be used to constrain the parton distributions in the photon and the proton and test perturbative QCD. Jets have been identified using two different cone algorithms and one cluster algorithm. Some comparative study of these algorithms was made. A cut on x_γ^{OBS}, the fraction of the photon energy participating in the production of the two jets of highest transverse energy, is used to define and separate resolved and direct processes. Cross sections of these two types of process, and also for the full range of x_γ^{OBS} have been measured for dijets with transverse energies above 6, 8, 11, and 15 GeV. The cross sections are corrected for detector acceptance and compared to next to leading order QCD calculations. Agreement with these calculations is seen for the pseudorapidity dependence of the direct photon events with $E_T^{jet} > 6$ GeV and of the resolved photon events with $E_T^{jet} > 11$ GeV. Calculated cross sections for resolved photon processes with 6 GeV $< E_T^{jet} <$ 11 GeV lie below the data.

Contents

List of Figures

List of Tables

Acknowledgments

There are many people who gave me help, support, advice, and friendship, without which I would not have been able to produce this great work. Firstly, for useful comments and suggestions, and simply for making the work more interesting and enjoyable, I wish to thank Tegid Jones, Jon Butterworth, Lutz Feld, Costas Foudas, Dave Gilkinson, the members of the ZEUS Hard Photoproduction/Jets and High E_T working group, the members of the UCL High energy physics group, Steve Campbell-Robson, and Arnulf Quadt. I would also like to express my appreciation for the work of the HERA staff, and the ZEUS collaboration as a whole. For inspiring me to become Dr. Bob I thank Rolf the pianist from the muppets. To those people who I have forgotten, or not mentioned individually by name I apologise.

For making my life in Hamburg very enjoyable and easier than it might otherwise have been, I would like to thank Susan Kettels, Friederike Timm, Nicola Thiermann, Elgin Kremser, Magdalena Lange, Sonia Shiffmann, Deborah Kuschel, and Minna Rikander. Also, for being a good friend, if somewhat geographically distant at times, I thank Carol O'Connor.

A special thanks to my parents for their support, and for giving me somewhere to stay on my return to London. I also acknowledge the existence of my brother Matthew, which, given the philosophy discussions we have had, is probably more than he does himself.

Finally I would like to express my gratitude to PPARC for funding my studies and research.

Robert Saunders 14/9/1997

Chapter 1

HERA and the ZEUS Detector

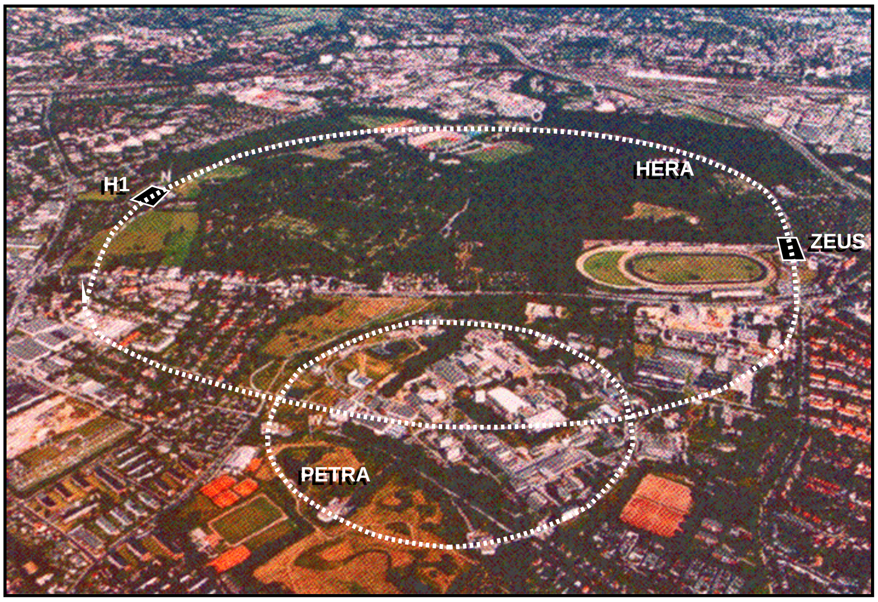

Figure 1.1: *Aerial view of Hamburg showing the locations of the two rings,* **HERA** *and* **PETRA**, *and the experiments,* **ZEUS** *and* **H1**.

1.1 Introduction

The construction of the **H***adron* **E***lektron* **R***ing* **A***nlage* **HERA**, the world's first electron-proton collider, began in April 1984 at the **D***eutsches* **E***lektronen* **SY***nchrotron* (**DESY**) laboratory in Hamburg, Germany. By August 1987 the

6.34km tunnel which houses the collider had been finished, and in the autumn of 1990 the electron ring, equipped with normal magnets, and the proton ring, equipped with superconducting magnets, became operational.

After a period of machine tests with separated beams, the first electron-proton collisions were observed in October 1991. Regular data taking by the **H1** and **ZEUS** detectors began in May 1992. In the summer of 1994 electrons were replaced with positrons to provide the possibility of longer beam lifetimes.

The technical proposal for the **ZEUS** detector [1] was received by the **DESY** directorate in 1986. The detector was approved in November of the same year and **ZEUS** was allocated the south experimental hall of **HERA**. Final installation of the detector was completed in the autumn of 1991. Upgrades to the detector, including the addition of new components, have been made during each of the subsequent shutdown periods.

There are over 500 physicists in the **ZEUS** collaboration, and about the same number of technical staff, who come from over 50 institutes in 12 different countries: the UK, the USA, Canada, Germany, Israel, Italy, Japan, Korea, Poland, the Netherlands, Russia and Spain.

1.2 HERA

1.2.1 The injection system

Injection of electrons and protons into **HERA** takes place in several stages. The layout of the various pre-accelerators is shown in figure 1.2.

Protons are accelerated as H^- ions in the proton linear accelerator (**LINAC**) to an energy of 50MeV. These in turn are accelerated to 7.5GeV by the **DESY-III** proton synchrotron. At this point the electrons are stripped and the protons passed to the **PETRA** storage ring where they are accelerated to 40GeV. At this energy they are injected into **HERA** where, guided by superconducting dipole and quadrupole magnets, they are accelerated using conventional radio frequency cavities to the design operating energy of 820GeV.

Electrons and positrons are also accelerated by **LINACs**, first to 220MeV and then 450MeV. They are then transferred to **DESY-II** for further acceleration to 7.5GeV. From here they go into **PETRA** where they are accelerated to 12GeV, at which point they are injected into **HERA**. In **HERA** the electrons(positrons) are accelerated using conventional and superconducting radio frequency cavities to an energy of around 30GeV. In 1994 the positron beam energy was 27.52GeV.

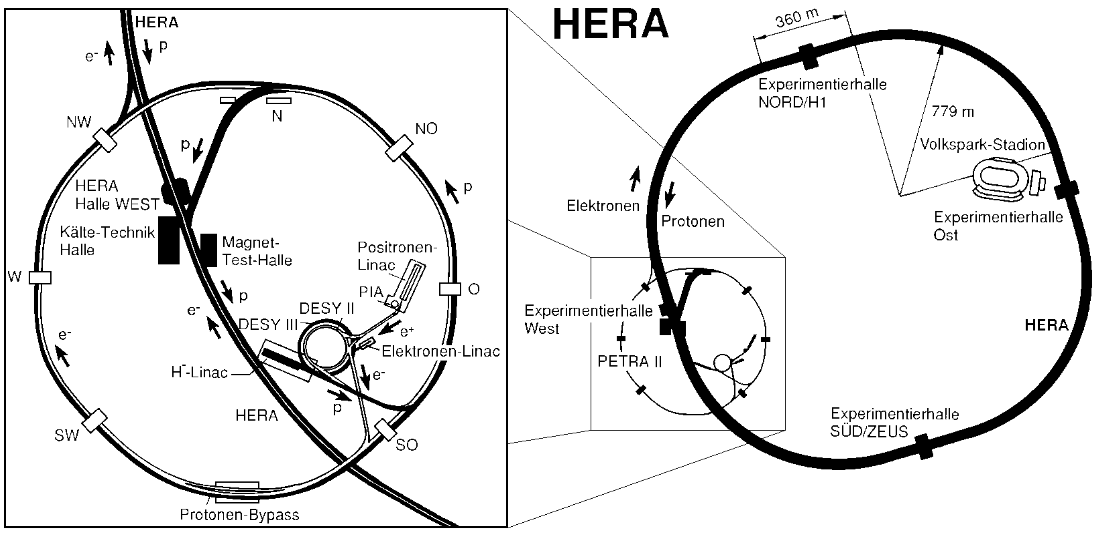

Figure 1.2: *Plan of* **HERA** *with enlarged detail of the injection system.*

1.2.2 Design parameters

The dimensions of the **HERA** ring can be seen in figure 1.2. Table 1.1 gives some of the design parameters for the collider, and typical performance for the 1994 running period. Eventually, using the designed specific luminosity, 100pb^{-1} per year is expected. In 1992 the **ZEUS** experiment collected 30nb^{-1}, and this increased to 540nb^{-1} in 1993. Of the total 6pb^{-1} of luminosity collected by **ZEUS** in 1994,

Parameter	Typical 1994 Value	Design Value
$e^{\pm}$ beam energy (GeV)	27.52	30
P beam energy (GeV)	820	820
Particles per bunch ($e^{\pm}/P$)	$2.6 \times 10^{10}/3.1 \times 10^{10}$	$3.5 \times 10^{10}/1.1 \times 10^{11}$
Number of bunches ($e^{\pm}$+satellite/P+satellite)	153+15/153+17	210+0/210+0
Centre of mass energy $\sqrt{s}$ (GeV)	300	314
Current ($e^{\pm}/P$) (mA)	23/37	60/160
Luminosity (cm^{-2}s^{-1})	3.3×10^{30}	1.5×10^{31}
Integrated Luminosity pb^{-}1	6	100

Table 1.1: *Design parameters for* **HERA** *and typical values attained in 1994.*

3.2pb^{-1} was taken with positrons instead of electrons circulating in **HERA**. For part of this time the machine ran with a shifted vertex, that is the beams collided at a point significantly removed from the nominal interaction point. The analysis presented in this thesis uses 2.7pb^{-1} of the positron-proton data, collected while the beams were colliding at the nominal interaction point.

During 1994 running, apart from the 153 paired bunches for each beam, an additional 15 unpaired positron bunches and 17 unpaired proton bunches were filled. This was to facilitate the study of backgrounds caused by interactions between the beams and any residual gas in the beam pipes. Positron beam currents were $\sim$ 22mA and proton currents were often in excess of 40mA [2, 3].

1.3 ZEUS

The **ZEUS** detector is a multi-purpose magnetic detector, and hermetic apart from a small region close to the beam pipe. Figure 1.3 shows the layout of the various detector components in x-y and z-y cross sections. In the case of the longitudinal

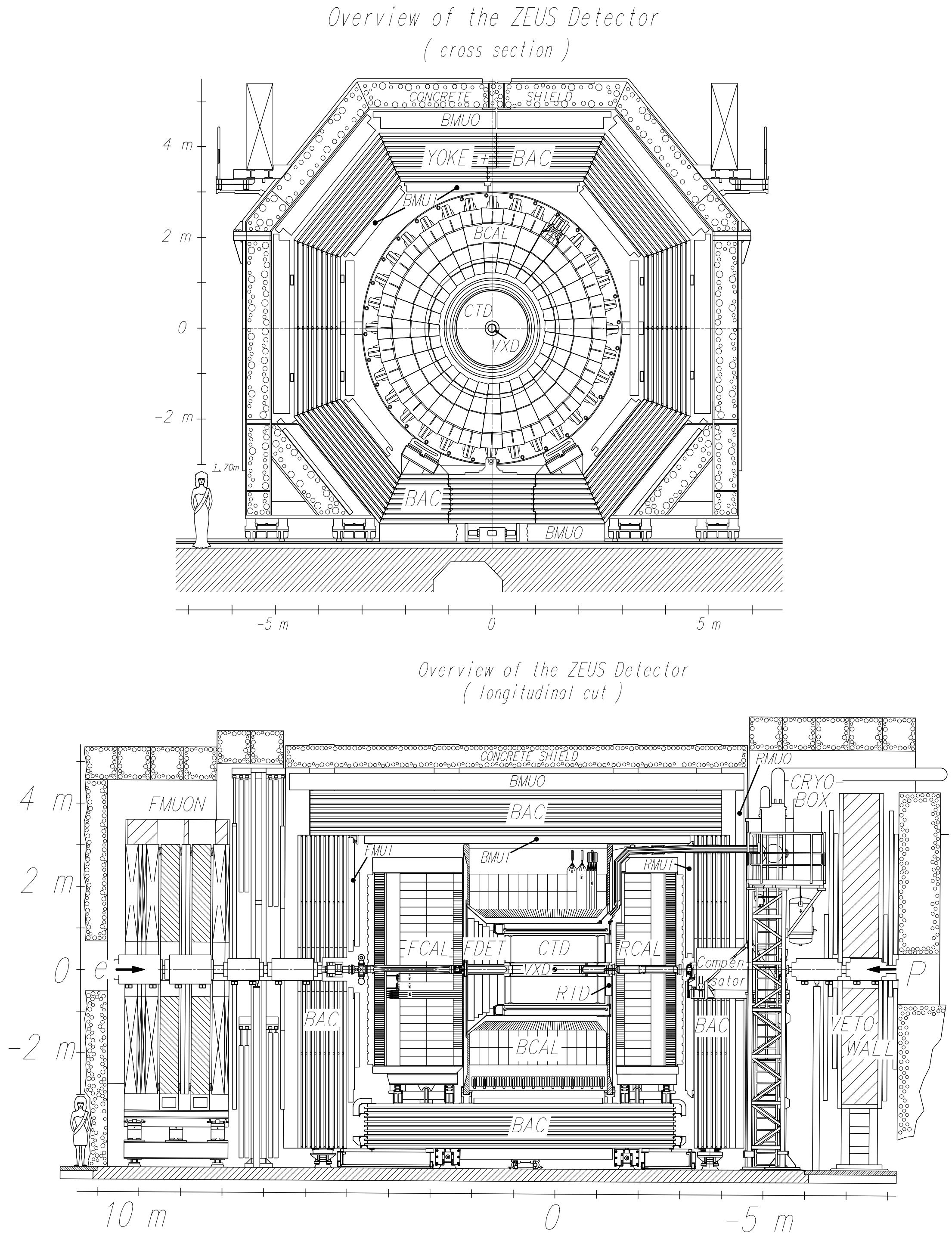

Figure 1.3: *Cross sections through* **ZEUS***: above x-y, below z-y. In the Lower picture the proton enters from the right, so z becomes more positive from right to left.*

cut the proton enters the detector from the right and the positron(electron) from the left. The most important components active during 1994 are described in the following sections. A more complete description of the experiment and it's component detectors can be found in [4].

In general a right handed Cartesian coordinate system is used for the **ZEUS** detector with the $z - axis$ defined as the proton beam direction and the positive $y - axis$ pointing upwards, which means that the x-axis points towards the centre of the **HERA** ring. The origin is defined as the nominal interaction point. For event analysis a cylindrical polar coordinate system is often used. This has the same z-axis and the azimuthal angle ϕ is measured from the x-axis. At HERA the boosts between the lab frame and the more physically motivated frames, such as the centre of mass, are in the z direction. For this reason pseudorapidity $\eta = -ln(tan(\theta/2))$, which is only modified by an additive constant with such boosts, is very often used instead of the polar angle θ.

1.4 Tracking in Zeus

At the centre of the detector, closest to the beam pipe and the interaction region, is a **V**erte**X** **D**etector (VXD). This is surrounded radially by the **C**entral **T**racking **D**etector(CTD), which is the main component used for tracking charged particles. To the front and rear of the CTD respectively are the **F**orward **T**racking **D**etector(FTD) and the **R**ear **T**racking **D**etector(RTD). In addition a **S**mall angle **R**ear **T**racking **D**etector(SRTD) was installed to improve the position resolution for charged particles entering the rear calorimeter. Together the inner tracking chambers allow measurement of charged particles emitted from the nominal interaction point at angles between $\theta = 7.5°$ and $\theta = 170°$. All of the tracking detectors operate in a magnetic field of 1.43T which is provided by a superconducting solenoid. This sits radially between the CTD and the calorimeter.

1.4.1 The VXD

The vertex detector is a cylindrical drift chamber with an inner radius of 10.9cm and an outer radius of 15.9cm. It is divided azimuthally into 120 drift cells, each cell occupying 3° in azimuth. Each cell has 12 sense and 13 field wires running parallel to the beam. These alternate in a plane extending radially from the beam pipe. On either side of this are planes of 25 drift wires. The entire detector is filled with dimethylether (DME) gas to provide a slow drift velocity which gives accurate particle time resolution.

The VXD has a design performance of $\frac{\sigma(p)}{p} \approx 9 \times 10^{-4} p$ (when used in conjunction with the CTD) and an error on the primary vertex radius of $\sim 50\mu$m. However, it was not fully operational in 1994.

1.4.2 The CTD

The central tracking detector of **ZEUS** is a multiwire proportional chamber which extends from the VXD to an outer radius of 85cm, and in the z direction from -100cm to $+100$cm. The polar angle coverage is $15^\circ < \theta < 164^\circ$. The detector was designed to be used with a 50% Ar, 50% C_2H_6 mix. However, mainly for safety reasons, the mixture used to fill the CTD for 1994 running was 85% Ar, 5% C_2H_6, 10% CO_2.

The CTD consists of 4608 sense wires grouped into 8-wire cells, and an azimuthal distribution of angled cells forming a *superlayer*. There are 9 such superlayers in the chamber as indicated in figure 1.4, which shows one segment of the detector in cross section. The sense wires in the CTD are separated by ground wires (0V) and planes formed by the sense and ground wires alternate with planes formed by field-shaping wires. Odd-numbered superlayers are known as *axial* superlayers and have their wires parallel to the CTD axis. The even-numbered superlayers, known as *stereo* superlayers, have their wires at a small angle ($\sim 5^\circ$) to

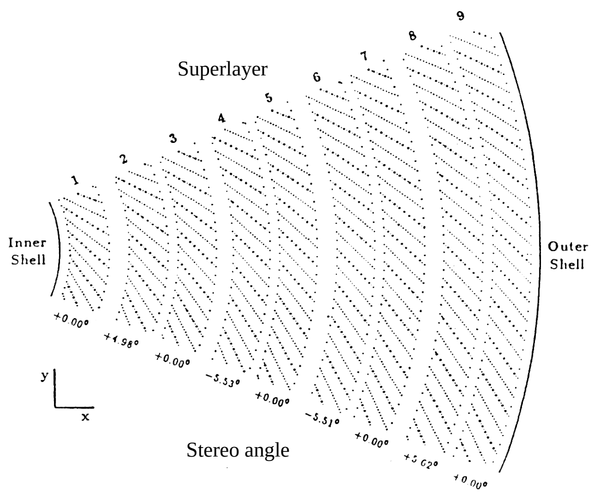

Figure 1.4: *One octant of the* CTD *showing the layout of superlayers and cells. Each of the* CTD *cells contains eight sense wires evenly-spaced down it's centre.*

the chamber axis.

Two methods are used to determine the z-position of a track element. The z-by-timing method exploits the time difference of a signal arriving at the two ends of a wire [5] whereas the z-by-stereo method takes advantage of the even-numbered superlayers. Signals on axial superlayers, when projected onto the end of the chamber, can be aligned to form a track. Hits from the same track in the stereo layers, however, are rotated due to the stereo angle. An extrapolation of the stereo layer projection along the z of the chamber until the track segment matches that from an axial layer gives the z-position of that track [6]. This z-by-stereo method achieves z position resolution of $\approx$ 2mm. The z-by-timing method alone achieves a z position resolution of 4.5cm but is by far the faster system (several nanoseconds versus several hundred milliseconds).

During the 1994 runing period, the CTD achieved a tracking resolution of 180μm and $\frac{\sigma(p_T^2)}{p_T^2} \approx (0.005)^2 p_T^2 \pm (0.016)^2$.

1.4.3 The RTD

The rear tracking detector was designed to extend the polar angle tracking acceptance to the rear of the CTD. It is a single planar drift chamber positioned at $z \approx -130cm$, covering the polar range from $160°$ to $170°$.

The chamber consists of three layers perpendicular to the beam, two of which are rotated by $\pm 60°$. Each layer is subdivided into cells of 6 sense wires. This gives three projections of the path taken by a charged particle, which can be combined to reconstruct a track segment. The resolution achieved is around 200μm.

1.4.4 The SRTD

The primary task of the small angle rear tracking detector (SRTD) is to improve the angular resolution for the scattered positron. In addition it is used as a pre-sampler for the calorimeter by measuring the showering of particles in the inactive material (cables and flanges) in front of the rear calorimeter. This allows a correction for the energy lost to the dead material and improves the calorimeter energy resolution.

The SRTD covers an area of 68cm $\times$ 68cm around the beam-pipe hole, and sits at $z = -1.46$m. It consists of two planes of scintillator strips, each plane sectioned into four 24cm $\times$ 44cm pieces. The strips have a width of 1cm and are oriented alternately along x and y. There are 272 strips in total which are read out via photomultipliers. Each of the planes is 0.5cm thick and they are separated by a support plane which reduces cross-talk. The SRTD can achieve a position resolution of 5mm in x and y.

1.4.5 The FDET

The collective term for the FTD and the **T**ransition **R**adiation **D**etector(TRD) components, which are sandwiched together, is the FDET.

The FTD consists of three planar drift chambers identical in construction to the RTD. These are separated in z by 21cm, and the detector as a whole covers the polar range 7.5° to 28°. Sandwiched between the layers of the FTD are the two TRD modules which are designed to enhance differentiation between hadrons and electrons in the energy range of 1GeV to 30GeV.

The FDET was fully installed in 1994 but was not available for physics analyses.

1.5 Calorimetry at ZEUS

The **U**ranium **CAL**orimeter(UCAL) is the most important part of **ZEUS** for the analysis to be presented in this thesis. The calorimeter, which encloses the inner tracking detectors and the solenoid, comprises a cylindrical **B**arrel **CAL**orimeter(BCAL), a **F**orward **CAL**orimeter (FCAL) and a **R**ear **CAL**orimeter (RCAL). A **H**adron-**E**lectron **S**eparator(HES) is installed between the RCAL layers. Surrounding the UCAL is the **BA**cking **C**alorimeter(BAC), which measures energy leakage out of the main calorimeter.

1.5.1 The UCAL

A large effort was made to make the energy resolution of the calorimeter as good as possible. It contains electromagnetic and hadronic sections in order to have an equal response to both types of energy deposits. Such calorimeters are said to be *compensating*.

The **ZEUS** calorimeter is constructed using depleted uranium ^{238}U as an absorber [7], and a plastic scintillator as the readout material. A schematic of a calorimeter tower is shown in figure 1.5. Charged particles traversing the scintillator produce light which travels by internal reflection to wavelength shifters. The light is converted to a longer wavelength by the wavelength shifters and travels to the photomultiplier tubes (PMTs) at the back of the tower. An electrical signal

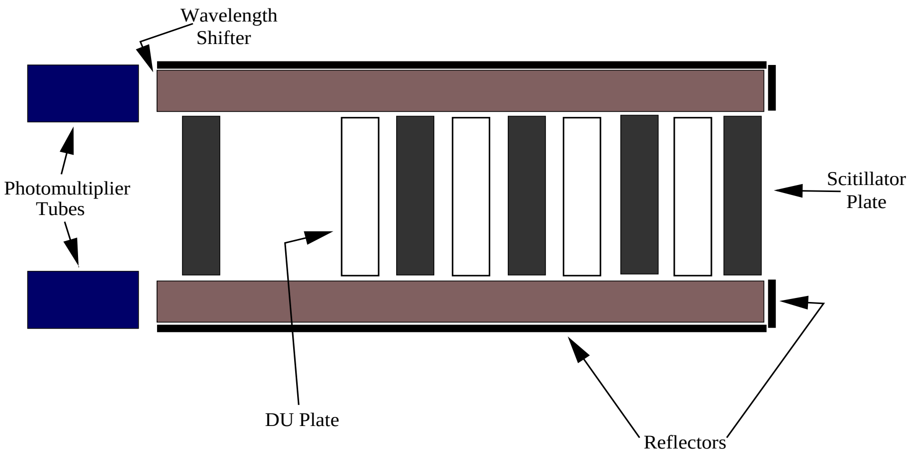

Figure 1.5: *Schematic of an* FCAL *tower viewed from above. Particles are incident on the right-hand face.*

is produced by these and passed out of the detector. There are two PMTs for each cell (one at each side in x) as indicated in figure 1.5. This provides some redundancy and an indication of the x-position of a deposit.

Showers caused by electrons, positrons, photons, or muons are well understood [8], and relatively easy to deal with. Showers initiated by hadrons, on the other hand, cannot be described analytically. They may contain both hadronic *and* electromagnetic components, and the relative fractions of these components vary from one shower to another, even if the incident energies are the same. The difficulty arises because some of the energy from the hadronic component goes into nuclear reactions which are not visible to the scintillator. This means that in general hadronic showers produce less photons in the scintillators than electrons of the same energy. In the uranium, however, the nuclear reactions release high energy photons which can be detected in the scintillator. By a suitable choice of thicknesses for the layers of scintillator and uranium, compensation can be achieved for a very wide range of energies [4], so that a hadron and electron of the same energy produce, on average, the same number of photons in the scintillator, and hence the signals from the PMTs are the same.

The energy which the calorimeter is required to absorb is a function of the polar

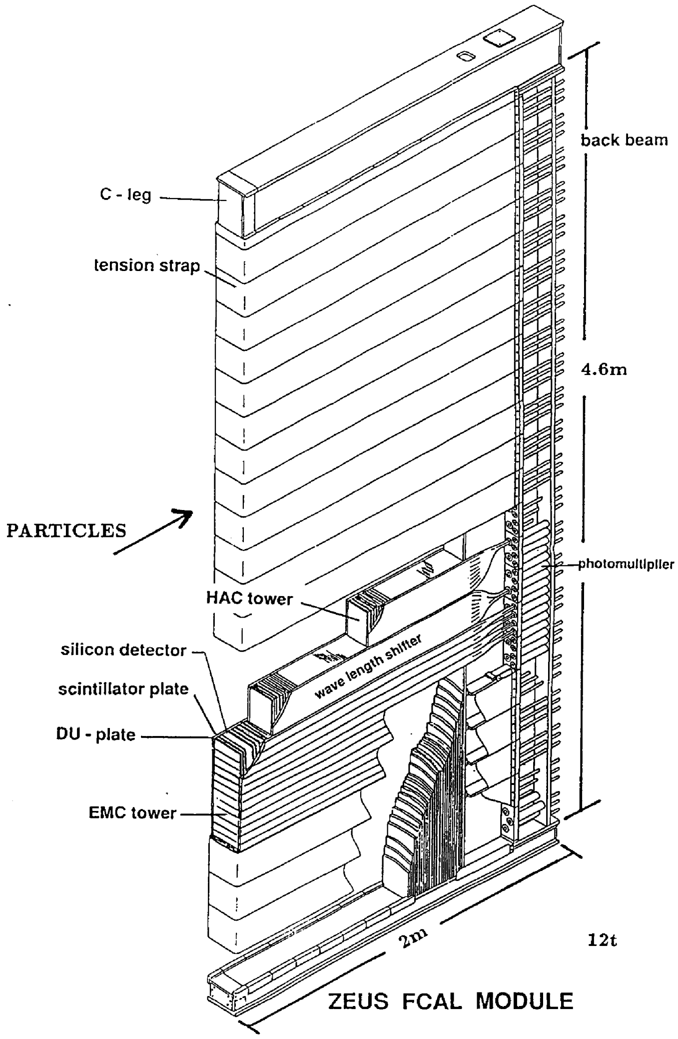

Figure 1.6: *Structure of a typical* FCAL *module.*

angle. It ranges from approximately the proton energy (820GeV) in the forward direction to the electron energy (27.5GeV) in the rear. The mean particle energies are somewhat lower however. To cope with this angular dependence the FCAL has a depth of 7λ(absorption lengths), the BCAL has a depth of 5λ and the RCAL a depth of 4λ. Much higher jet energies can be contained with the surrounding BAC. The polar angle coverage of the FCAL and the RCAL are $2.3° < \theta < 36.7°$ and $129.1° < \theta < 176.5°$ respectively, with the BCAL covering the intervening region.

The FCAL is divided into 23 vertical modules numbered with increasing x.

Figure 1.6 shows the construction of a typical FCAL module. Each module has a width of 20cm, and is in turn segmented into 20cm x 20cm towers numbered with increasing y [9]. One module is divided up into three sections in z, an inner electromagnetic part (FEMC) and two hadronic parts (FHAC1 and FHAC2). The FEMC part is further subdivided into four 20cm x 5cm sections. Each of the sections is called a calorimeter *cell*. (The central module has a 20cm x 20cm hole in the middle to accommodate the **HERA** beam-pipe).

The BCAL contains 32 wedge-shaped modules and, in a similar manner to the FCAL, has an electromagnetic part(BEMC), and two hadronic parts (BHAC1 and BHAC2). Each of these modules has 14 towers with the EMC part containing four cells per tower.

The structure of the RCAL is also very similar to that of the FCAL except that REMC is subdivided into two 20cm x 10cm cells instead of four. The RCAL has only one hadronic section.

All of the calorimeter towers are made with a sandwich of alternate layers of 3.3mm-thick depleted uranium and 2.6mm-thick plastic scintillator. For these thicknesses the ratio of electromagnetic response to hadronic response is 1.00 ± 0.02 in the energy range 10 to 100GeV [10, 11]. With this compensation an optimal energy resolution for hadrons is achieved, since one is independent of the statistical fluctuations in the proportions of electromagnetic and hadronic energy in a shower.

To take advantage of the high resolution achievable by the calorimeter an accurate calibration for all the calorimeter channels must be performed. This is an ongoing process. The principal method is to use the naturally-occurring radiation from the depleted uranium (energy $\approx$ 2.3MeV), in combination with a point-like ^{60}Co source, which can be moved parallel to each scintillator plate's position. The variation of calorimeter response to this is stable at the level of a few percent [12]. Modules from the RCAL and FCAL have also been calibrated at **CERN** using test-beams with various particles at known energies. The results from these tests show that the calorimeter has a linear response to the incident energy at the level of $\sim 1\%$.

The energy resolution is found to be $17.5\%(\pm 1\%)/\sqrt{E}$ for electrons and $35\%(\pm 2\%)/\sqrt{E}$ for hadrons, and the time resolution is 0.5 ns. At lower energies this resolution is somewhat degraded by noise [10].

For this analysis the effects of noise in the calorimeter, defects in photomultipliers and discharges in the photomultipliers were dealt with by placing cuts on the cell energies and the imbalance between signals from the two photomultiplier tubes connected to each cell. Cells were only used if the measured energy was more than 60 MeV for the EMC and 100MeV for the HAC, and for isolated energy deposits in single cells these thresholds are raised to 100MeV and 150MeV respectively.

1.5.2 The BAC

The BAC is made out of 7.3 cm thick iron plates which also serve as the return yoke for the superconducting magnets. The iron is instrumented with proportional counters, with which any energy that has leaked from the UCAL can be detected. The energy resolution is $\sigma(E)/E = 1000/\sqrt{E}\%$.

1.6 The Luminosity Monitors

Two small lead-scintillator calorimeters are placed at -34.7m (LUMI-e) and -106.0m (LUMI-γ) from the nominal interaction point, which detect photons and electrons respectively. A carbon filter shields the photon calorimeter from synchrotron radiation. These form the luminosity monitors.

The primary role of these detectors is to measure the luminosity provided by **HERA**. They do this using the Bethe-Heitler process $ep \rightarrow e'p\gamma$ where a photon is emitted by the electron at very low angles [13]. The cross-section for this process is high and very well known. It is observed as signals in both of the luminosity monitors whose energy sum is that of the incoming electron.

Additionally the two monitors serve as tagging devices for collisions occurring at very low Q^2 (photoproduction processes) where the electron is scattered at very low angles, and for initial state bremsstrahlung in neutral current deep inelastic scattering events (ISR-DIS). The tagged photoproduction signal is of some importance to the analysis presented here as it is used to study the cuts used in the event selection procedure. The Lumi tag is not however used as a requirement for events to enter the final data sample. An event is tagged as photoproduction when a signal is encountered in the LUMI-e monitor with no corresponding signal in the LUMI-γ detector. In ISR-DIS events, no signal is encountered in the LUMI-e monitor but the emitted photon is seen in the LUMI-γ detector.

Both of the LUMI detectors have been designed with an energy measurement resolution of $0.16/\sqrt{E}$. The error on the luminosity measurement in 1994 was around 1.5%.

1.7 Other Components

The following components were not particularly important to the analysis presented in this thesis, but are worth describing briefly.

1.7.1 The C5 counter

The C5 counter, so called because it is attached to **HERA** collimator number 5, is a lead plate sandwiched between two scintillator plates within the beam-pipe. It is placed perpendicular to the beams at $z = -315$cm, with an inner radius which varies from 12mm to 30mm depending on whether the collimator is "closed" or "open".

As they pass the collimator particles from the beam halos register in the C5 counter and thus give the time of arrival for the bunches. From this a number of useful things can be deduced; in particular the true position of the interaction vertex. The counter also measures the rate of interactions produced by the beam, gives information about the beam shapes, and helps to reduce the proton-beam-gas background by vetoing events which are not in the time window of a positron-proton interaction. The C5 counter has a time resolution of $\sim$ 1ns.

1.7.2 The Veto Wall.

The veto wall protects the detector from particles produced by interactions between the protons and pieces of the machine or residual gas in the beam pipe. It is made of 87cm-thick iron placed around the beam-pipe at $z = -7.5$m. Attached to this are two planes of scintillator counters, one on either side. The scintillators allow the veto wall, not only to protect the detector from proton-beam-gas collisions, but also to veto the event in the trigger if hits are detected on both sides of the wall.

1.7.3 The Muon detectors

Muons with energies greater the 2GeV generally pass straight through the UCAL and BAC. In order to be able to detect them a system of drift chambers divided into forward, barrel, and rear regions was installed.

The first layer of the muon chambers is inside the iron yoke between the UCAL and the BAC, while the outer part is installed outside the end cap in the forward direction, and outside the iron yoke in the barrel and rear regions. The magnetic field from the yoke, and a complimentary pair of toroids in the forward direction, allow these detectors to make momentum measurements.

1.8 The ZEUS trigger system

There are two major difficulties to overcome for experiments using the **HERA** beams. Firstly the beam-crossing interval is only 96ns. Secondly there is a very high background to signals ratio caused by beam particles colliding with residual gas in the beam pipes. The combination of these leads to a signal in the region of 100kHz, of which only $\sim 2 - 3$Hz are interesting ep events. A three layer trigger system is employed by **ZEUS** to deal with the high background rates, whilst keeping genuine ep events [14].

The first-level trigger (FLT) reduces the signal to $\sim$ 1kHz. Since most detector components cannot make a useful trigger decision in the 96ns beam crossing interval data is "pipelined", that is it is put into a 5μs buffer. The UCAL, for example, uses a switched capacitor array to pipeline its (analogue) data whereas the CTD uses a digital pipeline to store it's hit information, which is already digitised. Each component participating in the FLT must make a "sub-trigger" decision within 5μs. To achieve this only a subset of the available data is used.

The decision from each of the components is then passed to the global first level trigger (GFLT) where an overall decision is made. An example is the use of the CTD to pattern-recognise whether or not an event has produced a primary vertex in the expected region. If such a vertex has been found then the CAL can be used to add a cut on the transverse energy (E_T) of the event. The GFLT then decides which events are likely to be ep interactions. The FLT is the most efficient and least pure of the triggers and around 98% of the events passed are background events.

The second-level trigger (SLT) uses parallel processing on transputer networks to reduce the output from the FLT ($\sim$ 1kHz) to $\sim$ 100Hz and has 1ms to make a decision. As with the FLT, sub-triggers from components are passed to a global trigger (GSLT) where a decision for the whole event is made. Since the time allowed for the decision to be made is much longer than in the FLT, charged particle tracking, better vertex position determination, muon, jet, and scattered electron finding is used in the event decision.

The GSLT sends events which have passed its criteria to the event builder (EVB). This collects all the data from the various components and merges it into a ZEBRA bank [15], reformats this into a single event record, according to the ADAMO package [16], and sends it to the next trigger stage (ZEBRA and ADAMO are software packages which manage data structures).

The third level trigger (TLT) is a farm of very fast processors which view the event as a whole. It uses a version of the offline reconstruction software, modified to reduce time overheads, to calculate kinematic properties, and perform more refined tracking vertex finding and jet finding. After this reconstruction the TLT classifies *ep* events into physics categories according to various filters set by the physics working groups. The final output rate of the TLT is $\sim$ 5Hz.

Events that pass all the trigger stages are put onto mass storage devices. The data is then dealt with offline where the only time constraints come from physicists wanting to analyse the events. Software is run which fully reconstructs the events using information from all available components. The exact trigger criteria used for the analysis presented in this thesis is dealt with in chapter 5.

Chapter 2

Hard Photoproduction and QCD

The purpose of this chapter is to introduce the theoretical and phenomenelogical background to the analysis presented in later chapters. A general description of electron proton scattering leads on to photoproduction and photon proton interactions. There is then a brief discussion of the models for the photon and the parameterisations of its hadronic nature. Finally there is a quick introduction to the idea of multiparton interactions in a single photon proton scatter.

2.1 Screening, Asymptotic Freedom and Jets

In QED an electron is constantly emitting and re-absorbing virtual photons, some of which momentarily fluctuate into e^+e^- pairs before they are re-absorbed. Thus the electron is effectively surrounded by a cloud of e^+e^- pairs which **screen** it, so that at large distances it appears to have a reduced charge. At smaller distances the screening is reduced, the coupling constant α gets larger, and the interactions become stronger. A similar situation exists in QCD with quarks emitting and re-absorbing gluons, some of which fluctuate into $q\bar{q}$ pairs. However, since gluons can couple to each other, fluctuations into glue-glue pairs are also possible. Such glue-glue pairs have an **anti-screening** effect that dominates over the screening provided by the $q\bar{q}$ pairs. This means that at large distances the strong coupling constant α_s becomes large and interactions become very strong. Conversely at small distances α_s is small and the interactions are much weaker. This is known as **asymptotic freedom**.

From the point of view of performing calculations, the above effects mean that some characteristic momentum scale must be sufficiently large (hard) that a perturbative description in terms of quarks and gluons interacting weakly over short distances is valid. If the characteristic momentum scale is too small such a picture is not possible, since the distances involved will be large, and the quarks and gluons will arrange themselves into strongly bound clusters, namely hadrons. From this the characteristic **hard scale** can be equated with the ability to resolve individual quarks and gluons, i.e. in an experiment where one or both of the incoming particles are hadrons, the ability to resolve the structure of the initial hadrons increases as the momentum scale becomes larger.

Another consequence of the anti-screening is that as two colour charges are separated, the potential energy in the gap between them becomes rapidly larger. At some point it becomes energetically favourable to 'pop' further particles out of the vacuum to screen the colour. This occurs at large distances and therefore small momentum scales. In this way a spray of colour neutral particles develops which generally follows the direction of the initiating (coloured) particle. Hence the outgoing quarks and gluons from perturbatively calculable hard interactions form hadronic jets, and it is these jets that are observed in experiments. Therefore the study of the jets should yield information about the hard scattering processes from which they were produced.

2.2 Electron Proton Scattering

The basic process of lepton proton interactions, which are either weak ($W^{\pm}$,Z° exchange) or electromagnetic (γ exchange), is shown schematically in figure 2.1.

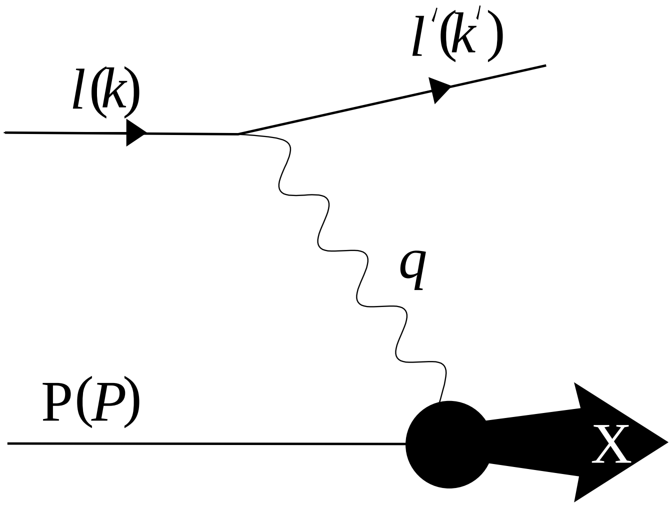

Figure 2.1: *Lepton proton scattering*

The incoming electron exchanges a photon, $W^\pm$ or Z^0, with the proton in an interaction that produces a hadronic final state X. When the exchanged boson is an electrically neutral photon or Z^0 the incoming lepton is simply scattered through some angle θ, but in the case of $W^\pm$ exchange the lepton converts to an (anti-)neutrino in the final state. This leads to the frequently used classification of neutral current (NC) ($e^\pm + \mathrm{P} \to e^\pm \mathrm{X}$) and charged current (CC) ($e^\pm + \mathrm{P} \to \nu \mathrm{X}$) events. In figure 2.1 the 4-momenta of the incoming and scattered lepton are $k = (E, \mathbf{k})$, $k' = (E', \mathbf{k}')$, and those of the proton and the photon are $P = (E_p, \mathbf{p})$ and $q = (E_\gamma, \mathbf{q})$. At fixed center of mass energies ($\sqrt{s} = \sqrt{(k+P)^2}$) the kinematics of the lepton are completely described by two of the three Lorenz invariant quantities:

$$Q^2 = -q^2 = (k' - k)^2 \tag{2.1}$$

$$y = \frac{q \cdot P}{k \cdot P} \tag{2.2}$$

$$\text{and} \quad x = \frac{-q^2}{2P \cdot q} \tag{2.3}$$

Q^2, the negative square of the momentum transfer, is always positive and specifies the virtuality of the exchanged boson. In the proton rest frame y is the fraction of the energy of the incoming lepton carried by the exchanged boson

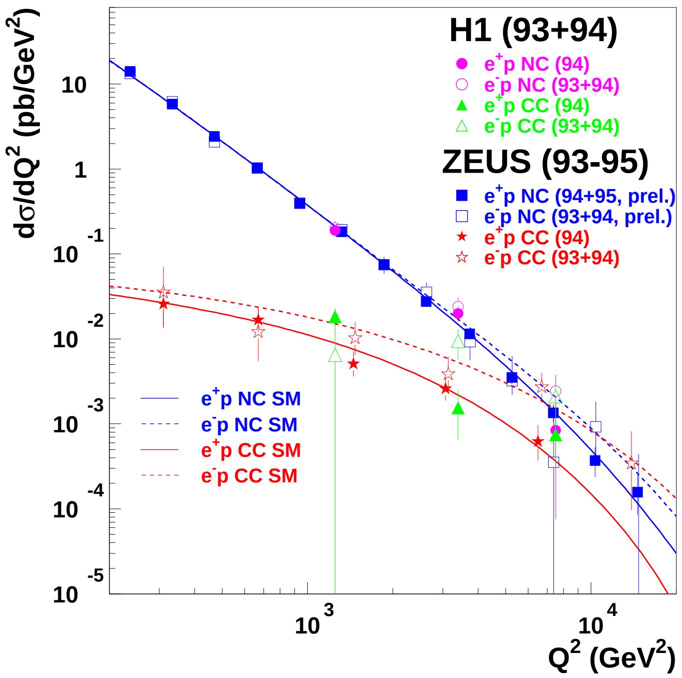

Figure 2.2: *Neutral Current and Charged Current cross sections as a function of Q^2, measured by H1 and ZEUS, compared to standard model predictions.*

$y = \frac{E-E'}{E} = \frac{E_\gamma}{E}$. In the infinite momentum frame where the proton has arbitrarily large momentum, x corresponds to the fraction of the proton's momentum taking part in the interaction, see section 2.3.

In photon exchange the propagator $\frac{-ig_{\mu\nu}}{q^2}$ causes the cross section to fall rapidly with Q^2, so that processes in which the photon is almost real ($Q^2 \approx 0$) are the most common. Figure 2.2 shows the neutral and charged current cross sections measured by ZEUS and H1 compared to standard model predictions [17, 18]. The weak interaction only contributes a significant amount to the total interaction cross section at large Q^2 of around the mass squared of the weak bosons ($\mathrm{M_{W^\pm}} = 80.2$ GeV and $\mathrm{M_{Z^0}} = 91.2$ GeV) or larger. At $Q^2 \gtrsim M^2_{Z,W}$ the neutral current and the charged current cross sections are found to be of comparable magnitude, which is a direct demonstration of electro-weak unification. $\mathrm{W}^\pm$ and Z^0 processes will not be discussed any further here, as their contribution to the total ep cross section at the very low Q^2 of interest in this thesis are negligible in comparison to photon exchange.

In events where Q^2 is large it provides the hard scale for perturbative calculations. The Q^2 scale at which this breaks down completely, and the effective coupling becomes large is referred to as Λ_{QCD}. This scale can only be determined from experimental measurements, and has been found to be $\Lambda_{QCD} = 0.2 \pm 0.1$ GeV [21]. Events where Q^2 can safely be used as the hard scale ($Q^2 \gg \Lambda_{QCD}$) are called **Deep Inelastic Scattering (DIS)**.

The analysis presented in this thesis is primarily concerned with **Photoproduction** events, in which a low Q^2, quasi-real photon is exchanged. Therefore Q^2 can't be used as the characteristic scale of the interaction. A common choice for the hard scale in these events is the transverse momentum of the jets produced.

In the previous section an explanation was given of how an increase in the characteristic hard scale of the interaction corresponds to an increase in the power to resolve the structure of the proton. Another way to approach this is to consider the wave length of the exchanged boson. In order for a boson to be able to resolve an object its wavelength must be of similar size or smaller than the object itself.

$$\lambda = \frac{h}{|\bar{q}|}$$

So for larger values of Q^2, smaller objects can be resolved. Alternatively from Heisenberg's uncertainty principle: $\Delta l \approx h/\Delta p_t \approx h/\sqrt{Q^2}$, where Δl is the spatial resolution, leads to the same conclusion.

Since the lepton-photon vertex is purely electromagnetic and essentially identical for incoming electrons or positrons there will be no differentiation between the two in this chapter, and the term 'electron' will be used throughout.

2.3 The Simple Quark Parton Model

In Feynman's parton model the proton is made up of free point like objects referred to as partons [19]. Although it had been suggested previously, it wasn't until the mid 1970's that these partons were generally accepted to be the quarks of Gell-Mann [20], and the model became known as the quark parton model (QPM).

In this model inelastic electron-proton scatters are viewed as elastic electron-parton scatters. At lowest order the photon emitted by the electron couples to a single quark in the proton, knocking it out and so causing the break up of the proton. To describe this process the Bjorken scaling variable

$$x_p \equiv \frac{Q^2}{2\ P \cdot q} \approx \frac{Q^2}{ys} \tag{2.4}$$

is introduced, where $s = (k + P)^2$ is the square of the centre of mass energy. In the proton's infinite momentum frame the quarks can be considered to be travelling collinear to each other and the proton direction, thus all quark transverse momenta are negligible. If ξ is the fraction of the proton's momentum carried by the struck quark then, neglecting the parton mass, 4-momentum conservation implies:

$$0 \approx m^2 = (\xi P + q)^2 = \xi^2 P^2 - Q^2 + 2\xi P.q$$

$$\Rightarrow \xi = \frac{Q^2}{2P.q} = x_p$$

Thus x_p, in this frame, is effectively the fraction of the proton's longitudinal momentum carried by the struck quark.

Following on from the above description of individual interactions, the inelastic electron-proton cross section is calculated as the incoherent sum of the electron-parton scatters. Assuming the quarks have spin-$\frac{1}{2}$ one can use the fermion-fermion scattering cross-section [22]:

$$\frac{d\sigma}{dQ^2} = \frac{4\pi\alpha^2 e_q^2}{Q^4}\left(1 - y + \frac{y^2}{2}\right) \tag{2.5}$$

where e_q is the electric charge of the quark, and electron and quark masses are neglected. Defining the parton distribution function $f_{\mathrm{q}}^{\mathrm{p}}(x_p)dx_p$ as giving the probability of finding a quark of the type q, carrying momentum fraction x_p of the proton, one can write:

$$\frac{d\sigma^{ep}}{dQ^2} = \frac{4\pi\alpha^2}{Q^4}(1 - y + y^2/2) \int \sum_q e_{\mathrm{q}}^2 f_{\mathrm{q}}^{\mathrm{p}}(x_p)dx_p \tag{2.6}$$

This can then be rewritten as:

$$\frac{d^2\sigma^{ep}}{dx_p dQ^2} = \frac{4\pi\alpha^2}{x_p Q^4}\left(x_p y^2 F_1(x_p, Q^2) + (1-y)F_2(x_p, Q^2)\right) \tag{2.7}$$

Where

$$F_2(x_p, Q^2) \;\; = F_2(x_p) \;\; = \sum_{\mathrm{q}} \mathrm{e_q}^2 x_p f_{\mathrm{q}}(x_p) \tag{2.8}$$

$$F_1(x_p, Q^2) \;\; = F_1(x_p) \;\; = \frac{1}{2x_p} F_2(x_p) \tag{2.9}$$

are called structure functions. Alternatively the structure function

$$F_L = F_2 - 2xF_1 = \frac{Q^2}{4\pi^2\alpha} \cdot \sigma_L, \tag{2.10}$$

is often used, which is related only to the absorption of longitudinally polarised photons. The cross section then becomes:

$$\frac{d^2\sigma^{ep}}{dx_p dQ^2} = \frac{2\pi\alpha^2}{x_p Q^4}\left[\left[1 + (1-y)^2\right] F_2 + 2(1-y)F_L\right] \tag{2.11}$$

Equation 2.9 is known as the Callan-Gross Relation [23], and has been experimentally confirmed (for not too large Q^2) [24]. It is closely related to the assumption that the quarks have spin $\frac{1}{2}$. If quarks had spin-0 the relation would be:

$$\frac{2F_2}{F_1} = 0$$

A Comparison of the Callan-Gross relation and the expression for F_L (eqn.2.10) indicates that the cross section for longitudinally polarised photons vanishes.

It was Bjorken in 1968 who predicted that in the high energy limit $Q^2 \to \infty$, $\nu \to \infty$, the F_i would depend only on one dimensionless variable x [25]. Where $\nu = \frac{p.q}{M}$ is the photon energy (E_γ) in the proton rest frame, and M is the mass of the proton. This behaviour is known as scaling. It can be understood by considering that increases in Q^2 are related to the ability to resolved smaller and smaller objects. Assuming the proton consists of point like constituents makes scaling possible as an increase in resolution does not improve the view of a point. Bjorken scaling was confirmed very clearly by results from SLAC (see for example [26]).

2.4 The QCD Improved Parton Model

If the proton consisted solely of charged quarks, their momenta would be expected to add up to the momentum of the proton. However, when measured experimentally a value of

$$\sum_q \int x_p f_q(x_p) dx_p \approx 0.5 \tag{2.12}$$

is found, implying that about half of the proton's momentum is carried by neutral partons. Direct evidence of these partons, called gluons, was provided in 1979 at DESY via the observation of three-jet events in e^+e^- annihilation [27].

In quantum chromodynamics (QCD) quarks interact via the radiation and absorption of gluons. Gluons radiated by the quarks in the proton can in turn split into quark anti-quark pairs (sea quarks) or more gluons. Therefore the naive QPM, where the quarks were free and the only constituents of the proton, has to be modified. Gluon radiation results in transverse components to the quark momenta, such that it is no longer possible to define a frame of high enough momentum that p_t can be neglected. The transverse components to the quark momenta allows them to couple to both longitudinally and transversely polarised photons. Hence the Callan-Gross relation is no longer exactly satisfied and the longitudinal structure function F_L is not zero but lies in the range $0 < F_L < F_2$.

Another important consequence of the gluon radiation is that the structure functions now exhibit a logarithmic dependence on Q^2 at fixed x_p, i.e. scaling is violated. This can be interpreted in terms of the resolving power of the exchanged photon. At low Q^2 the resolution of the exchanged photon is rather broad, so it can only 'see' the valence quark substructure of the proton. At higher Q^2 however, a finer resolution is achieved and quark-antiquark pairs originating from radiated gluons can be resolved. Hence as Q^2 increases the 'history' of the quark before it interacted with the photon becomes important. This is of course a frame dependent statement, but it offers a useful way of understanding the effects associated with the gluon radiation. The struck quark may previously have radiated a gluon and thus, although it had momentum fraction x_p when it was struck, it originally had a larger momentum fraction $x'_p > x_p$. Alternatively it may be that the struck quark was one of a $\mathrm{q\bar{q}}$ pair produced by a gluon with momentum fraction x'_p, and again $x_p < x'_p$. Consequently when considering a process involving a quark of momentum fraction x_p one must also take into account the quark and gluon distribution functions $f(x'_p, Q^2)$ for all $x_p < x'_p < 1$.

At large x_p the dominant effect is from valence quarks radiating gluons, which causes the high x_p quark densities and hence F_2 to fall with Q^2. Conversely, at small x_p, F_2 rises with Q^2 because the number of $q\bar{q}$ pairs and gluons in the partonic 'sea' increases. The observation of the strong rise in the cross section with decreasing x_p at large Q^2, and the discovery that this behaviour persists to relatively low $Q^2 \approx 2$ GeV^2, is one of the major discoveries of HERA to date [28].

If the rise in the parton distributions at small x_p were unlimited it would lead to saturation or violation of the unitarity bound. The area occupied by the gluons would become comparable to the size of the proton, implying that below a certain x_p the partons must begin to over lap. One solution is that the partons could recombine, and in this way the rise of the parton distribution functions would eventually be damped [29]. However this has not yet been seen.

2.5 DGLAP Evolution of Parton Distributions

In the leading log approximation (LLA) the evolution of the quark ($f_{\mathrm{q}}(x)$) and gluon ($f_{\mathrm{g}}(x)$) distributions with Q^2 is described using the Dokshitzer-Gribov-Lipatov-Altarelli-Parisi (DGLAP) equations [30]:

$$\frac{d\, f_{\mathrm{q}}(x_p, Q^2)}{d\ln Q^2} = \frac{\alpha_s}{2\pi}\int_{x_p}^{1}\left[P_{\mathrm{q}\to\mathrm{q}}\left(\frac{x_p}{x_p{}'}\right) f_{\mathrm{q}}(x_p{}', Q^2) + P_{\mathrm{g}\to\mathrm{q}}\left(\frac{x_p}{x_p{}'}\right) f_{\mathrm{g}}(x_p{}', Q^2)\right]\frac{dx_p{}'}{x_p{}'} \tag{2.13}$$

$$\frac{d\, f_{\mathrm{g}}(x_p, Q^2)}{d\ln Q^2} = \frac{\alpha_s}{2\pi}\int_{x_p}^{1}\left[\sum_{\mathrm{q}} P_{\mathrm{q}\to\mathrm{g}}\left(\frac{x_p}{x_p{}'}\right) f_{\mathrm{q}}(x_p{}', Q^2) + P_{\mathrm{g}\to\mathrm{g}}\left(\frac{x_p}{x_p{}'}\right) f_{\mathrm{g}}(x_p{}', Q^2)\right]\frac{dx_p{}'}{x_p{}'} \tag{2.14}$$

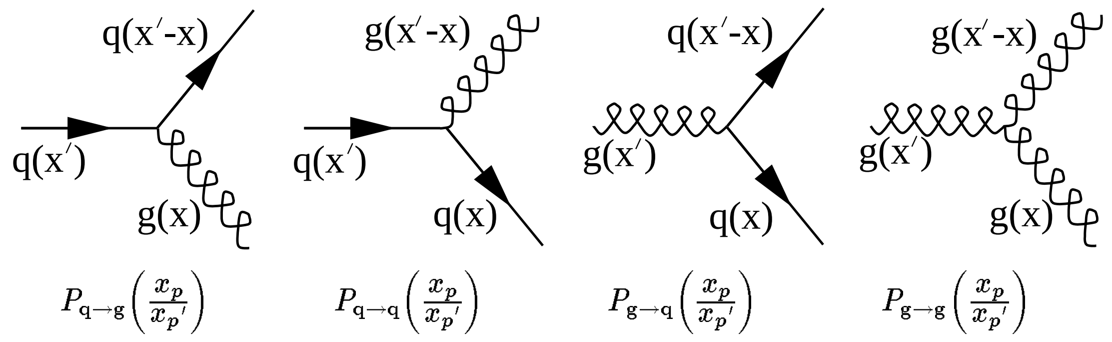

Figure 2.3: *First order representations of the splitting functions $P_{ij}\left(\frac{x_p}{x'_p}\right)$, used in the DGLAP equations.*

where $P_{\mathrm{a}\to\mathrm{b}}\left(\frac{x_p}{x_{p'}}\right)$ is the probability that a parton a with momentum fraction x'_p becomes parton b with momentum fraction x_p, by the emission of another parton, as the scale changes from Q^2 to $Q^2 + d\ln Q^2$. These splitting functions, to first order, are illustrated in figure 2.3.

The formal derivation of the DGLAP equations in the LLA sums to all orders terms of the form $(\alpha_s \cdot \ln Q^2)^n$. These terms give the dominant contribution at large $Q^2$and large x. In a field theory with asymptotic freedom such an approximation proves to be asymptotically exact. The amplitude for the inelastic ep scattering process is then obtained as the sum of ladder diagrams of consecutive gluon emissions (fig 2.4). The final struck quark evolves from the incoming proton via this gluon emission, gradually losing its longitudinal momentum. The rungs of the ladder are strongly ordered in transverse momentum so that:

$$k_{t_1}^2 \ll k_{t_2}^2 \ll \ldots \ll k_{t_{n-1}}^2 \ll k_{t_n}^2 \ll Q^2$$

The solutions of the DGLAP equation give how the parton distribution functions $f_i(x_p)$ vary with Q^2, but make no prediction about the x_p dependence at fixed Q^2. Therefore it is necessary to provide an input x_p dependence at some Q_0^2, which can then be evolved to higher Q^2. At present this Q_0^2 cannot be calculated but has to be determined experimentally.

At small x_p terms involving $\ln\frac{1}{x_p}$, which are neglected in the derivation of the DGLAP equations, may become important. The summing of leading $\ln\frac{1}{x_p}$

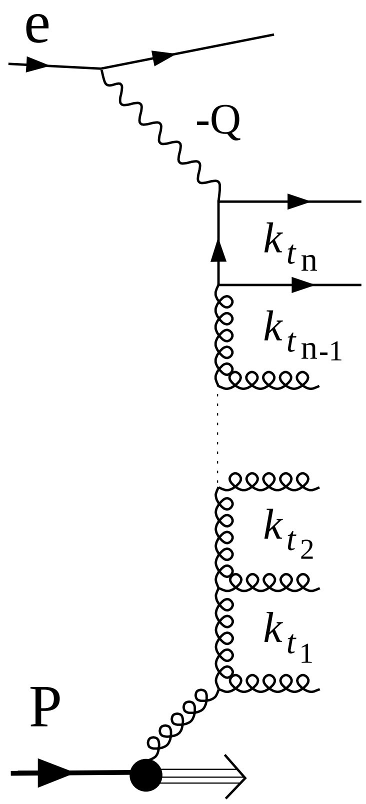

Figure 2.4: *A ladder diagram, illustrating the parton evolution*

terms, independent of $\ln Q^2$, results in the Balitsky-Fadin-Kuraev-Lipatov (BFKL) equation, which could be used to describe the evolution of the structure functions to very small x_p [31]. At moderate x_p region, where $\alpha_s(Q^2)\ln Q^2 \ll 1$ and $\alpha_s(Q^2)\ln\frac{1}{x_p} \ll 1$, but $\alpha_s(Q^2)\ln Q^2 \ln\frac{1}{x_p} \sim 1$, the Double Leading Logarithm Approximation (DLLA) is used in the DGLAP approach. Here leading terms in $\ln\frac{1}{x}$ are summed when they also contain a leading $\ln Q^2$ dependence, resulting in a small x_p behaviour of the gluon density like [32]

$$x_p g(x, Q^2) \approx \exp\sqrt{\ln\left[\frac{Q^2}{Q_0^2}\right]\cdot\ln\frac{1}{x_p}},$$

where Q_0^2 is the starting scale. Given a long enough evolution length from Q_0^2 to Q^2, this will generate a steeply rising gluon distribution at small x_p, even if the gluon distribution input at Q_0^2 is relatively flat. This rise is then faster than any power in $\ln\frac{1}{x_p}$, but slower than any power of x. Over a limited x, Q^2 range, as is the case at HERA, the x_p dependence of the gluon distributions from the BFKL equation ($x_p g(x_p, Q^2) \sim {x_p}^{-1/2}$) is very similar to that of the DGLAP evolution ($x_p g(x_p, Q^2) \sim exp\sqrt{\ln 1/x_p}$)[33]. This means that experimentally a differentiation is not possible.

2.6 Photoproduction

As mentioned earlier, most of the total ep cross section comes from the exchange of virtual photons. In the very low Q^2 interactions of photoproduction it is useful to consider the scatters in two parts, first the radiation of the photon, and then the photon interaction with a parton in the proton. The radiation of the virtual photons from the incoming electron is an elementary QED process and can therefore be calculated with no further assumptions. The electron beam can then be regarded as a source for massless quasi-real photons ($q^2 \equiv p_\gamma^2 \approx 0$) emitted collinear to the beam line. Thus the ep cross section can be expressed in terms a photon flux $f_\gamma^e(y)$ and the cross section for virtual photon proton scattering $\sigma_{tot}^{\gamma p}$ [34].

The function $f_\gamma^e(y)$ can be thought of as the probability to find a photon of energy $E_\gamma = yE_e$ in the electron. For $Q^2 > 0$ the photons may have both longitudinal and transverse polarisation. Thus total cross section can be expressed as the sum of the absorption cross sections for transversely and longitudinally polarised photons, σ_T and σ_L respectively.

$$\sigma_{tot}^{\gamma p} = \sigma_L + \sigma_T \tag{2.15}$$

So the ep cross section can be written as:

$$\sigma(ep \to e\mathrm{X}) = \int \left[f_{\gamma_T}^e(y)\sigma(\gamma_T p \to \mathrm{X}) + f_{\gamma_L}^e(y)\sigma(\gamma_L p \to \mathrm{X}) \right] dy \tag{2.16}$$

In the DIS limit of large Q^2 the structure functions are related to σ_T and σ_L by

$$F_1 \approx \frac{Q^2}{8x\pi^2\alpha} \cdot \sigma_T \tag{2.17}$$

$$F_2 \approx \frac{Q^2}{4x\pi^2\alpha} \cdot (\sigma_T + \sigma_L) \tag{2.18}$$

In this way one obtains:

$$\frac{d^2\sigma^{ep}}{dydQ^2} = \frac{\alpha}{2\pi}\frac{1}{Q^2}\left[\left(\frac{1+(1-y)^2}{y} - 2\frac{(1-y)}{y}\frac{Q^2_{min}}{Q^2}\right)\sigma_T^{\gamma p}(y,Q^2) + 2\frac{(1-y)}{y}\sigma_L^{\gamma p}(y,Q^2)\right] \tag{2.19}$$

where $Q^2_{min} = m_e^2\frac{y^2}{1-y}$ is the kinematic lower bound [35]. In the limit $Q^2 \to 0$ the photons are only transversely polarised. $\sigma_L^{\gamma p}$ must therefore disappear and $\sigma_{tot}^{\gamma p} = \sigma_T^{\gamma p}$. Hence the low Q^2 ep cross section can be approximated to.

$$\frac{d^2\sigma^{ep}}{dydQ^2} = f_\gamma^e(y,Q^2)\sigma_{tot}^{\gamma p}(y,Q^2), \tag{2.20}$$

where

$$f_\gamma^e(y,Q^2) = \frac{\alpha}{2\pi}\frac{1}{Q^2}\left(\frac{1+(1-y)^2}{y} - 2\frac{(1-y)}{y}\frac{Q^2_{min}}{Q^2}\right) \tag{2.21}$$

gives the photon flux. This is know as the *equivalent photon approximation* (EPA). If one restricts one's self to the region of very small Q^2, then the Q^2 dependence of $\sigma_{tot}^{\gamma p}$ can be neglected and integrated over. This gives the often used Weizacker-Williams Approximation (WWA) [36].

$$f_\gamma^e(y) = \frac{\alpha}{2\pi}\left[\frac{1+(1-y)^2}{y}\ln\frac{Q^2_{max}}{Q^2_{min}} - 2\frac{(1-y)}{y}\left(1-\frac{Q^2_{min}}{Q^2_{max}}\right)\right] \tag{2.22}$$

Q^2_{max} is the upper limit on the photon virtuality, which is usually fixed by experimental criteria. Now the photon flux is known to a good accuracy, attention can be turned to the γp scattering.

2.7 Photon-Proton Scattering

The photon is the gauge boson of QED, which implies that it is massless and structureless, i.e. pointlike. However Heisenberg's uncertainty principle tells us that a photon can, for short periods of time, fluctuate into a pair of charged particles. Fluctuations into two leptons are well understood, and are an important factor in the quantitative success of QED. Fluctuations into $q\bar{q}$ pairs, on the other hand, are much more problematic. If the life time of the virtual $q\bar{q}$ pair is long enough it can evolve into a complex hadronic state that cannot be described by perturbative methods alone [37]. Understanding these virtual hadronic states becomes particularly important when they are kicked on mass shell by an interaction of the photon. One can therefore expect hadronic photon reactions to be suited to the study of both perturbative and non perturbative aspects of strong interactions. γP interactions allow us to probe some aspects of the hadronic nature of the photon.

The fact that the photon behaves like a hadron in many ways allows us to borrow a lot of the terms and methods of Hadron-Hadron scattering, the difference being that photons, unlike hadrons, also couple to quarks in a point like way. It should be noted that, at present, the theoretical description of γP scattering is if any thing more complex than that of $P\bar{P}$ scattering. However it is still reasonable to argue that γp collisions are simpler at some fundamental level since, however complex it becomes, the hadronic nature of the photon originates from a single $\gamma q\bar{q}$ vertex. HERA increased the center of mass energy available for hard γp interactions by about a factor 10 over earlier experiments.

2.7.1 Direct Photon Interactions

These are the hard interactions in which the photon interacts in a pointlike manner. The photon enters completely into the interaction of the hard subprocess, and couples directly to a parton from the proton. This is unique to photons as opposed to hadrons for example which are composite objects. The dominant leading order diagrams for direct photons are shown in figure 2.5. In (a) the photon couples to a quark in the proton, which then achieves a high virtuality, and via the emission of a gluon becomes real once again. This is known as QCD Compton scattering. In (b) the photon couples to a quark in a quark antiquark pair produced by a gluon from the proton, this is known as photon gluon fusion. Since the whole photon

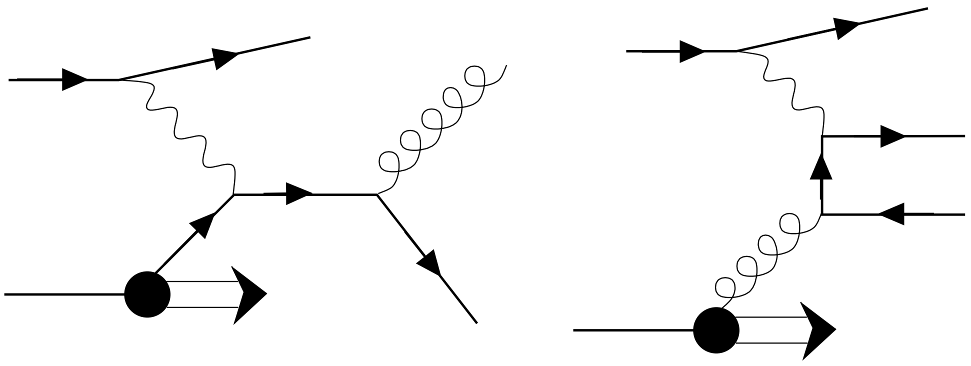

Figure 2.5: *Leading order direct processes. (a) QCD Compton (b)Photon gluon fusion*

enters the hard subprocess in these interactions, it can be expected that they will have higher transverse momenta than the hadronic type interactions in which only a part of the photon participates.

As mentioned at the start of this chapter, the high photon virtuality (Q^2) in DIS ensures that the processes shown above can be calculated in pQCD. In photoproduction a hard scale is provided if the two outgoing partons have high, equal and opposite transverse momentum. In the case of photon gluon fusion, the virtuality of the photon in DIS plays an analogous role to the virtuality of the internal quark line which resolves the gluon in the proton. Therefore these direct photon photoproduction events can only occur when the transverse momentum, and hence the resolution, is high enough to 'see' the partons in the proton.

Photoproduction processes are more directly sensitive to the gluon distribution in the proton than high Q^2 DIS. In DIS the proton is probed by a photon, which can not couple to the gluons directly, whereas in photoproduction it is probed by quarks and gluons which can.

2.7.2 Vector Meson Dominance

In early fixed target experiments, such as WA57, it was noted that the photon behaved like a vector meson in its interaction with the proton. The vector mesons

V=ρ^0, ω, ϕ.... have the same quantum numbers as the photon and it is therefore possible for the photon to fluctuate into one of these states for a short time. In this Vector Meson Dominance (VMD) model [39], the photon-proton cross section is [40]:

$$\sigma^{\gamma \mathrm{p}}_{\mathrm{VMD}}(W) = \sum_{\mathrm{V}=\rho^\circ,\omega,\phi} \frac{4\pi\alpha}{f_{\mathrm{V}}^2}\sigma^{\mathrm{Vp}}(W), \tag{2.23}$$

where the f_{V} are the specific scaling factors which give the probability that the photon will fluctuate into any given meson V. One finds $\frac{f_{\mathrm{V}}^2}{4\pi} = 2.20, 23.6, 18.4$ for ρ°, ω, ϕ, and can deduce from this that there is a 4% probability that a high energy photon will interact as a vector meson. The fact that these processes dominate can be explained by the large cross section σ^{Vp} for the vector meson-proton scattering. The life time of such vector meson fluctuations can be estimated as

$$t_{fl} = \frac{2E_\gamma}{m_{\mathrm{V}}^2 + Q^2}. \tag{2.24}$$

where E_γ is the energy of the photon, and m_V is the mass of the vector meson. As t_{fl} is inversely proportional to Q^2, the probability that such fluctuations occur in DIS is strongly suppressed. However in the rest frame of the proton $x_p = Q^2/(2m_{\mathrm{p}}E_\gamma)$, and $t_{fl} \sim {x_p}^{-1}$, so these hadronic manifestations of the photon do play some role at small x_p.

VMD photon processes can be both soft, where no significant transverse momentum is produced, and hard, where the final state particles have large transverse momentum. The high p_t of the hard processes indicates that the vector mesons and the proton don't interact as a whole, rather that there was an interaction between their component partons. In this way partonic scattering processes arise in photoproduction which can be described using pQCD. As opposed to DIS, where it is Q^2 that gives both a hard scale and the ability to resolve partonic structure, in these processes it is the p_t^2 of the scatter.

2.7.3 Anomalous Photon Interactions

The VMD model takes into account the cases in which $q\bar{q}$ pairs of small mass arising from fluctuations of the photon have enough time, via the evolution of a cloud of soft gluons, to form vector mesons. The production of unbound quark anti-quark pairs of higher virtuality leads to an additional component, the *anomalous photon.* This state is another way in which the hadronic photon differentiates itself from a normal hadron. The high virtuality of the quark-antiquark pair and the associated high transverse momentum of the quarks at the $\gamma \rightarrow q\bar{q}$ vertex mean anomalous photon processes can be calculated in pQCD [38]. As the partons from the anomalous photon have a harder transverse momentum distribution than those from vector mesons, high transverse momentum processes are dominated by anomalous and direct photons. Bearing this in mind it was initially hoped that it would be possible to calculate the entire interaction at these high transverse momenta using pQCD. It turns out however that, in the limit of very small momentum fractions, singularities arise for both the anomalous and VMD photons. Only the sum of the two contributions gives a finite result. Therefore the VMD-fraction can not be neglected even at high transverse momenta.

2.7.4 Resolved Photon Interactions

In the two previous sections the VMD and anomalous photons were discussed separately. However the separation between these two components is not very well defined, rather there is a continuous transition from one to the other. In a model where they are handled separately the transition point must be given by a suitable phenomenological cut on the invariant mass of the quark-antiquark pair. Usually however the two components are combined as the *resolved photon.* This is a generic label used for all cases in which the photon acts as a source of partons for the hard scatter.

In resolved photon events there is a photon remnant formed by the partons from the photon which didn't take part in the scatter. The partons in this photon remnant continue in approximately the direction of the incoming photon. In the case of the VMD photon, in the same way as in the proton remnant, the partons have a small intrinsic momentum component k_t perpendicular to the photon direction $d\sigma/dk_t^2 \sim e^{-bk_t^2}$. For the anomalous photons one expects a harder spectrum $d\sigma/dk_t^2 \sim 1/k_t^2$, due to the $\gamma \rightarrow q\bar{q}$ vertex. Experimental evidence for this has been found [41]. As the invariant mass of the quark-antiquark pair produced by the photon rises there will come a point when the transverse momentum of the photon remnant will be of the same order as the transverse momentum produced in the hard sub-process. Here there is a continuous transition from anomalous to direct photons, where the highest transverse momentum is produced at the photon vertex.

In summary, at this point it is conventional to separate the total photon-proton interaction cross section into VMD, anomalous and direct photons:

$$\sigma_{tot}^{\gamma p} = \sigma_{VMD}^{\gamma p} + \sigma_{anom}^{\gamma p} + \sigma_{dir}^{\gamma p} \tag{2.25}$$

If no differentiation is made between the VMD and anomalous this becomes:

$$\sigma_{tot}^{\gamma p} = \sigma_{res}^{\gamma p} + \sigma_{dir}^{\gamma p} \tag{2.26}$$

2.8 Description In Lowest Order

An important feature of the QCD improved parton model is that γp cross sections can be written as a convolution of a short range perturbative part, describing the hard scatter, and a long range non-pertubative part, for the parton distribution functions [42]. Figure 2.6 shows hard photon-proton interactions in lowest order.

The dotted lines (μ's) show the factorisation scale where we choose to separate the hard process from the non perturbative parton distribution functions. μ_γ and

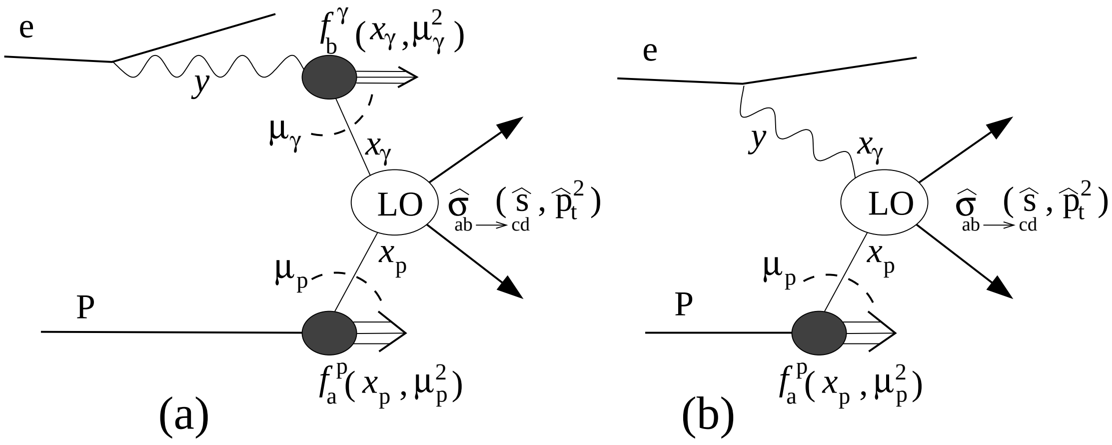

Figure 2.6: *Schematic diagrams of the leading order Photoproduction processes for (a) resolved and (b) direct photons*

μ_p are in principle arbitrary, but a common choice is $\mu_p^2 = \mu_\gamma^2 = \mu^2 = \hat{p}_t^2$, where $\hat{p}_t^2$ is the transverse momentum of the outgoing partons from the hard scatter. μ^2 enters into the photoproduction cross section in the same ways that Q^2 does in DIS, and gives the apparent resolution with which the structures of the photon and the proton can be sampled.

The Photon emitted from the electron is quasi-real ($Q^2 \approx 0$) and in this limit y simply becomes the fraction of the electron energy carried by the photon $y = E_\gamma/E_e$. Similarly to x_p for the proton, x_γ is the fraction of the photon momentum entering the hard sub process $\hat{\sigma}_{\mathrm{ab}\rightarrow\mathrm{cd}}$. Unlike in higher orders (see section 2.9), in this lowest order there is a clear distinction between resolved and direct processes. With the direct case the whole of the photon takes part in the interaction and x_γ=1, conversely for the resolved case $x_\gamma < 1$.

The leading order cross section, as a function of the transverse momentum $\hat{p}_t$ of the hard interaction is [43]:

$$\frac{d\sigma^{ep}}{d\hat{p}_t^2} = \sum_{\mathrm{a,b}} \int\int\int f_\gamma^e(y) f_{\mathrm{b}}^\gamma(x_\gamma,\mu_\gamma^2) \frac{d\hat{\sigma}^{\mathrm{ab}\rightarrow\mathrm{cd}}(\hat{s},\hat{p}_t^2)}{d\hat{p}_t^2} f_{\mathrm{a}}^p(x_p,\mu_{\mathrm{p}}^2) dx_p dx_\gamma dy. \qquad (2.27)$$

This factorisation scale μ is an artificially introduced parameter, on which the results of a full QCD calculation must not depend. However any theoretical calculation will exhibit a strong sensitivity to variations in the factorisation scales since, while the $2 \to 2$ hard sub process contains no dependence upon the μ_a, the parton distribution functions certainly do (see section 2.10). This results in a large uncertainty in the theoretical predictions.

$\hat{\sigma}_{\mathrm{ab}\to\mathrm{cd}}(\hat{s}, \hat{p}_t^2)$ is the cross section for the hard sub process and is calculable in pQCD. The direct photon diagrams for these scatters are those shown in figure 2.5, and for the resolved photon it is all lowest order $2 \to 2$ QCD diagrams. A summary of the possible processes and the results of the lowest order QCD calculations is given in [44]. As well as depending on the center of mass energy $\sqrt{\hat{s}} = \sqrt{y x_\gamma x_p s}$, $\hat{\sigma}_{\mathrm{ab}\to\mathrm{cd}}(\hat{s}\hat{p}_t^2)$ also depends on the scattering angle of the outgoing partons. This is implicit in the above given that $\hat{p}_t^2 = \frac{\hat{s}}{4}(1 - \cos^2\theta^*)$, where θ^* is the angle between the out going partons and the beam direction in their center of mass system. The different subprocesses possess quite different angular distributions, and in particular for $|\cos\theta^*| \to 1$, i.e. small scattering angles, the cross sections for resolved photon processes rise much faster than the direct [45]. Hence restricting the scattering angle θ^* in any measurement will have an impact on the relative fractions of the different processes.

2.9 Higher Order and Fragmentation Corrections

At the scale of a few GeV relevant to photoproduction, the strong coupling constant α_s has a relatively high value $\sim$0.2. From this it may be assumed that higher order corrections will have a significant effect.

Above leading order the fact that the hard subprocess can radiate off 3 partons into the final state, as well as virtual corrections to the 2 parton final state must be accounted for. There are divergences associated with these NLO terms which arise when parton loops occur in internal lines, and when one parton splits into two parallel travelling partons. However when an integration over all possible diagrams is performed these divergences either cancel or can be factorised into the parton distribution functions.

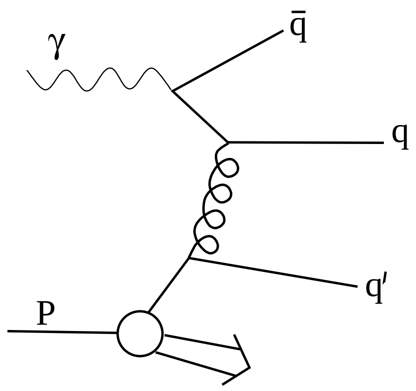

Figure 2.7: *Example of a diagram that can be interpreted as either NLO direct or LO resolved or direct.*

Though the separation can no longer be defined uniquely, interactions can still be classified as direct or resolved. Varying μ_γ affects the amount of the NLO $2 \rightarrow 3$ processes that should really be counted as lowest order resolved, in particular the amount of NLO direct from diagrams such as figure 2.7 that should rightfully be factorised into the LO resolved changes. Hence including NLO contributions reduces the strong dependence upon the factorisation scales present in the LO calculations, since these diagrams are always included in one way or another.

Several groups have made calculations in the last few years including [46–48]. The inclusion of NLO diagrams produces corrections to the calculated cross section for $\mu = \hat{p}_t$ of up to 50% in parts. For the most part, however, the corrections just raise the cross section by some constant factor K, and the form remains fundamentally the same.

Apart from the NLO interaction corrections, the outgoing partons must go through some process in which they form the observed hadrons. The first step is to fragment the single outgoing partons into a spray of many partons. One approach is to use the leading log approximation, summing terms of the form $(\alpha_s ln(\mu^2/\mu_0^2))^n$. As with the DGLAP evolution, these leading terms correspond to successive radiations from partons and are described by the splitting functions $P_{a\rightarrow b}(z)$, where z is the fraction of parton a's momentum carried by parton b.

There is a strong ordering in transverse momentum k_t of the radiated partons, and hence in the virtualities μ^2 along the cascade. It begins at the scale of the hard sub process, and reduces monotonically with each successive radiation. This approximation, again similarly to the DGLAP evolution, becomes exact in the limit of small transverse momentum. High transverse momentum radiations that are not accurately dealt with by this approximation are ideally covered by the matrix element of the hard subprocess. This way of approaching the problem is known as the parton shower model.

The parton shower of the outgoing partons is broken off, when the scale μ^2 is of the order of the hadron masses. At this point the final transition into hadrons needs to be described. This is a soft process in which long range colour interactions play a role. Therefore, unlike the parton shower described above, it can not be calculated in pQCD and a phenomenelogical hadronisation model must be used (see chapter 4).

The above method can also be used to describe the production of the incoming partons by working back from the hard scatter to the original incoming hadronic states. The large technical advantage of this method is that the corrections due to higher order processes can be dealt with as a series of parton emissions. Another method is to use the *string model* described in section 4.2

2.10 Photon Parton Distribution functions

By analogy to hadrons, the structure of the photon is described using parton distribution functions. While the hadronic structure of the photon certainly has non perturbative aspects, it must all originates from a $\gamma q\bar{q}$ vertex, however complicated it becomes. No such (in principle) simple starting point can be defined for normal hadrons such as the the proton, constituent quarks themselves being highly complicated objects.

The first thing to consider is that the photon appears in three forms. Taking this into account its parton distribution function can viewed as:

$$f_a^{\gamma}(x_\gamma, \mu^2) = f_a^{dir}(x_\gamma, \mu^2) + f_a^{anom}(x_\gamma, \mu^2) + f_a^{VMD}(x_\gamma, \mu^2) \tag{2.28}$$

Fluctuations into hadronic states are suppressed by a factor of the order $\alpha = \frac{1}{137}$, so that most of the time the photon appears as an elementary photon. In this state it interacts as a direct photon coupling to a charged quark or lepton in a point like manner. Despite the fluctuations being suppressed, interactions of the hadronic photon dominate simply because the cross section for their scattering with the proton is much larger than for the direct photon.

Normally $f_a^{dir}(x_\gamma, \mu^2)$ is not considered a parton distribution as such, and direct photon processes are calculated separately. The photon parton distribution function then consists of a pertubatively calculable part ($\gamma \rightarrow q\bar{q}$) and a nonpertubative part characterised by the VMD model where the photon fluctuates into a bound $q\bar{q}$ state. This leaves [49]:

$$f_a^{res}(x_\gamma, \mu^2) = f_a^{anom}(x_\gamma, \mu^2) + f_a^{VMD}(x_\gamma, \mu^2) \tag{2.29}$$

The anomalous part is calculable with equation 2.22. According to this the probability $f_\gamma^q(y)$ that a quark emits a photon with momentum fraction y is:

$$f_\gamma^q(y) = \frac{e_q^2 \alpha}{2\pi} \left(\frac{1 + (1-y)^2}{y} \right) \ln \frac{Q^2_{max}}{Q^2_{min}}. \tag{2.30}$$

where the second term in the brackets of equation 2.22 has been neglected. Using this the probability $f_q^\gamma(x_\gamma)$ that the photon fluctuates into a $q\bar{q}$ pair is given by:

$$f_q^\gamma(x_\gamma) = N_f x_\gamma f_\gamma^q(1/x_\gamma) \tag{2.31}$$

where N_f is the number of quark flavours, so that

$$f_q^{anom,LO}(x_\gamma, Q^2) = N_f \frac{e_q^2 \alpha}{2\pi} \left({x_\gamma}^2 + (1 - x_\gamma)^2 \right) \ln \frac{Q^2}{m_q^2}. \tag{2.32}$$

Here the Q^2 from equation 2.22 has been replaced with the virtuality of the $q\bar{q}$ pair to which the anomalous photon couples. This is bounded below by its mass and above by the scale μ^2 of the hard process. Were it bigger, the $\gamma \to q\bar{q}$ vertex would have to be considered the hard process. This means that the anomalous part in the photon parton distribution depends on μ^2 at the lowest order, and therefore no scale invariance is shown. As mentioned earlier, this scale dependence doesn't occur for hadrons until higher orders when the radiation of gluons is included. Apart from this the parton density rises for all x_γ with μ^2. In the proton it rises with $\mu^2(Q^2)$ only for small x_p, while for large x_p it falls with $\mu^2(Q^2)$. This can be understood in that, in the language of the proton, the q$\bar{\text{q}}$ pair in the photon are sea quarks, and as μ^2 becomes smaller they can't be separately resolved.

The interaction cross section for the hard sub process with anomalous photons is of the order α_s^2. However given $\alpha_s \sim \frac{1}{ln\frac{\mu^2}{\Lambda_{QCD}}}$, then $f_q^{anom,LO}(x_\gamma, \mu^2) \sim \frac{\alpha}{\alpha_s}$. Consequently the photon-proton cross section is of the order $\alpha\alpha_s$. This means that anomalous photon proton interactions are of the same order as direct photon proton interactions.

The radiation of gluons from the $q\bar{q}$ pair can be described by slightly modified versions of the DGLAP equations as used for the proton (eqns 2.13):

$$\frac{d\,f_q^\gamma(x_\gamma,\mu^2)}{d\ln\mu^2} = 3e_q^2\frac{\alpha}{2\pi}\left({x_\gamma}^2 + (1-x_\gamma)^2\right)$$
$$+\frac{\alpha_s}{2\pi}\int_{x_\gamma}^{1} P_{q\to qg}\left(\frac{x_\gamma}{x_\gamma{}'}\right) f_q^\gamma({x_\gamma}',\mu^2) + P_{g\to q\bar{q}}\left(\frac{x_\gamma}{x_\gamma{}'}\right) f_g^\gamma({x_\gamma}',\mu^2)\frac{d{x_\gamma}'}{{x_\gamma}'} \quad (2.33)$$

$$\frac{d\,f_g^\gamma(x_\gamma,\mu^2)}{d\ln\mu^2} = \frac{\alpha_s}{2\pi}\int_{x_\gamma}^{1}\sum_{q,\bar{q}} P_{q\to gq}\left(\frac{x_\gamma}{x_\gamma{}'}\right) f_q^\gamma({x_\gamma}',\mu^2) + P_{g\to gg}\left(\frac{x_\gamma}{x_\gamma{}'}\right) f_g^\gamma({x_\gamma}',\mu^2)\frac{d{x_\gamma}'}{{x_\gamma}'} \quad (2.34)$$

The $\gamma \to q\bar{q}$ vertex necessitates an additional inhomogeneous term for the quark densities in the photon. This is the first term on the right hand side of equation 2.33.

The quarks with large x_γ originate predominately from the $\gamma \to q\bar{q}$ vertex directly. Due to the electromagnetic coupling at this point four times as many u quarks are produced as d quarks. At small x_γ conversely the quarks come predominately from pair production by gluons. The strong interaction doesn't differentiate between the quark charges, so that here equal numbers of u and d quarks are produced. The equivalent statements are true for the heavy quarks.

In addition to the anomalous photon contributions, the VMD part is needed to cover the production of bound $\mathrm{q\bar{q}}$ pairs. This fraction, which is not perturbatively calculable, is expressed using the parton distributions of the vector mesons f^V as:

$$f_a^{VMD}(x_\gamma, \mu^2) = \sum_{\mathrm{V}} \frac{4\pi\alpha}{f_{\mathrm{V}}^2} f_a^{\mathrm{V}}(x_\gamma, \mu^2). \tag{2.35}$$

The relatively accurately measured parton densities of the pion are used for the f^V. The only free parameter in the VMD model are the constants f_V^2.

If the VMD part is considered separate from the anomalous part its evolution can be describe by the hadronic DGLAP equations without the inhomogeneous term. In both the VMD and anomalous parts $f_{\mathrm{q}}^\gamma = f_{\bar{q}}^\gamma$.

The rise of the quark distributions with μ^2 in the anomalous photon ensures it dominates ever more over the VMD photon as the scale increases. It is, however, not possible to neglect the VMD part and still obtain a real QCD prediction of the photon structure. This is because, considered separately as $x_\gamma \to 0$, both parts contain singularities, and only the sum is finite.

It is obvious that there must be a gradual and continuous transition between the VMD and the anomalous contributions. For small transverse momentum p_t of the quarks at the $\gamma \to \mathrm{q\bar{q}}$ vertex they become a bound state, which is represented by the VMD part. When the p_t becomes larger than about half the mass of the lightest vector meson, the anomalous state arises. The gives a way to combine the two parts by using this mass as the lower limit on the virtuality of the $\mathrm{q\bar{q}}$ pair in equation 2.32.

A number of different parameterisations of the parton distributions in the photon have been proposed. A few of these, those that will later be compared to data, will be briefly described here. These include only parameterisations which include both the VMD and the anomalous parts. All parameterisations begin with an assumed form, based on the above discussion, for small μ_0^2, and containing some particular set of free parameters. This form is then evolved, using the DGLAP equations 2.33, 2.34, to the μ^2-values of existing measurements from photon-photon interactions, and the free parameters are determined by fitting to these measurements. The only experimental input for these distributions to date comes from the measurement of $F_2^\gamma(x, Q^2)$ in DIS ($e\gamma \to eX$) interactions at e^+e^- colliders.

Drees and Grassie (DG)

In 1984 Drees and Grassie produced the first parameterisation to start from input distributions [50]. At the time of this fit, only a single measurement of F_2^γ at fixed $\mu^2 \approx 5.3$ GeV^2 existed. In order to determine the input distributions two assumptions were made. Firstly all input quark densities were assumed to be proportional to the squared quark charges, i.e. $u^\gamma = 4d^\gamma = 4s^\gamma$ at μ_0^2=1 GeV^2, for all x_γ, and the gluons in the photon only arise through QCD emissions in the DGLAP evolution. The x_γ dependence of the quark distributions was separated into a hadronic (${x_\gamma}^\alpha(1-x_\gamma)^\beta$) and an anomalous (${x_\gamma}^2+(1-x_\gamma)^2$) part. They chose $\mu_0^2 = 1$ GeV^2 and fitted the free parameters to the available data (PLUTO, 7 Data points at $\mu^2 = 5.9$ GeV^2). This parameterisation only exists in LO. Moreover, it treats flavour thresholds by introducing three independent sets of distributions for $N_f = 3, 4, 5$ so that the transition across a threshold is not automatically smooth.

Levy, Abramowicz and Charachula (LAC)

These parameterisations are based on a much larger data set. By 1990 the number of data points had been greatly enlarged by measurements at PETRA, PEP and TRISTAN. Levy, Abramovicz and Charchula used these for a more exact analysis of the parton densities in the photon [51]. The quark densities are assumed similar to Drees and Grassie, but a hadronic distribution $({x_\gamma}^\alpha(1-x_\gamma)^\beta)$ was added for the gluons at the starting scale μ_0^2. The main point of these fits was to demonstrate that data on F_2^γ constrained the gluon density in the photon f_g^γ very poorly. In particular they allow a very hard gluon, with $x_\gamma f_g^\gamma$ having a maximum at $x \approx 0.9$ (LAC3), as well as very soft gluons, with $x_\gamma f_g^\gamma$ rising steeply at low x_γ(LAC1,LAC2). LAC1 and LAC2 have a $\mu_0^2 = 4$ GeV^2, where LAC2, for $x_\gamma \to 0$, contains a smaller gluon fraction. LAC3 uses $\mu_0^2 = 1$ GeV^2, and the large gluonic part at large x_γ was achieved by including measurements down to 1.31 GeV^2 in the fit. All three parameterisations fitted the available data, though LAC3 has since been excluded by new measurement from TRISTAN, and the first HERA data [54, 55].

The LAC parameterisations exist only for $N_f = 4$ massless flavours and in LO. In all three LAC parameterisations gluons carry significantly more momentum than quarks for $\mu^2 \leq 20$ GeV^2 this is counter intuitive, since in known hadrons, and hence presumably in a VMD like low-μ^2 photon, gluons and quarks carry about equal momentum fractions, while at very high μ^2 the inhomogeneous evolution equations predict that quarks in the photon carry about three times more momentum than gluons.

Glück, Reya and Vogt (GRV)

This parameterisation is available at LO and NLO. The idea behind GRV parton distributions is to start from a very simple input at a very low input scale (0.25 GeV^2 in LO, and 0.3 GeV^2 in NLO). The observed structure is then generated 'dynamically' using the evolution equations [53].

$$\left(f_q^\gamma, f_g^\gamma\right)(x_\gamma, \mu_0^2) = \kappa \frac{4\pi\alpha}{f_\rho^2}\left(f_q^{\pi^0}, f_g^{\pi^0}\right)(x_\gamma, \mu_0^2). \tag{2.36}$$

This input is motivated by VMD ideas, where f_ρ^2 is the transition probability for $\gamma \to \rho$, and κ has been intruded to describe contributions from heavier vector mesons. κ is the only free parameter in this formulation, and is limited to the range $1 < \kappa < 2$. LO(NLO) fits to the data give a value of $\kappa = 2(1.6)$. Apart from the normalisation, the GRV parameterisation gives a real prediction of the quark and gluon distributions in the photon. However it should be made clear that equation 2.36 is an assumption that needs to be tested experimentally; In particular it is not obvious that the parton densities in a pion resemble those in a VMD photon, or that QCD is applicable at such small input scales. On the positive side the GRV parameterisation ensures a smooth onset of the charm density, using an x-independent threshold.

Gordon and Storrow (GS)

Gordon and Storrow developed their parameterisation shortly after GRV, but followed a quite different strategy [52]. Problems with low input scales are avoided by choosing $\mu_0^2 = 5.3$ GeV^2. This is certainly in the perturbative region, but necessitates a rather complicated form for the input distributions:

$$q_0^\gamma(x) = \kappa \frac{4\pi\alpha_{em}}{f_\rho^2} q_0^\pi(x, Q^2) + q_{anom}^\gamma(x, {Q^2}_0) \tag{2.37}$$

This is based on a sum of the anomalous contribution and the quark distributions in the pion. The free parameters in the fit are the momentum fractions carried by gluons and sea-quarks in the pion, the parameter κ, and the light quark masses. The fit to the data gives $m_u = m_d = 0.29$ GeV and κ =1.96, which are not unreasonable values. However, while this formulation holds in the perturbative region of μ^2, it is not invariant under the evolution equations. On the other hand, for practical purposes it includes a sufficient number of free parameters to allow a good description of the data. GS give a parameterisation in LO and NLO.

Figure 2.8 shows the comparison of the parameterisations described above for the gluon content, and the quark content for u, d, and s quarks. The different quark distributions differ by 20 to 30%. Conversely, the gluon densities, even if one ignores LAC3, differ by up to a factor 5. This clearly indicates that the the two

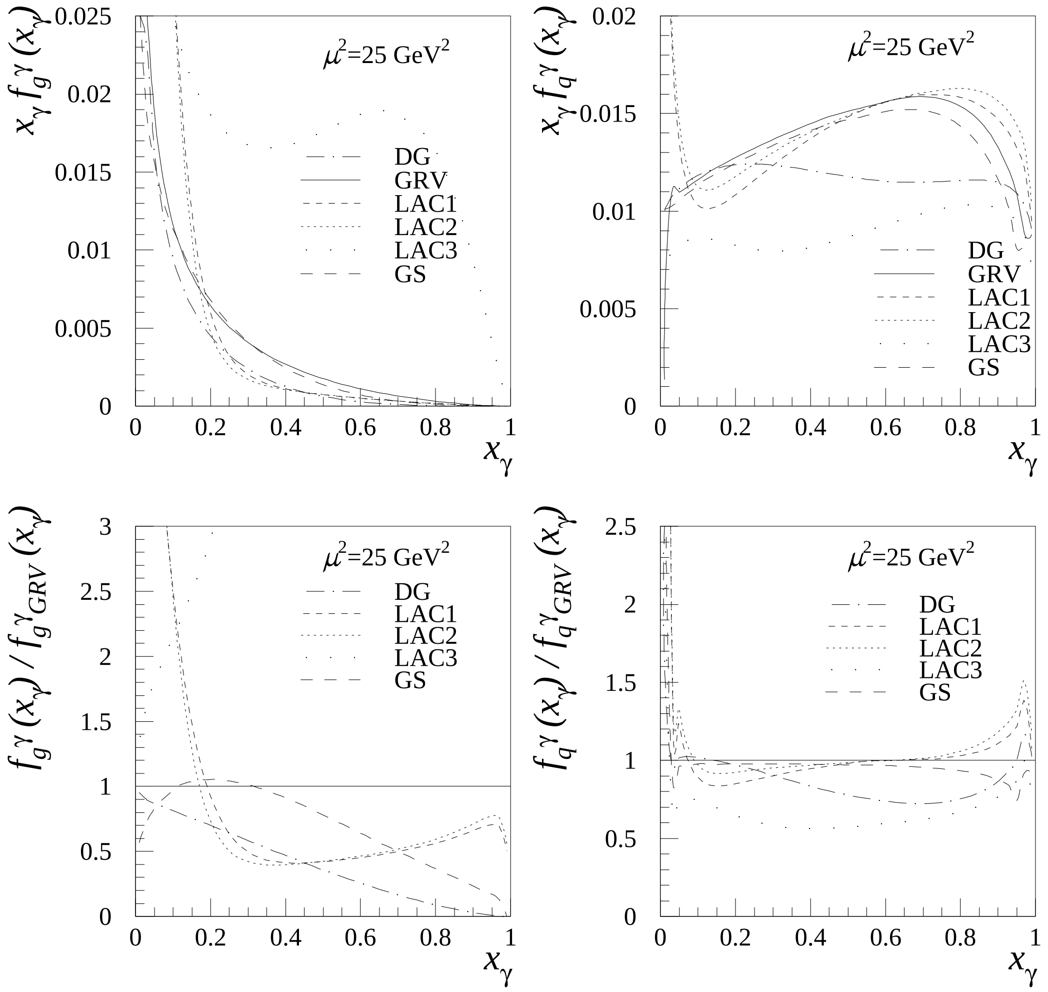

Figure 2.8: *Comparison of different photon parton distribution functions at a scale of $\mu^2 = 25$ GeV for: (a) The gluons, (b) up, down and strange quarks, (c)The gluons divided by the GRV-LO parameterisation, (d) the quarks (u,d,s) divided by the GRV-LO parameterisation.*

photon measurements made to date do nothing to restrict the gluon distributions in the photon.

Of course, jet cross sections in photoproduction at HERA will be dependent on the parton distributions of the proton and the photon. In particular, it has been suggested that dijet cross sections can be devised which are sensitive to the gluon distributions of the proton and the photon [56]. Also, the quark distributions in the photon are poorly constrained by the two photon measurements for $x_\gamma \to 1$. This is because for large x_γ the hadronic final state has a small invariant mass, which is hard to measure. This is a problem that is not present in hard photoproduction at

HERA, which means that this is another area where HERA can provide potentially useful information [46, 57].

2.11 Multiparton Interactions

There are two reasons why the model discussed so far cannot be complete.

I The QCD cross section

$$\frac{d\sigma^{\gamma\mathrm{p}}}{d\hat{p}_t^2} = \sum_{\mathrm{a,b}} \int \int f_{\mathrm{b}}^{\gamma}(x_\gamma, \mu^2) \frac{d\hat{\sigma}^{\mathrm{ab}\to\mathrm{cd}}(\hat{s}, \hat{p}_t^2)}{d\hat{p}_t^2} f_{\mathrm{a}}^{\mathrm{p}}(x_p, \mu^2) dx_p dx_\gamma \tag{2.38}$$

(cf. eqn. 2.27) diverges for $\hat{p}_t^2 \to 0$ approximately like $\frac{1}{\hat{p}_t^4}$. In the attempt to calculate the total non diffractive photon proton cross section of the form

$$\sigma_{QCD}^{\gamma\mathrm{p}}(\hat{p}_{tmin}^2) = \int_{\hat{p}_{tmin}^2}^{W^2/4} \frac{d\sigma^{\gamma\mathrm{p}}}{d\hat{p}_t^2} d\hat{p}_t^2 \tag{2.39}$$

a lower bound $\hat{p}_{tmin}$ must be introduced. This is reasonable since if the resolution, given by $\hat{p}_t$, becomes too small, the constituents can no longer be resolved, and there is no partonic interaction. It turns out, however, that even for relatively high lower bounds of $\hat{p}_{tmin} \approx 1.5$ to 2.0 GeV, the resulting cross section lies above the measured total non diffractive cross section.

II There is a higher energy flow outside the jets in the data than predicted by simulations based on the QCD model described so far [58–60]. The experimental evidence also shows that this extra energy is only found in resolved photon events [40, 61].

Point II is linked to the fact that in resolved photon processes, apart from the hard scatter, there can be further scatters between the hadronic photon and the proton. This is in contrast to the direct photon case where the extra energy flow doesn't appear. With the resolved photon and proton two extended objects with partonic content pass through each other. It is therefore possible that in this

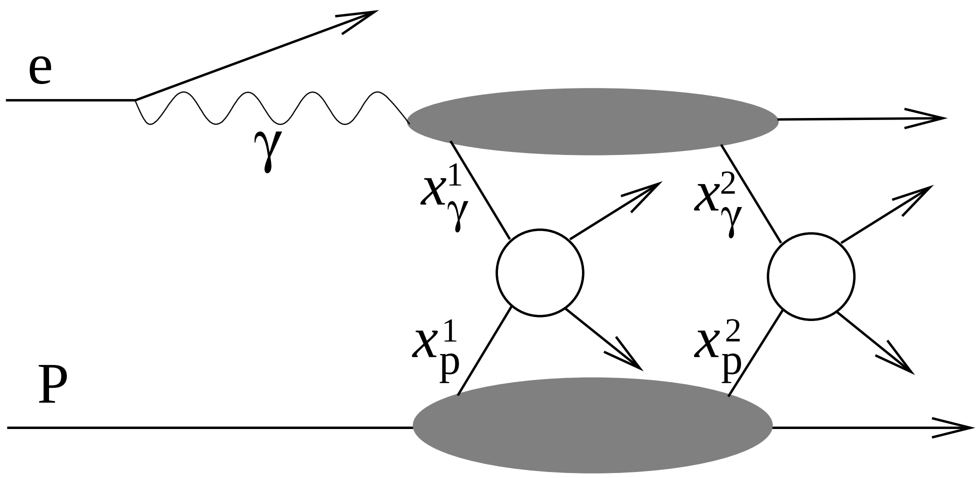

Figure 2.9: *Multiple interactions in a single photon proton collision*

sort of photon proton interaction, more than one pair of partons will interact (figure 2.9) [62]. This gives a solution for point I. The QCD cross section $\sigma^{\gamma p}_{QCD}(\hat{p}_{tmin})$ (equation 2.39) gives the frequency of parton-parton scatters, and for the QCD calculation the photon and proton beams are streams of free partons. No statement is made about the ordering of the individual photon proton scatters. The ratio of the QCD cross section $\sigma^{\gamma p}_{QCD}(\hat{p}^2_{tmin})$ and the total non diffractive photon proton cross section $\sigma^{\gamma p}_{nd} = \sigma^{\gamma p}_{ndVMD} + \sigma^{\gamma p}_{anom}$ then gives the average number of partonic interactions with $\hat{p}_t > \hat{p}_{tmin}$ per photon proton interaction:

$$\langle n \rangle = \frac{\sigma^{\gamma p}_{QCD}(\hat{p}_{tmin})}{\sigma^{\gamma p}_{nd}}. \tag{2.40}$$

The partonic QCD cross section is in this way reduced to the observed photon proton cross section, by combining the multiple partonic interactions (MI) into one photon proton interaction. If the interactions are taken to be independent, their number per event corresponds to a Poisson distribution about this average value of $\langle n \rangle$. The probability for exactly m such interactions is

$$P_m = \frac{\langle n \rangle^m}{m!} exp(-\langle n \rangle). \tag{2.41}$$

According to this there are no partonic interactions in a fraction $exp(-\langle n \rangle)$ of events. This corresponds to the fraction of soft non diffractive events contained in $\sigma^{\gamma p}_{nd}$.

From equation 2.24, the life time and hence the size of the hadronic fluctuation of the photon is bound up with its virtuality: The higher the virtuality, the smaller the hadronic state. In the context of multiple partonic interactions this means that with growing virtuality the additional interactions are suppressed. The description of MI given here has ignored this, and allowed MI in all resolved photon proton collisions. Models in which the VMD and anomalous photons are treated separately choose the other extreme and allow only one partonic interaction for anomalous photons (see sections 4.1.1 and 4.2.1).

Multiparton interactions have a direct effect on the hadronic final state of an event, and greatly complicate its interpretation. The observed jets now develop from the out going partons from a hard subprocess and further softer processes. In extreme cases the additional interactions could produce separate jets themselves. Therefore it is practically impossible to draw any conclusions about the partons from the jets. If an attempt is made it will be decidedly model dependent. Clearly it is no longer sensible to associate a definite partonic x_γ or x_p to an event. This is the main reason that, in the analysis presented in later chapters, no attempt is made to extract partonic quantities. However the improved description of the data achieved by including MI in the Monte Carlo (see section chapter 4) is used to correct for detector effects and to extract jet cross sections for the hadronic final state. These cross sections can naturally be confronted with different models, but are themselves model independent.

Events with direct photons can not contain MI. Hence photoproduction at HERA offers the opportunity to compare events with and without MI in the same physical environment, and investigate the effect of the additional interactions.

Chapter 3

Hard Photoproduction and Jets in ZEUS

This chapter deals with the experimental definitions important to photoproduction, the way in which the kinematic variables are reconstructed, the jet algorithms used in this analysis, and what the photoproduction events actually look like in the experiment. Throughout the chapter, the arguments for making the cross section measurements described in this thesis are developed. Finally the definitions of these cross sections are given.

3.1 Reconstruction of the Kinematic Variables

This section looks at how the variables y, Q^2, x_p and x_γ are derived from experimentally measurable quantities.

Both y and Q^2 can be calculated from the scattered positron. Conservation of energy and momentum at the $e^+\gamma$ vertex give:

$$y_e = 1 - \frac{E'_e}{2E_e}(1 - cos\theta_e) \tag{3.1}$$

$$\text{and} \quad Q^2 = 2E_e E'_e(1 + cos\theta_e) \tag{3.2}$$

where E_e and E'_e are the energies of the incoming and scattered positrons respectively, and θ_e is the angle between the outgoing positron and the incoming proton direction. From 3.2 one can see that θ_e will be large in the low Q^2 events of interest in this thesis, i.e. the positron will hardly be deflected in the scatter. In fact the experimental definition of photoproduction in ZEUS is the absence of the scattered positron in the uranium calorimeter, which corresponds to a scattering angle of $\theta_e > 176.5°$. Hence Q^2 is effectively limited to be less than 4 GeV^2, and it has been estimated that the median value is $Q^2 \sim 10^{-3}$ GeV^2 [64]. Putting the large value of θ_e back into the expression for y_e one obtains:

$$y_e \approx \frac{E_e - E'_e}{E_e} = \frac{E_\gamma}{E_e} \tag{3.3}$$

Where E_γ is the energy of the exchanged photon. So y simply becomes the fraction of the electron energy carried by the exchanged photon.

Another approach for reconstructing y and Q^2 is the Jacquet-Blondel method [65] which uses the hadronic final state. Summing over all final state particles except for the electron:

$$y_{JB} = \frac{\sum_i (E_i - P_{z_i})}{2E_e} \tag{3.4}$$

$$Q^2_{JB} = \frac{(\sum_i p_{x_i})^2 + (\sum_i p_{y_i})^2}{1 - y_{JB}} \tag{3.5}$$

Experimentally the sum runs over all the cells of the uranium calorimeter, except when the scattered positron enters the detector. In these events cells belonging to the cluster identified as being caused by the scattered positron are excluded from the sum. The angular position of each calorimeter cell is determined using the cell centre, and is corrected using the reconstructed position of the event vertex. This method is relatively insensitive to the loss of particles down the forward beam pipe, and in low Q^2 photoproduction events, where the scattered positron is lost undetected down the rear beam pipe, it is the only way to measure these variables.

The centre of mass energy, $\sqrt{s_{\gamma p}}$ or $W_{\gamma p}$, of the γp interaction can be calculated from

$$\sqrt{s_{\gamma p}} = \sqrt{4E_\gamma E_p} \approx \sqrt{4yE_eE_p} = \sqrt{ys_{ep}}. \tag{3.6}$$

Where E_p is the energy of the incoming proton. For reasons explained in chapter 5, the hard photoproduction sample is restricted to events with $0.2 < y < 0.8$, corresponding to 134 GeV $< W_{\gamma p} <$ 269 GeV, and an average centre of mass energy of $W_{\gamma p} \sim 200$ GeV.

In lowest order models, the fractional momentum carried by the incoming partons of the photon and the proton can be reconstructed from the final state jet kinematic variables. Simple conservation of energy and momentum gives

$$x_\gamma^{LO} = \frac{\sum_{partons} E_T^{partons} e^{-\eta^{partons}}}{2E_\gamma} \tag{3.7}$$

$$\text{and} \quad x_{\mathrm{p}}^{LO} = \frac{\sum_{partons} E_T^{partons} e^{\eta^{partons}}}{2E_p} \tag{3.8}$$

Where $E_T^{partons}$ and $\eta^{partons}$ [1] are the transverse energy and pseudorapidity of the outgoing partons from the hard scatter. As shown above, in the low Q^2 events $y \approx E_\gamma / E_e$ so that 3.7 can be rewritten as

$$x_\gamma^{LO} \approx \frac{\sum_{partons} E_T^{partons} e^{-\eta^{partons}}}{2yE_e} \tag{3.9}$$

For those events in which two jets are observed in the detector it is possible to estimate the fraction of the photon momentum which participates in the hard process by replacing the sum over partons in equations 3.8 and 3.9 with the sum over jets. At higher orders and in events where the photon remnant carries significant transverse energy more than two jets may appear in the final state. For this reason the following explicit operational definitions are made:

$$x_\gamma^{OBS} = \frac{E_T^{jet1} e^{-\eta^{jet1}} + E_T^{jet2} e^{-\eta^{jet2}}}{2yE_e} \tag{3.10}$$

$$\text{and} \quad x_p^{OBS} = \frac{E_T^{jet1} e^{\eta^{jet1}} + E_T^{jet2} e^{\eta^{jet2}}}{2E_p} \tag{3.11}$$

[1] $\eta = -\ln(tan(\frac{\theta}{2}))$

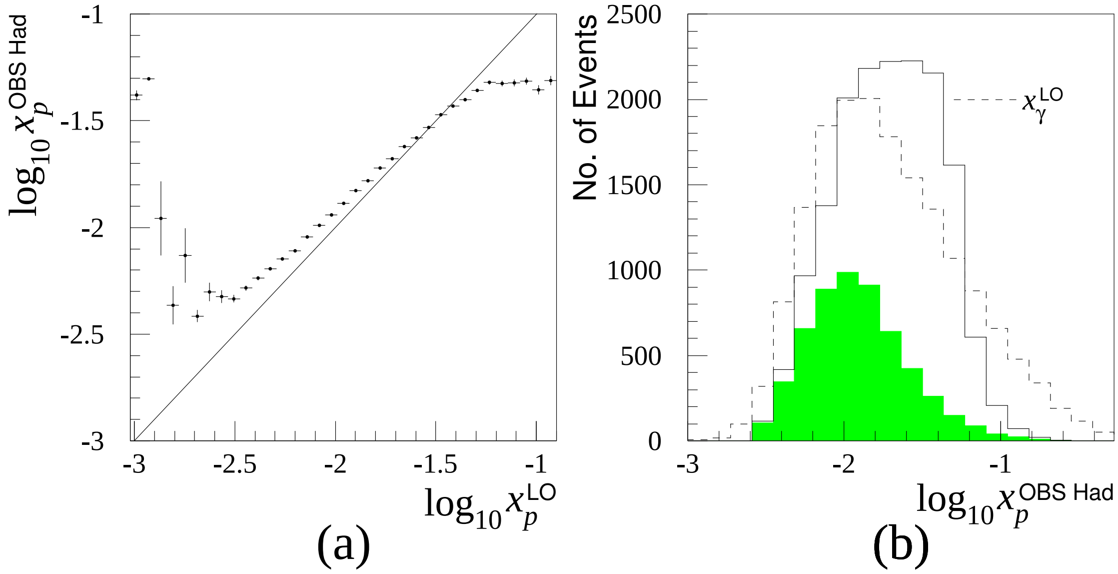

Figure 3.1: *From HERWIG Monte Carlo: (a)* $\log_{10} x_p^{OBS}$ *vs* $\log_{10} x_p^{LO}$ *and (b)* $\log_{10} x_p^{OBS}$ *for all events (solid line) and for only direct photon events (shaded histogram), and for the same events* $\log_{10} x_p^{LO}$ *(dashed line). For these plots jets were identified using the KTCLUS algorithm on the hadronic final state before it was passed through the detector simulation.*

where the sum now runs over the two jets of highest transverse energy, E_T^{jet}. Thus x_γ^{OBS} and x_p^{OBS} are the fractions of the photon and proton energies participating in the production of the two highest E_T^{jet} jets. No matter how many jets there are in the final state, as long as all events are treated consistently in experiment and theoretical calculations, the above definitions of x_γ^{OBS} and x_p^{OBS} are valid.

Figure 3.1 (a) shows the $\log_{10} x_p^{OBS}$ vs $\log_{10} x_p^{LO}$ distribution for events from the LO Monte Carlo generator HERWIG [83]. As with all the plots in this chapter, the events in this distribution are those in the standard HERWIG with MI sample described in the next chapter, and the jets are found by applying KTCLUS, described in section 3.2.2, to the final state particles before the Monte Carlo is put through the detector simulation. It can be seen that the correlation between the 'true' and reconstructed variables is good. Figure 3.1 (b) shows the $\log_{10} x_p^{OBS}$ and $\log_{10} x_p^{LO}$ distributions for the same events. The events lie in the range $-2.75 < \log_{10} x_p^{OBS} < -0.5$, with the $\log_{10} x_p^{LO}$ distribution being slightly wider. The direct photon events (shaded histogram) lie towards smaller values of $\log_{10} x_p^{OBS}$. This is reasonable since in these events the maximum photon mo-

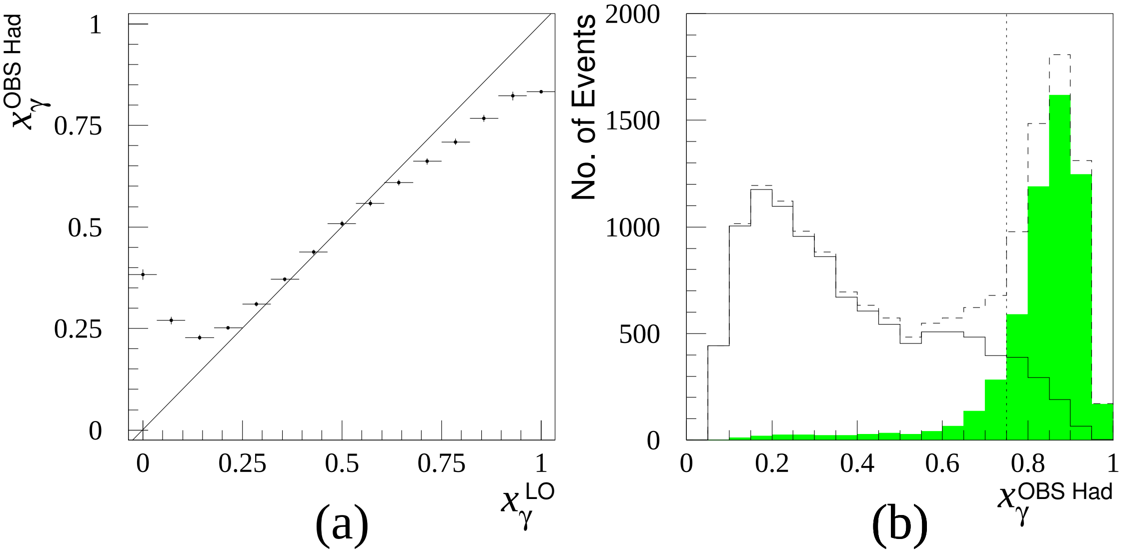

Figure 3.2: *From HERWIG Monte Carlo:(a) The mean x_γ^{OBS} vs x_γ^{LO} (b) x_γ^{OBS} for all events (dashed line), resolved photon events only (solid line) and direct photon events only (shaded histogram). For these plots jets were identified using the KTCLUS algorithm on the hadronic final state before it was passed through the detector simulation. The dotted line gives the cut used for the experimental definition of direct and resolved processes*

mentum is available for jet production, and so it is possible for the partons with smaller fractions of the proton momentum to be involved. For each event in these distributions the difference between x_p^{OBS} and x_p^{LO} is due to hadronisation and parton shower effects. The data distribution will also be affected by higher order effects and detector smearing. The limits on x_p^{OBS} arise from the thresholds set on η^{jet} and E_T^{jet} in the jet search. The x_p^{OBS} distribution contains events that have migrated in from higher and lower x_p^{LO} values, which is why the $\log_{10} x_p{}^{LO}$ distribution is wider. As a result of this the average $\log_{10} x_p^{OBS}$ is above $\log_{10} x_p^{LO}$ for small $\log_{10} x_p^{LO}$ and below it for larger values.

Figure 3.2(a) and (b) show the x_γ^{OBS} vs x_γ^{LO} and x_γ^{OBS} distributions respectively, for the same events as appear in the plots of figure 3.1. The solid line in (b) is for those events generated as resolved processes, the shaded histogram is for those generated as direct, and the dashed line is for the whole sample. The correlation between x_γ^{OBS} and x_γ^{LO} is generally good, and the resolved and direct processes populate different regions of the x_γ^{OBS} distribution, though there is some overlap.

The x_γ^{OBS} values in this figure are again subject to hadronisation and parton shower effects, which are what cause the direct events to be spread out and peaked below their x_γ^{LO}=1 value. The reconstructed value of x_γ^{OBS} in the data will also be affected by higher order effects and detector smearing. In (a) it can be seen that for $x_\gamma^{LO} \gtrsim 0.65$, x_γ^{OBS} tends to be a little low. As will be seen later, the jets from events with higher x_γ^{OBS} tend to be further towards the rear of the detector and the direction of the (low energy) photon remnant in resolved events. In this case there may be some interaction between the photon remnant and the partons in the showers that form the jets. This could cause some of the particles to end up outside the jet, and thus the energy of the jet and x_γ^{OBS} are lowered. Conversely at low x_γ the jets are further forward and there may be some **overlap** with the (high energy) proton remnant, thus raising the jet energy and x_γ^{OBS} as seen in the figure. However the main effect at low x_γ^{OBS} is from the cuts applied to η^{jet} and E_T^{jet} in the jet search. It is these cuts that cause the sharp drop of at $x_\gamma^{OBS} \approx 0.1$ in the distributions shown in (b). Thus for lower values of x_γ^{LO}, only events that have migrated to higher x_γ^{OBS} values are selected.

The relationships between x_γ^{OBS} and x_γ^{LO}, and x_p^{OBS} and x_p^{LO} are highly dependent on the models used to describe the hadronic state and the assumptions made in the calculation of the hard process. The definition of x_γ^{OBS} is model independent and can be implemented in theoretical calculations of any model, unlike the parton level definition which becomes ambiguous even at next to leading order. Following this argument there is no attempt in this analysis to correct back to parton kinematics in the cross section measurements.

Although the direct contribution in the data will not lie at exactly 1 due to higher order and/or hadronisation and parton shower effects, it is still possible to choose a working experimental definition for direct and resolved photoproduction. In this analysis direct events are defined as those with $x_\gamma^{OBS} \geq 0.75$ and resolved as those with $x_\gamma^{OBS} < 0.75$. However, for reasons explained in section 4.6.2, only the range $0.3 < x_\gamma^{OBS} < 0.75$ is used for the resolved cross section measurement.

In addition to the separate direct and resolved cross sections, a measurement is made for the whole range of x_γ^{OBS}. As can be seen from figure 3.2(b) the cut at x_γ^{OBS}=0.75 gives the optimum separation between the HERWIG events generated as direct processes from those generated as resolved. More important however is that the events with $x_\gamma^{OBS} \geq 0.75$ will still correspond to the kinematic region where most of the energy of the photon is available to probe the proton at low x_p. This separation of direct and resolved is used in both data and theoretical calculations. Above LO the distinction between direct and resolved processes is ambiguous in any case, and this definition is as valid as any other.

3.2 Jet Algorithms

Since a jet is not a fundamental QCD object it is necessary to find an exact definition. The intention in measuring the jet cross sections is to learn something about the partons from the final hadronic state. However because of QCD confinement it is not possible to 'see' these quarks and gluons directly, but only via the produced hadrons. This leads to the study of properties of the hadronic final state which are: strongly related to the gluons and quarks, experimentally well defined and well measured, and well defined and reliably calculable to all orders in theory. One class of objects that satisfy these conditions is jets.

This definition has a number of unavoidable consequences. There are obviously many ways to define these jets in both theory and experiment, and a more detailed discussion of this point is entered into later in this section. There are however two general constraints on the exact definition of a jet. Firstly it should be independent of a particle splitting into two parallel travelling partons, or in the calorimeter the energy deposit from one particle being split between two cells. In theoretical calculations this would give rise to collinear divergences, which only disappear when no distinction is made between a single particle with energy E', and two colinear particles whose energies sum to the same value ($E_1 + E_2 = E'$), and the contributions from both cases are integrated over. Experimentally this means determining that the results are largely independent of the granularity of the detector. Secondly the result must not be influenced by the emission of very low energy particles. In theory this causes infrared divergences, over which can also be integrated, and in experiment such low energy deposits are considered in connection with detector noise and the cuts used to remove this, which shouldn't affect the result. Algorithms that satisfy these criteria are said to be infrared and colinear safe

Jets can be considered at several different levels [66]:

$$\begin{tikzcd}
\text{Partons} \arrow[r, "\text{Parton Shower}"] \arrow[d] & \text{Many Partons} \arrow[r, "\text{Hadronisation}"] \arrow[d] & \text{Hadrons} \arrow[r, "\text{Measurement}"] \arrow[d] & \text{Detector} \arrow[d] \\
\text{Jets} & \text{Jets} \arrow[l, "\text{Correction}"'] & \text{Jets} \arrow[l, "\text{Correction}"'] & \text{Jets} \arrow[l, "\text{Correction}"']
\end{tikzcd}$$

An important question is on what level experiment and theory should be compared. Obviously it would not be sensible to make the comparison on the detector level. On the other hand the hadronisation and shower corrections are not trivial, and decidedly model dependent. Therefore it seems that a comparison on the hadron level is best, since the data is then independent of the physical detector, and from the other side it is as model independent as possible. Hence the cross sections in this analysis were measured on this hadronic level.

For a jet algorithm to be used in photoproduction there are two further demands. For one, the final state, in addition to the partons produced by the hard subprocess, contains the remnant(s) of the incoming hadron (and photon for resolved processes). Any remnant should be separated from the jets, and minimally influence the jet finding. The algorithm should therefore either restrict the size of the jets or handle the hadron remnant as a separate object. Also, for a photoproduction event the laboratory frame is in general not the same as any of the physically motivated systems such as the photon-proton centre of mass or the partonic centre of mass. A transformation into any one of these frames would involve a nontrivial measurement. However all these systems have the property that they are boosted in the direction of the beam with respect to the lab. Therefore the jet algorithm should be as independent of such boosts as possible. This is automatically achieved when only the transverse energy, E_T, is considered for jet finding in a plane of pseudorapidity, η, and azimuth, ϕ. While E_T and ϕ are unaffected by a boost in the beam direction, η alone is shifted by an additive constant. So the form of the transverse energy distribution in η - ϕ is the same in all frames.

3.2.1 Cone Algorithms

These are the type of algorithm normally used to study jets in hadron-hadron physics. A definitive standard form for these algorithms was set by the 'Snowmass Convention' [67]. A jet here is a cone of radius R in the η - ϕ plane which contains a maximum in transverse energy of the hadrons or calorimeter cells (or partons in theoretical calculations). The jet consists of calorimeter cells (or partons) i with a distance

$$R_i = \sqrt{(\eta_i - \eta^{jet})^2 + (\phi_i - \phi^{jet})^2} \leq R \tag{3.12}$$

from the jet centre. Here ϕ_i and η_i are the azimuthal angle and pseudorapidity of the cell (or parton), and R is the jet cone radius. In this analysis, the geometric centre of the cell is used to define the position. The transverse energy and centre of a jet are determined using the following equations:

$$\begin{aligned} E_T^{jet} &= \sum_i E_{t,i} \\ \eta^{jet} &= \frac{1}{E_T^{jet}} \sum_i E_{t,i}\eta_i \\ \phi^{jet} &= \frac{1}{E_T^{jet}} \sum_i E_{t,i}\phi_i \end{aligned} \tag{3.13}$$

in which the sums run over all hadrons, calorimeter cells, or partons within the cone. The expressions defining the centre mean that the jet finding must be an iterative process, since for a particular group of enclosed objects the centre calculated from equations 3.13 may differ from the geometric centre of the cone. For a new cone about the calculated centre a slightly different group of objects will be enclosed, and hence a different centre again is likely to be found. Therefore this procedure must be repeated until the sample of enclosed objects is stable. Due to the radius constraints cone jets have a maximum size and in this way the inclusion of the hadron remnant is avoided.

The Snowmass Convention makes no constraint on the starting point for the jet finding however. It also contains no rule for dealing with overlapping jets. This leaves quite a significant amount of room for differences in implementation. In order to asses the effects of this freedom two cone algorithms were used in this analysis each of which apply the Snowmass Convention in very different ways, though both have the cone radius fixed at R=1.0.

PUCELL

PUCELL [68] is an adaptation of the jet algorithm used at CDF. It begins with the defining of preclusters. All calorimeter cells, particles or partons above a certain transverse energy threshold (0.3 GeV in this analysis) are ordered in E_T. Starting with the object of highest E_T all the other objects are checked to see if they lie within R of this first object. Those objects that do are then removed from the list and combined with the original object to from a precluster. The parameters of each precluster are determined according to equations 3.13. When all objects are associated to preclusters the centres of the preclusters are recalculated. Next the sample of objects that lie within a radius of R from this new centre is determined, which defines a new precluster. The centre of this new precluster is then calculated, and the objects that lie within a radius of R from this centre found. This is repeated until the list of objects is stable (or until some maximum number of iterations is reached). In this way clusters arise, which are provisionally accepted as jets. If two clusters overlap, and the energy in the overlap is more than 75% of the energy of the smallest involved cluster, then the clusters are combined. Otherwise each object is associated to the nearest cluster. Finally the parameters of the clusters are recalculated and all clusters with a transverse energy above a preselected threshold are then considered to be jets

It has been shown that algorithms of this style are, in principle, not completely infrared and colinear safe [69]. However they are normally saved by the experimental cuts applied during analyses. Alternatively applying the R_{sep} parameter, described in section 3.3, in theoretical calculations offers a way round the problem.

EUCELL

EUCELL [70] also uses preclustering. The clusters are however determined by using a grid in the η - ϕ plane. The size of the cells that make up the grid is determined such that $\Delta\eta^{gridcell} \approx \Delta\phi^{gridcell} \approx R/2$. Preclusters are then found by sliding a 3×3 cell window over the grid. If the total summed transverse energy of any 3×3 section is above a certain level (1 GeV for this analysis) it is counted as a precluster. About the centre of each precluster is placed a cone of radius R, then the same iterative process as with PUCELL is performed until the set of included objects is stable. The cone with the highest transverse energy, independent of which precluster it comes from, is accepted as a jet. The enclosed objects that make up this jet are excluded from further jet finding. The whole procedure is repeated again and again until there are no cones with energy above the predetermined threshold. In this way EUCELL produces no over lapping jets. Every object is associated to a jet such that the highest E_T jet in that part of the η - ϕ plane is produced. In actual fact it is possible that two jet cones may overlap, but all the energy in the overlap will be associated with the highest E_T jet. This situation occurs so rarely, and the jets overlap to such a small extent that it is insignificant, especially considering the resolution of the measured η^{jet}.

EUCELL does not suffer from the same problems of infrared safety as PUCELL. However the square window in the seed finding phase is difficult to model in theoretical calculations.

3.2.2 Cluster Algorithms

Cluster algorithms are well known from e^+e^- experiments. Their application to photoproduction was until recently opposed by the fact that they do not treat the beam direction differently to any other, and the separation of the jets from hadron remnants is difficult. These disadvantages are avoided in newer variations. For this analysis the KTCLUS [71, 72] algorithm was used.

KTCLUS

For each pair of calorimeter cells or particles in a particular sample the quantity:

$$d_{i,j} = \min(E_{t,i}, E_{t,j})^2 \left(\Delta\eta^2 + \Delta\phi^2\right), \tag{3.14}$$

and for each individual cell or particle the quantity:

$$d_i = E_{t,i}^2 \tag{3.15}$$

are calculated. If of all the numbers $[d_{i,j}, d_i]$ the quantity $d_{k,l}$ is smallest then objects k and l are combined into a single object. The parameters of this new object are calculated according to the equations of the Snowmass Convention (equation 3.13). If however d_k is the smallest, then object k is complete and is removed from the sample. This is repeated until there are no incomplete objects. The result is an E_T ordered list of objects, and objects above some threshold are accepted as jets.

Although this algorithm may at first appear somewhat more complex than a cone algorithm, it has the advantage that there is a clear choice for the starting point and a clear treatment of overlapping jets in both experiment and theory. The starting point is simply all the calorimeter cells (or particles/partons) present. Neighbouring objects are then combined successively if they satisfy the criterion: $\min\{E_T^{obj}\}^2\ [(\Delta\eta)^2 + (\Delta\phi)^2]\ <\ min\{E_T^{obj}\}^2$. If an object is separated from all other objects by more than one in the η - ϕ plane, then it is considered a completed object. This would make it either a well isolated jet or part of the hadron remnant, in either case it should take no further part in the clustering. Every calorimeter cell (particle/parton) is clearly associated to a jet and the problem of overlapping jets does not arise. This means that this algorithm has the advantage of being completely infrared and colinear safe [69, 71]. As the algorithm is well defined in E_T, η and ϕ the boost invariance is automatically satisfied. The use of the $\eta\phi$ metric and the E_T recombination scheme allows the assumption that the results should be very similar to those of a cone algorithm. The algorithm is completely different in method however, and allows an estimation of the effect of different types of algorithm on the measurement of the cross section.

The comparison of results from several different jet finders is useful in at least two ways. Firstly purely as an investigation into jet finding, particularly for this type of process. Secondly if any comment on parton distributions is to be made it should be independent of the algorithm used to find the jets.

In this analysis the jet finding initially selects jets with transverse energy above 4 GeV, and $\eta^{CALjet} < 3$. The E_T^{CALjet} threshold of 4 GeV is to compensate for energy losses from inactive material in front of the calorimeter when trying to reconstruct jets of $E_T^{jet} \geq 6$ GeV, which is the lowest threshold used for the cross section measurements (see section 3.6). The η^{CALjet} cut is to minimise the interdependence of forward going jets and the proton remnant. After this events are selected separately for each jet finder if they contain at least two jets with E_T-weighted centres within -1.375$< \eta^{jet} <$ 1.875.

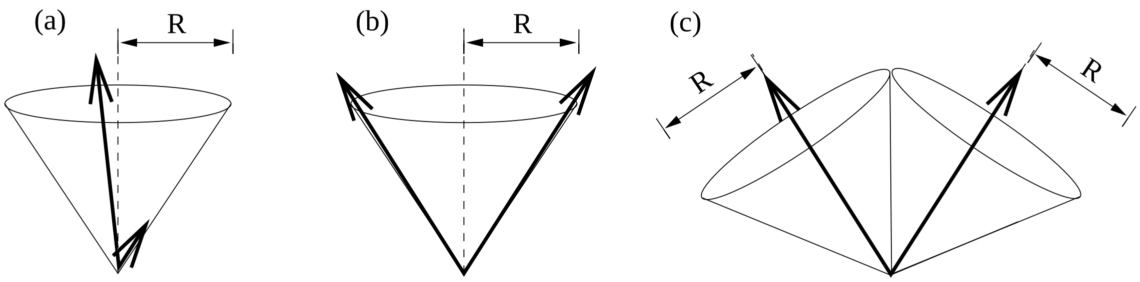

Figure 3.3: *The possible configurations of two partons separated by 2R or less (where R is the cone radius of a jet), and the jet cones they are assigned to.*

3.3 Jet Definition in a NLO Calculation

In order to compare NLO calculations with experimental results it is necessary to know how a three parton final state will be treated by the jet algorithm used on the data, i.e. how and when will two partons be combined into one jet. If Δ is defined as the separation of partons in the η-ϕ plane then the equations of the Snowmass convention (equation 3.13) imply that the partons are combined into a single jet if:

$$\Delta < \frac{E_T^1 + E_T^2}{max\{E_T^1, E_T^2\}} R$$

where R is the radius of the jet cone and $E_T^{1(2)}$ is the transverse energy of particle 1(2).

This works well in cases where one of the partons has a much larger transverse energy, which effectively defines the jet axis, and the other parton lies clearly within the jet cone, as in figure 3.3(a). However if the two partons have similar transverse energy and are separated by 2R, then under the Snowmass convention they could be combined into one jet, each being at the edge with no parton at or near the jet axis, as in figure 3.3(b). In cases like this a better agreement with jet finding in an experiment would be achieved by placing each parton in a separate jet, with the jet cones just touching, as in figure 3.3(c). In order to deal with this a modified Snowmass formula was constructed [73, 74]:

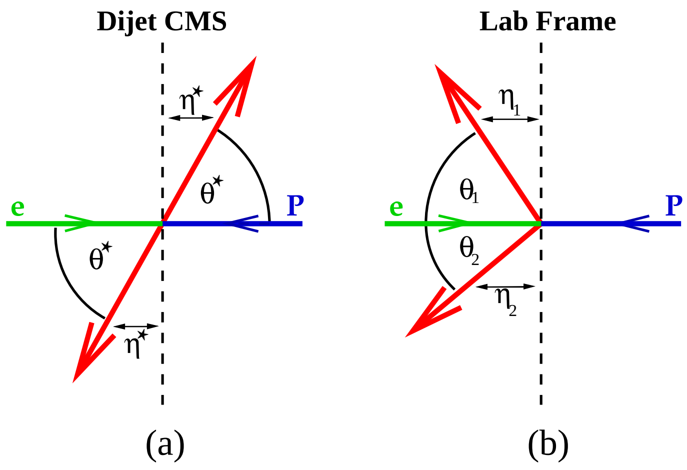

Figure 3.4: *The kinematics of the two jets in (a) the centre of mass system, and (b) the lab frame*

$$\Delta < min\left\{\frac{E_T^1 + E_T^2}{max\{E_T^1, E_T^2\}}R, R_{sep}\right\}$$

Here R_{sep} is effectively the maximum separation particles can have and still be combined. This modification also removes the infrared and colinear safety problems associated with the PUCELL type cone algorithms. The jet algorithms used in this analysis correspond approximately to using $R_{sep} = 1.0$ for KTCLUS, 1.0R for PUCELL and $1.5R < R_{sep} < 2.0R$ for EUCELL. The uncertainty in the exact value that should be used to match EUCELL is due to the square window in the initial phase of the algorithm.

3.4 Two Jet Kinematics

In the centre of mass system (CMS) the two jets have a simple kinematics, as shown in figure 3.4(a). The jets point in exactly opposite directions, and apart from an isotropic distribution in the azimuthal angle ϕ, a single polar angle θ^* is enough to describe the distribution of the jets. θ^* is the angle between the jet-jet axis and the beam axis. This can easily be converted into a pseudorapidity $\eta^* = -\ln(tan(\theta^*/2))$. In the change to the Lab frame there is a boost in the proton beam direction. The jet rapidities are shifted by some constant factor B such that the pseudorapidities of the jets in the lab frame are:

$$\eta_1 = B - \eta^* \qquad \text{and} \qquad \eta_2 = B + \eta^* \tag{3.16}$$

So using linear combinations of the measured jet pseudorapidities from the lab frame it is possible to derive the scattering angle in the CMS (η^*) and the boost (B):

$$\eta^* = \frac{1}{2}|\eta_1 - \eta_2| \tag{3.17}$$

$$B = \frac{1}{2}(\eta_1 + \eta_2) = \bar{\eta} \tag{3.18}$$

Thus the boost is simply the average pseudorapidity of the two jets, and the CMS jet rapidity η^* is half the difference between them. These quantities give two possible independent measurements. The CMS scattering angle is related only to the matrix element of the hard subprocess, and the boost is obviously connected with the momentum fractions of the proton and photon carried by the incoming partons, and thus with the structure functions.

As already mentioned in the previous chapter, the angular distribution measurement has been made at ZEUS [45], which showed different dependence on $|cos\theta^*|$ for resolved and direct event samples. This is directly linked to the dominance of fermion (quark) exchange for direct processes and boson (gluon) exchange in resolved processes.

The angular distribution of the two jets is very much independent of the parton densities in the photon and proton. The momentum fractions x_p and x_γ carried by the incoming partons have a much larger impact on the boost. If one assumes that the jets have equal transverse energy then it can be shown that:

$$\bar{\eta} = \frac{1}{2}\ln\frac{x_p^{OBS}E_p}{x_\gamma^{OBS}yE_e} \tag{3.19}$$

The measurement of $\bar{\eta}$ therefore gives a way to study the structures of the proton and photon. This is the central point of the analysis presented in this thesis.

Although the boost, $\bar{\eta}$, is already directly dependent on the momentum fractions x_p and x_γ, it proves sensible to restrict the η^* in this measurement, and thus remove the angular dependence. There are many reasons for this. Firstly it is reasonable to believe that the jets can best be measured when they are emitted perpendicular to the beam direction in the CMS, i.e. at $\eta^* \approx 0$. This is also the configuration in which the smallest x_p^{OBS} and x_γ^{OBS} can be achieved since $(2E_T^{jet})^2 \leq \hat{s} = yx_\gamma^{OBS}x_p^{OBS}s^{\text{ep}}$, and the equality is reached for perpendicular scattering. The approximate equality of $2E_T^{jet}$ and $\sqrt{\hat{s}}$ also has the advantage in theoretical calculations that the range of possible choices of scale is reduced (cf. 2.27). In addition, by assuming that the two jets have equal E_T^{jet} the equations for x_γ^{OBS} and x_p^{OBS} can be rewritten as:

$$x_\gamma^{OBS} = \frac{E_T^{jet} e^{-\bar{\eta}}}{yE_e} cosh\frac{\Delta\eta}{2} \tag{3.20}$$

$$\text{and} \quad x_p^{OBS} = \frac{E_T^{jet} e^{\bar{\eta}}}{E_p} cosh\frac{\Delta\eta}{2} \tag{3.21}$$

From here it is possible to see that for fixed $\Delta\eta = 2\eta^*$ there is a strong correlation between $\bar{\eta}$ and both yx_γ^{OBS} and x_p^{OBS}. These equations also confirm that the minimum available x values are probed for $\frac{\Delta\eta}{2} = \eta^* = 0$, since the cosh terms are then at their minimum of unity. Considering the resolution of the measurement of the pseudorapidity of the jets (see section 6.2) a cut at $|\Delta\eta| < 0.5$ ($\eta^* < 0.25$) seems a good choice.

Implicit in the measurement of the dijet cross sections presented in this thesis is that the two jets in an event are related to the two partons of a QCD hard scattering subprocess. However it should be stressed that no explicit requirement is made to this effect, and no attempt has been made to unfold back to parton kinematics based on Monte Carlo models. The only requirement made in the selection of the data sample is that it consists of clean hard photoproduction events of high transverse energy in regions of the detector that we understand.

In a hard photoproduction event, the two jets of highest transverse energy should approximately balance each other in the scalar variable E_T^{jet} and in the

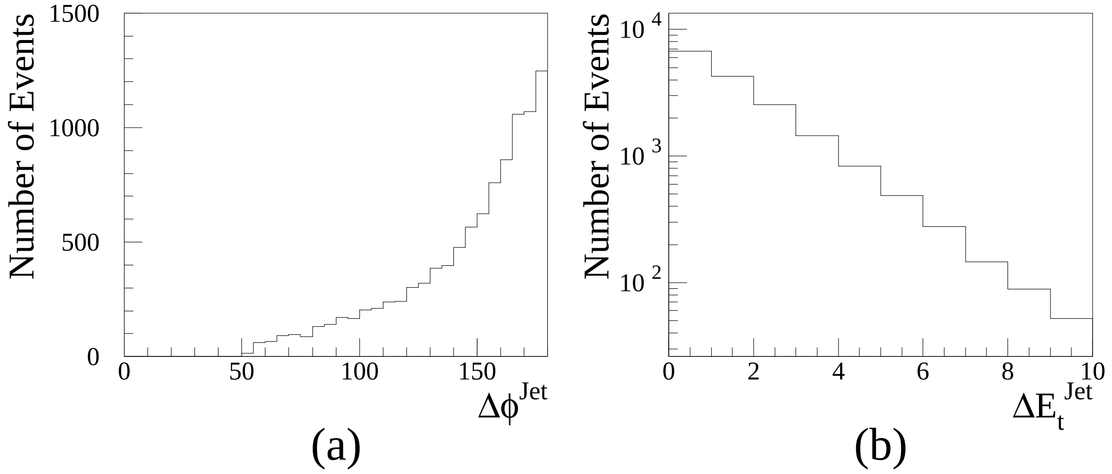

Figure 3.5: *For the events in the data selected for this analysis: (a) $\Delta\phi^{Jet}$ and ΔE_t^{Jet} for the two jets with highest transverse energy in an event, with $-1.375 < \eta^{jet} < 1.875$ and $\Delta\eta < 0.5$. For these plots jets were identified using the KTCLUS algorithm.*

variable ϕ^{jet}, since to leading order nothing else carries the transverse energy of the interaction. Figure 3.5(a) shows $(\phi^{CALjet_1} - \phi^{CALjet_2})$ for the two jets of highest transverse energy (E_T^{CALjet}) in an event, for all events in the final data sample entering the measured cross sections. The shape of this distribution indicates that the jets tend to be separated by 180°, which can be interpreted as evidence that the two jets come from a hard 2→2 scatter. Higher order processes, parton showering and hadronisation give rise to further particles which take away some of the transverse momentum so that the two jets are no longer of equal and opposite transverse momentum. The plot in figure 3.5(b) shows that in the data some very large separations are seen (here the jet with the greater E_T^{CALjet} value is assigned the label jet 1), though it should be noted that the y-axis has a logarithmic scale.

3.5 Hard Photoproduction in ZEUS

In photoproduction at HERA, where the centre of mass energy is much higher than earlier experiments, one expects contributions from direct and resolved photons. In events with resolved photons there is a photon remnant, and with direct processes the entire photon energy enters the hard sub process. As already mentioned, the experimental definition of photoproduction at ZEUS is the absence of a scattered positron in the uranium calorimeter, which corresponds to a positron scattering angle of $\theta_e > 176.5^\circ$ and photons of $Q^2 < 4$ GeV^2. Hard photoproduction interactions are defined by demanding 'large' values of transverse energy in the final hadronic state of $\gamma p \rightarrow X$, such that a scale is reached at which the internal structures of the photon and proton can be resolved [55, 75–80]. Any photoproduction event that contains jets satisfies this criteria.

In this thesis only dijet hard photoproduction interactions are considered; that is events with 2 or more jets of $E_T^{jet} \geq 6$ GeV. The expected event topology consists of a certain number of particles with high transverse momenta, a proton remnant, and in the case of resolved photon processes, a photon remnant.

3.5.1 Examples

Figure 3.6 shows an event from the '94 data sample. Left is an r-z projection of the central tracking and calorimetry. The protons enter from the right, and the positrons from the left. There is no obvious scattered positron in the calorimeter in this event and no activity in the rear direction. Since the transverse momentum of the observed reaction products balance, to a good approximation, it is unlikely that this is a charged current interaction. The scattered positron must therefore have disappeared in the rear beam pipe. Therefore this event must have low Q^2, and satisfies the ZEUS definition of photoproduction. In the upper and lower halves of the BCAL one sees energy deposits, each of about 20 GeV. As the particles registered here are practically perpendicular to the beam axis, this corresponds to a large transverse momentum. Hence the interaction shown definitely contains a hard partonic interaction. In the proton direction, around the beam pipe, one also sees energy deposits totalling around 50 GeV. As these particles have only a small angle to the beam axis, the associated transverse momentum is small. This

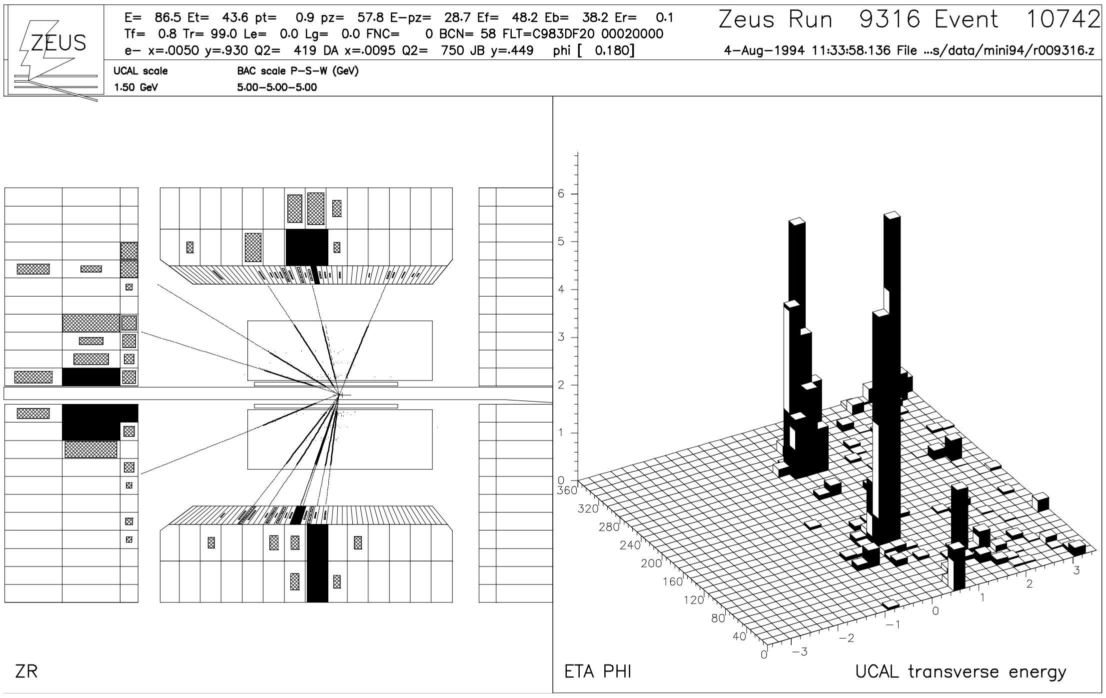

Figure 3.6: *An example of a candidate direct hard photoproduction event in the ZEUS detector*

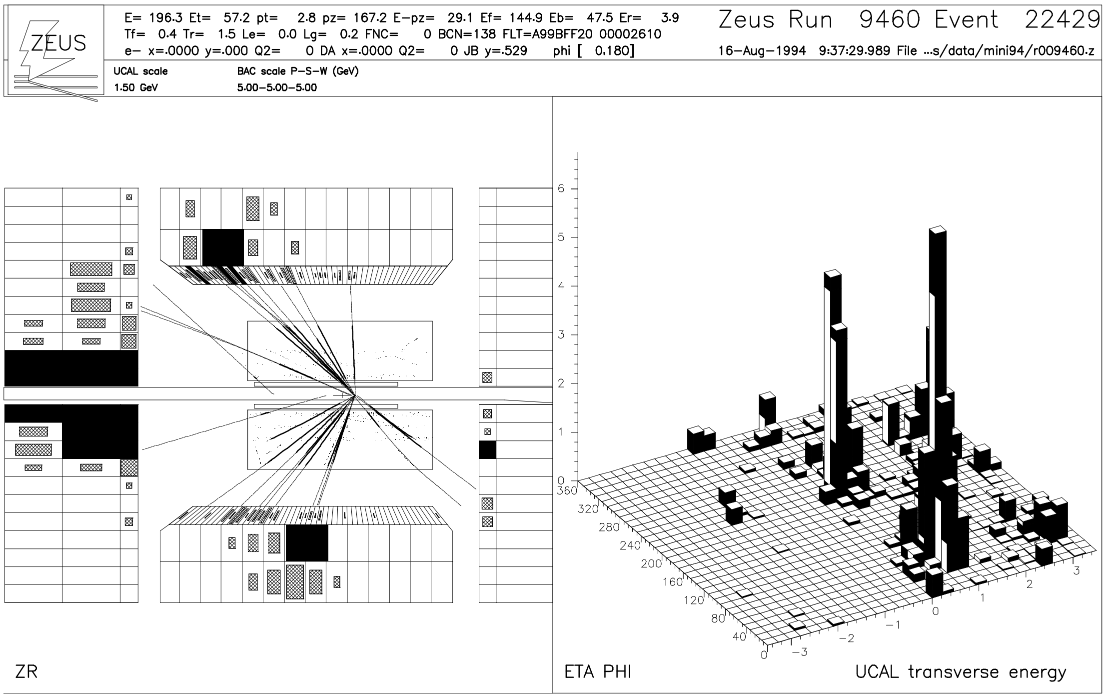

Figure 3.7: *An example of a candidate resolved hard photoproduction event in the ZEUS detector*

is a part of the proton remnant. In the positron (≡photon) direction there are no particles detected. Here one would expect the photon remnant, whose absence means this events is a candidate for a direct photon interaction. There is also a clear interaction vertex reconstructed using tracks from the VXD and the CTD.

A better feeling for the topology of an event can be gained by studying its appearance in the η - ϕ space where jet finding is performed. This is shown in the 'lego' plot on the right of figure 3.6. The vertical scale on this plot gives the transverse energy deposited in the calorimeter cells ($E_T^{cell} = E^{cell} \sin\theta^{cell}$) at each point in the η-ϕ plane. With this choice of parameters the depicted topology is invariant under boosts along the beam axis. E_T and ϕ don't change and η is only changed by an additive constant. This is useful since the lab system is, in general, not a physically useful frame of reference like the γp rest frame or the centre of mass system. One can see two distinct towers of transverse energy at $\eta \approx 0$ which approximately balance one another in scalar E_T and are separated in azimuth by $\phi \approx 180°$. This allows the conclusion to be drawn that the two partons from the hard sub-process, each produce a tight bundle of particles. These bundles of particles are the jets. Such a clear event topology in which one sees the produced partons as jets and nothing else could not be seen by fixed target experiments. It is a result of the high centre of mass energy at HERA. The proton remnant hardly shows in this representation, as it only has small transverse energy.

Figure 3.7 shows another event. Once again one can see two isolated jets at about $\eta^{jet} = 1$ that approximately balance in E_T^{jet} and ϕ^{jet}, so this also is a hard partonic process. This time however, there is a photon remnant in the rear of the detector in addition to the proton remnant in the forward direction. Therefore this is a good candidate for a resolved photon event. On an event by event basis one can not discern whether a VMD or anomalous photon is involved. However the relatively high transverse momentum of the photon remnant in this event would favour an anomalous photon.

3.6 Choice and Definition of Cross Sections

In this section the cross sections measured in this thesis will be defined, and some of the more important reasons behind this choice of cross section will be reviewed.

Taking photoproduction ($ep \rightarrow e\gamma p \rightarrow eX$) events in which the final state X contains at least two jets within the pseudorapidity range $-1.375 < \eta^{jet} < 1.875$ with transverse energies above some minimum E_T^{min}, and following the arguments of [81, 82] the differential cross section:

$$\frac{d\sigma}{d\bar{\eta}} \quad ; \quad |\Delta\eta| = |\eta^{jet1} - \eta^{jet2}| < 0.5$$

is measured, where $\bar{\eta} = (\eta^{jet1} + \eta^{jet2})/2$ is the average pseudorapidity of the two jets of highest transverse energy (E_T^{jet}) in an event. This was done for direct ($x_\gamma^{OBS} \geq 0.75$) and resolved ($0.3 < x_\gamma^{OBS} < 0.75$) two jet photoproduction, and also for the full range of x_γ^{OBS}, in the following kinematic regions:

$$0.2 < y < 0.8$$

$$E_T^{min} = \ 6,\ 8,\ 11 \text{ and } 15 \text{ GeV} \tag{3.22}$$

$$-1.125 < \bar{\eta} < 1.625$$

$$Q^2 < 4 \text{ GeV}^2$$

This cross section was chosen because it is sensitive to the parton densities in the proton and photon.

The $|\Delta\eta^{jet}| < 0.5$ cut restricts the angular distribution of the jets in the jet-jet centre of mass frame, and thus reduces the sensitivity of this cross section to the matrix element for the hard sub process. It also selects a region of phase space where the jets are most easily identified, the minimum values of x_p and x_γ are probed, and the range of choice of scale for calculations is reduced. In addition fixing $\Delta\eta^{jet}$ means that there is maximum correlation between $\bar{\eta}$ and both x_p and x_γ. On top of these arguments, which have been discussed in earlier sections of this chapter, the requirement that $|\Delta\eta| = |\eta_1 - \eta_2| < 0.5$ ensures that both jets lie well within the acceptance of the ZEUS detector for the $\bar{\eta}$ bins in which the cross sections are measured. Hence no additional cuts at high or low η^{jet} need be imposed.

The cut at x_γ^{OBS}=0.75 gives the best separation between direct and resolved events at LO (after hadronisation effects), and a good working experimental definition for these two classes of event which holds to all orders. The reason for the lower cut of $x_\gamma^{OBS} < 0.3$ on the resolved cross sections is explained in chapter 4. The cross section for the full range of x_γ^{OBS} was also measured because its shape is less biased by kinematic cuts than the cross sections for specific ranges of x_γ^{OBS}.

The y interval above corresponds to a range in the γp centre-of-mass energy $W_{\gamma p} = \sqrt{4yE_eE_p} = \sqrt{ys}$ of 134 GeV $< W_{\gamma p} <$ 269 GeV, where E_p is the incoming proton energy. The reasons for these limits are explained in chapter 5.

Raising the E_T^{min} threshold should give better agreement with theory, since pQCD predictions are more reliable because the soft effects like fragmentation of the partons into jets are less relevant. The reason for measuring cross sections for several E_T^{min} thresholds was to get some idea of the E_T^{jet} dependence. Also measurements at lower E_T are more sensitive to the photon structure in the region $x_\gamma \sim 0.05$ - 1 and the proton structure in the region $x_p \sim 0.002 - 0.04$.

The limits on $\bar{\eta}$ are chosen simply to select a range where the jets are reliably reconstructed, and where there are enough events for a statistically significant measurement (see chapter 6).

The Q^2 limit is to select the events where the exchanged photon is almost real.

The value of 4 GeV is a sensible choice since it is satisfied simply by requiring that the scattered positron does not enter the detector.

No attempt was made in the analysis presented in this thesis to correct the measurement back to the parton level. The cross section as defined above is at the hadron level, and the correction from the detector to hadron level measurement is covered in chapter 6. The reasons for this are that while it is obviously bad to try and compare theoretical calculations to a detector dependent measurement, any correction for hadronisation would be extremely model dependent. A hadron level measurement is detector independent, but can still be used to confront calculations made with any particular models for the hard subprocess and hadronisation.

Although a LO QCD picture was used to formulate the ideas behind this cross section, the measurement that has been prepared is independent of this picture and comparable to calculations of any order or made in the framework of models perhaps more complicated than those described in this thesis.

Chapter 4

Monte Carlo

This chapter introduces the Monte Carlo (MC) programs used during the analysis presented in this thesis. These programs use the parton distribution functions, and the cross section for the hard subprocess to generate individual events. Some of them take the out going partons and use parton shower and hadronisation models to produce events as they are in the experiment. By treating these generated events in an equivalent way to the data from the detector it is possible to come up with predictions for the measured cross sections. As well as providing predictions, Monte Carlo programs can offer a way to study, and correct for detector effects in the measurement.

Some Monte Carlo programs serve purely to calculate cross sections. It is this type of program that both Klasen and Kramer [46], and Harris and Owens [47] use for their NLO QCD cross section calculations, the results of which are compared to the data in section 7.3. These generators produce events with a final state containing the two or three outgoing partons from the hard subprocess. The events are then given weights corresponding to the calculated probability of their occurrence, some of which may be negative. After this equivalent cuts are made as for the data, and the events are binned to provide a prediction of the measured cross sections.

Monte Carlo programs and simulated event samples are also needed to study experimental effects on the measurements made using the real data, and to extract a detector independent cross section. For a Monte Carlo event sample to be of any use in this respect it is necessary that the generator produces events as they appear in the data. There are basically two types of experimental effect that can be dealt with using such Monte Carlo. Firstly correcting for the efficiency and purity with which events can be selected. For the analysis presented here this will include correcting for the loss of events where only one of the jets was found, and the gain and loss of events whose true and reconstructed kinematics are on different sides of the limits that define the cross section. Secondly there is the correction of measured quantities. For example correcting the measured jet energies for losses in the inactive material in front of the face of the calorimeter. This is effectively recalibrating the detector for the events and objects of interest.

In addition, Monte Carlo events that have been through the detector simulation can be treated in exactly the same way as the data, and the two samples compared at all stages of the analysis. This is useful both in determining how well the Monte Carlo describes what happens in the real data, and in evaluating the relationships between the measured quantities, such as y_{JB} and x_γ^{OBS}, and the true kinematics of the events (as was already done in chapter 3).

In this analysis two generators of this second sort are used. The primary reason for using two generators is to give some estimate of the model dependence of the cross section extraction. Both generators calculate the hard subprocess in LO, and evolve the outgoing partons through to stable particles. The events are then put through a simulation of the detector to produce an output that looks identical to that from the real data, though of course the information from all levels of the simulation is still available.

4.1 HERWIG

The HERWIG (**H**adron **E**mission **R**eactions **W**ith **I**nterfering **G**luons) generator attempts to provide as complete an implementation of the LO pQCD as possible [83]. Non-perturbative effects are described using the simplest possible universal model. The aim is to describe the largest possible number of processes with the fewest possible free parameters, and thereby to have a large predictive power. For this analysis version 5.8 was used.

For resolved events HERWIG starts by generating the radiated photon from the incoming electron using the EPA. The next step is to produce the hard subprocess using the LO QCD matrix element. For direct photon events HERWIG starts with the LO matrix element for the $2 \rightarrow 3$ body scatter. HERWIG uses $\mu^2 = \frac{2\hat{s}\hat{t}\hat{u}}{\hat{s}^2+\hat{t}^2+\hat{u}^2}$ as the factorisation scale, where $\hat{s}, \hat{t}, \hat{u}$ are the Mandelstam variables for the hard subprocess. In the limit of massless partons and scattering perpendicular to the beam axis μ^2 is the same as $\frac{4}{3}\hat{p}_t^2$. A cut on the transverse momentum $\hat{p}_t$ of the outgoing partons must be introduced, since the cross section is divergent for $\hat{p}_t \rightarrow 0$. The QCD radiation from the in and out going partons is described using the parton shower model described in section 2.9. In both cases the starting point for the evaluation of the chain of emissions is the hard sub process. The emissions are ordered such that at each branching the angle between the two partons is smaller than that in the previous branching. In the final state the shower is stopped when a scale of the order of the mass of the lightest mesons is reached. In the initial state the chain of radiations evolves backwards from the hard sub process to the incoming hadrons. At each point in the cascade the partons have an equivalent x and Q^2, and the types of partons produced are consistent with the chosen parton distribution function parameterisation for this x and Q^2. The initial state emission chain is broken off when $Q = Q_0 = 2$ GeV is reached. This is around the starting scale of most parton distribution function parameterisations. With this backwards evolution in the initial state, HERWIG can produce a $\gamma \rightarrow q\bar{q}$ vertex, and thus anomalous photon events, dynamically. The limit for the productin of anomalous photons is given by Q_0^2. This is a relatively hard cut, and means that in HERWIG relatively few of the events generated have anomalous photons, and that the other resolved photon events are much more numerous than a purely VMD parton density would give.

When the scale of the outgoing parton shower has reached the mass of the light mesons, a non perturbative model must be used to cover the transition to hadrons. HERWIG uses the *cluster model*, which exploits the *pre-confinement* property of QCD where partons are grouped into colour neutral objects. This is done firstly by splitting all the gluons into $q\bar{q}$ pairs, where a gluon mass of 750 MeV is assumed. Next the quarks are grouped into colourless clusters, which are then fragmented into hadrons. If a cluster is too light to decay into two hadrons, it is taken to be the lightest hadron of the corresponding flavour. Its mass is shifted to the appropriate value by an exchange of momentum with a neighbouring cluster in the jet formed from the parton shower. The remaining clusters decay into pairs of hadrons by randomly selecting a flavour f so that for a cluster $f_1\bar{f}_2$ the hadrons are $f_1\bar{f}$ and $f\bar{f}_2$. The clusters decay isotropically except that hadrons containing a quark from the parton shower are emitted in the direction this quark was travelling. In a last step the decay of unstable particles is simulated.

4.1.1 Implementation of MI in HERWIG

As mentioned in section 2.11, it is possible for more than one interaction to take place between the photon and proton. The formulation for this followed in HERWIG [84, 85] starts by considering the scattering of two overlapping hadronic objects. It is assumed that the partons taking part in the interaction are distributed according to the electric form factors of the hadrons, where the form factor of the pion is used for the photon. From the Fourier transform of the product of the two form factors one obtains the overlap function $A(b)$, which gives the relative density of the parton content of the two hadrons where they overlap, for a scatter with impact parameter b. Multiplying this with the parton density functions gives the partonic luminosity for a photon proton collision with this impact parameter:

$$d\mathcal{L} = A(b) f^{\mathrm{p}}(x_p) \frac{f^{\gamma}(x_\gamma)}{P_{res}} dx_\gamma dx_p \tag{4.1}$$

The factor P_{res} is the probability that the photon fluctuates into the hadronic state with parton density $f^{\gamma}(x_\gamma)$. In the simulation this factor is ignored, since for any particular interaction the photon has either fluctuated or it hasn't. The partonic luminosity integrated over all impact parameters must simply be equal to the product of the parton density functions, hence $\int A(b)\pi d^2 b = 1$. The average number of partonic interactions in photon proton interactions with impact parameter b is then:

$$n(b) = \int_{\hat{p}^2_{tmin}}^{W^2/4} \int\int A(b) f^{\mathrm{p}}(x_p) \frac{f^{\gamma}(x_\gamma)}{P_{res}} \frac{d\hat{\sigma}^{\mathrm{ab}\to\mathrm{cd}}}{d\hat{p}^2_t} dx_p dx_\gamma d\hat{p}^2_t \tag{4.2}$$

$$= \frac{A(b)}{P_{res}} \sigma^{\gamma\mathrm{p}}_{QCD}(\hat{p}^2_{tmin}). \tag{4.3}$$

c.f. equation 2.39. Analogously to 2.41, the probability of there being m partonic interactions is:

$$P_m(b) = \frac{\langle n(b)\rangle^m}{m!} exp(-\langle n(b)\rangle) \tag{4.4}$$

Taking the sum of all probabilities for $m = 1 \to \infty$ and integrating over b gives the total photon proton cross section.

$$\sigma^{\gamma\mathrm{p}}_{ND} = P_{res} \int \sum_{m=1}^{\infty} P_m \pi d^2 b = \pi P_{res} \int \left[1 - exp(-\langle n(b)\rangle)\right] d^2 b. \tag{4.5}$$

Thus by using the form factors and P_{res} the total non-diffractive photon proton cross sections for $\hat{p}_t > \hat{p}_{tmin}$ can successfully be calculated. The result of this method is strongly dependent on $\hat{p}_{tmin}$, and the calculation can always be brought into agreement with a measurement at a particular centre of mass energy W using a suitable choice of $\hat{p}_{tmin}$. This approach does, however, make a real prediction of the W dependence of the cross section. The choice of $\hat{p}_{tmin}$ is always bound up with the particular structure function being used, and for different combinations of parameterisations of photon and proton structure functions, there are various different optimal values of $\hat{p}_{tmin}$.

The average number of partonic interactions per event calculated using this model is:

$$\langle n \rangle = \frac{\int \sum_{m=1}^{\infty} m P_m d^2 b}{\int \sum_{m=1}^{\infty} P_m d^2 b} = \frac{\int \langle n(b) \rangle d^2 b}{\int [1 - exp(-\langle n(b) \rangle)] d^2 b} = \frac{\sigma_{QCD}^{\gamma p}}{\sigma_{ND}^{\gamma p}}, \tag{4.6}$$

This is the same as the ad hoc result (eqn. 2.40) assumed in section 2.11.

HERWIG uses the above method to calculate the probability of finding m partonic scatters in an event with photon proton centre of mass energy W. Where a poison distribution is assumed about the average value found from equation 4.6. No explicit impact parameter dependence is used. From this probability distribution, the number of partonic interactions m is determined for each event. Every one of these scatters is generated according to the QCD cross section.

$$\frac{d^3 \sigma_{QCD}^{\gamma p}}{dx_\gamma dx_p d\hat{p}_t^2}(x_\gamma, x_p, \hat{p}_t^2).$$

In HERWIG the tunable $\hat{p}_{tmin}$ threshold, once selected, is used for all the partonic interactions. For the analysis presented in this thesis the threshold was set at $\hat{p}_{tmin} = 2.5$ GeV. This value was selected so that, to a good approximation, all events containing jets of interest to this analysis are generated. Also using $\hat{p}_{tmin} = 2.5$ GeV means that (with GRV for the photon) the best description of the data is achieved.

The fact that the partons all come from a common parent hadron is dealt with by breaking of the production of further scatters as soon as a parton would take more of the proton or photon energy than remains after the proceeding scatters. One problem is how the products of the additional scatters fit into the fragmentation and hadronisation phases of the simulation. In HERWIG the outgoing partons of the additional interactions are produced as colour singlets, and emissions from the incoming partons to these scatters are not simulated.

As explained earlier, HERWIG can produce anomalous photons dynamically from the backwards evolution of the incoming partons. When such an event occurs no additional partonic interactions are generated. With the parameters chosen in this analysis HERWIG produces an average of 1.05 scatters per event.

4.2 PYTHIA

PYTHIA [86], named after the oracle at Delphi, is also in a position to simulate a large variety of processes and, like HERWIG, it has detailed models for non-perturbative effects. The version used in this analysis is 5.7. The simulation of an event divides into the same stages as for HERWIG. The execution is however completely independent and the main differences should be pointed out. Firstly, the photon spectrum in PYTHIA is generated using the WWA for both direct and resolved processes. Also, the factorisation scale used is the transverse mass $m_t^2 = \frac{1}{2}(m_1^2 + \hat{p}_{t1}^2 + m_2^2 + \hat{p}_{t2}^2)$, where m_i and $\hat{p}_{ti}$ are the masses and transverse momenta of the partons produced from the hard sub process. In the parton shower, the production of which is conceptually the same in both generators, the evolution is ordered in the virtuality of the radiated partons. As this ordering doesn't imply coherence, this is dealt with separately. The cascade of emissions is broken off at 1 GeV, so that in PYTHIA more radiation is expected near the beam axis and in the direction of the out going partons. The transition of the out going partons into hadrons is done using the Lund Model of string fragmentation. Strings corresponding to the QCD field lines are stretched between the quarks and the gluons. These strings have a strength of around 1 GeV/fm, and as the partons separate from each other, the strings gain more and more energy. Finally they break to produce one or more $q\bar{q}$ pairs. When the energy of the individual strings is small enough, mesons and baryons are formed from the quarks and diquarks at the end of the strings. Once again the last step is to decay unstable hadrons.

4.2.1 Implementation of MI in PYTHIA

The model for MI used in PYTHIA is based on the assumption that the partonic interactions in an event form a decreasing series in $\hat{p}_t$ [58]. Where HERWIG makes a prediction for total non-diffractive photon proton cross section $\sigma_{nd}^{\gamma p}$, PYTHIA uses measured values. The probability that in a given photon proton interaction a hard interaction with $\hat{p}_t$ takes place is:

$$P(\hat{p}_t^2) = \frac{1}{\sigma_{ND}^{\gamma p}} \frac{d\sigma_{QCD}^{\gamma p}}{d\hat{p}_t^2}(\hat{p}_t^2). \tag{4.7}$$

In the decreasing series in $\hat{p}_t$, the probability that the hardest scatter (i.e. the one with highest $\hat{p}_t$) takes place at a certain $\hat{p}_{t1}$ is then:

$$P(\hat{p}_{t1}^2) exp\left(-\int_{\hat{p}_{t1}^2}^{W^2/4} P(\tilde{p}_t^2) d\tilde{p}_t^2\right). \tag{4.8}$$

This is the product of the probability from equation 4.7, that a scatter takes place at this $\hat{p}_{t1}$, and the probability that between the maximum value $\sqrt{W^2/4}$ and $\hat{p}_{t1}$ no further scatter occurs. Following this logic the probability for the nth scatter at $\hat{p}_{tn}$ is:

$$P(\hat{p}_{tn}^2)\frac{1}{(n-1)!}\left(\int_{\hat{p}_{tn}^2}^{W^2/4} P(\tilde{p}_t^2) d\tilde{p}_t^2\right)^{n-1} exp\left(-\int_{\hat{p}_{tn}^2}^{W^2/4} P(\tilde{p}_t^2) d\tilde{p}_t^2\right). \tag{4.9}$$

Taking the sum over n is equivalent to not asking which scatter in the series takes place at this $\hat{p}_t$, and, as should be the case, the result is the original probability of equation 4.7:

$$\sum_{n=1}^{\infty} P(\hat{p}_{tn}^2)\frac{1}{(n-1)!}\left(\int_{\hat{p}_{tn}^2}^{W^2/4} P(\tilde{p}_t^2) d\tilde{p}_t^2\right)^{n-1} exp\left(-\int_{\hat{p}_{tn}^2}^{W^2/4} P(\tilde{p}_t^2) d\tilde{p}_t^2\right) = P(\hat{p}_t^2). \tag{4.10}$$

This also shows that this method of finding the probability for the nth scatter, on average, gives the right number of scatters per photon proton interaction:

$$\int_{\hat{p}_{tmin}^2}^{W^2/4} P(\hat{p}_t^2) d\hat{p}_t^2 = \frac{1}{\sigma_{ND}^{\gamma p}} \int_{\hat{p}_{tmin}^2}^{W^2/4} \frac{d\sigma_{QCD}^{\gamma p}}{d\hat{p}_t^2} d\hat{p}_t^2 = \frac{\sigma_{QCD}^{\gamma p}(\hat{p}_{tmin})}{\sigma_{ND}^{\gamma p}}. \tag{4.11}$$

For each event, starting from the maximum value $\sqrt{W^2/4}$, the partonic interactions are generated according to the probabilities from equation 4.8. For the additional scatters the parton distribution functions must depend on all the preceding x values and flavours chosen. However not enough is known about hadrons to write down such correlated probability distributions. To take account of the energy that has already gone into the previous scatters, PYTHIA uses $x = \frac{x_n}{\sum_{i=1}^{n-1} x_i}$, instead of x_n, to evaluate the parton distribution functions for the nth scatter.

PYTHIA, like HERWIG, produces all additional interactions as $gg \rightarrow gg$, where the two outgoing gluons are in a colour singlet. In this way they are decoupled from the rest of the event, and the problem of connecting the colour lines from different scatters is avoided.

As the number of interactions per event has a Poisson distribution about the average $\langle n \rangle$, then according to this model, there is a probability $exp(-\langle n \rangle)$ that events without a hard partonic interaction, but in which there is a soft interaction must be generated. However, in the Monte Carlo samples used for this analysis every event was required to have a hard sub process with $\hat{p}_t > 2.5$ GeV. This is for the same reason as given for HERWIG, that all events with jets of interest to this analysis are then generated. The threshold for the additional scatters can be set separately in PYTHIA. It was chosen to be $\hat{p}_{tn(n>1)} > 1.4$ GeV in this analysis because this value produces the best description of the data when using the GRV photon parameterisation.

With the photon structure functions used in this analysis PYTHIA can not differentiate between VMD and anomalous photons. Therefore all resolved photon events can be generated with multiparton interactions. PYTHIA also offers the opportunity to use more complicated, impact parameter dependent models. These are not, however, used in this thesis. In general multiparton interactions can only be generated in the γp mode of PYTHIA. Hence, in the version used in this analysis, the photon spectrum is generated using the WWA, and PYTHIA is then run in the γp mode with variable photon energy. With the parameters chosen in this analysis PYTHIA produces an average of 1.66 scatters per event.

4.3 Absolute Normalisation of the Monte Carlo

Both Monte Carlos contain a series of approximations which influence the prediction of the cross section. The most important is that they only consider the hard subprocess at LO. This means that the results are highly dependent on the factorisation scale chosen (see sections 2.8 and 2.9). Also HERWIG uses the two loop calculation for α_s the strong coupling constant. In a LO QCD calculation simply changing from a one to a two loop calculation for α_s introduces a difference of a factor 1.3 [87]. In addition the choice of Λ_{QCD} used in the Monte Carlos is complicated by the fact that, as a rule, the parameterisations of the photon and proton structure functions are determined with different values of Λ_{QCD}.

For the most part these effects lead to a constant factor (K) in the cross section. Therefore it seems justified to vary the absolute normalisation of the Monte Carlo, and if necessary the predicted cross section.

4.4 Detector Simulation

HERWIG and PYTHIA produce final states similar to those produced from beam interactions in the experiment. How this final state will look in the ZEUS detector is found using the program MOZART, which is based on the GEANT [88] package. MOZART simulates the interactions of the final state particles with the various detector components using certain simplifying assumptions. Thus the Monte Carlo final state is converted into the same form as the genuine data, and can be put through exactly the same analysis.

4.5 The Monte Carlo Sample Used

For this analysis events from the HERWIG 5.8 [83] and PYTHIA 5.7 [86] event generators, which have been passed through the ZEUS trigger, and detector simulations and data reconstruction, were used. Both the PYTHIA sample, and the HERWIG sample used for the central analysis and most of the systematic checks were generated with multiparton interactions. A separate HERWIG sample was also generated without multiparton interactions as a systematic check, and for the sake of comparing distributions. Both generators were run with the cut on the minimum $\hat{p}_t$ of the hard scatter set at 2.5 GeV. The parton distribution sets used were GRV(LO) [53] for the photon and MRSA-$\overline{\text{MS}}$ [90] for the proton. For this the PDFLIB package was used, which contains all the current parton distribution functions in a consistent way [89]. Events with $Q^2 > 4$ GeV^2 were excluded for the analysis. Beyond this cut it can not be expect that the generators reliably describe the data such that they could be used to estimate of the background from DIS. For this purpose another Monte Carlo sample, produced with another generator specifically for DIS studies, was used (see section 6.6.2).

In both Monte Carlo programs direct and resolved photoproduction events were generated separately. We have taken samples of generated direct and generated resolved photoproduction events from each program and combined them to obtain a single sample of hard photoproduction events. The combination was done both according to the ratio of the total generated cross section for each process as given by Monte Carlo program, and by fitting the x_γ^{OBS} distributions to the data, as explained in section 4.6.2. Table 4.1 gives a summary of the generated samples.

As the analysis concentrates on events with at least two jets with $E_T^{jet} > 6$ GeV, it is necessary to have enriched Monte Carlo samples. The cut on $\hat{p}_{tmin}$ of the partons produced from the hard sub process goes some way to achieving this but on its own is not enough. In order to have a large enough number of events in which the jets had large transverse energies, Monte Carlo samples were generated with several different filters, all of which required two jets of $\eta < 3$ passing differing E_T^{min} cuts of 4, 6, 8, and 12 GeV. These were then combined into a single sample according to the reduction factors associated with each filter. The reduction factor is the total number of events generated divided by the number passing the filter.

Generator	Process	MI	p_{tmin}	# Events
HERWIG	direct	-	2.5 GeV	316032
HERWIG	resolved	✔	2.5 GeV	514164
HERWIG	resolved	✗	2.5 GeV	59181
PYTHIA	direct	-	2.5 GeV	127552
PYTHIA	resolved	✔	2.5 GeV†	208555
PYTHIA	resolved	✗	2.5 GeV	78248

Table 4.1: *The Monte Carlo samples used in the analysis. († see 4.2.1)*

By using this method all events, to within a few percent, that could contribute to the cross section were generated, and the efficiency of the Monte Carlo generation was increased by around a factor 5 for the $E_T^{jet} > 4.0$ GeV filter, and considerably more for the higher E_T^{jet} cuts.

The Monte Carlo simulation of our physics data is an essential tool in the measurement of the cross sections as it is the only way to determine the acceptance of the ZEUS detector (including triggers, cleaning cuts, and the reconstruction of kinematic quantities) in each bin of $\bar{\eta}$ for the cross sections $d\sigma/d\bar{\eta}$.

The Monte Carlo event and detector simulations are not perfect and will introduce additional uncertainties in the measurement of each data point. These uncertainties are small compared to the calculated corrections and are included in the error bars on the measured cross sections as described in section 6.7.

The standard Monte Carlo for this analysis was a combination of direct and resolved photon events with MI produced with HERWIG. The normalisation of the Monte Carlo is discussed in section 4.6.2.

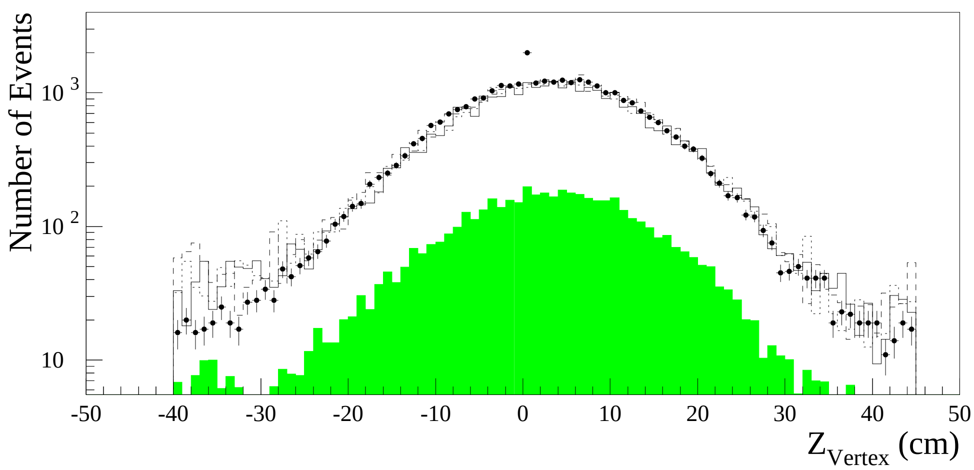

Figure 4.1: *The z_{vertex} distribution for all events in the data which pass the data selection cuts (points), compared to Monte Carlo distributions for events passing the same cuts. The solid line is HERWIG with MI, the dotted line is HERWIG without MI, the dashed line is PYTHIA and the shaded histogram gives the fraction of the HERWIG sample generated as direct.*

4.6 Comparison of Data and Monte Carlo

In this section the degree to which the Monte Carlo simulations, HERWIG and PYTHIA, reproduce the distributions of reconstructed quantities seen in our final data samples is examined. The goal of the whole exercise is to understand with what level of confidence the Monte Carlo simulations can be used for acceptance corrections in the cross section measurements. Throughout this section, where E_T^{jet} or y_{JB} are used, or their distributions are shown, the corrected quantities described in sections 6.3 and 6.4 are used.

4.6.1 General Distributions

Here the data and Monte Carlo distributions for some general quantities are compared. Since the Monte Carlo is all hard photoproduction and the data is not, it is necessary to make some preliminary selection. For this the criteria explained in chapter 5 are applied to both the data and the Monte Carlo.

Figure 4.1 gives the z_{vertex} distribution for the data and the three Monte Carlo

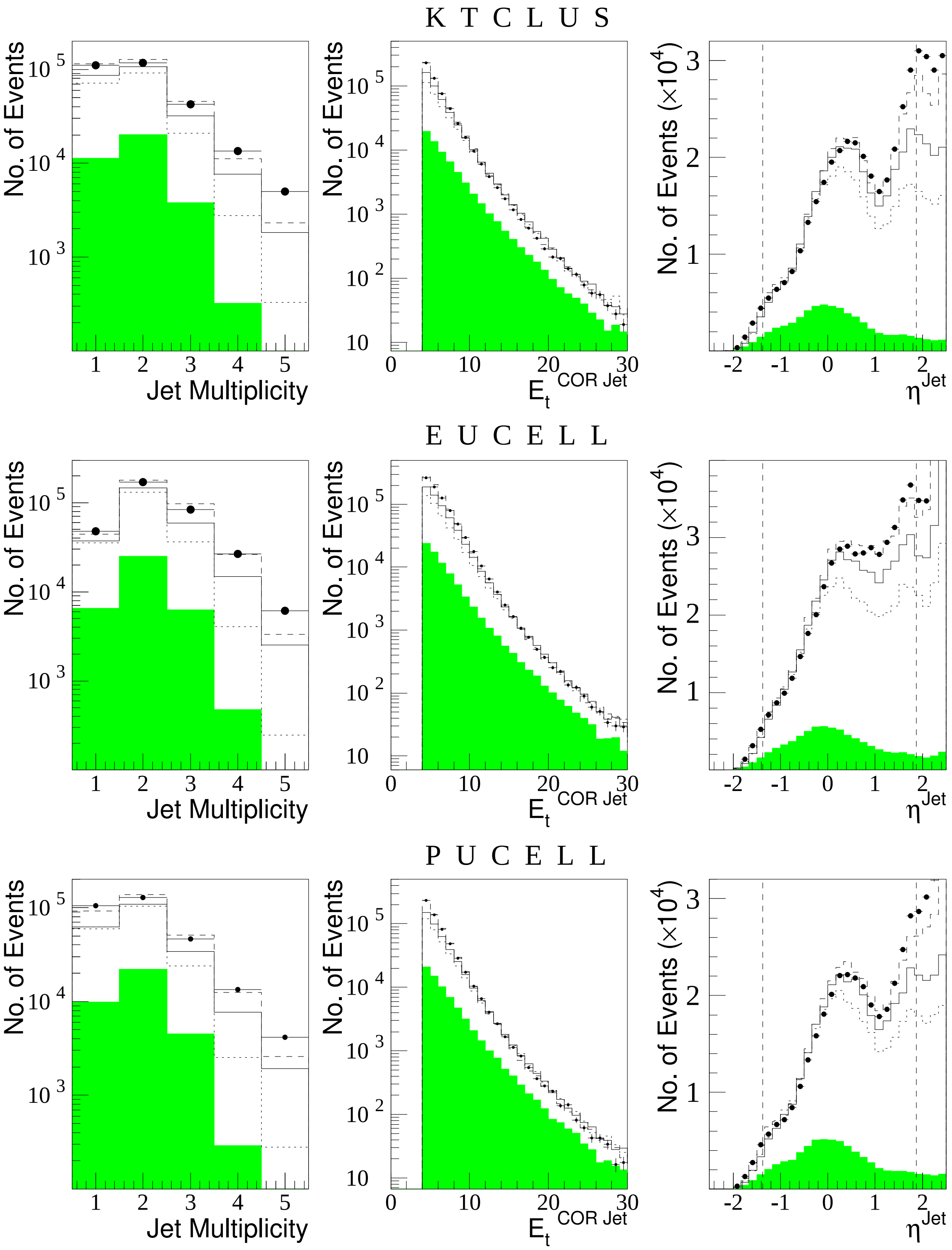

Figure 4.2: *For all three jet algorithms and all jets in events passing the data selection cuts: distributions for the jet multiplicity, E_T^{CORJet} and η^{jet}. The solid points are the data, the solid line is HERWIG with MI, the dotted line is HERWIG without MI, the dashed line is PYTHIA and the shaded histogram gives the fraction of the HERWIG sample generated as direct. The dashed vertical lines on the η^{jet} plots give the cuts imposed for the cross section measurements.*

samples. Also shown as the shaded histogram is the fraction of HERWIG events generated with direct photons. The agreement between data and all three Monte Carlo curves is good. The Monte Carlo distributions do lie above the data in the tails, but statistics are low in these regions. The data point at $z = 0$ is raised as this is the value assigned by default when it was not possible to obtain a vertex position. This is because the data sample contains some contamination from beam gas events.

Distributions for the jet multiplicity, corrected transverse energy, and η for all jets in the photoproduction data sample are compared to the Monte Carlo in figure 4.2. Plots are shown for each of the three jet algorithms used in this analysis. While the distributions for the different jet finders are not the same, the agreement between data and Monte Carlo is similar. The data shows a somewhat higher jet multiplicity than the Monte Carlo. This is probably because the Monte Carlo only includes the leading order QCD processes. HERWIG without MI, as might be expected, shows a significantly lower jet multiplicity than the other Monte Carlo samples. Both HERWIG and PYTHIA describe the E_T^{jet} distribution well, although they are a little below the data at the threshold. In the η distribution this shows up forward of $\eta = 1$, while the description of the data at lower values is good. When the multiparton interactions are turned off the E_T spectrum becomes noticeably too flat, and the divergence between data and Monte Carlo in η starts at around zero. The large dip at around $\eta = 1$ coincides with a large amount of inactive material at the boundary between the BCAL and FCAL (see figure 4.3). The effect is less pronounced for EUCELL, where it is smeared by the large square window used in the initial precluster phase of the algorithm.

Together these plots indicate that the data contains more jets at low E_T^{jet} in the forward region. This is probably due, in part, to some of the proton remnant scattering into the detector. Most of the far forward region, where the discrepancy becomes very large, is however excluded from the cross section measurements. It will be seen later in this chapter that the η^{jet} distributions in data and Monte Carlo for the jets used in cross section measurement do not show such large disagreement.

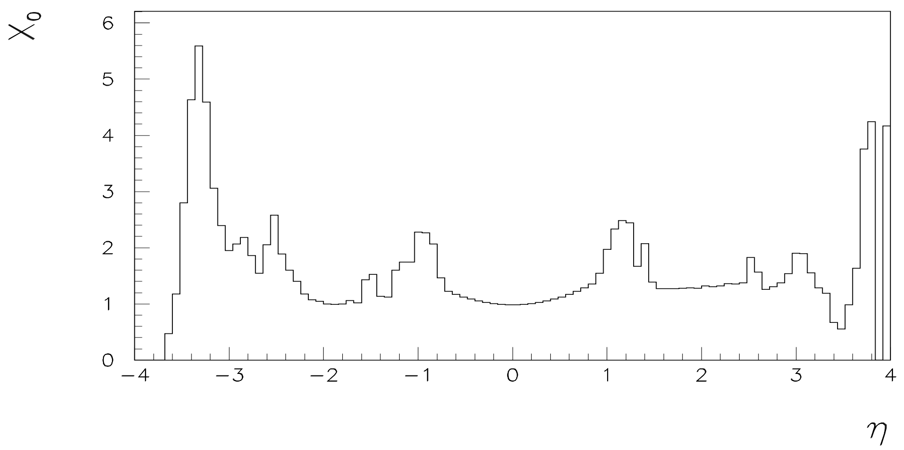

Figure 4.3: *Dead material in front of the calorimeter in radiation lengths as a function of η.*

4.6.2 x_γ^{OBS} and the Normalisation of the Monte Carlo

This section examines the reconstructed variable x_γ^{OBS}, as measured at the calorimeter, and the normalisation of the Monte Carlo. In figure 4.4 the x_γ^{OBS} distributions, for each of the three jet algorithms are shown. The events in these distributions are those in the final data sample after all the data selection cuts, and the cuts in the the $E_T^{jet} > 6$ GeV cross section definition. The x_γ^{OBS} shown here is calculated using the corrected y_{JB} and jet energies. The corrections to these quantities are to reduce detector effects, and are explained in sections 6.4 and 6.3. The x_γ^{OBS} distributions from the data are compared to those from the various generated HERWIG and PYTHIA Monte Carlo samples. That fraction of the HERWIG sample generated as direct is also shown separately as the shaded histograms.

The primary method of normalising the Monte Carlo samples and combining samples generated as direct and resolved was by comparison to this distribution. The normalisation was determined by eye such that a reasonable match between data and Monte Carlo distributions was found for all jet algorithms simultaneously. For HERWIG it was found that the direct cross section needed to be scaled by a factor 1.5, and the resolved by 1.9. For PYTHIA the scaling factor for direct was also 1.5. In the γp mode PYTHIA uses for resolved events with MI, only a γp cross section is given for an average W, so that the scaling of this event sample is not the same as for the others. However the scale factor used (0.35) is

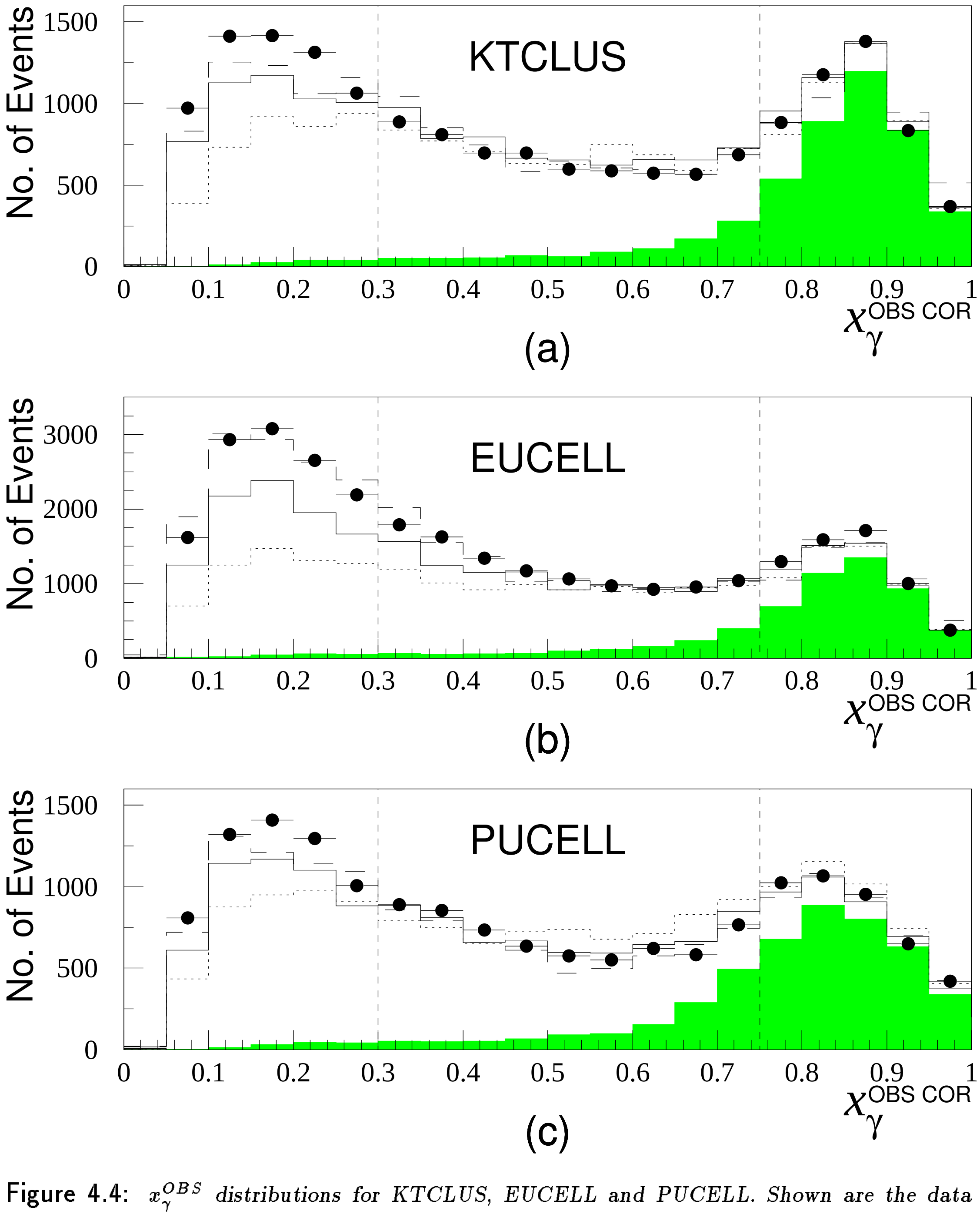

Figure 4.4: *x_γ^{OBS} distributions for KTCLUS, EUCELL and PUCELL. Shown are the data (points), HERWIG with (solid line) and without (dotted line) MI, and PYTHIA (dashed line). The shaded histogram is the fraction of HERWIG events generated as direct. The dashed vertical lines show where the cuts for the cross section measurements are made.*

approximately equivalent to the 1.9 found for HERWIG. These normalisations are used for all Monte Carlo distributions given in this thesis, including those in the previous section. As part of the systematic checks described in section 6.7, the relative quantities of resolved and direct events were also determined using the cross sections given by HERWIG with no additional scaling.

The histograms show that, while there are differences for the different jet finders, the agreement between data and Monte Carlo is good down to $x_\gamma^{OBS} \approx 0.25$. With this normalisation, EUCELL produces the largest disagreement between data and Monte Carlo, particularly for low values of x_γ^{OBS}. One effect of MI is to increase the number of events at low x_γ^{OBS}. However, even after the inclusion of MI with the parameters used here, the data lie above the simulation at low x_γ^{OBS}. PYTHIA which has more, softer additional interactions fits the data a little better than HERWIG.

It can be seen that the cut on x_γ^{OBS} at 0.75 provides an optimum separation of those events generated as direct from those generated as resolved. More important however is that for all the events in the $x_\gamma^{OBS} \geq 0.75$ sample the majority of the incoming photon's energy is carried by the parton probing the proton.

As was mentioned briefly in section 3.6, an additional cut was placed on x_γ at 0.3, thus selecting the region $0.3 < x_\gamma^{OBS} < 0.75$ for the resolved measurement. This was done to pick out the region where the Monte Carlo agrees well with the data. 0.3 was chosen because the Monte Carlo and data are in reasonable agreement on both sides of this value.

4.6.3 Other Kinematic Variables

The kinematic region in which we measure the cross sections $d\sigma/d\bar{\eta}$ is defined by the variables y and E_T^{jet}, η^{jet}, and $\Delta\eta$ for the two jets with highest transverse energy. The reconstructed values of these quantities, E_T^{CORjet}, y_{JB}, η^{CALjet}, and $\Delta\eta^{CALjet}$, for the final sample of two jet events are shown in figures 4.5 to 4.7. In

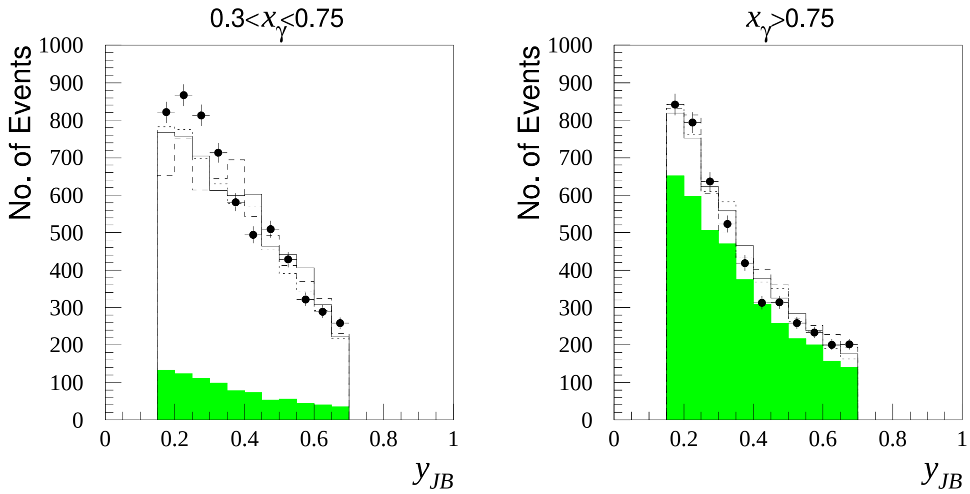

Figure 4.5: *y_{JB} distributions for events in the high and low x_γ^{OBS} regions used for the cross section measurements. Shown are the data (points) HERWIG with (solid line) and without (dotted line) MI, and PYTHIA (dashed line). The shaded histogram is the fraction of HERWIG events generated as direct.*

these plots the corrected variables for jet energies and y_{JB} are used (as described in sections 6.3 and 6.4), and the samples have been separated into the high and low x_γ^{OBS} regions used for the cross sections. The events in these distributions are those in the final data sample after all the data selection cuts, and the cuts in the cross section definition (except for the $|\Delta\eta|$ cut in the $\Delta\eta$ distributions). Again the data is compared to the PYTHIA, and HERWIG with and HERWIG without MI event samples. The shaded histograms give the fraction of HERWIG events generated with direct photons.

Figure 4.5 gives the y_{JB} distributions for (a) the low, and (b) the high x_γ^{OBS} regions. The agreement between the data and the Monte Carlo is reasonable for the high x_γ^{OBS} region, however the disagreement for low values of y_{JB} in the lower x_γ^{OBS} region is of some concern. This could be a source of error in the acceptance corrections for this quantity in the resolved cross section, and is accounted for in the determination of systematic errors as described in section 6.7

Figures 4.6 and 4.7 compare the data and Monte Carlo distributions for all three jet algorithms for E_T^{CORjet}, η^{CALjet}, and $\Delta\eta^{CALjet}$ of the two jets of highest E_T^{jet}, for the low and high x_γ^{OBS} regions respectively. The agreement between the Monte

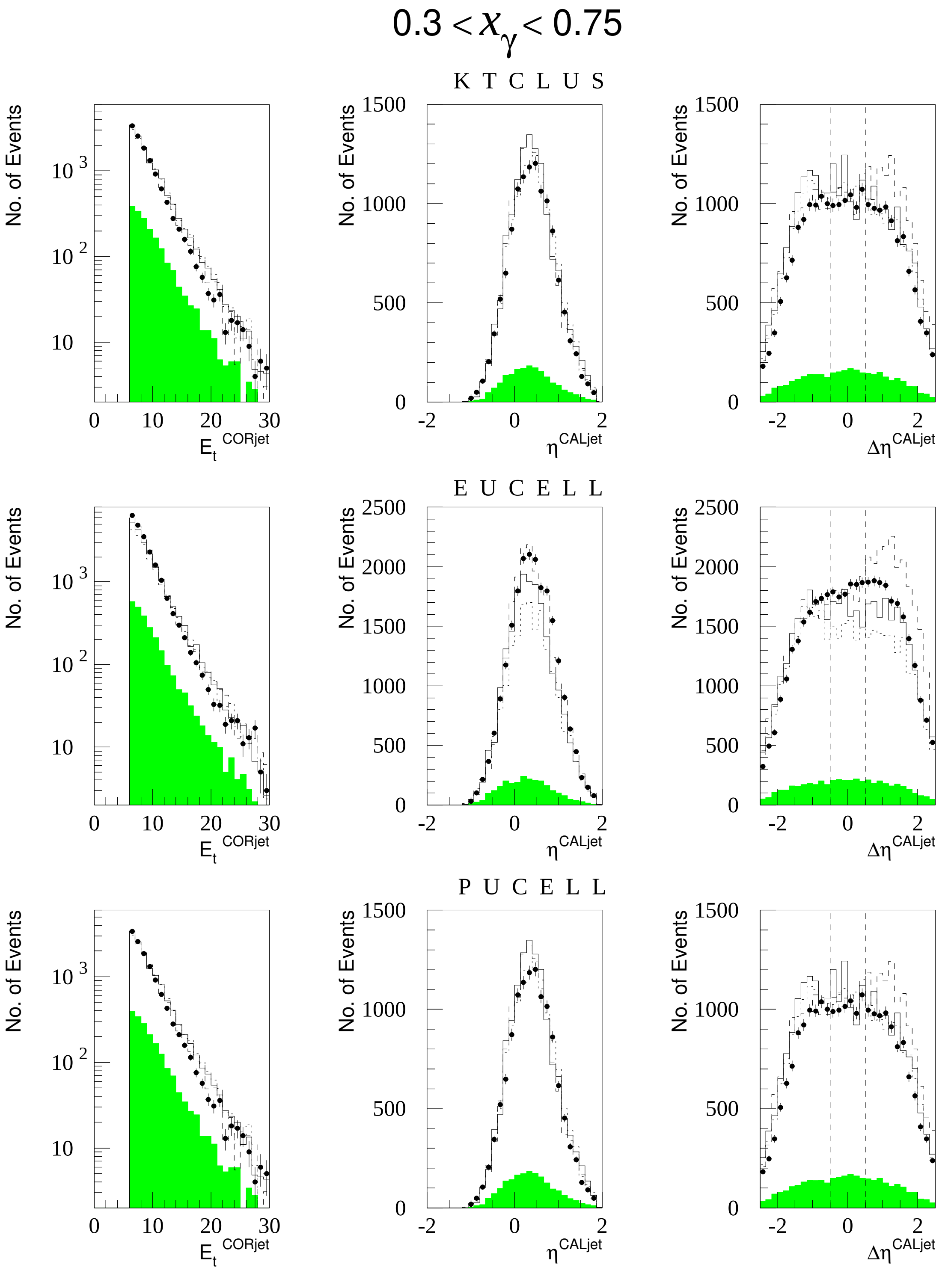

Figure 4.6: *Corrected E_T^{jet}, η^{CALjet} and $\Delta\eta^{CALjet}$ distributions for events in the low x_γ^{OBS} region used for the cross section measurement. Shown is the data (points) HERWIG with (solid line) and without (dotted line) MI, and PYTHIA (dashed line). The shaded histogram is the fraction of HERWIG events generated as direct. The dashed vertical lines on the $\Delta\eta^{CALjet}$ plots show the cut used to define the cross sections to be measured.*

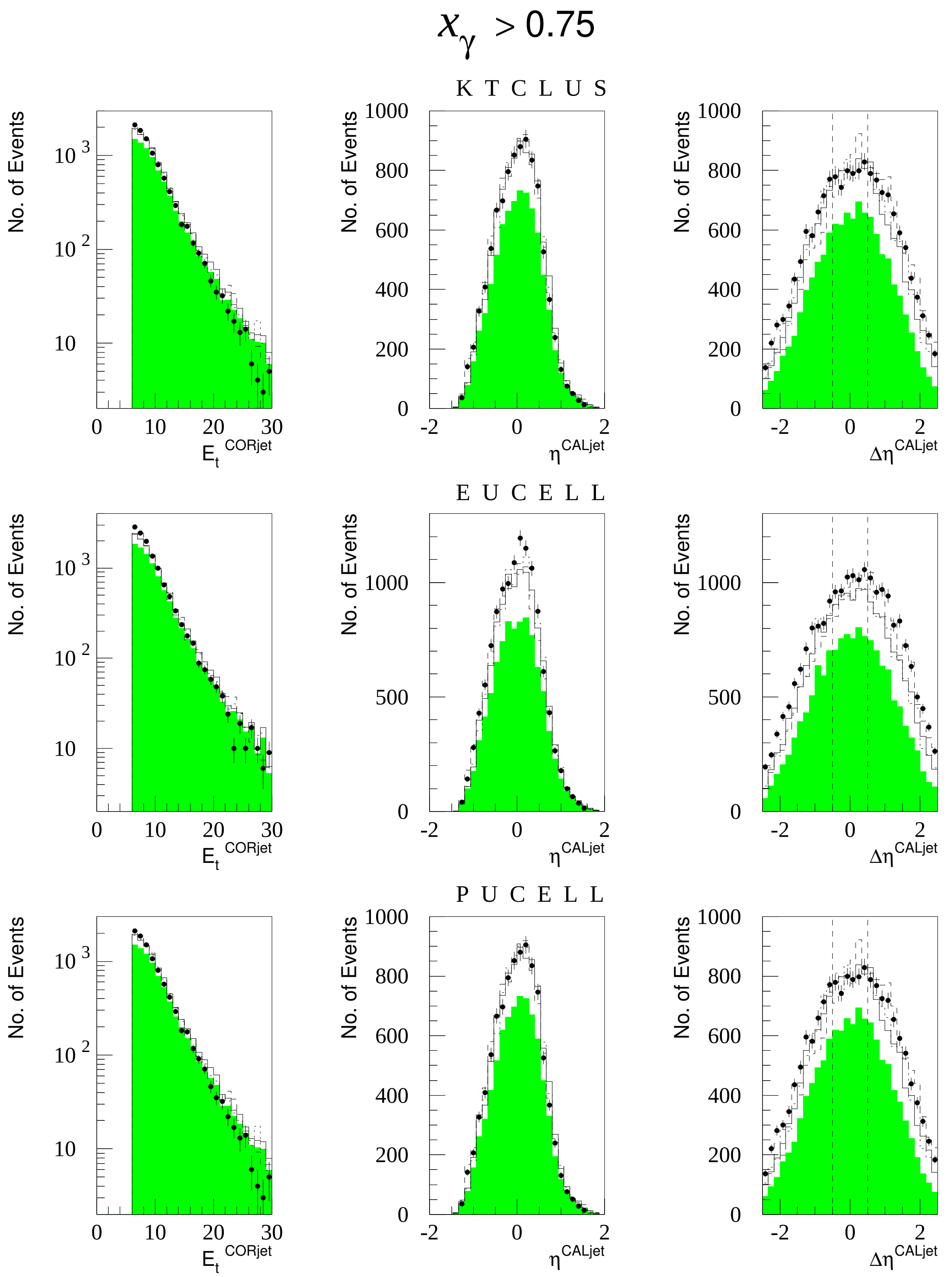

Figure 4.7: *Corrected E_T^{jet}, η^{CALjet} and $\Delta\eta^{CALjet}$ distributions for events in the high x_γ^{OBS} region used for the cross section measurement. Shown is the data (points) HERWIG with (solid line) and without (dotted line) MI, and PYTHIA (dashed line). The shaded histogram is the fraction of HERWIG events generated as direct. The dashed vertical lines on the $\Delta\eta^{CALjet}$ plots show the cut used to define the cross sections to be measured.*

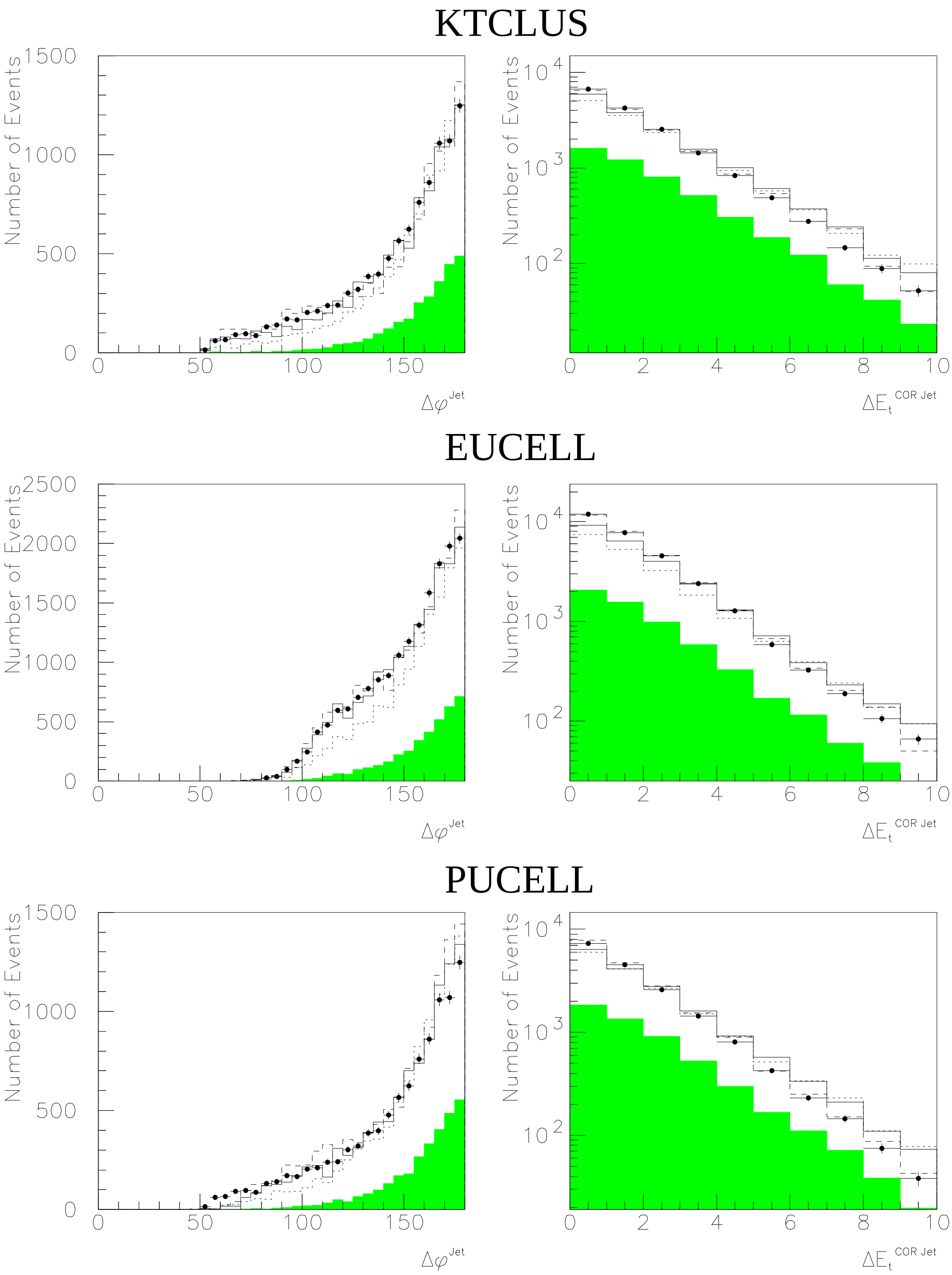

Figure 4.8: *Comparison of data and Monte Carlo distributions of $\Delta\phi^{Jet}$ and ΔE_t^{CORJet} for all three jet algorithms for the two jets of highest transverse energy in each event. Shown are the data (points) HERWIG with (solid line) and without (dotted line) MI, and PYTHIA (dashed line). The shaded histogram is the fraction of HERWIG events generated as direct.*

Carlo simulations and the data is in general good, although it appears that there may be an excess of jets with $E_t^{jet} > 20$ GeV in the Monte Carlo, particularly for the high x_γ^{OBS} region. Also the η^{CALjet} and $\Delta\eta^{CALjet}$ distributions are slightly less well described by the Monte Carlo in the low x_γ^{OBS} case. The major differences in the $\Delta\eta^{CALjet}$ distribution occur outside the region used for the cross section measurement. Again the agreement between data and Monte Carlo is worse for EUCELL than the other two jet finders.

Figure 4.8 shows the comparison between data and Monte Carlo for ΔE_T^{CORjet} and $\Delta\phi^{jet}$ between the two jets of highest transverse energy, for all three jet algorithms. The jet of highest E_T is always jet one, so ΔE_T^{CALjet} is always positive. The agreement between the data and Monte Carlo for these distributions is reasonable. The width of the $\Delta\phi$ distribution is matched for the Monte Carlo with MI. For the ΔE_T^{CALjet} distribution the HERWIG sample without MI lies below the data for low values of ΔE_T^{CALjet}. This should however be considered in conjunction with the too hard E_T spectrum, as seen in figures 4.2, 4.6, and 4.7. This, together with the minimum E_T^{jet} threshold, leads to larger differences in E_T between the jets. All the Monte Carlo distributions show a tendency to lie above the data for large ΔE_T^{jet}, but it should be noted that the y-axis has a logarithmic scale so these differences are not as significant as they may appear. The EUCELL distributions again show the largest discrepancy between data and Monte Carlo.

Figure 4.9 Shows the corrected x_p^{OBS} range sampled by these events for both data and Monte Carlo (HERWIG and PYTHIA) for each of the jet algorithms. Also the direct contribution from HERWIG is given as a shaded histogram. The data lies in the region $-2.5 \lesssim \log_{10}(x_p^{OBS}) \lesssim -1$, which is largely due to the limits set on η^{jet} and E_T^{jet}. The data distributions are well described by both Monte Carlo generators, though the Monte Carlo, particularly the HERWIG without MI, is a little below the data for $-1.75 \lesssim \log_{10}(x_p^{OBS})$. This corresponds to the deficit at low x_γ^{OBS}.

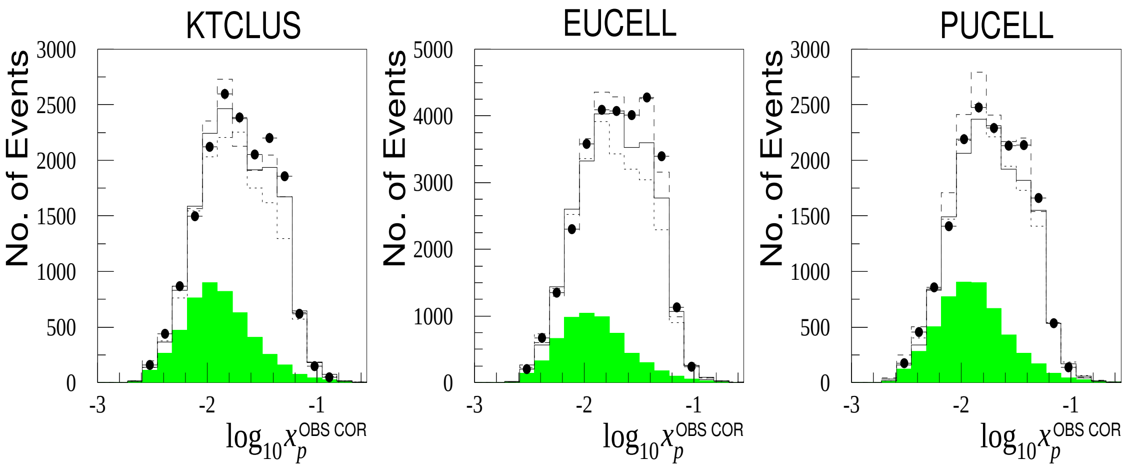

Figure 4.9: $\log_{10} x_p^{OBS}$ *distributions for all three jet finders, for events in the final data sample (points), compared to Monte Carlo distributions for events passing the same cuts. The solid line is HERWIG with MI, the dotted line is HERWIG without MI, the dashed line is PYTHIA and the shaded histogram gives the fraction of the HERWIG sample generated as direct.* x_p^{OBS} *here is calculated using corrected* E_T^{jet}.

4.6.4 Jet Profiles

In chapter 6 the correction of the jet energies using the Monte Carlo is described. Before this can be done, however, it is necessary to be confident that the Monte Carlo correctly models the jets present in the data. In order to verify this the jet profiles were investigated. That is the shape of the transverse energy distribution around the jet axis, averaged over a large number of jets. Profiles in both η and ϕ produced by the following method were considered. For each jet the transverse energy measured in the calorimeter was binned as a function of $\eta(\phi)$, for cells within $|\phi^{jet} - \phi^{cell}| < 1$ ($|\eta^{jet} - \eta^{cell}| < 1$), where the origin was defined as $\eta^{jet}(\phi^{jet})$. These distributions were then averaged over all jets, so that each $\delta\eta(\delta\phi)$ bin contained the average transverse energy at that distance from the jet axis. Particular attention was paid to energy deposits in cells within a radius of 1 from the jet axis as these actually form the jet as defined for this analysis. In figures 4.10, 4.12 and 4.14 the Monte Carlo and data jet profiles in η can be compared for specific intervals of E_T^{jet} and η^{jet}. The HERWIG with MI and PYTHIA profiles describes the data reasonably in all E_T^{jet} and η^{jet} regions. Although small discrepancies for jets with low E_T^{jet} and large η^{jet} are apparent these lie mainly in the forwards direction outside the jet cone. On the same histograms are shown the profiles generated when HERWIG without multiparton interactions was used. In this case the descriptions of the jet profiles are significantly worse. Figures 4.11, 4.13 and 4.15 shows the jet profiles in ϕ. These profiles are also well described by HERWIG with MI and PYTHIA, and less well by HERWIG without multiparton interactions. In all it seems justified to use the Monte Carlo samples with MI to correct the jet energies.

4.7 Summary

In general both HERWIG and PYTHIA with multiparton interactions describe the data well. HERWIG without Multiparton interactions describes the data less well, particularly at low x_γ^{OBS}. All samples describe the data well enough to be used in correcting for detector effects and acceptance, and for extracting a detector independent cross section. On more detailed comparison there is a deficit in the Monte Carlo, which shows up for events with low y and for low transverse energy jets and jets in the forward region. These differences are to be considered in the assessment of the systematic errors. A major part of the deficit is, however, dealt with by applying the lower cut on x_γ, see section 4.6.2. Of the three jet algorithms used in this analysis, and with the Monte Carlo normalisation used here, EUCELL produces the largest differences between data and Monte Carlo distributions.

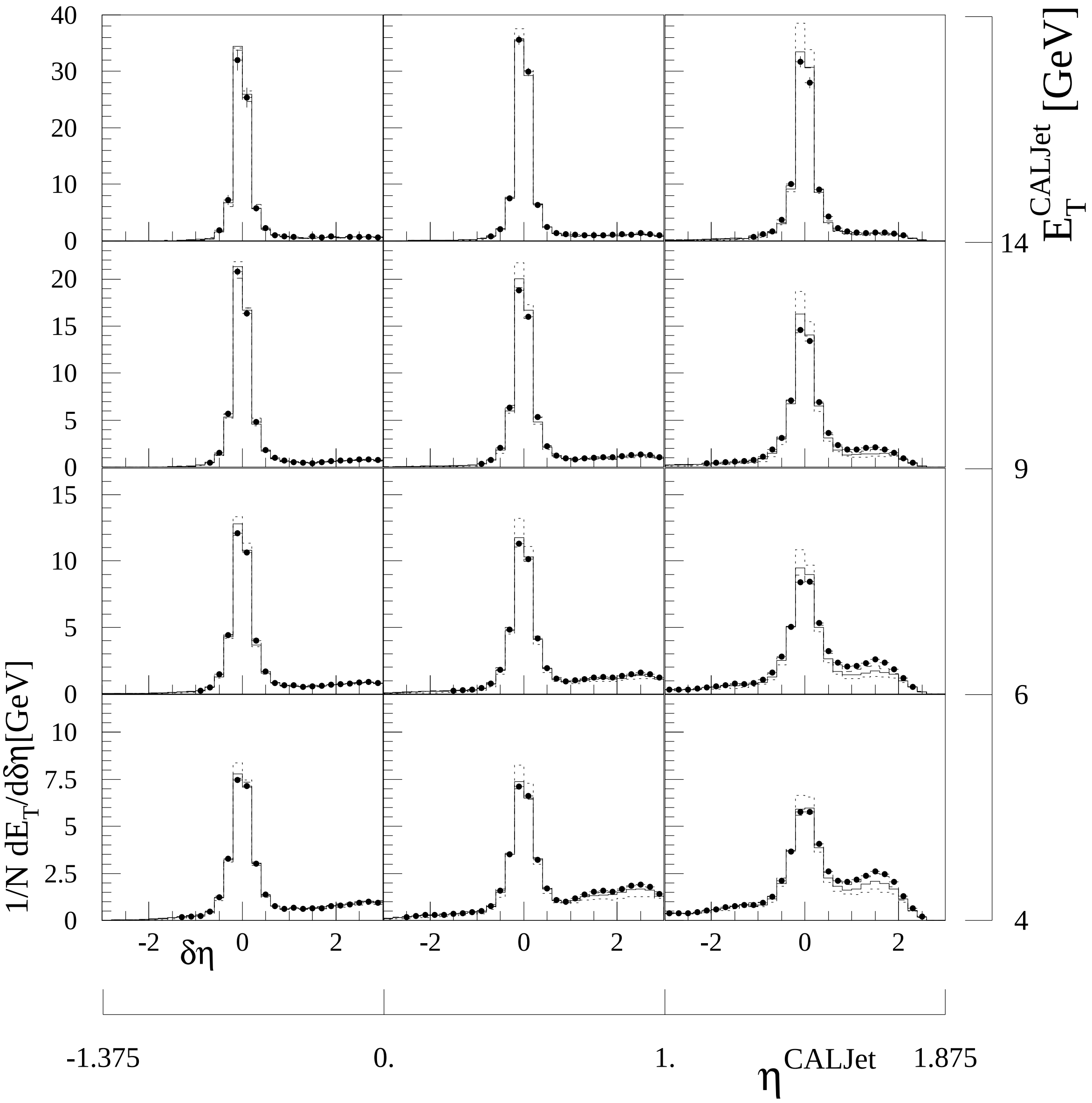

Figure 4.10: *KTCLUS jet profiles in η for different bins in η^{jet} and E_T^{jet}. The solid points are the data, the solid line is HERWIG with MI, the dashed line is PYTHIA and the dotted line is HERWIG without MI.*

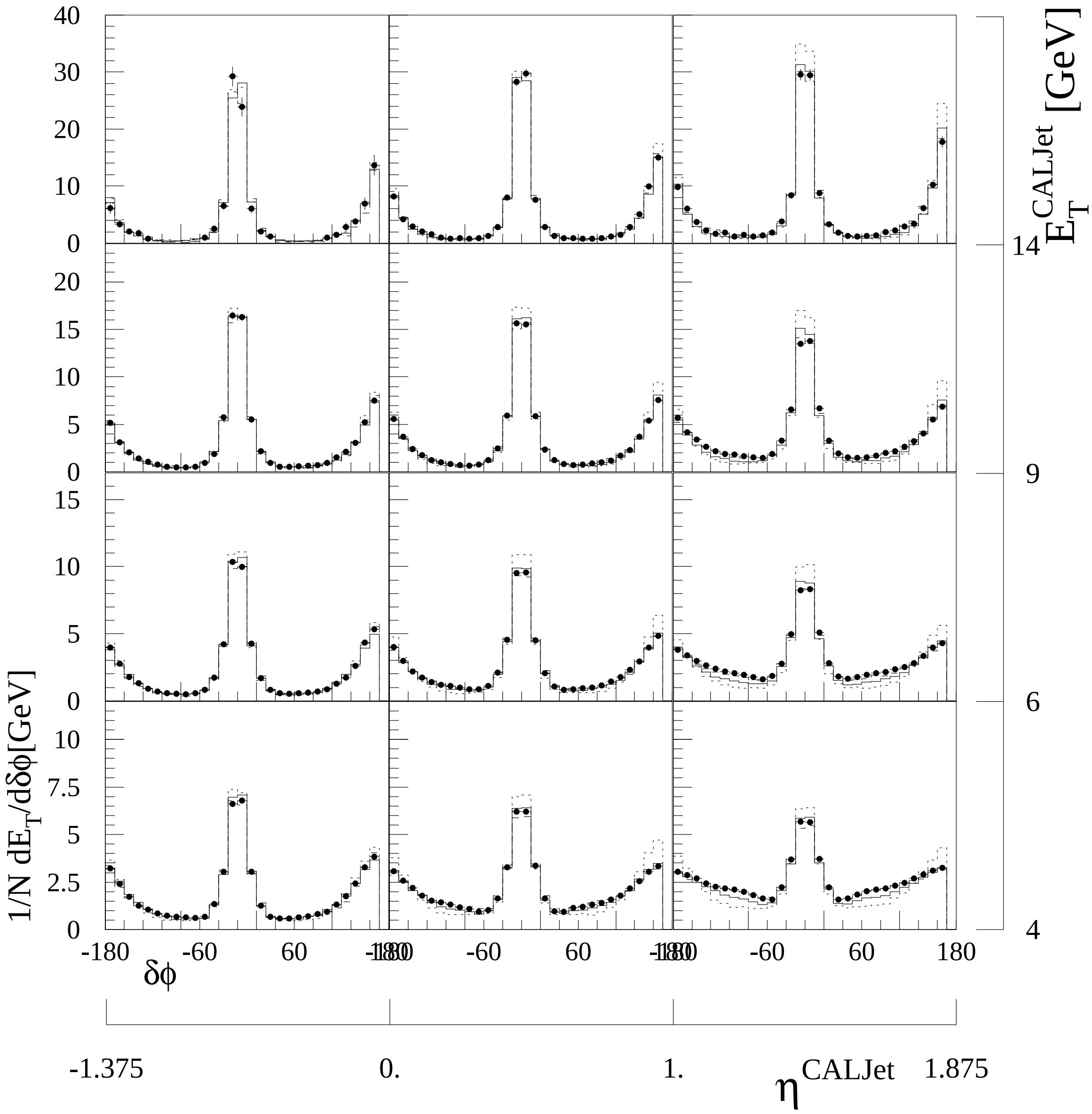

Figure 4.11: *KTCLUS jet profiles in ϕ for different bins in η^{jet} and E_T^{jet}. The solid points are the data, the solid line is HERWIG with MI, the dashed line is PYTHIA and the dotted line is HERWIG without MI.*

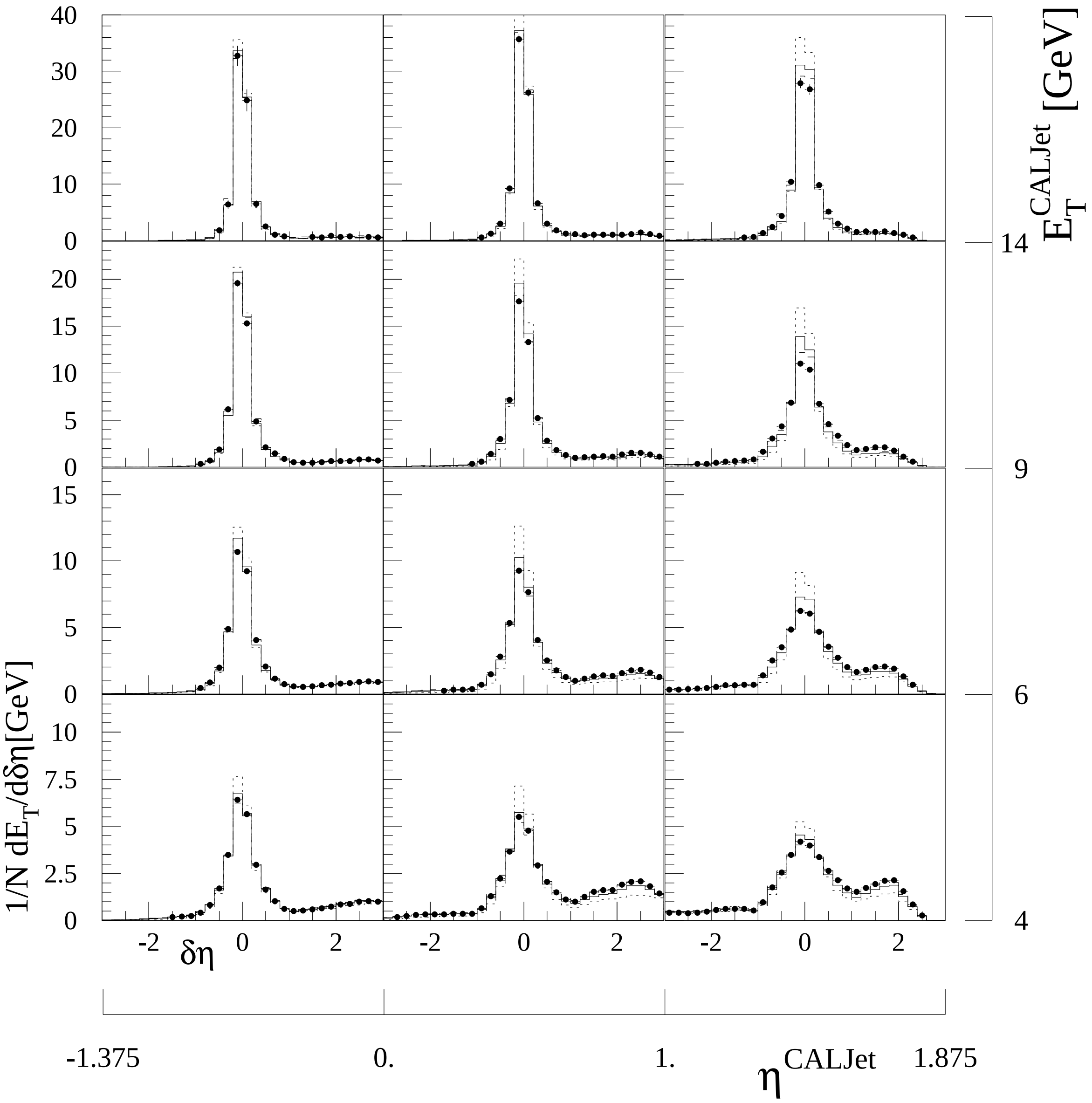

Figure 4.12: *EUCELL jet profiles in η for different bins in η^{jet} and E_T^{jet}. The solid points are the data, the solid line is HERWIG with MI, the dashed line is PYTHIA and the dotted line is HERWIG without MI.*

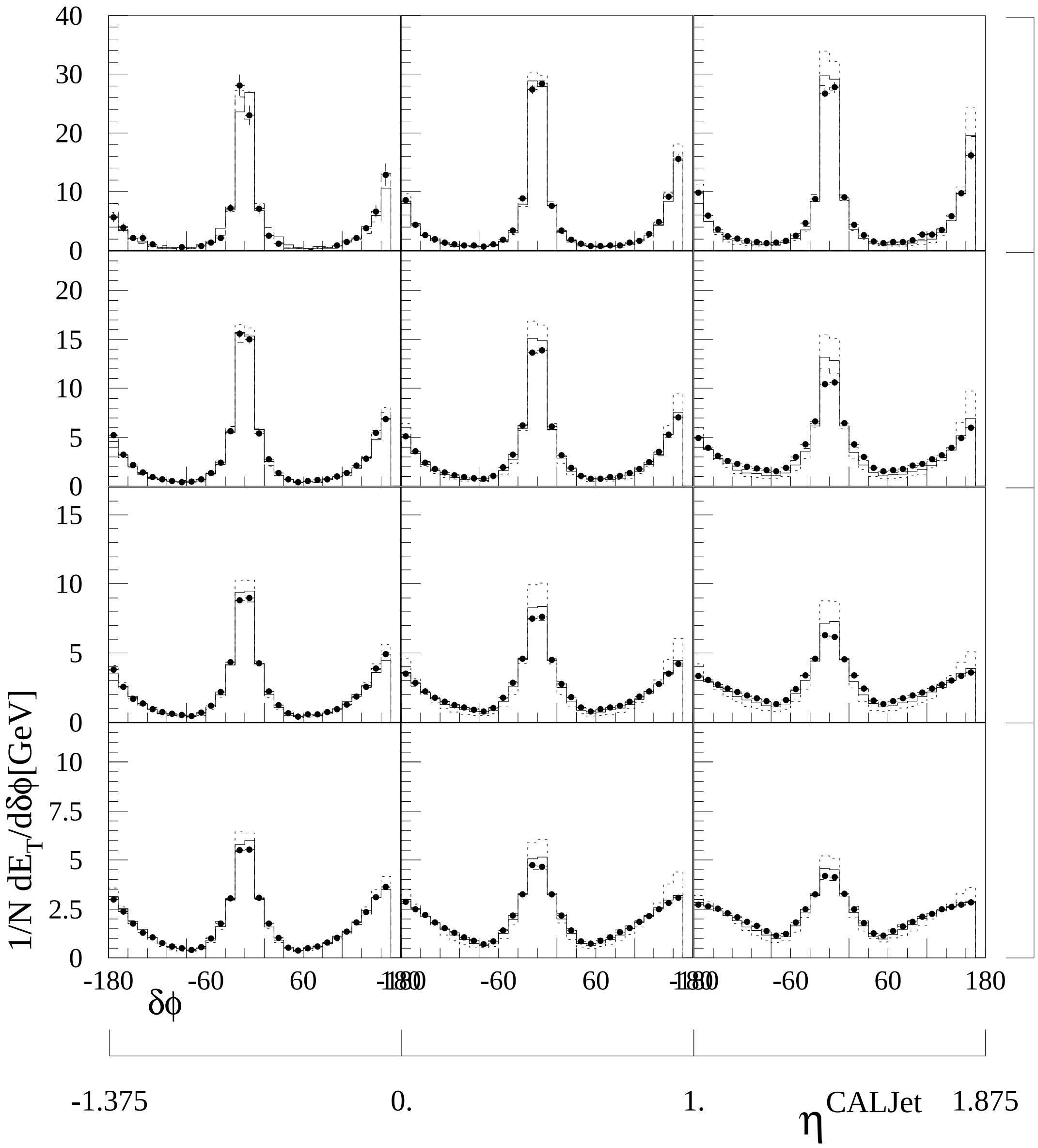

Figure 4.13: *EUCELL jet profiles in ϕ for different bins in η^{jet} and E_T^{jet}. The solid points are the data, the solid line is HERWIG with MI, the dashed line is PYTHIA and the dotted line is HERWIG without MI.*

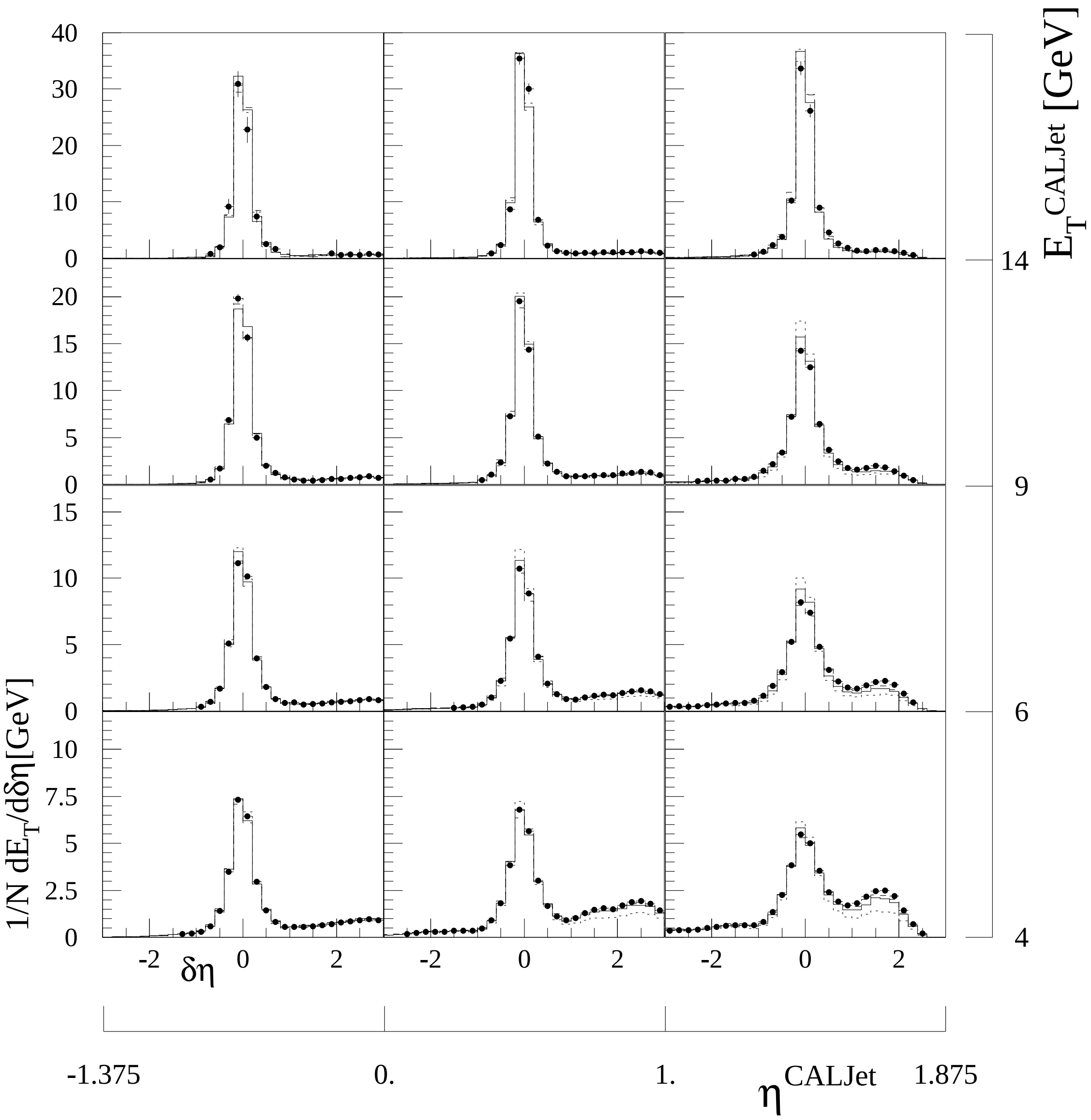

Figure 4.14: *PUCELL jet profiles in η for different bins in η^{jet} and E_T^{jet}. The solid points are the data, the solid line is HERWIG with MI, the dashed line is PYTHIA and the dotted line is HERWIG without MI.*

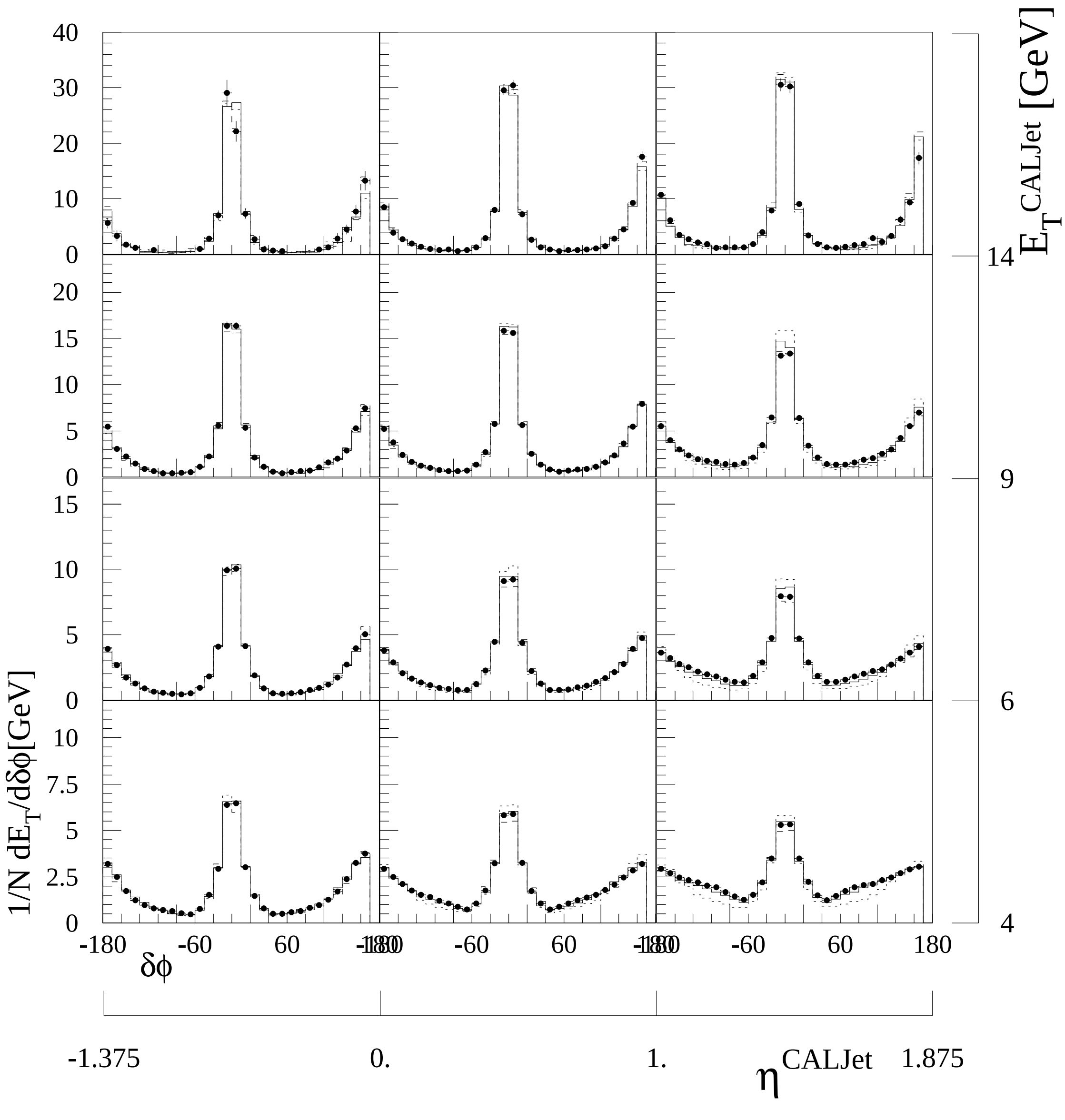

Figure 4.15: *PUCELL jet profiles in η for different bins in η^{jet} and E_T^{jet}. The solid points are the data, the solid line is HERWIG with MI, the dashed line is PYTHIA and the dotted line is HERWIG without MI.*

Chapter 5

Data Selection

For this analysis a data sample collected during the 1994 positron-proton **HERA** run period, corresponding to an integrated luminosity of 2.7pb^{-1}, was used. The data selection can conveniently, if somewhat artificially, be divided into three separate stages:

1. First, second, and third level triggers.

2. Cleaning cuts.

3. Jet finding and kinematic selection.

5.1 Triggers

5.1.1 FLT

At the first level trigger (FLT) events were passed which satisfied any one of a number of criteria based primarily on regional energy or regional transverse energy sums in the uranium calorimeter. Table 5.1 shows the first level triggers used in this analysis and their respective energy thresholds. Apart from regional energy

Trigger	Description	Threshold (MeV)
BEMC_E	Barrel EMC energy	4778
ET	Transverse energy excluding the first FCAL towers around the beam pipe.	15102
EMC_E	Electromagnetic energy excluding the first FCAL towers around the beam pipe.	14968
CAL_E	Total Energy in the calorimeter	20064
CALxgTRK94	A combination of the other triggers with lower thresholds in coincidence with a good track in the CTD	CAL_E 14968 EMC_E 10068 Et 11574 BEMC_E 3404 REMC_E 2032

Table 5.1: *First level triggers*

thresholds the CALxgTRK94 trigger also required at least one good track to be found in the CTD. For a track to be positively identified as either good or bad it was required to have 20 or more degrees of freedom, more than 5 hits on axial and on stereo wires of the CTD, $5° < \theta < 70°$, and p_t >200MeV. Tracks were then classified as bad if their z at the inner radius of the CTD was less than -75cm, and good if it was forward of this. In these terms a good track is one with a high probability of originating from an ep collision, and a bad track is one with a high probability of originating form a proton−beam gas interaction.

To assess the efficiency of the calorimeter first level triggers for this analysis, and the accuracy of their description in the Monte Carlo simulations, a study was made of an independent sample of events triggered by the LUMI branch of the first level trigger, and containing at least two jets as found by the EUCELL algorithm. The LUMI trigger branch requires the scattered positron to be found in the LUMI detector, some low thresholds in the different parts of the calorimeter (much lower than those otherwise being used), and has a veto on photon detection by the lumi_γ.

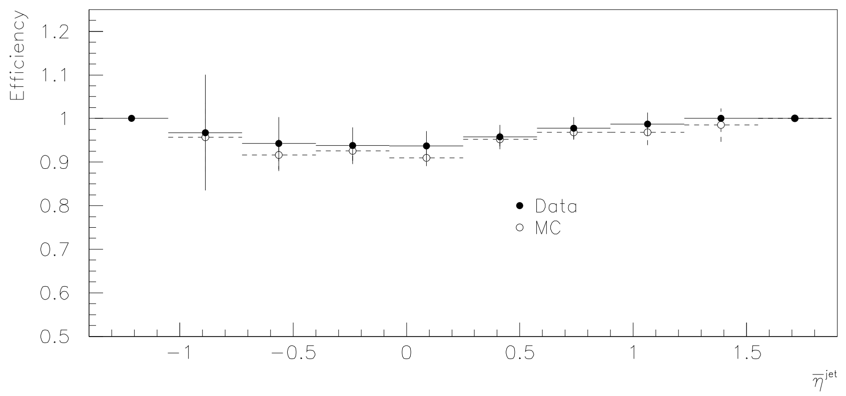

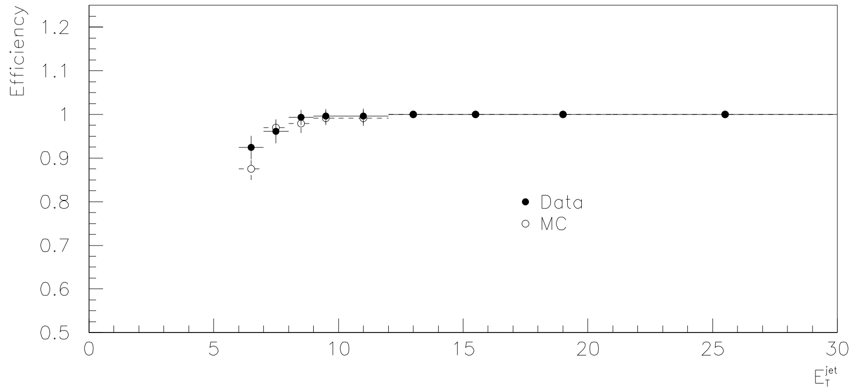

Figure 5.1: *The efficiency of the FLT below as a function of E_T^{jet} for the lower E_T jet of the two selected, and above as a function of $\bar{\eta}$. The data is shown with solid error bars and the Monte Carlo with dashed error bars.*

The fraction of these lumi triggered events which also passed one or more of the calorimeter triggers, thus entering our final data sample, is shown in figure 5.1 as a function of $\bar{\eta}^{cal}$ and E_T^{cal} for the two highest E_T jets in an event. Also shown is this fraction for a HERWIG Monte Carlo sample. The agreement with the data is reasonable, which means that none of the FLT selection criteria bias the final data sample or introduce the need for a large correction factor.

5.1.2 SLT

At the second level trigger (SLT) some general cuts were made primarily to remove three classes of event. The following selections on calorimeter timing were used firstly to remove events caused by interactions between the proton beam and residual gas in the beam pipe:

FCAL time valid with 2 or more cells $> 200MeV$ and FCAL Energy $> 2GeV$

RCAL time valid with 1 or more cells $> 200MeV$ and RCAL Energy $> 2GeV$

Both valid reject: $t_{FCAL} - t_{RCAL} > 8ns$ $t_{RCAL} <$ -8ns

Only t_{FCAL} valid: $|t_{FCAL}|$ >8ns

Only t_{RCAL} valid: $|t_{RCAL}|$ >8ns

and secondly to remove cosmic muons:

$$\text{(time(upper half BCAL)-time(lower half BCAL))} < -8ns$$

Here 'valid' means within the time window of a bunch crossing.

Thirdly first level triggers caused by discharges in the calorimeter photomultiplier tubes were removed. To do this events in which the calorimeter was empty (FCAL/BCAL/RCAL energy lower than 0.8/0.6/0.4GeV), and all events with $E - p_z \geq$75 GeV were rejected.

In addition to these general rejections a filter was used to select events with high transverse energy. This required $E - p_z > 8\ GeV$, and the total transverse energy, excluding the first FCAL towers around the beam pipe, Et_woBP $> 8\ GeV$, and a track, and $E - p_z > 12GeV$ or p_z/E <0.95 for the entire calorimeter.

The SLT efficiency was assessed in a similar way to that of the FLT. An investigation was made of the fraction of events passing the SLT Lumi trigger which also passed the other SLT cuts. The SLT Lumi trigger only adds the requirement that the energy in the LUMI is more than 5GeV to the conditions of the FLT Lumi trigger. These distribuitons are shown in figure 5.2. Once more the same fraction for a HERWIG event sample is also shown. The agreement between data and Monte Carlo is again reasonable, indicating that the SLT selection criteria do not bias the data sample or introduce the need for a correction factor.

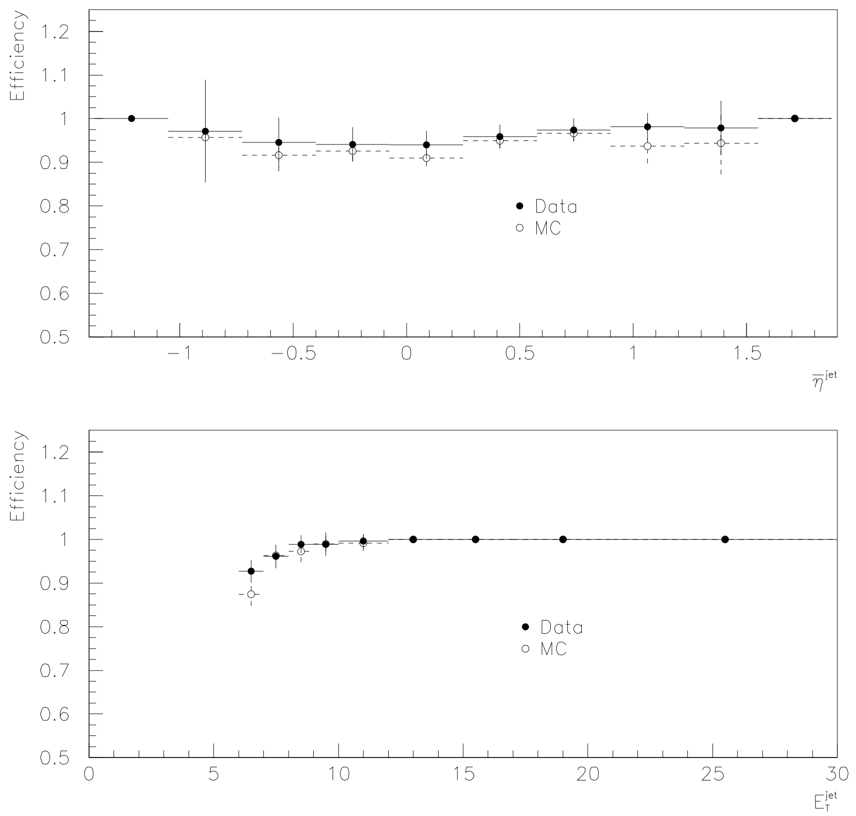

Figure 5.2: *The efficiency of the SLT below as a function of E_T^{jet} for the lower E_T jet of the two selected, and above as a function of $\bar{\eta}$. The data is shown with solid error bars and the Monte Carlo with dashed error bars.*

5.1.3 TLT

The third level trigger (TLT) was used to reject events with more than 5 bad tracks. Events were also rejected if $E - p_z \geq$75GeV. The last stage in this part of the selection process is the filters set by the physics working groups. The analysis presented in this thesis uses a sample selected by the hard photoproduction working group's dijet filter. This requires that a crude cone algorithm find two or more jets with $E_t > 4.0$ GeV in the range $2.0 \leq \eta^{jet} < 2.5$, or $E_t > 3.5$ GeV backwards of $\eta^{jet} = 2.0$.

In addition to the efficiency checks already described for the FLT and SLT, the investigation of the effect of the calorimeter energy scale on the trigger described in chapter 6.7 can be considered a check on the cuts in the SLT and TLT.

At this stage there is an event sample of 523992 events.

5.2 Cleaning Cuts

After the DST selection there will still be some contamination from beam gas interactions and cosmic ray events ($\sim 5\%$), and charged current and DIS events ($\sim 15\%$). To reduce this background we select events satisfying the following cuts, which are explained over the next few pages:

$$\text{NO positron with } \; y_e < 0.7$$

$$0.15 \;\leq\; y_{JB} \;\leq\; 0.7$$

$$(E - p_z) > 12\ GeV \;\; \text{.OR.} \;\; p_z/E < 0.95$$

$$\frac{\not{E}_t}{\sqrt{E_T}} = \sqrt{(\sum p_X)^2 + (\sum p_Y)^2 / \sum E_T} \leq 1.5\ \text{GeV}^{\frac{1}{2}}. \tag{5.1}$$

$$\text{Calorimeter timing } \; t_{up} - t_{down} \geq -7ns$$

$$[\#\ \text{tracks} - (\#\ \text{vertex tracks})^2] < 0$$

$$-40cm < z_{vertex} < 45cm$$

In order to determine these cuts a number of test data samples were used:

1. Events where a positron with y_e <0.7 was found in the calorimeter.
2. Events where a positron was found in the lumi_e detector and no photon in the lumi_γ detector (Lumi Tagged).
3. Events from unpaired proton bunches.
4. Events from unpaired positron bunches
5. Events where neither positrons nor protons were present.

The relevant distributions from these samples are shown in figures 5.3—5.5. It can be assumed that the sample with a positron in the LUMI contains essentially no background, the unpaired bunches are primarily beam gas interactions, the events

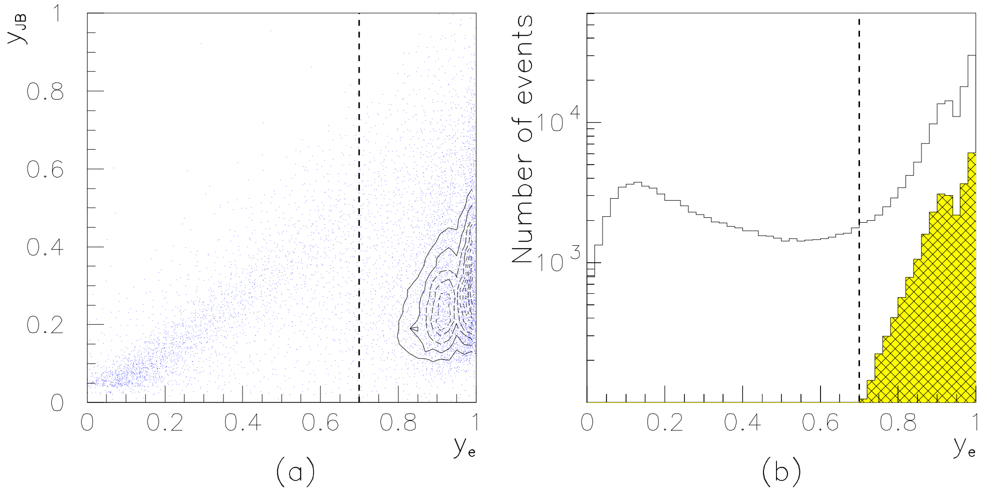

Figure 5.3: *For events where a positron candidate was found in the calorimeter (a) y_{JB} vs y_e; superimposed on this is a contour plot for those events where the scattered positron was identified in the* lumi$_e$ *calorimeter. (b) The distribution of y_e for all events (empty histogram), and for those events where the scattered positron was identified in the* lumi$_e$ *calorimeter (filled histogram). In both (a) and (b) the dashed line shows the cut used.*

with neither protons nor positrons are cosmics, and those where a low y_e positron was found in the calorimeter are DIS candidates(which is why this is also used as a data selection veto). It should be noted that only ~1/14 of the total e and ~1/12 p bunches were unpaired, and ~1/9 of the time both the proton and positron bunches were empty. Hence to estimate the background due to proton(positron) beam gas interactions the respective sample needs to be multiplied by 12(14), and for cosmics the empty bunches sample needs to be multiplied by 9. This has been done for all the histograms that follow.

To reject higher Q^2 events (DIS) on the basis of finding the scattered positron in the detector it is necessary to be confident that this is indeed what has been found. The electron finding method used works by looking at the shower characteristics of deposits in the UCAL. Figure 5.3(a) shows y calculated using the Jaquet-Blondel method [65](y_{JB}) plotted against y calculated from the scattered positron (see 3.1). The points represent all events with a positron candidate, while the contours represent the distribution of the subset of these events in which the scattered positron was found in the LUMI detector. The dashed line indicates the cut used to identify and remove probable DIS events. The fact that any significant number of Lumi tagged events enter this histogram indicates that to reject an event solely on the basis of finding a candidate for the scattered positron in the calorimeter would plainly be wrong, and would reduce the signal from genuine photoproduction events.

The correlation between $y_{_{JB}}$ and y_e is good for events with y_e <0.7, whereas the wide spread above this cut indicates that here only very seldom has the scattered positron been correctly identified. This is because positrons with y_e >0.7 are low in energy. The contours for the Lumi tagged events underline the fact that candidates that obviously can not be the scattered positron populate values of y_e >0.7. Figure 5.3(b) Shows the distributions of events in y_e for all events with a positron candidate(empty histogram), and for the subset of these with a Lumi tag(shaded histogram) on a log scale. It can be seen that by putting the cut at y_e =0.7(dotted line) the number of Lumi tagged events rejected is negligible. The candidates in the Lumi tagged events are largely due to electromagnetic showers from π^0 and η mesons.

Obviously putting a cut on y_e is not sufficient to reject all DIS events: it does not remove events where the positron was correctly identified to have y_e >0.7, nor does it remove events where the scattered positron entered the detector but was not identified. Figure 5.4(a) shows the $\frac{1}{2E_e}(E-p_z) = \frac{1}{2E_e}\sum(E^{cell} - p_z^{cell})$ distributions for all the test samples mentioned previously. For the case where the scattered positron is not found in the calorimeter this quantity is identical to $y_{_{JB}}$. However where the scattered positron did enter the detector $E - p_z \Rightarrow$ 2Ee, and so DIS events should have values of $\frac{1}{2E_e}(E-p_z) = \frac{1}{2E_e}\sum(E^{cell} - p_z^{cell})$ approaching 1. This can be seen to be the case for events where a positron candidate with y_e <0.7 was found(hollow triangles). For this reason the cut of $y_{_{JB}}$ <0.7 was used to reject the remaining DIS events, where $y_{_{JB}}$ was calculated assuming the scattered positron did not enter the calorimeter.

Since there is the cut on $E-p_z$ >8GeV in the trigger $y_{_{JB}}$ must be greater than

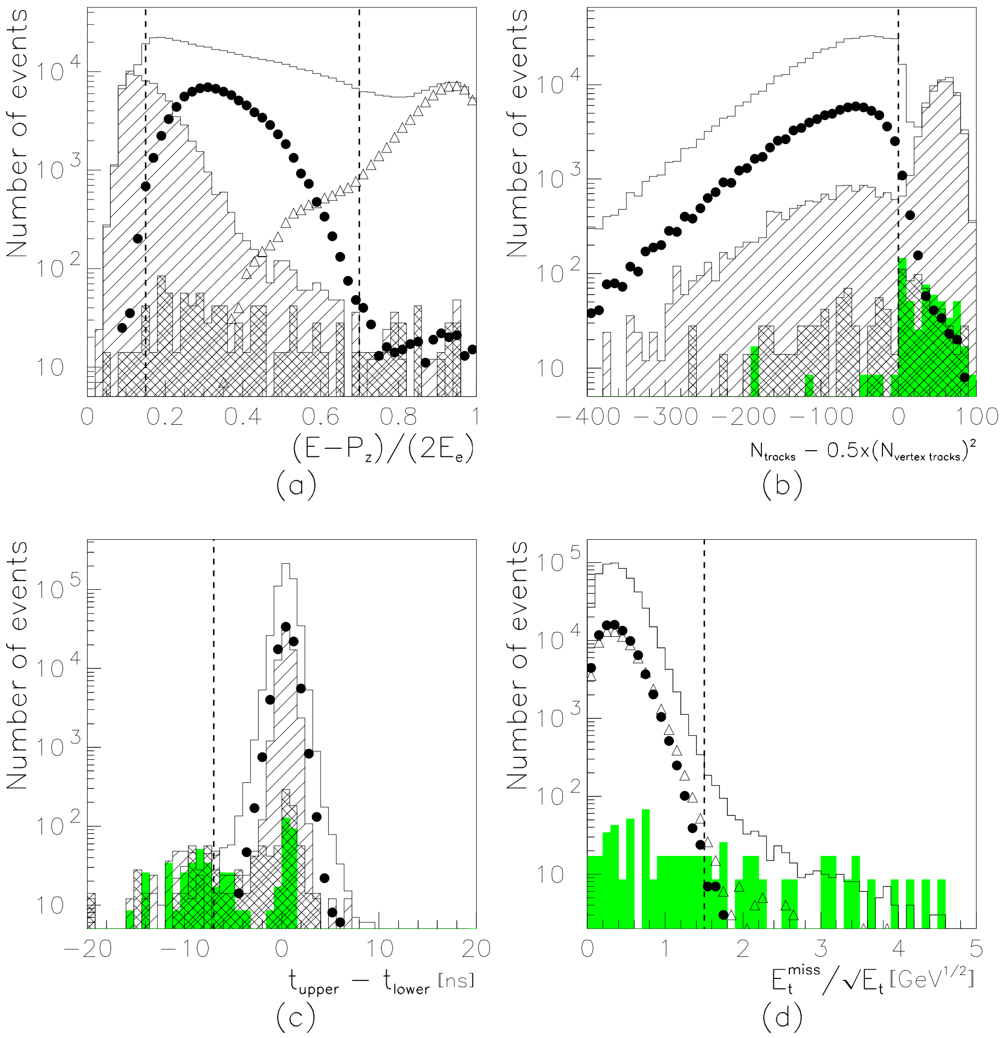

Figure 5.4: *Distributions of (a) $(E-p_z)/2E_e$, and (b) (Total Number of tracks)$-0.5\times$(Number of vertex tracks)^2 (c) the time of an event in the upper part of the calorimeter $-$ the time in lower part of the calorimeter, and (d) $\frac{\not{E}_t}{\sqrt{E_T}}$ for: all events(empty histogram), events where the scattered positron was found in the* lumi$_e$ *calorimeter(solid points), events in which a positron with $y_e < 0.7$ was found in the calorimeter(hollow triangles), events from unpaired proton bunches(diagonally lined histogram), events from unpaired positron bunches(cross hatched histogram), events from empty bunches(solid shaded histogram). The dashed lines indicate the data selection cuts.*

$\sim$0.15. This cut in the trigger is the cause of the sharp drop off at the low end of the distribution in figure 5.4(a). The Proton-Beam gas background is boosted forwards, and thus has low values of $E-p_z$ and is concentrated at low values of $y_{_{JB}}$, as can be seen by the rise of the diagonally lined histogram. This is the reason for the lower cut of 0.15$<$ $y_{_{JB}}$. Thus events in the central region 0.15$<$ $y_{_{JB}}$ $<$0.7 are used for this analysis. Additionally the E-pz.OR.pz/E cut was applied to remove beam gas because it was in the trigger for part but not all of the data taking.

Beam gas interactions normally take place upstream of the detector and produce tracks which are not assigned to a vertex. In contrast the tracks from ep collisions almost all come from the vertex, so by comparing the relative numbers of vertex tracks and all tracks the histograms in figure 5.4(b) were made. Here it can be seen that the number of Lumi tagged events falls off rapidly at $(N_{tracks}) - 0.5 \times (N_{vertextracks})^2 \approx 0$, while the number of events from unpaired proton bunches rises to a peak at around 60. Also cosmic particles which pass directly through the detector produce two tracks which can define a good vertex. Using the cut $(N_{tracks}) - 0.5 \times (N_{vertextracks})^2 < 0$ both beam gas and cosmic events (for which this quantity typically $=$ 0) can be removed.

Figure 5.4(c) is of the difference in signal time between the upper and lower halves of the calorimeter. For cosmic particles that go through the detector from top to bottom this time difference should be about -10 ns, while for events in the centre of the detector it should be approximately zero. In the histograms for the empty and unpaired bunches(cross hatched, diagonally lined, and solid shaded histograms) there is an excess of events evident at around -10 ns. Placing the cut at -7ns appears to remove successfully the majority of cosmic rays without cutting into the peak at zero.

As the incoming beams have no transverse component the total transverse energy of an event should be zero. Therefore $\not{E}_t$, the 'missing' E_T, should ideally be exactly zero but due to the calorimeter resolution a distribution arises. The width of this distribution is largely due to statistical fluctuations in the energy losses to

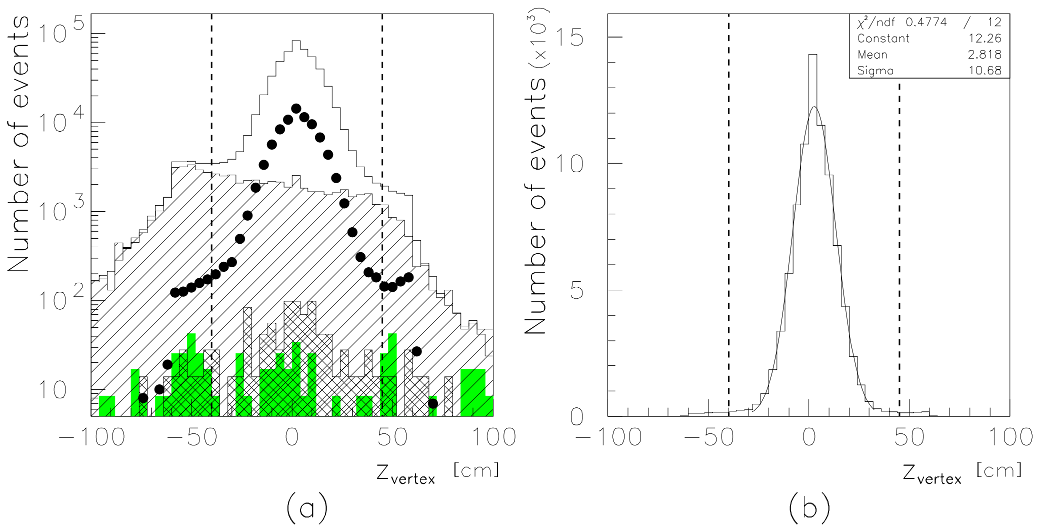

Figure 5.5: *(a) z_{vertex} distributions for: all events(empty histogram), events where the scattered positron was found in the* lumi$_e$ *calorimeter(solid points), events from unpaired proton bunches(diagonally lined histogram), events from unpaired positron bunches(cross hatched histogram), events from empty bunches(solid shaded histogram). (b) A Gaussian fit to the z_{vertex} distribution for events where the scattered positron was found in the* lumi$_e$ *calorimeter. The dashed lines indicate the data selection cuts.*

inactive material and is therefore proportional to $\sqrt{E_T}$. Figure 5.4(d) shows $\frac{\not{E}_t}{\sqrt{E_T}}$. From this it can be seen that the region above 1.5 is obviously populated purely by background. The cut on $\frac{\not{E}_t}{\sqrt{E_T}}$ <1.5GeV$^{\frac{1}{2}}$ removes mainly charge current events, where a neutrino went undetected, and cosmics.

Looking at the z_{vertex} distribution shown in figure 5.5(a) a Gaussian distribution of the ep vertices on top of the almost uniform distribution of background vertices can be seen. So the cut on the z_{vertex} at 4σ was made to remove the regions which are virtually all background. Figure 5.5(b) shows a Gaussian fit to the Lumi tagged photoproduction events. The cut at 4σ causes a minimal loss of genuine events, while the outer parts of the background distributions from non ep interactions are removed. The general fall off of the background distributions is due to the physical dimensions of the tracking detectors. The sharper fall offs are due to general vertex requirements in the trigger.

After all these cleaning cuts and the further requirement of two jets of E_T^{Jet} >4GeV and $-1.375 < \eta^{jet} < 1.875$ and $\Delta\eta^{jet} < 0.5$ we are left with the event sample sizes shown in table 5.2, which naturally differ for each of the jet finders.

Jet algorithm	Total	Proton-Beam gas	Positron-Beam gas	Cosmic
EUCELL	45940	3×12	5×14	0×9
PUCELL	33294	1×12	3×14	0×9
KTCLUS	26851	1×12	0×14	0×9

Table 5.2: *Total and estimated background number of events present in the sample after the background rejection cuts.*

Chapter 6

Analysis of the Data

This chapter describes all aspects of the process used to produce the measured cross sections. The resolution of the measured jet and event parameters is assessed. Where appropriate the measured values of these parameter are corrected for detector effects. Then the method of correcting for detector acceptance to extract the cross sections defined in chapter 3 is described. The background contributions to the measured cross sections are estimated, and finally there is an evaluation of the systematic errors.

6.1 Calorimeter Energy Scale

In evaluating these cross sections three separate but related problems concerning the calorimeter energy scale had to be considered.

1. How well is the energy response of the calorimeter described in the Monte Carlo?

2. How well do the jet algorithms reconstruct jets in terms of η and E_T?

3. How well does the calorimeter measure jet energies and global energy sums involved in our events?

The second two of these are addressed in sections 6.2 and 6.4, the first is discussed here.

The five fold increase in statistics in 1994 over previous years allowed the calorimeter energy scale to be studied in more detail than before. Over the period in which this analysis was conducted several approaches were used to try to determine the relative calibration of the calorimeter in the experiment itself and in the Monte Carlo detector simulation. These break down into basically three methods:

- Compare the energies of particles measured in the CTD with those measured in the calorimeter.
- In DIS compare the expected hadronic energy, calculated from the measured positron energy, with the hadronic energy actually measured in the calorimeter.
- In Photoproduction, for those events in which the scattered positron entered the LUMI detector, compare y_{JB} from the uranium calorimeter with the reconstructed y_e from the measurement in LUMI detector.

Each of these methods, when applied to data and Monte Carlo, give the relative discrepancy in the energy scale of the calorimeter between measurement and simulation. Each method has different uncertainties, but all produced consistent results. It was discovered that the calibration of the BCAL(RCAL) was 6%(2.5%) lower in the data than in the Monte Carlo simulation [91, 92]. Therefore, for the purpose of this analysis, the measured energies were scaled in the BCAL by +6% and in the RCAL by +2.5%. None of the available methods can be reliably used for the FCAL, however results suggest that the FCAL energies require no scaling [92].

When an attempt was made to determine these numbers from a jet analysis, it became apparent that it was not possible to achieve a sufficient degree of accuracy. It seems reasonable, however, to go into the investigation of the energy scale made

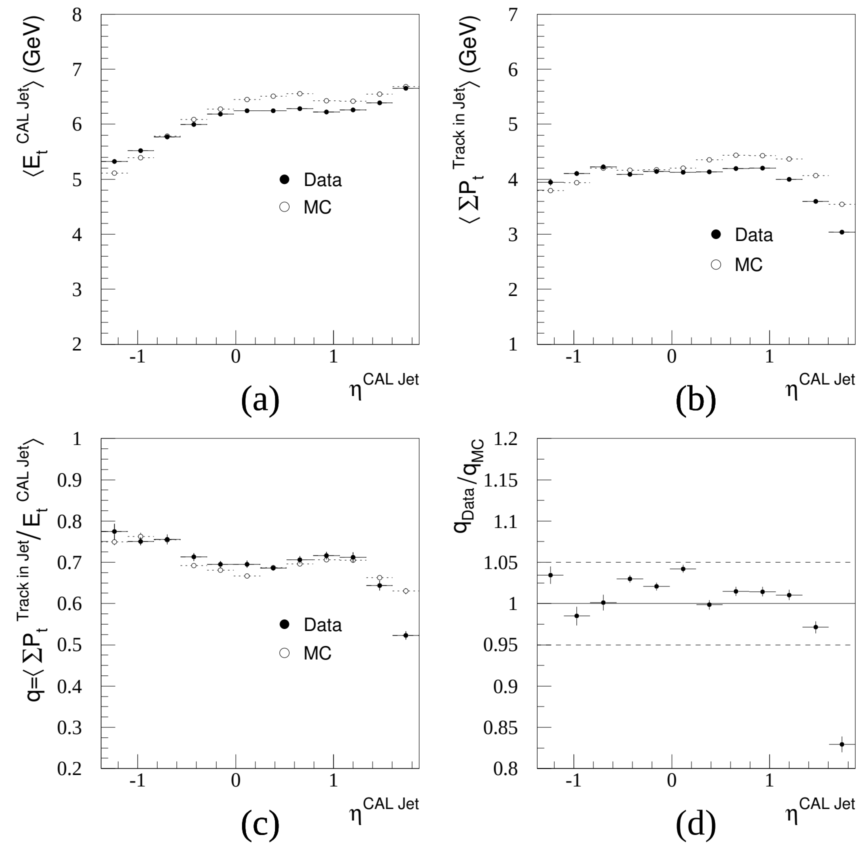

Figure 6.1: *Relative energy scale of the calorimeter in data and Monte Carlo from the jet energy flow. Shown as functions of η^{CALjet} are (a) the average E_T of the calorimeter jets. (b) the average sum of the momenta of tracks ending within the jet cone at the face of the calorimeter. (c) The ratio of the summed track transverse momenta, and the jet transverse energy. (c) the ratio of the distribution in (c). The jets used in this plot were identified using the EUCELL algorithm*

during this analysis as it can be used to estimate the errors to be attributed to the measured jet energies. It also indicates that these may not be due to the calibration of the calorimeter alone, but also to differences in the absorption of the jet energies in the calorimeter between the real data and the Monte Carlo simulation. This is important as it will affect both the efficiency for selecting a complete data sample of two jet events, and the determination the acceptance corrections. The absorption of the jet energies is sensitive to the composition of the jets, which isn't accounted for in the constant scale factor of $+6\%(2.5\%)$. Also there is the possibility of nonlinearities in the calorimeter energy response at low energies, which would introduce additional sensitivity to the composition of the jets.

For events in the selected dijet sample described in chapter 5, the transverse momenta of tracks measured in the CTD that ended within the cone of a particular jet at the calorimeter were summed. This summed track momentum was then compared to the transverse energy of the jet in the calorimeter pointed to by the tracks. For this comparison tracks with $p_t > 300$ MeV and at least 35 hits were considered, independent of whether they were assigned to a vertex. Figure 6.1(a) and (b) show the average transverse energy of the jets, and sum of the transverse momenta of tracks within the jets as a function of the pseudorapidity of the jets. The agreement between the data and Monte Carlo distributions is good, though there is a small divergence forward of $\eta \simeq 0.25$. This is present in both distributions and therefore indicates a difference in the E_T spectrum between data and Monte Carlo, and not a discrepancy in the detector simulation. Forward of $\eta \approx 1$ the jet and track distributions are very different. As the jets move forward they start to overlap with calorimeter energy deposits caused by the proton remnant, and thus their energy is raised. Tracks in this forward direction travel through the tracking detectors at shallow angles, and therefore pass close to fewer wires, and through fewer layers of the CTD, thus causing fewer hits. This means that they are less likely to register as hits, and when they do they give a poorer position resolution. Both these factors mean that these tracks will have fewer hits, and therefore fewer tracks will pass the criteria given above. For this reason the average summed track momenta associated with each jet falls off as η^{jet} increases.

Figure 6.1(c) shows the quotient of the summed track transverse momenta, and the calorimeter jet transverse energy. This quantity, which was calculated individually for each jet, gives information about the relative energy scale between the calorimeter and tracking. When the distributions in (c) are divided the histogram shown in figure 6.1(d) is produced. This is the relative energy scale between the data and Monte Carlo. From this method the relative energy scale is close to the ideal value of 1, agreeing within $\pm 5\%$ and showing no overall trend. The plots shown here were produced with the EUCELL algorithm. The results for the other algorithms are very similar

From this investigation and others [93] it can be deduced that the energy measurement and in particular the measurement of the jet energies in the data are described by the detector simulation with an accuracy of $\pm5\%$. It has been shown by further studies that of this 5%, 3% can be attributed purely to uncertainty in the absolute energy scale of the calorimeter [92, 95]. This uncertainty is the source of the largest systematic error in the measurement of jet cross sections. Therefore this is a point where there is a large potential for improving the accuracy of the measurement. This remains a challenge for the future using higher statistics, and possibly a presampler. Unfortunately, due to the difficulties in calibrating the calorimeter, this has proved to be problematic. The evaluation of the errors the 5/3% uncertainty induces in the cross sections measured in this thesis is described in section 6.7.

6.2 Jet Parameters

The parameters of the jets are transverse energy (E_T^{jet}), pseudorapidity (η^{jet}) and azimuth (ϕ^{jet}). The measurements of these parameters in the calorimeter deviate from the true values of the hadron jets because of the dead material in front of the calorimeter and the resolution with which measurements can be made.

In order to determine the resolution with which these parameters are measured, and make any corrections for systematic effects, it is necessary to use Monte Carlo. The procedure followed in this analysis starts by performing jet finding on the final hadronic state of the MC, before it is passed through the detector simulation. These jets are considered to be the '**true**' jets which define events in the two jet cross sections. Events were selected if they have $Q^2 < 4$ GeV, $0.2 < y < 0.8$, and 2 jets of $E_T^{HADjet} \geq 4$ GeV and $\eta^{HADjet} < 2.6$. Jet finding was then performed on the calorimeter cells using the same jet finding algorithm, and events selected if they had at least one jet of $E_T^{CALjet} \geq 4$ GeV. Calorimeter and hadron jets were matched in each event by sequentially calculating the separation of each hadron jet from each calorimeter jet in η - ϕ space, $\Delta R = \sqrt{(\eta^{CALjet} - \eta^{HADjet})^2 + (\phi^{CALjet} - \phi^{HADjet})^2}$. The pair for which this separation was smallest was then considered matched (provided $\Delta R < 1$), and removed from the list before the process was repeated. Calorimeter jets which match up with hadron jets were then used to evaluate any shift in the measured quantities at the calorimeter. Any events with unmatched or missing jets in the calorimeter are included as part of the efficiency and purity evaluations in the determination of the final cross sections.

6.2.1 Jet Angular Resolution

The angular separation of matched pairs of hadron and calorimeter jets for both η, and ϕ for all three jet algorithms used in this analysis are shown in the first three rows of figure 6.2. The first three rows of figure 6.3 are the same but with the results for events generated as direct and resolved shown separately. The plots in the first row of each of these figures shows the magnitude of the separation in the η - ϕ plane, the second the separation in η alone, and the third the separation in ϕ alone, each as a function of η^{CALjet}. The error bars are the spread of the distribution for each bin, and hence provide an indication of the resolution. The dashed lines give the typical r.m.s. of the distributions for the whole event sample. As can be seen the discrepancy in position in the η - ϕ plane between matched true and measured jets is typically 0.125 for all events for KTCLUS and PUCELL, and 0.1 (0.15) for direct (resolved) processes. When compared to the jet radius of unity this is a very good correlation. The discrepancies for EUCELL are ~ 0.025 larger, which is still a good correlation. There is very little divergence from zero for η or ϕ separately for any of the jet algorithms, η having the wider distribution with an r.m.s. of $\sim$0.1 for the complete sample. Jets from resolved photon process are, on the whole, measured with worse resolution than those from direct, which is probably because these events typically have a larger amount of activity in the calorimeter, and the jets are wider in shape [94]. KTCLUS and PUCELL have

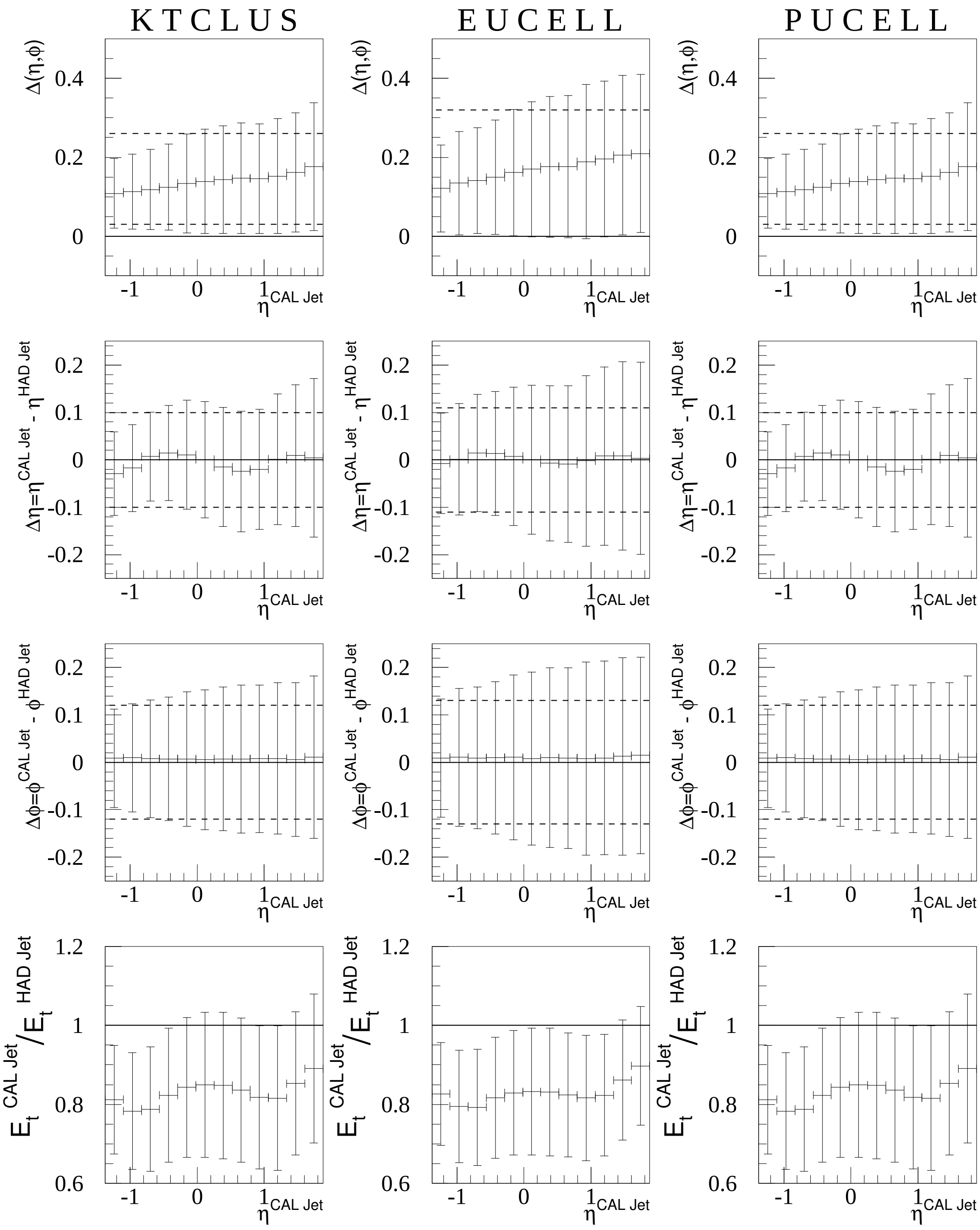

Figure 6.2: *Jet resolution. Shown for matched hadron and calorimeter jets are the separations in the η - ϕ plane, η alone, ϕ alone, and the ratio of their transverse energies for all HERWIG monte Carlo events, and the three jet algorithms used in this analysis. The dashed lines give the typical r.m.s. of the distributions.*

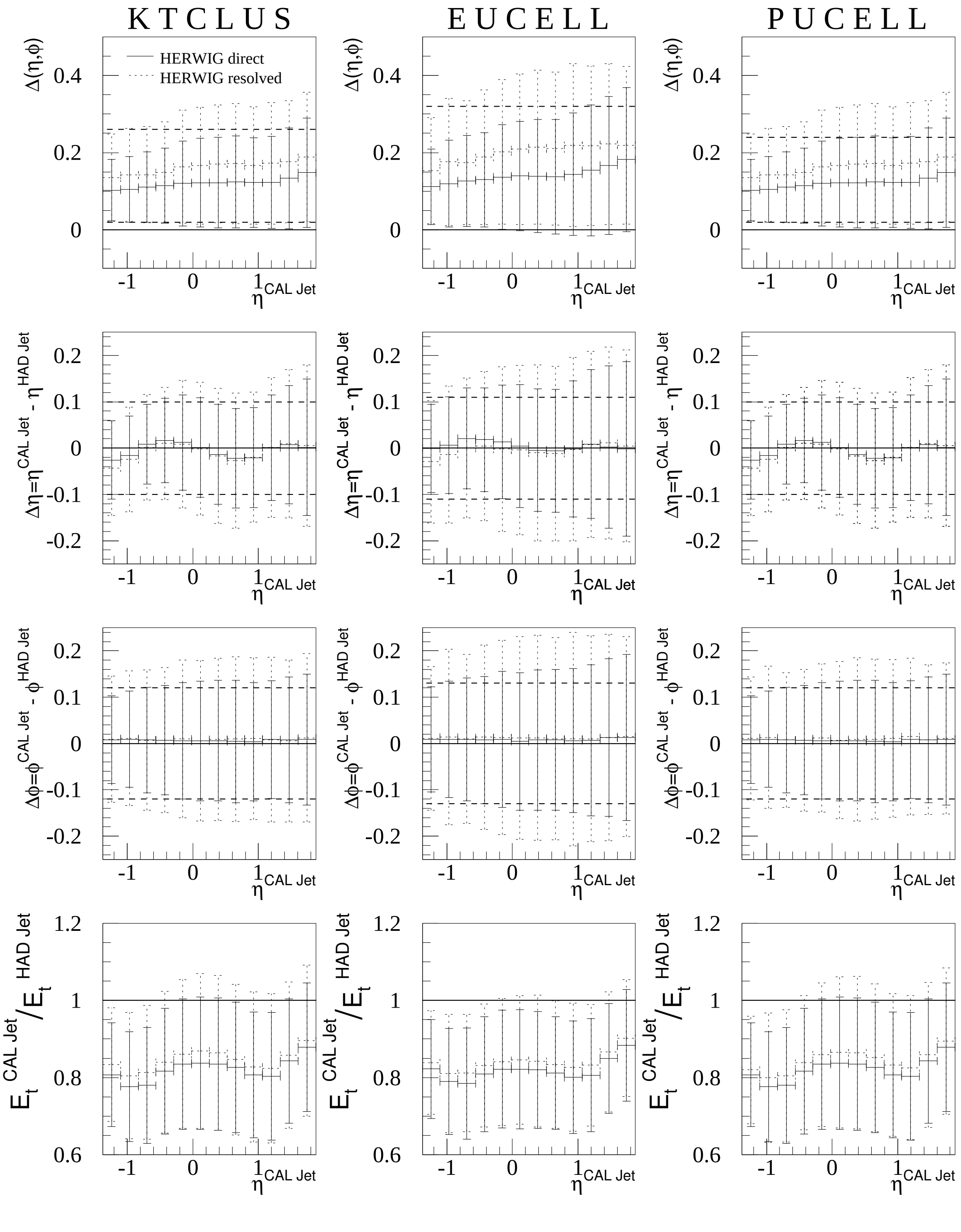

Figure 6.3: *Jet resolution. Shown for matched hadron and calorimeter jets are the separations in the η - ϕ plane, η alone, ϕ alone, and the ratio of their transverse energies for the three jet algorithms used in this analysis. In each case HERWIG resolved(Solid) and direct(dotted) Monte Carlo are shown separately. The dashed lines give the typical r.m.s. of the distributions for the whole event sample.*

consistently better position resolution than EUCELL.

6.2.2 Jet Energy Resolution

Once the shift in the measurement of global energy sums using the uranium calorimeter, and how well this shift was reproduced in the Monte Carlo had been determined (section 6.1), it was possible to begin an evaluation of how well the jet transverse energies were measured.

The last line in figures 6.2 and 6.3 shows the ratio of the measured and true jet transverse energy. While this quantity differs greatly from unity for all η, it does show some systematic dependence on position in the calorimeter. Comparing with figure 4.3, in which the amount of inactive material in front of the calorimeter is shown in radiation lengths, it is plausible that this discrepancy is due to energy losses in the dead material in front of the calorimeter. The r.m.s. of the distribution in each bin is typically around 15%, which is comparable with the energy resolution of the calorimeter. In this case EUCELL shows slightly better resolution than the other two algorithms.

6.3 Correction of Jet-Energy

While a good resolution for jet pseudorapidity measurements has been achieved, it is necessary to correct the measured transverse energies of the jets. This was again done using Monte Carlo, so it was necessary to be confident that the Monte Carlo correctly models the jets present in the data. In order to verify this the jet profiles were investigated. These are shown in section 4.6.4. The HERWIG with MI and PYTHIA profiles describe the data reasonably in all E_T^{jet} and η^{jet} regions. Although small discrepancies for jets with low E_T^{jet} and large η^{jet} are apparent, these lie mainly in the forwards direction outside the jet cone. The conclusion

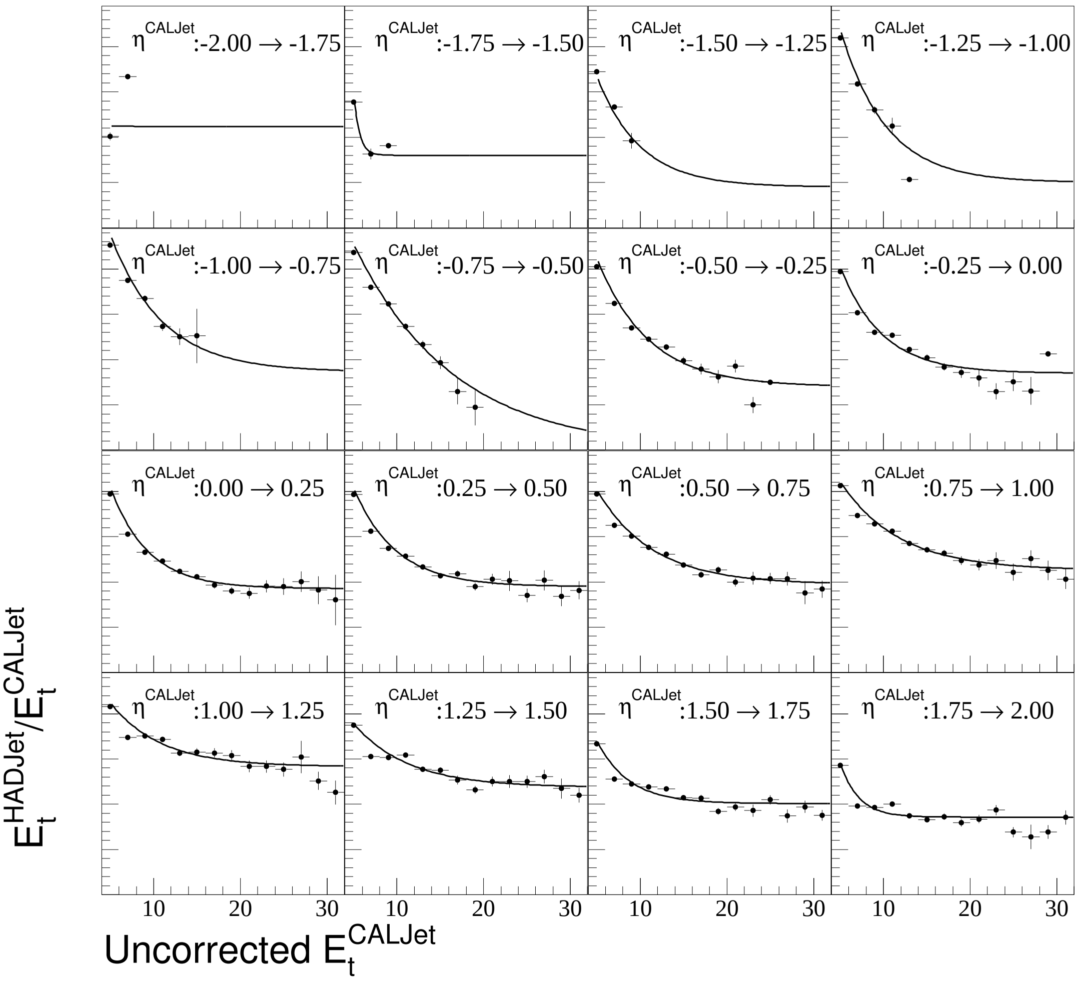

Figure 6.4: *The ratio of E_t^{HADjet} and E_t^{CALjet} in different η bins, for HERWIG and KTCLUS jets. The curves show the fitted correction function, $C(E_T^{CALjet}, \eta^{CALjet})$ for each bin.*

drawn in section 4.6.4 was that it is justifiable to use HERWIG with MI to correct the jet energies.

6.3.1 Determining the Correction Function

In correcting the jet energies it was sought to correct the energies measured in the calorimeter so that on average they matched those of the corresponding hadron jets. It is to be expected that the energy loss in dead material varies not only with pseudorapidity but also with jet energy. Therefore a correction function $C(E_T^{CALjet}, \eta^{CALjet})$ was determined for each jet algorithm such that:

$$E_T^{CORjet} = C(\eta^{CALjet}, E_T^{CALjet}) E_T^{CALjet} \tag{6.1}$$

As an example, figure 6.4 shows, for HERWIG and KTCLUS jets, the average $E_T^{HADjet}/E_T^{CALjet}$ as a function of E_T^{CALjet} in a range of bins in η for matched hadron and calorimeter jets. The same plots for the other jet algorithms and Monte Carlos are very similar. As expected the measured energy approaches that of the hadron energy as E_T^{jet} increases. For $E_T^{CALjet} \approx 4$ GeV the correction factor has a maximum of 1.4. So, using this number, calorimeter jets of at least 4.3 GeV must be detected in order to make a measurement with a cut on the corrected transverse energy of $E_T^{CORjet} > 6$GeV. Even though this is only determined from averages it seems justified that cross sections for $E_T^{jet} > 6$GeV can be measured from detected jets of $E_T^{jet} > 4$GeV. Any events missed by the 4 GeV cut are taken care of as inefficiencies. Having divided the η range into a number of bins the form assumed for the correction function C was:

$$C(\eta^{CALjet}, E_T^{CALjet}) = a_1.\eta^{CALjet}[bin] + e^{(a_2.\eta^{CALjet}[bin].E_T^{CALjet} + a_3.\eta^{CALjet}[bin])} \tag{6.2}$$

Thus the dependence on E_T^{CALjet} is varied continuously in E_T and bin-wise in η. Figure 6.4 shows the least squares fit of this function to $E_T^{HADjet}/E_T^{CALjet}$ for the chosen η bins. As can been seen, this parameterisation describes the required corrections reasonably well.

The first two rows of plots in figure 6.5 show the results, for all three jet algorithms, of applying this correction function back onto the HERWIG Monte Carlo samples generated as resolved and direct respectively. Shown are the average ratios of E_T^{HADjet} to E_T^{CALjet} for uncorrected and corrected jet energies as a function of η^{CALjet}. Within a few percent the function works well for both classes of process individually. This indicates that this correction method is reasonably independent of the exact mixture of resolved and direct events. The last row in figure 6.5 shows

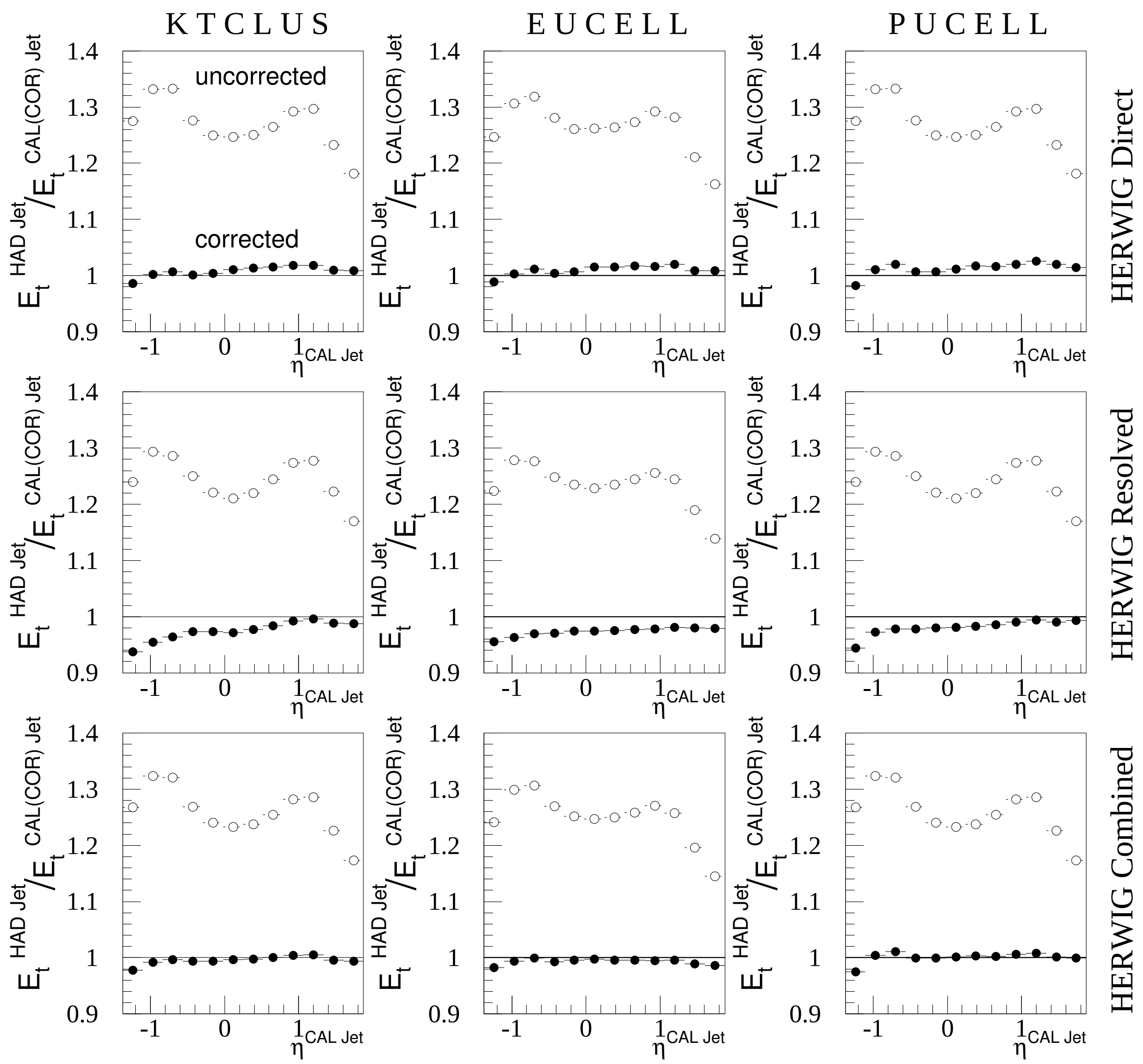

Figure 6.5: *The ratio of E_T^{jet} for Hadron and Calorimeter jets, before(open circles,E_T^{CALjet}) and after (filled circles, E_T^{CORjet}) applying the correction function $C(E_T^{CALjet}, \eta^{CALjet})$ to E_T^{CALjet}. Distributions are shown for the three jet finders used in this analysis, and for direct, resolved, and combined direct and resolved HERWIG event samples.*

the result for the total HERWIG sample. As expected the corrected transverse energy is on average practically identical to that of the corresponding hadron jets.

6.4 Correction of the y Measurement

The simplest way to calculate the energy of the interacting photon would be from the initial and final positron energies. However, since it is a requirement of this analysis that the scattered positron wasn't found in the calorimeter, a different method had to be used. This was done by calculating y by the Jaquet-Blondel method [65]. The accuracy of this method was investigated using Monte Carlo. Here the y_{true} value is known and can be compared to the y_{JB} calculated after detector reconstruction. This comparison, and the correction of y are shown in figure 6.6. The events entering all the plots in this figure pass the data selection described in chapter 5, except that the cut on y_{JB} has been relaxed a little to $0.1 < y_{JB} < 0.8$ to reduce the effect of the cuts on the determination of the correction function for the range of y used in the cross section measurement. The jets used in the selection of the events in these plots, and the calculation of x_γ^{OBS} for (c) and (d), were identified with EUCELL. The distributions when the other jet finders are used are very similar.

Figure 6.6(a) shows y_{JB} vs y_{true} for a HERWIG with MI event sample. It indicates a good correlation between y_{JB} and y_{true}, with y_{JB} systematically lower on average. The dashed horizontal and vertical lines give the cuts applied to the uncorrected y_{JB} (equations 5.1), and the y limits in the cross section definition (equation 3.22) respectively. It can be seen that with these cuts the majority of the events that pass the cuts applied to y_{JB} in the data selection also satisfy the y cuts in the cross section definition. In figure 6.6(b), which shows the difference between y_{JB} and y_{true}, it is evident that there is an average shift of around 0.12. This shift is primarily due to the energy losses as particles pass through inactive material in front of the calorimeter, and to particles lost down the beam pipe.

Beam pipe losses in the rear direction are particularly important because of the $E - p_z$ term in the expression for y_{JB} (equation 3.4).

The shift of the measured y_{JB} w.r.t. y_{true} is also dependent on the presence of a photon remnant, and therefore on x_γ. Indeed the ratio of y_{true}/y_{JB} shows a stronger dependence on x_γ^{OBS} than on η^{jet}, E_T^{jet} or y_{JB} itself. Figure 6.6(c) Shows the average y_{true}/y_{JB} as a function of x_γ^{OBS} for event samples generated as direct and resolved, and for the combined event sample. This can now provide a correction function for y_{JB} as a function of x_γ^{OBS} (figure 6.6(d)). As can be seen in figure 6.6(c), there is agreement between direct and resolved processes in the high x_γ region, where direct interactions dominate. In the low x_γ^{OBS} region where large differences between direct and resolved processes do occur, the number of direct events is a very small fraction of the total number of events, as can be deduced from the points for the combined sample or from figures 3.2 and 4.4. Therefore using this correction has the advantage that it is relatively independent of the mixture of the processes. A polynomial of the form

$$P(x_{\gamma_{CAL}}^{OBS}) = p_1 + p_2 x_{\gamma_{CAL}}^{OBS} + p_3 x_{\gamma_{CAL}}^{OBS^2} \tag{6.3}$$

is suited to fitting this distribution. The curve on figure 6.6(d) gives the log likelihood fit of the correction function to the points. The corrected y produced is then:

$$y_{corr} = y_{JB} \times P(x_{\gamma_{CAL}}^{OBS}) \tag{6.4}$$

Figure 6.6(e) shows the correlation between y_{corr} and y_{true} and (f) the difference. As can be seen there is now on average a good agreement and the spread of the distribution is more symmetric and has been very slightly reduced. Since the event samples selected with the different jet finders are not identical, it was necessary to determine this correction factor for events selected using each of the three algorithms. The results were all very similar however.

The dependence of the correction factor on x_γ shown in figure 6.6(d) can be used to estimate the importance of losses down the beam pipe. For the events

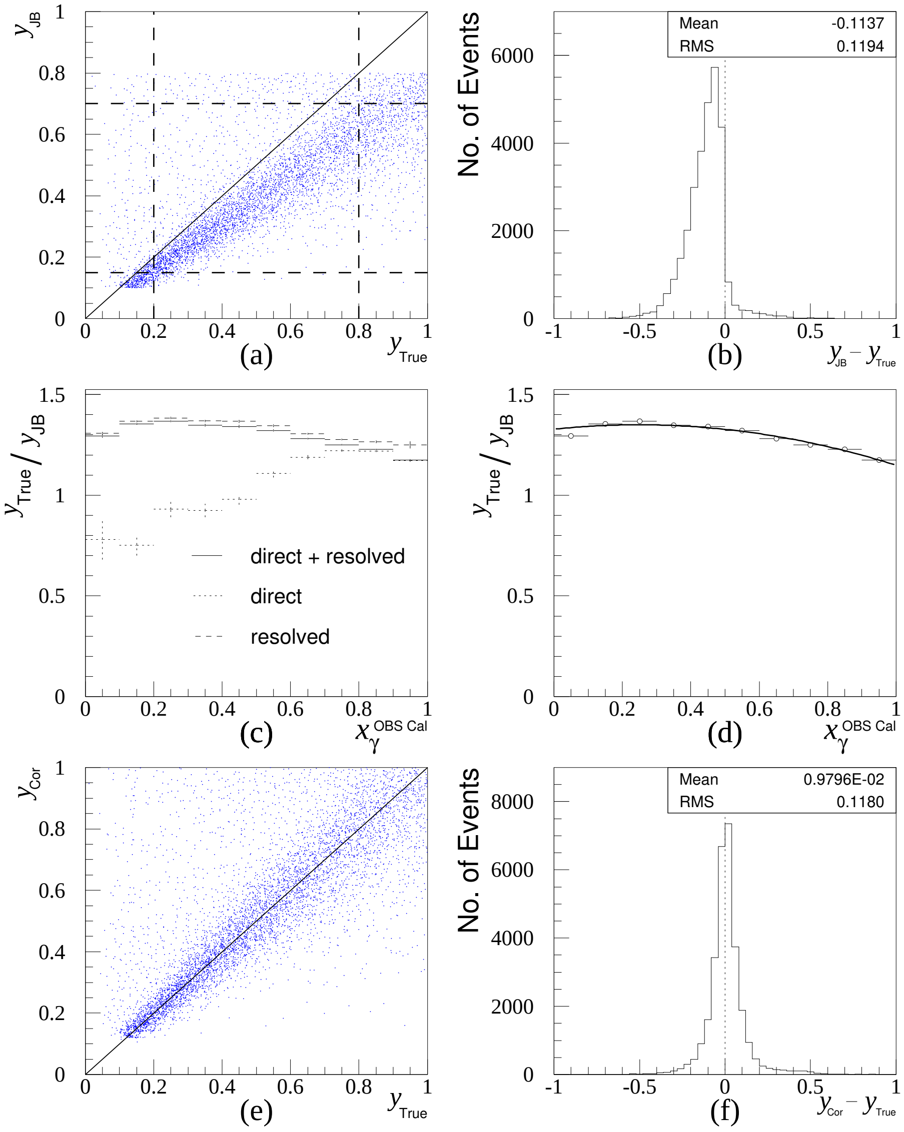

Figure 6.6: *Comparison of* y_true *and* y_{JB} *, and the correction of the measured y for events in the HERWIG with MI sample that pass the data selection (with the cut on* y_{JB} *slightly relaxed). The jets used in the selection of these events and the calculation of* x_γ^{OBS} *were identified using EUCELL.*

with a direct photon with $x_\gamma \approx 1$ almost the total shift should be due to losses to dead material only. Here $y_{true}/y_{JB} \approx 1.2$ so y_{JB} is ~83% of y_{true}. In events with a resolved photon the beam pipe losses add to this and the maximum possible loss occurs for a particularly energetic photon remnant, i.e. at $x_\gamma^{OBS} \approx 0$. In this region $y_{true}/y_{JB} \approx 1.3$ so y_{JB} is ~77% of y_{true}. From this it is possible to deduce that the energy loss in inactive material produces a shift in y of around 17% while the effect of the beam pipe losses is a less than half as large.

6.5 Measurement of the Cross Sections

6.5.1 Choice of Bins

If one assumes that the two jets have equal E_T^{jet} and η^{jet}, the curves shown on figure 6.7(a) for constant x_γ^{OBS} (for a certain y) and x_p^{OBS} can be drawn. The general equations for these curves are:

$$E_T^{jet} = x_\gamma^{OBS} y E_e e^{\eta^{jet}} \tag{6.5}$$

$$E_T^{jet} = x_p^{OBS} E_p e^{-\eta^{jet}} \tag{6.6}$$

From these and the plot it can be seen that the factors limiting the phase space for the cross section measurements are:

- The $E_T^{jet} > 6$ GeV cut
- The $\eta^{jet} < 1.875$ cut
- The combination of the maximum possible x_γ^{OBS}=1 and the chosen $y < 0.8$ cut.

The third restriction in particular means that as the E_T^{jet} rises the events lie further forwards, and that for a fixed pseudorapidity the E_T^{jet} spectrum has an upper limit.

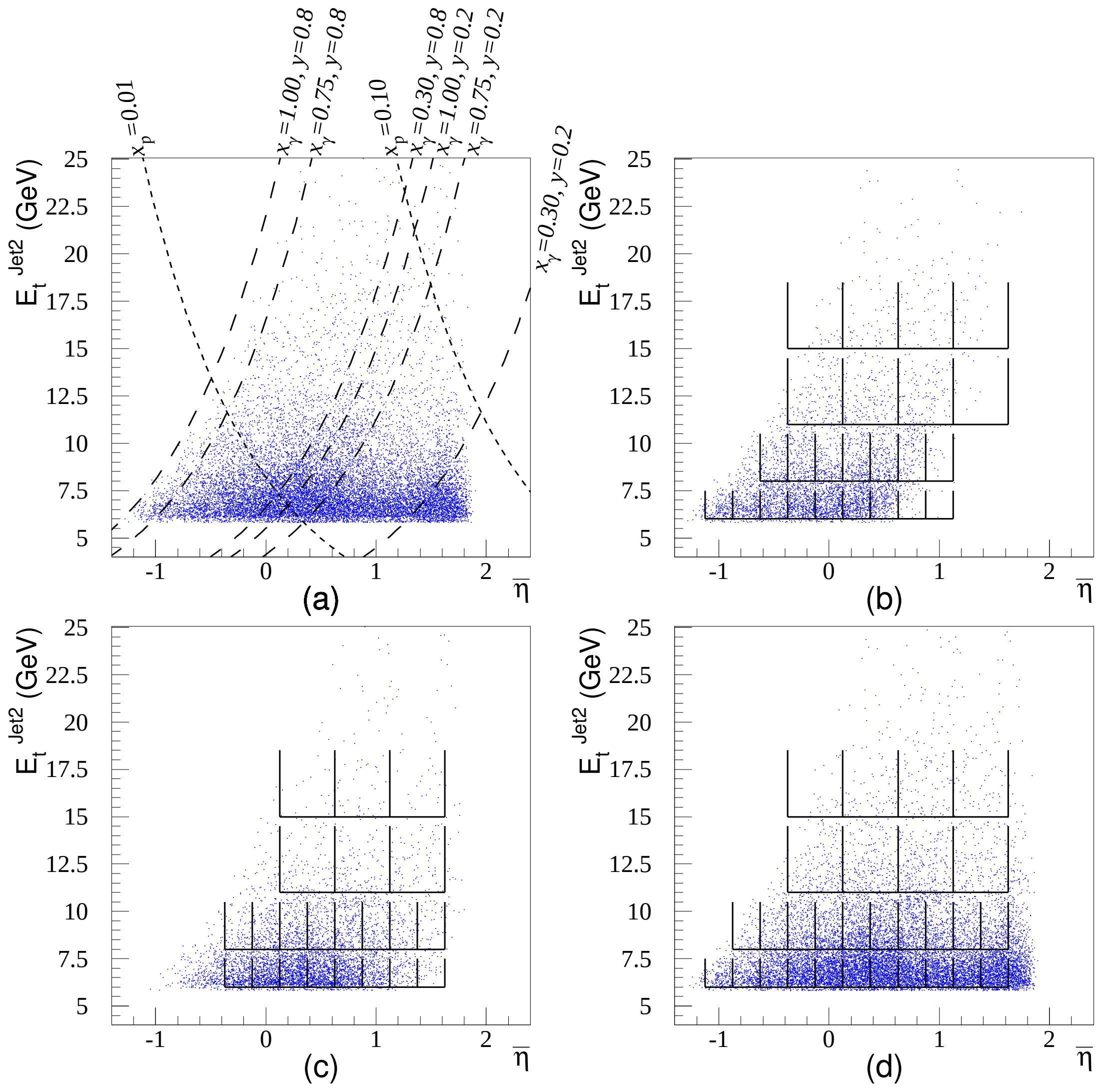

Figure 6.7: *The Kinematic Plane.(a) for all events in the final sample, with lines of constant x_γ and x_p, and showing the bins used for the cross sections: (b) the direct sample ($x_\gamma^{OBS} \geq 0.75$), (c) the resolved sample ($0.3 < x_\gamma^{OBS} < 0.75$) (d) the total sample. Jet2 is the the jet with the lower E_T^{jet} of the two jets selected as the dijet pair.*

As for fixed E_T^{jet} and y x_γ^{OBS} falls as η^{jet} increases, the resolved processes tend naturally to concentrate at higher values of $\bar{\eta}$ than the direct. In addition to this, as can be seen in figure 6.7(a), the cut at x_γ^{OBS}=0.75 gives rise to a forward limit on the direct cross section, and backwards limit on the resolved. In the same way the cut at x_γ^{OBS}=0.3 gives a forward limit to the two lowest E_T^{jet} resolved cross sections. Hence, after all the selection cuts are applied, the resolved and direct cross sections fall clearly into forward and backwards regions of $\bar{\eta}$ respectively, though there is a significant overlap. This can be seen in figure 6.7(b) and (c), and all figures where the cross sections for these two x_γ^{OBS} regions are given.

Figure 6.7 (b), (c) and (d) show the chosen binning for the measured cross sections. Bins were chosen to give a statistically significant measurement in the η range where the response of the calorimeter to jets is best understood, and to be wide enough to be largely independent of the angular resolution for measuring jets. The bins shown in the figure are open to high E_T^{jet} to indicate that there are no upper limits. This means that one event can contribute to more the one of the measured cross sections, though of course only within the respective x_γ^{OBS} range.

6.5.2 Extraction of the Cross Section

Application to the data of the relevant kinematic selection and cleaning cuts described in chapter 5 yields a final sample of hard photoproduction events containing at least two jets. These events were put into $\bar{\eta}^{cal}$ bins equal to those used for each of the cross section measurements. Acceptance correction factors are then applied to each bin to relate the number of events measured in each bin of $\bar{\eta}^{cal}$ to a cross section measured in bins of $\bar{\eta}$ at the hadron level. These correction factors are determined from the HERWIG with MI Monte Carlo sample.

The correction factors calculated from the Monte Carlo event simulation are composed of two independent factors, the efficiency and the purity:

$$\text{Efficiency(i)} = \frac{\#\text{Calorimeter(i).and.True(i)}}{\#\text{True(i)}} \tag{6.7}$$

$$\text{Purity(i)} = \frac{\#\text{Calorimeter(i).and.True(i)}}{\#\text{Calorimeter(i)}}. \tag{6.8}$$

The quantity True(i) is the number of Monte Carlo events at the level of the final hadronic state which, after applying the selection criteria outlined in section 3.6, are found in the i^{th} $\bar{\eta}$ bin of the cross section cross section. The quantity Calorimeter(i) is the number of Monte Carlo events evaluated using the reconstructed kinematic variables and the selection cuts of chapter 5, which are found in the i^{th} $\bar{\eta}^{cal}$ bin. So the numerator in both these equations is the number of events which pass the selection criteria at both the hadron and detector levels.

The combination of the efficiency and purity gives a correction factor to compensate for the detector acceptance:

$$\text{Correction(i)} = \frac{\text{Purity(i)}}{\text{Efficiency(i)}} \tag{6.9}$$

Using this the cross section is finally calculated as

$$\sigma\text{(i)} = \frac{\#\text{Events(i)} \times \text{Correction(i)}}{\int \mathcal{L}\, dt \times \text{Bin width}}. \tag{6.10}$$

For the evaluation of the errors the efficiency and purity were treated as probabilities. Thus, using the binomial theorem, the errors on the efficiency and purity are:

$$\Delta\text{Efficiency(i)} = \sqrt{(1 - \text{Efficiency(i)}) \times \text{Efficiency(i)}/\#\text{True(i)}} \tag{6.11}$$

$$\Delta\text{Purity(i)} = \sqrt{(1 - \text{Purity(i)}) \times \text{Purity(i)}/\#\text{Calorimeter(i)}} \tag{6.12}$$

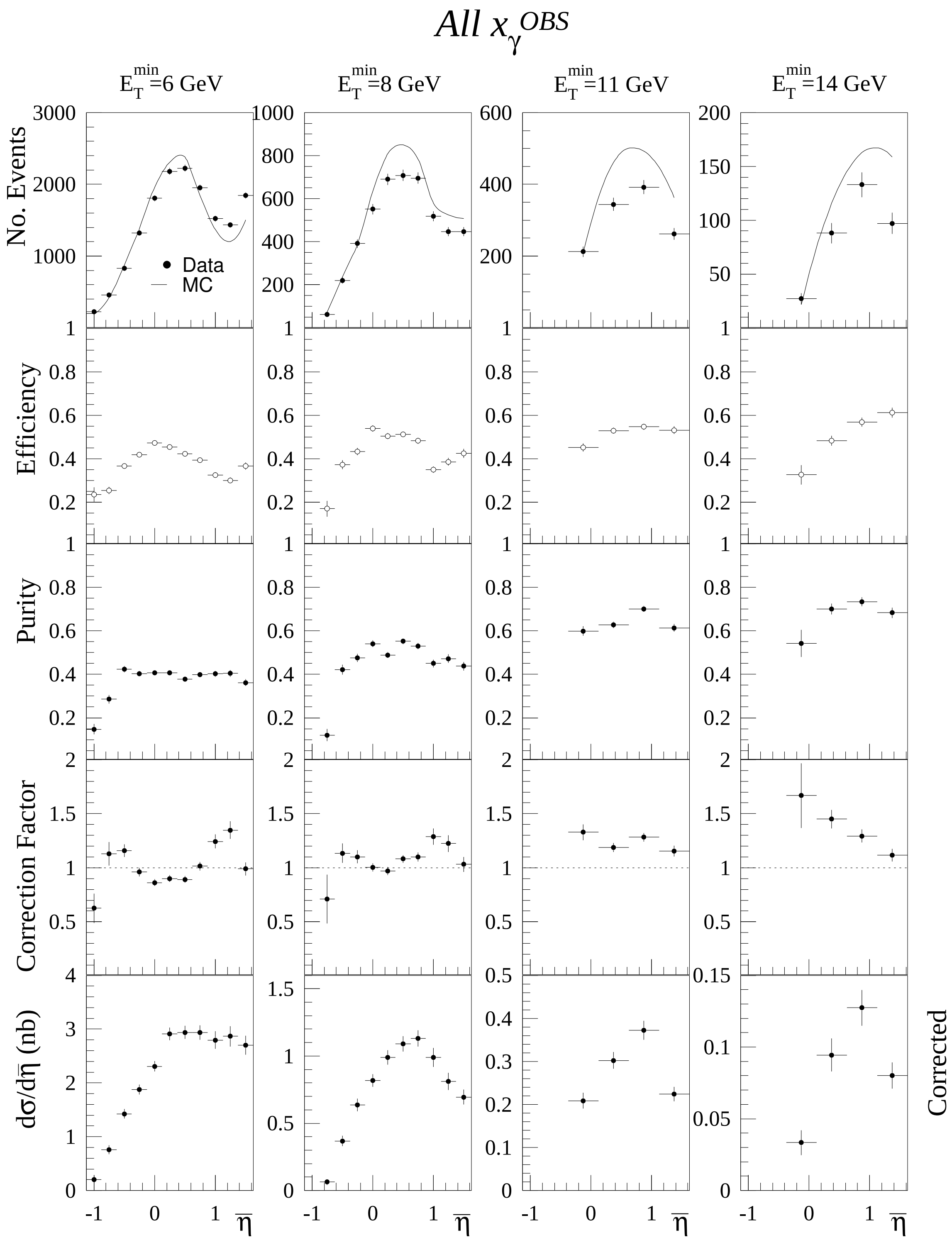

Figure 6.8: *The unfolding of the cross sections for KTCLUS with HERWIG, for the complete x_γ^{OBS} range*

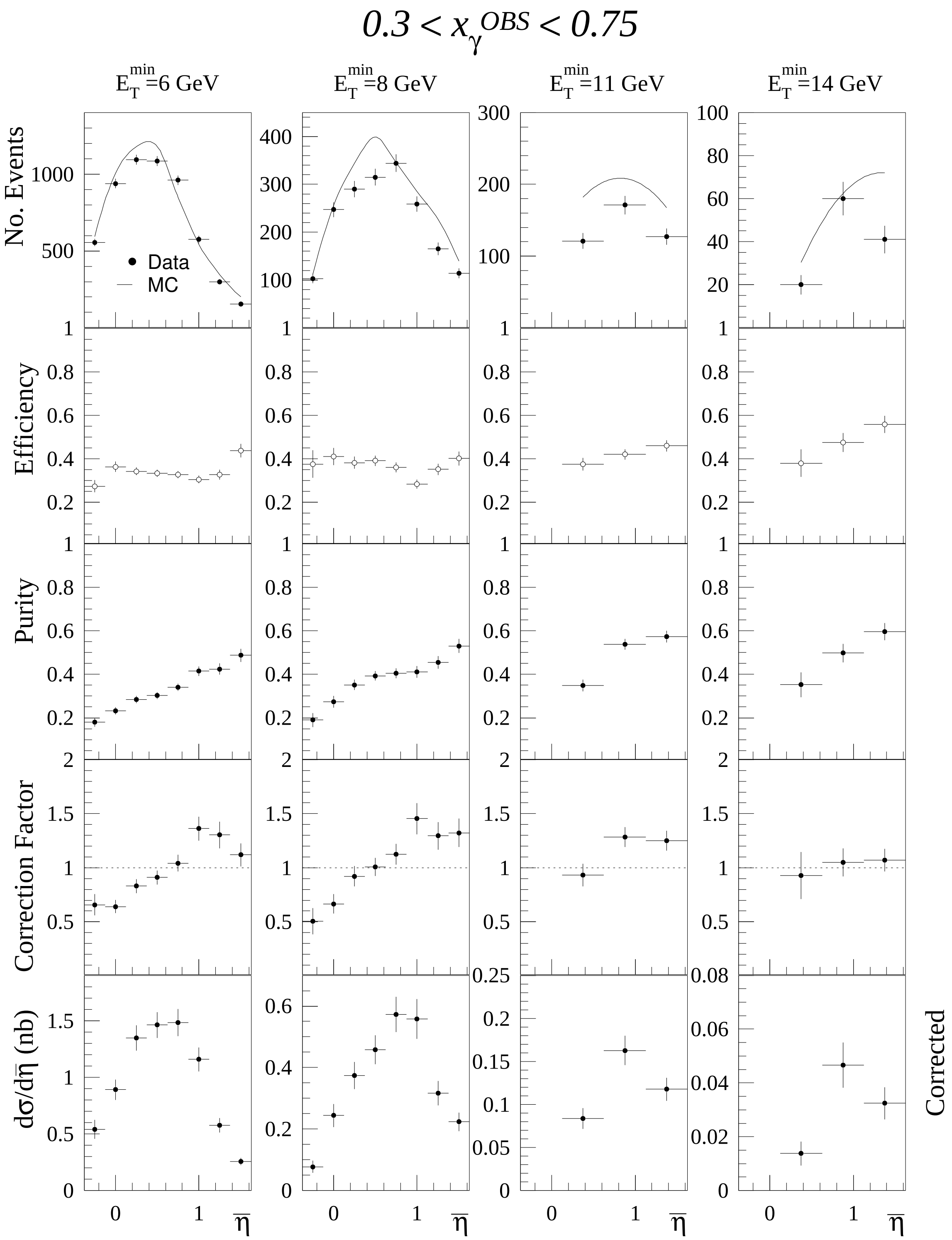

Figure 6.9: *The unfolding of the cross sections for KTCLUS with HERWIG, for resolved events.* $0.3 < x_\gamma^{OBS} < 0.75$

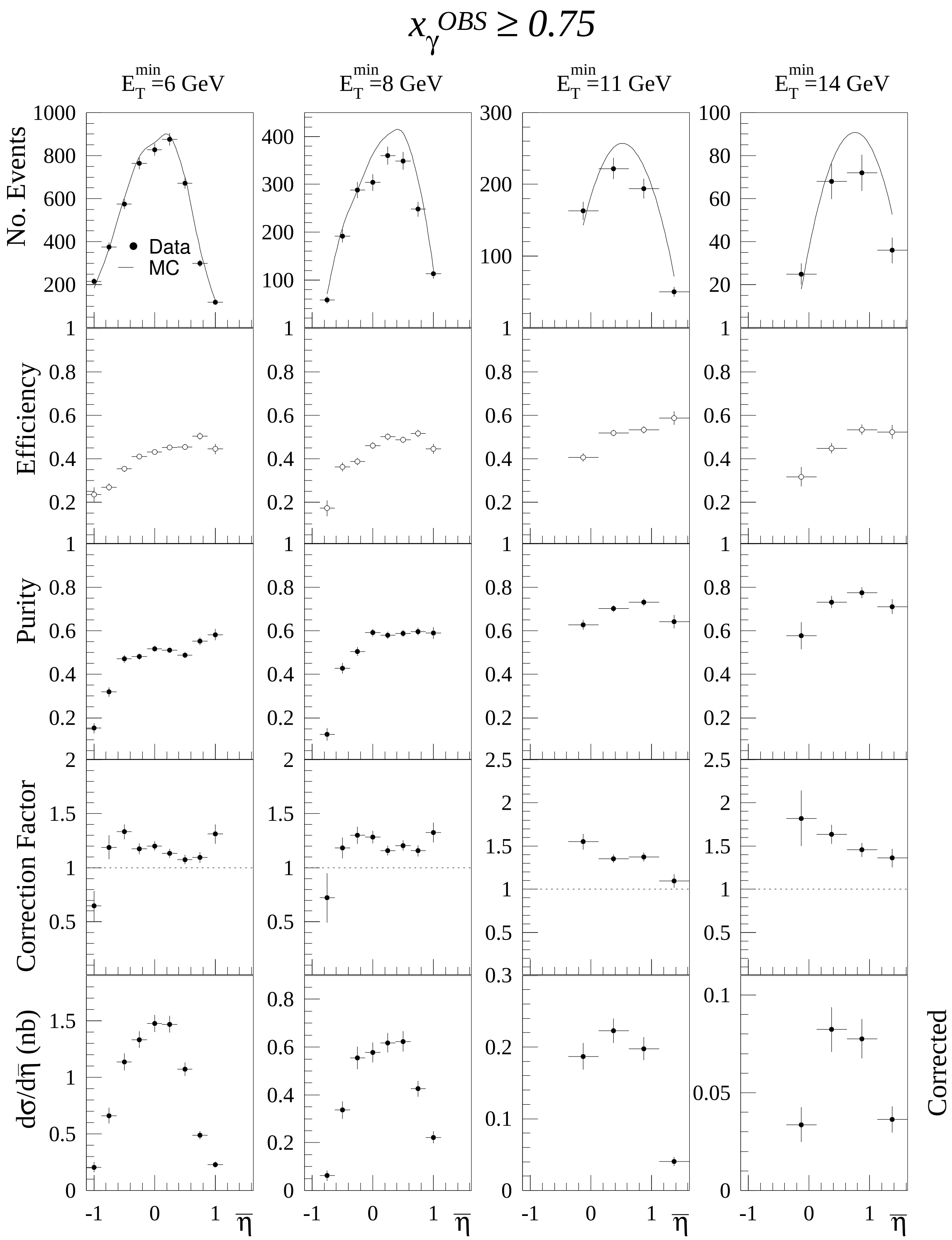

Figure 6.10: *The unfolding of the cross sections for KTCLUS with HERWIG, for direct events.* $x_\gamma^{OBS} \geq 0.75$

Given that the equation for the acceptance correction factor is of the form $X = a/b$, the statistical errors were calculated as:

$$\Delta X(\mathrm{i}) = \sqrt{\left(\frac{\Delta a(\mathrm{i})}{b(\mathrm{i})}\right)^2 + \left(\frac{\Delta b(\mathrm{i}) \times a(\mathrm{i})}{b(\mathrm{i})^2}\right)^2} \tag{6.13}$$

Figure 6.8 shows, for each E_T^{min} cut and the full x_γ^{OBS} range, the plots relevant to this unfolding. Here, and in figures 6.9 and 6.10, the unfolding of the KTCLUS cross sections are given as examples. The efficiencies and purities are similar for the other two jet finders, and the figures for the unfolding of their cross sections are given in appendix A. The first row shows the comparison of the uncorrected number of Monte Carlo and data events in each $\bar{\eta}^{cal}$ bin. The agreement here is reasonable, although in the three higher E_T^{min} bins the Monte Carlo lies systematically above the data, and for $E_T^{min} = 6GeV$ it is a little below the data for $\bar{\eta} > 0.5$. This indicates that the E_T^{jet} spectrum in the Monte Carlo is somewhat harder than for the data. Any influence these discrepancies may have on the results is checked by using HERWIG to unfold the PYTHIA cross section in section 6.7. It has also been checked using a matrix unfolding method [40, 96].

The next row of plots give the efficiency. This is similar for all E_T^{min} bins, rising from around 20% in the rear direction to around 50% in the central and forward regions, though it does rise slightly with increasing E_T^{min}. The dip at $\bar{\eta} \approx 1$ in the two lower E_T cross sections can be traced to the dead material in front of the calorimeter. The reason for the fall off in the efficiency in the rear direction can be seen in the plots of the kinematic plane shown in figure 6.7. At these low values of $\bar{\eta}$ the E_T^{min} distribution is very much thinner. The effective size of the open topped E_T bins is therefore much smaller, and hence the probability for an event to be measured in the E_T bin from which it originated is reduced. The same thing effects the purity (third line of figure 6.8) which shows an even stronger fall off in this region. For these effectively smaller bins the influence of migrations from below their respective E_T thresholds becomes more important. The purity also shows a clear dependence on E_T^{min} rising from about 40% for $E_T^{min} = 6$ GeV to over 70% for $E_T^{min} = 15$ GeV. The fourth row of figure 6.8 gives the acceptance correction factor. This is around 1 for $E_T^{min} = 6$ GeV, and as E_T^{min} rises it becomes clearly larger. The visible variation with $\bar{\eta}$ is related to the dead material in front of the calorimeter. The final line of this figure shows the measured cross sections extracted using this acceptance correction. The error bars being the statistical errors from the data measurement and Monte Carlo combined in quadrature.

Figures 6.9 and 6.10 give the same plots for the resolved($0.3 < x_\gamma^{OBS} < 0.75$) and direct($x_\gamma^{OBS} \geq 0.75$) cross sections respectively. For the direct sample the agreement between data and Monte Carlo is, as expected, better than for the total sample. The efficiency is very similar to that of the total sample but the purity is significantly better. Already 50% for $E_T^{min} = 6$ GeV it rises to near 80% for $E_T^{min} = 15$ GeV. For the resolved sample the efficiency is, once more, similar to that of the complete sample, but this time the purity is worse lying between 30% and 60%.

6.6 Background Contamination

The final data sample still contains a small number of background events from non e-p collisions. Apart from this it is expected that there will also be some contamination from deep inelastic scattering where the scattered positron did enter the detector, but was not found.

6.6.1 Background from Non e-p Collisions

As already shown in table 5.2 the fraction of events in the final data sample which did not come from e-p collisions is very small. It could however still be a problem if it were all concentrated in one bin. On inspection it is found that the events from empty or unpaired bunches only affect the $E_T^{min} = 6$ GeV cross section with no concentration in any single bin. For the region $x_\gamma^{OBS} > 0.75$ there is no

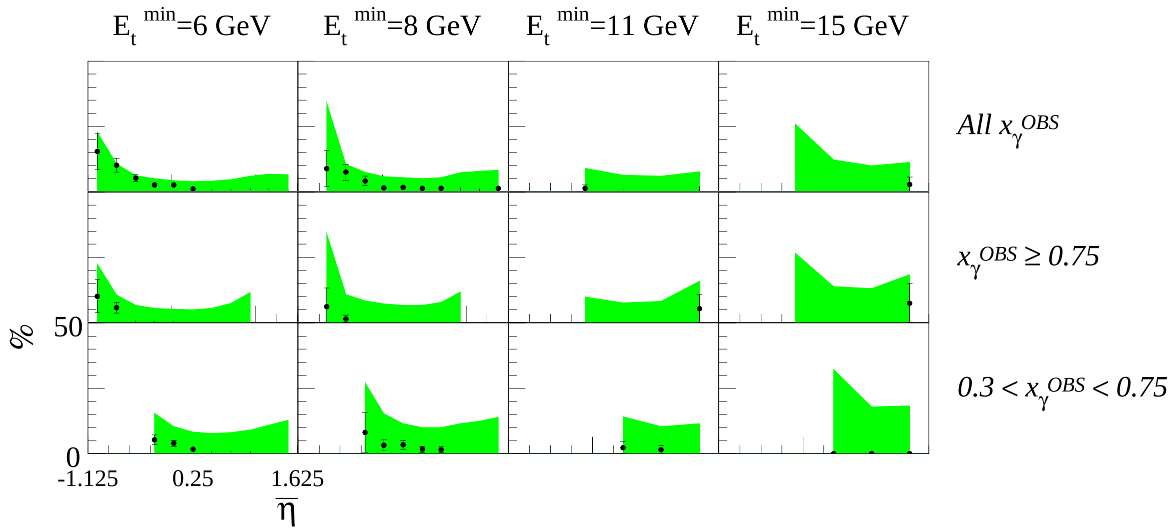

Figure 6.11: *The estimated DIS contamination as a percentage of the measured KTCLUS cross sections. The error bars indicate the statistical error on these points and the shaded band indicates the statistical error on the central analysis.*

contamination from these events at all. So even binwise the background from non e-p interactions is very small and can be ignored. Hence no background subtraction was performed for these events.

6.6.2 Background from Deep Inelastic Scattering

To estimate the background contribution from DIS a cross section measurement was made using only DIS Monte Carlo. In order to have the highest possible statistics several different event samples. These were generated with Django 6.1 and 6.2 [97] with LEPTO [98], in some samples ARIANDE [99] had been used for the parton cascade. In addition, some of the samples were pre selected to contain two jet events. This combination of various different samples should not however be significant for this background estimation. The total integrated luminosity for this sample was around 1.6 pb^{-1}. The contributions from DIS to the KTCLUS cross sections are shown in figure 6.11. The contribution is only significant for E_T^{min} = 6 GeV and E_T^{min} = 8 GeV, and then only in the rear direction. This is reasonable since the number of scattered positrons which are not found as such, but are instead misidentified as jets, decreases with larger values of η. With increasing transverse energy the misidentification becomes ever more improbable. So the bins with larger E_T^{min} are much less affected. Since the background due to DIS is small it too is not subtracted from the cross section measurements.

6.7 Systematic Checks

In order to estimate the systematic uncertainty in each bin of the final cross sections, the cross section evaluations were repeated several times with different variations in the procedure:

1. Cut on y_{JB} >0.15 changed to y_{JB} >0.20
2. Measured y cut changed from 0.15< y_{JB} <0.70 to 0.20< y_{Cor} <0.80
3. Cut on measured x_γ^{OBS} $\geq$0.75 changed to 0.7
4. Only for low x_γ^{OBS}: cut on measured x_γ^{OBS} >0.3 changed to x_γ^{OBS}0.25
5. Use PYTHIA instead of HERWIG
6. Reweight MC to LAC1 for the photon (was GRV(LO))
7. Reweight MC to GRV(LO) for the proton (was MRSA-$\overline{\text{MS}}$)
8. Use HERWIG Monte Carlo without multiple interactions
9. Mix Monte Carlo resolved and direct samples according to the cross sections given by HERWIG instead of fitting to the x_γ^{OBS} distribution
10. Constant E_T^{jet} correction factor (1.2)
11. Scale y_{JB} by +3% and E_T^{jet} by +5% in the data
12. Scale y_{JB} by -3% and E_T^{jet} by -5% in the data
13. Run the SLT and TLT trigger simulation on the Monte Carlo with the BCAL(RCAL) energy scaled down by 6(2.5)%

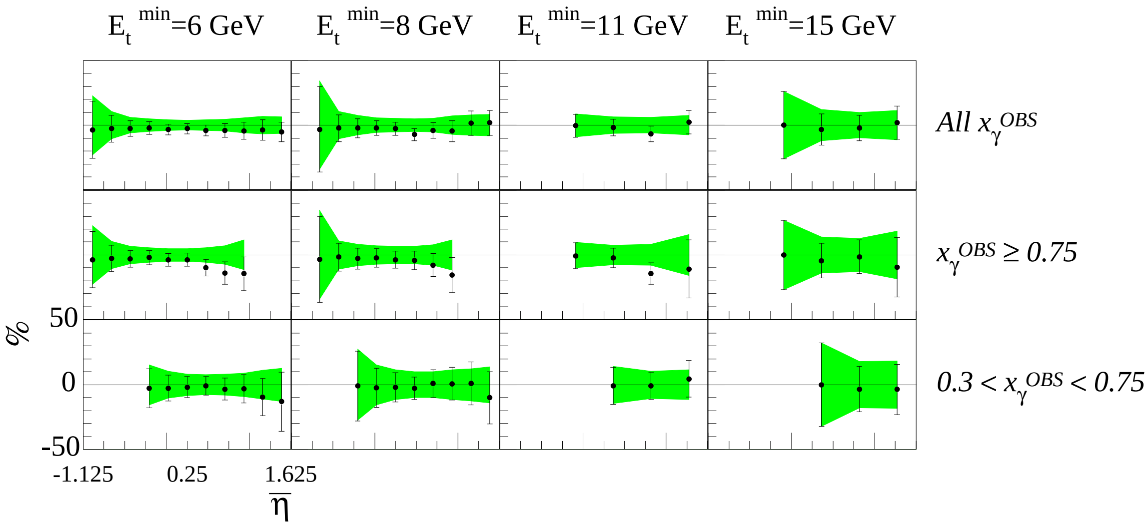

Figure 6.12: *Percentage effect on the KTCLUS cross sections of changing the cut on y_{JB} from 0.15 to 0.2. The error bars indicate the statistical error on these points and the shaded band indicates the statistical error on the central analysis.*

Figures 6.12 to 6.24 show the percentage difference between the final cross sections and each of these variations as a function of $\bar{\eta}$ for KTCLUS. In all of these figures the shaded region represents the statistical errors on the final cross section, the error bars are the statistical errors on the points, the four columns are the different E_T^{min} bins and the three rows are for the different regions in x_γ. The reasons for, and explanations of each of these checks are given below, but they can basically be grouped into 3 classes: 1 - 4 check the effect of the cuts used on the measured kinematic quantities, 5 - 9 check the effect of the choice of Monte Carlo for the acceptance corrections, and 10 - 13 check the effect of the uncertainties connected to the energy scale of the calorimeter and its response to jets.

Neither HERWIG nor PYTHIA describe the low end of the y_{JB} distribution very well. By shifting the data selection cut used from 0.15 to 0.20 it should be possible to estimate the degree to which this influences the measurement. The results of this change are shown in figure 6.12. It shows a shift in both restricted x_γ^{OBS} regions of up to $\sim$20% for the larger values of $\bar{\eta}$, which is where the events with smallest y values lie. Unfolding with the cut at $y_{JB} > 0.2$ does to some extent extract the cross section in the region of $y \approx 0.2$, but because of the discrepancies between data and Monte Carlo (figure 4.5), and between y_{JB} and y_{true} (figure 6.6)

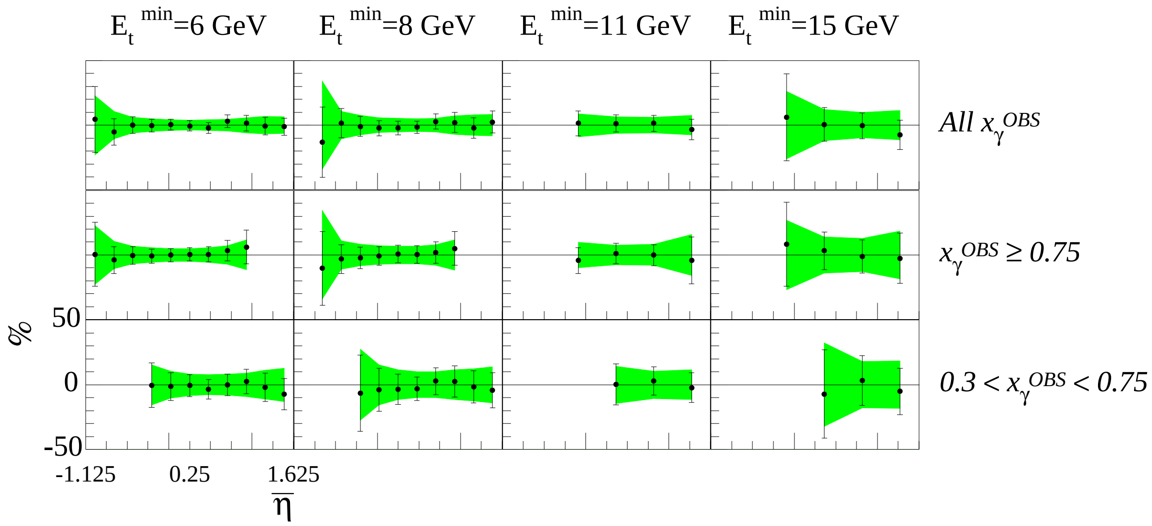

Figure 6.13: *Percentage effect on the KTCLUS cross sections of changing the y cut from 0.15< y_{JB} <0.70 to 0.20< y_{Cor} <0.80 The error bars indicate the statistical error on these points and the shaded band indicates the statistical error on the central analysis.*

the cross section is underestimated. As an alternative to using the 0.15< y_{JB} <0.70 selection one could cut on 0.2< y_{Cor} <0.8, though strictly speaking the y correction is only valid for the final dijet data sample. Figure 6.13 shows that this has very little impact on the measured cross sections.

A change in the x_γ^{OBS} cut from 0.75 to 0.7 hardly changes the cross sections, as shown in figure 6.14. This is a result of the good description of the data by the Monte Carlo in this region of x_γ^{OBS}. The shift in the lower cut on x_γ^{OBS} from 0.3 to 0.25 only has an influence on the lower x_γ^{OBS} cross section (figure 6.15). Effects are only seen in the high $\bar{\eta}$ region, where the cross section rises by around 10%. Similarly to the y_{JB} case this is a result of an imperfect description of the data by the Monte Carlo.

For the standard analysis and for the investigation of most of the systematic errors only HERWIG with MI is used. A comparison was made with the result of using PYTHIA in the standard analysis in order to see the effect that the Monte Carlo used has on the final result. This included redetermining all the correction functions for E_T^{jet}, y and acceptance etc. The results are shown in figure 6.16. Since the event sample from PYTHIA was smaller the statistical fluctuations are much

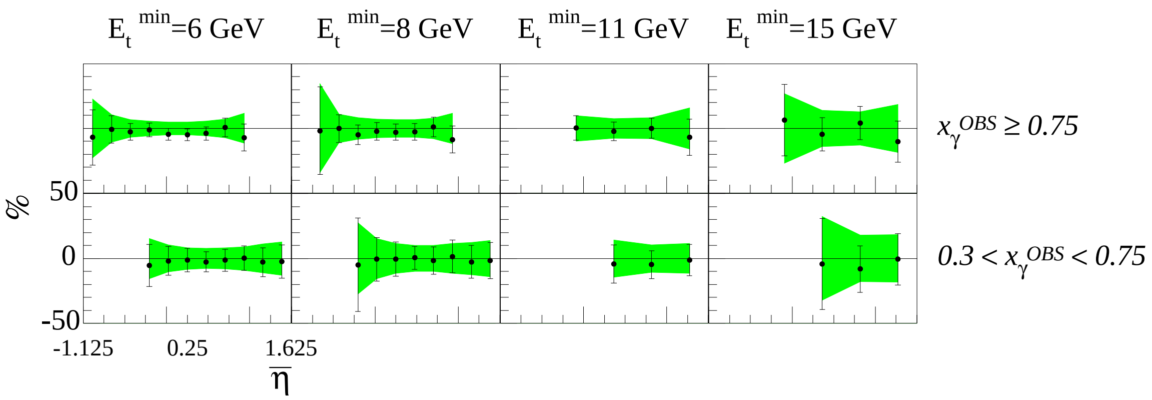

Figure 6.14: *Percentage effect on the KTCLUS cross sections of changing the higher x_γ^{OBS} cut from 0.75 to 0.70. The error bars indicate the statistical error on these points and the shaded band indicates the statistical error on the central analysis*

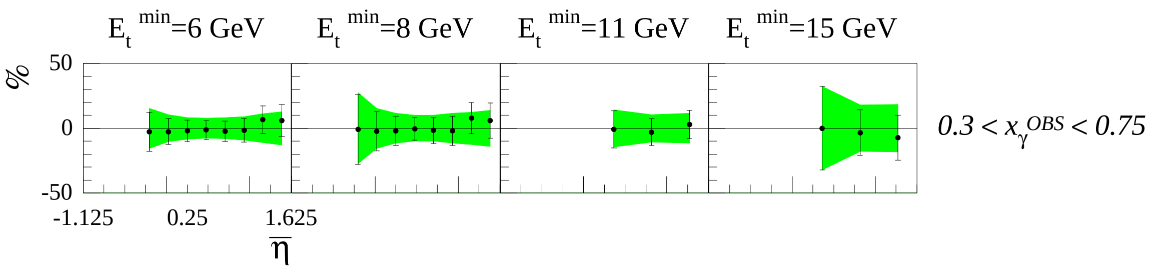

Figure 6.15: *Percentage effect on the KTCLUS cross sections of changing the lower x_γ^{OBS} cut from 0.3 to 0.25. The error bars indicate the statistical error on these points and the shaded band indicates the statistical error on the central analysis*

larger. Whilst the result for the complete x_γ^{OBS} range is practically unchanged, for $x_\gamma^{OBS} > 0.75$ the points lie a little lower. This difference is however on average less than 10%. For the $0.3 < x_\gamma^{OBS} < 0.75$ region the cross sections are in general a little larger. The changes here are around 10% as well. These changes are due to migrations in x_γ^{OBS} being somewhat differently described in each of the Monte Carlos.

Since to generate new Monte Carlo event samples, of sufficient size, with different structure functions would have involved a disproportionate amount of effort, the existing event sample was used and reweighted for the different parameterisations. To do this the parton densities for the new and original parameterisations for a given event and its hard subprocess were determined and the ratio of these used as a weighting factor for the event. This is only an approximation however since the structure functions don't actually factorise. Firstly the structure functions

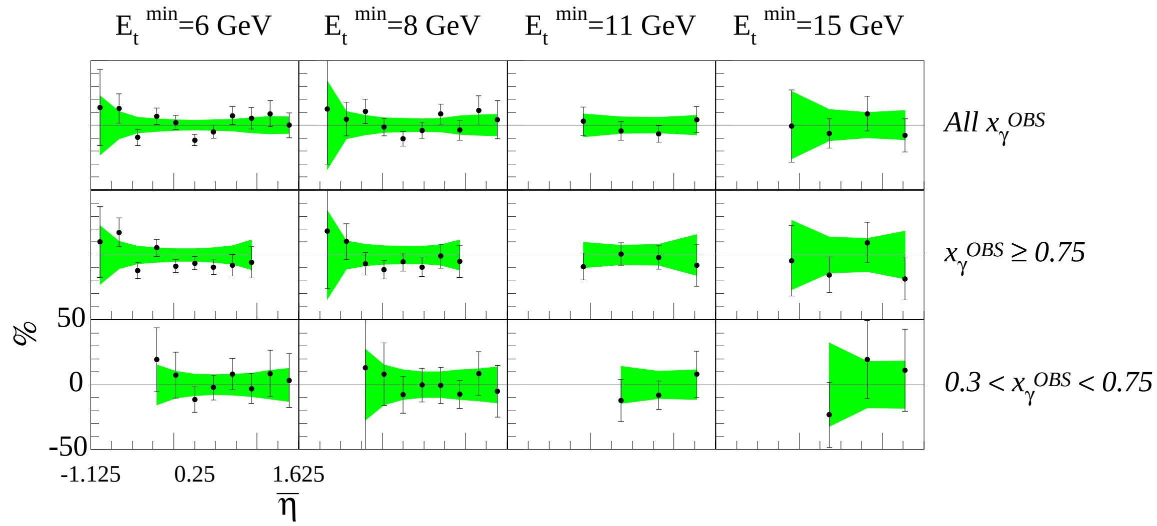

Figure 6.16: *Percentage effect on the KTCLUS cross sections of using PYTHIA instead of HERWIG for the unfolding of the cross sections. The error bars indicate the statistical error on these points and the shaded band indicates the statistical error on the central analysis*

are also used in the calculation of the parton shower and secondly in events with multiple interactions a number of hard subprocesses with different parameters will be present. In addition the different parton distribution functions have different starting scales for the heavier quark flavours, so some events may receive a zero weight. For the purpose of this investigation of systematic errors it is however an acceptable approximation as it is only important to see gross effects of the parton distributions in the Monte Carlo used to extract the cross sections.

Given these qualifications, figure 6.17 shows the effect of using LAC1 for the photon structure function instead of GRV(LO). As one sees the changes are in general smaller than or of the same order as the statistical errors. Only the cross section for the complete x_γ^{OBS} range in the $E_T^{min} = 6$ GeV bin shows a reduction of around 10%. This is understandable since the $x_\gamma^{OBS} < 0.3$ region is included which is particularly affected by a change in the photon structure function. Figure 6.18 shows the effect of a change in the proton structure function from MRSA-$\overline{\text{MS}}$ to GRV-LO. The effect here is very small.

It has been shown (chapter 4, and [61]) that by including the possibility for multiple interactions in the Monte Carlo the description of the data is greatly im-

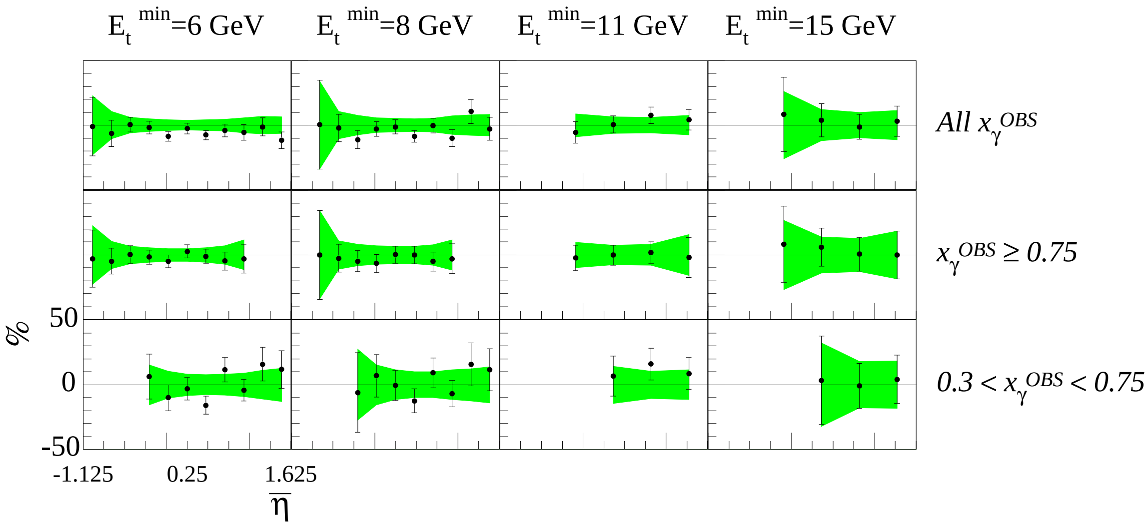

Figure 6.17: *Percentage effect on the KTCLUS cross sections of reweighting the Monte Carlo to LAC1 for the photon instead of GRV(LO). The error bars indicate the statistical error on these points and the shaded band indicates the statistical error on the central analysis*

proved. However this is an assumption of the model whose effect on the measurement of the cross section should be investigated. For this a HERWIG event sample of resolved processes without multiple interactions was generated and mixed with the standard direct photon Monte Carlo. This event sample was smaller than the one including multiple interactions. Hence the fluctuations seen in figure 6.19 from unfolding using this Monte Carlo can be explained as purely statistical in nature. Within statistical significance the changes seem small, as expected, for $x_\gamma^{OBS} > 0.75$ and $\sim \pm 10\%$ for $0.3 < x_\gamma^{OBS} < 0.75$. The most significant discrepancy arises for the complete x_γ^{OBS} region in the smallest E_T^{min} bin, particularly in the forwards region. Here the points are systematically higher by ~10%. This is where the low x_γ^{OBS} low E_T^{jet} events most influenced by MI are found.

For the main analysis the relative proportion of events from resolved and direct photons in the Monte Carlo was fitted to the x_γ^{OBS} distribution. If the cross sections as calculated by HERWIG are used a small discrepancy of the order of a few percent in the corrected measured cross sections is seen (figure 6.20).

For the standard analysis the jet energies were corrected using a function of E_T^{jet} and $\bar{\eta}$ as described in section 6.3. As a systematic check on this, the effect of

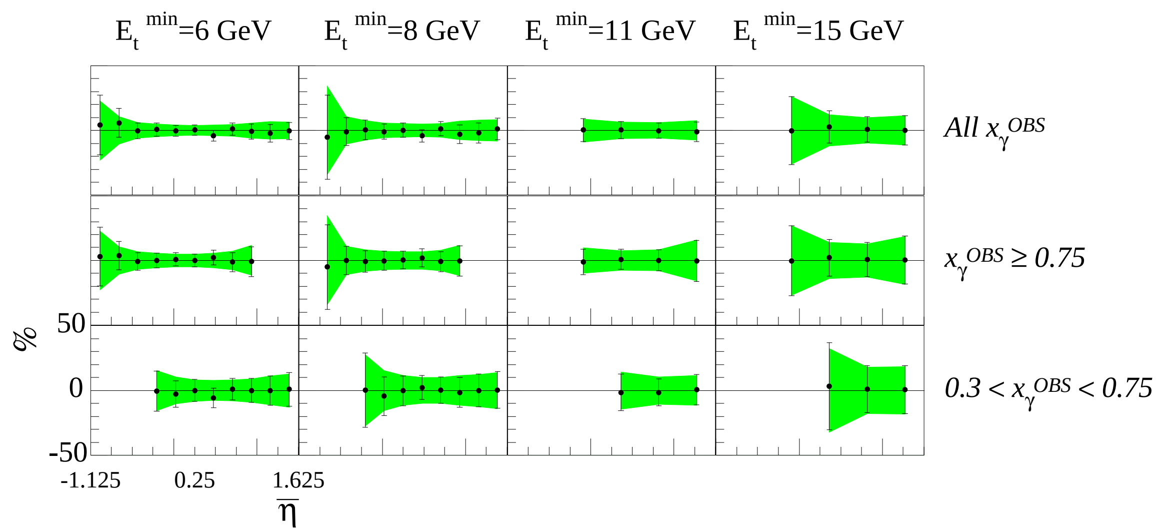

Figure 6.18: *Percentage effect on the KTCLUS cross sections of reweighting the Monte Carlo to GRV(LO) for the proton instead of MRSA-$\overline{MS}$. The error bars indicate the statistical error on these points and the shaded band indicates the statistical error on the central analysis*

using a constant correction factor of 1.2 was investigated. The justification for this factor comes from figures 6.2 and 6.4. The results of this are shown in figure 6.21, where it can be seen that in general only the cross sections for $E_T^{min} = 6$ GeV and $E_T^{min} = 8$ were affected. Here the cross section seems to be slightly reduced. This is due to the E_T dependence of energy losses to inactive material. The differences are of the order of the statistical errors and often smaller. This can be seen as a measure of the uncertainty in the determination of the cross section due to any discrepancies in the E_T^{jet} distribution between data and Monte Carlo.

In section 6.1 it was found that there was an uncertainty of $\pm 5\%$ in determining the relative calorimeter energy response for jets between the data and the Monte Carlo. It has also been shown [95] that in general the uncertainty in the absolute energy scale of the calorimeter is $\pm 3\%$. In order to estimate the effect of these uncertainties on the measured cross sections the analysis was repeated, first with y_{JB} scaled by $+3\%$ and E_T^{jet} scaled by $+5\%$ in the data, and then again with y_{JB} scaled by -3% and E_T^{jet} scaled by -5%. Figures 6.22 and 6.23 show the percentage changes in the measured cross sections for the $+3/5\%$ and -3/5% cases respectively. For the $+3/5\%$ case all points lie around 10-20% higher than the standard analysis, and for the lower E_T^{min} bins they are clearly outside the statistical errors. Two

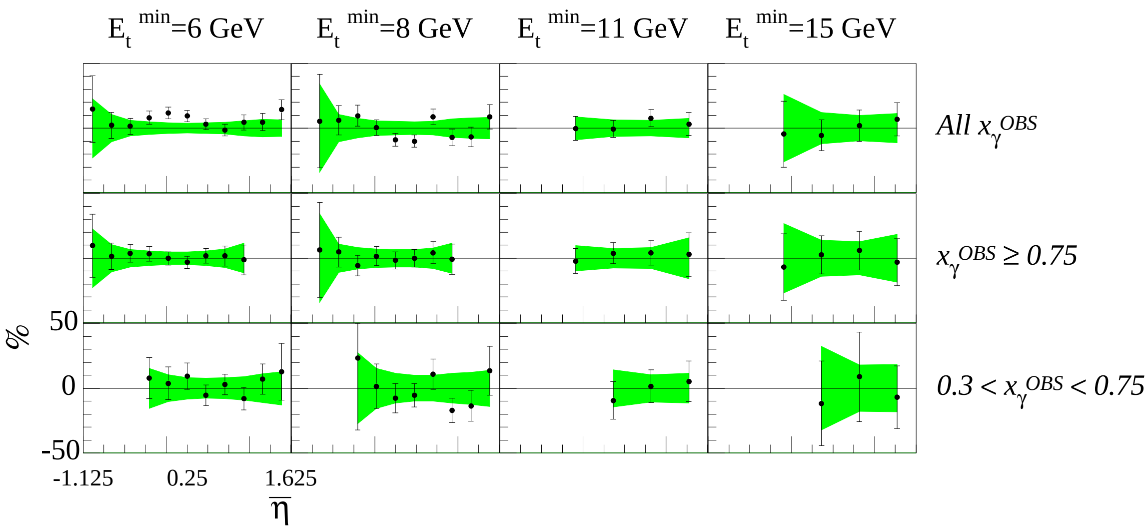

Figure 6.19: *Percentage effect on the KTCLUS cross sections of using HERWIG without multiple interactions for the unfolding of the cross sections. The error bars indicate the statistical error on these points and the shaded band indicates the statistical error on the central analysis*

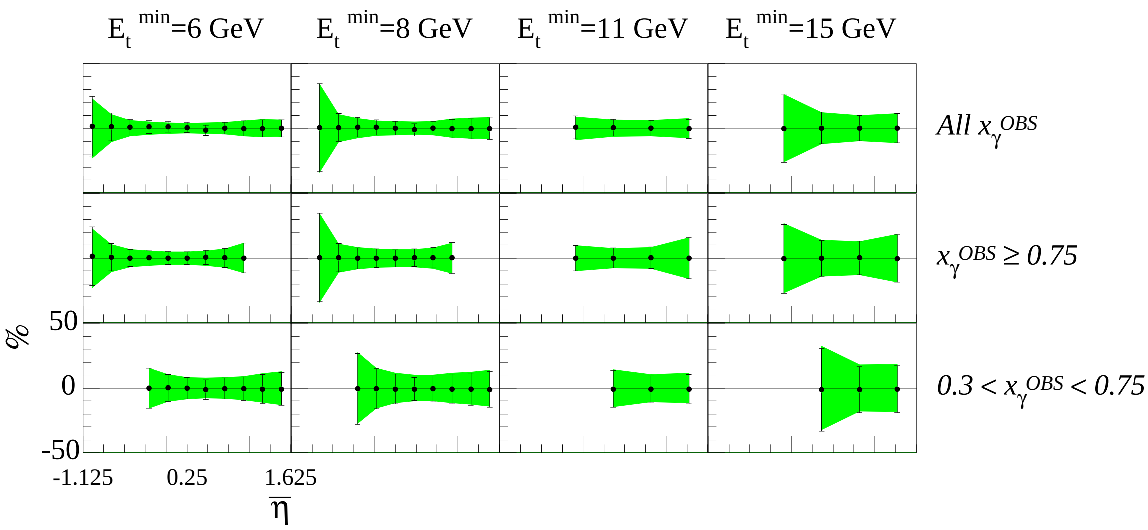

Figure 6.20: *Percentage effect on the KTCLUS cross sections of using the cross sections as calculated by HERWIG for the relative mixing of the resolved and direct samples, instead of fitting to the x_γ^{OBS} distribution. The error bars indicate the statistical error on these points and the shaded band indicates the statistical error on the central analysis*

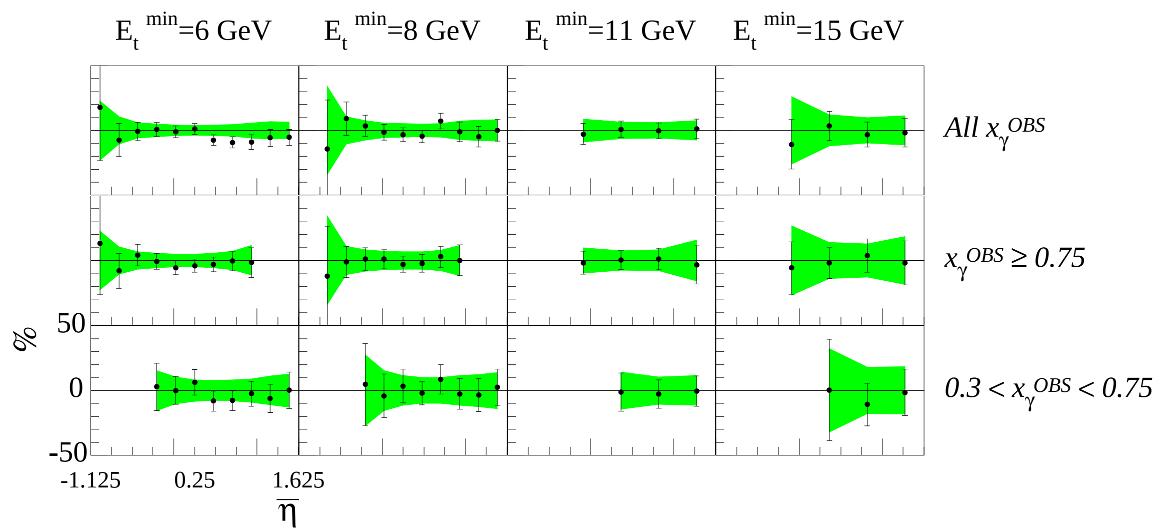

Figure 6.21: *Percentage effect on the KTCLUS cross sections of using a constant correction factor of 1.2 for the jet transverse energies, instead of a function $C(\eta^{jet}, E_T^{jet})$. The error bars indicate the statistical error on these points and the shaded band indicates the statistical error on the central analysis*

effects are responsible for this: firstly the jets have increased E_T, so more now lie above the threshold, and secondly the y_{JB} is also larger, so more events will pass the low y_{JB} cut. On the whole the effect of scaling by -3/5% is similar and opposite. This is the largest systematic uncertainty, and is highly correlated with the bins. Hereafter it will be referred to as the principal correlated error.

The trigger decisions in the Monte Carlo simulation were made directly from the calorimeter energies and other criteria in the standard way used for data. This was done before it was concluded that the calibration of the calorimeter in the data in the BCAL(RCAL) needed to be scaled by +6(2.5)%. This scaling effectively meant that the trigger had been operating with higher energy thresholds in the data than in the Monte Carlo. However the various selection criteria, kinematic and otherwise, made within this analysis should mean that the final data sample is largely independent of such effects. In order to estimate the effect that this scale problem in the trigger would have on the final results, the trigger simulation was rerun on the Monte Carlo with the calorimeter energies scaled down by 6(2.5)% in the BCAL(RCAL). Figure 6.24 shows the results of this are small variations of up to 5% for the large $\bar{\eta}$ region. Obviously on the whole only the acceptance for

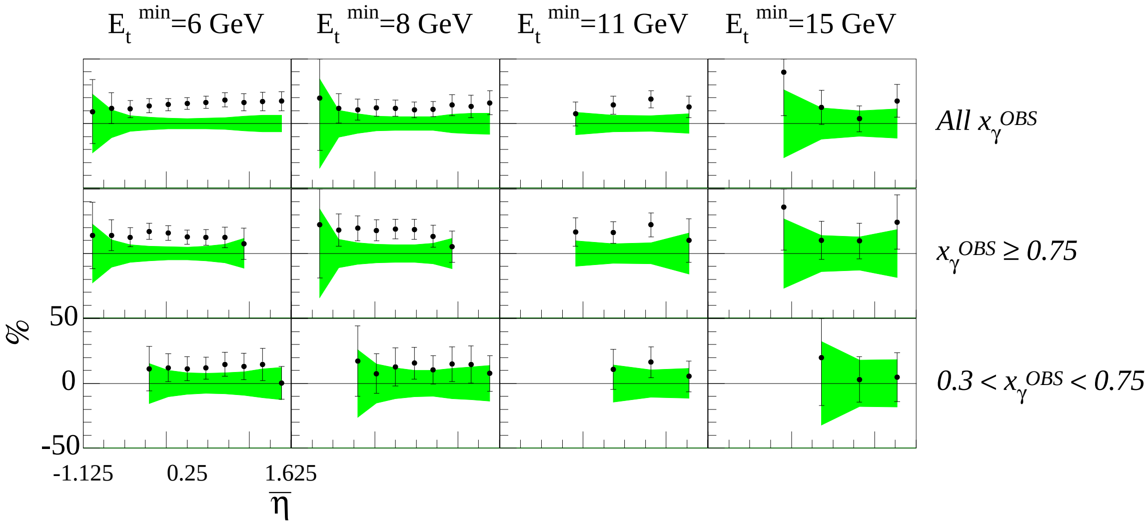

Figure 6.22: *Percentage effect on the KTCLUS cross sections of scaling E_T^{jet} by +5% and y_{JB} by +3% in the data. The error bars indicate the statistical error on these points and the shaded band indicates the statistical error on the central analysis*

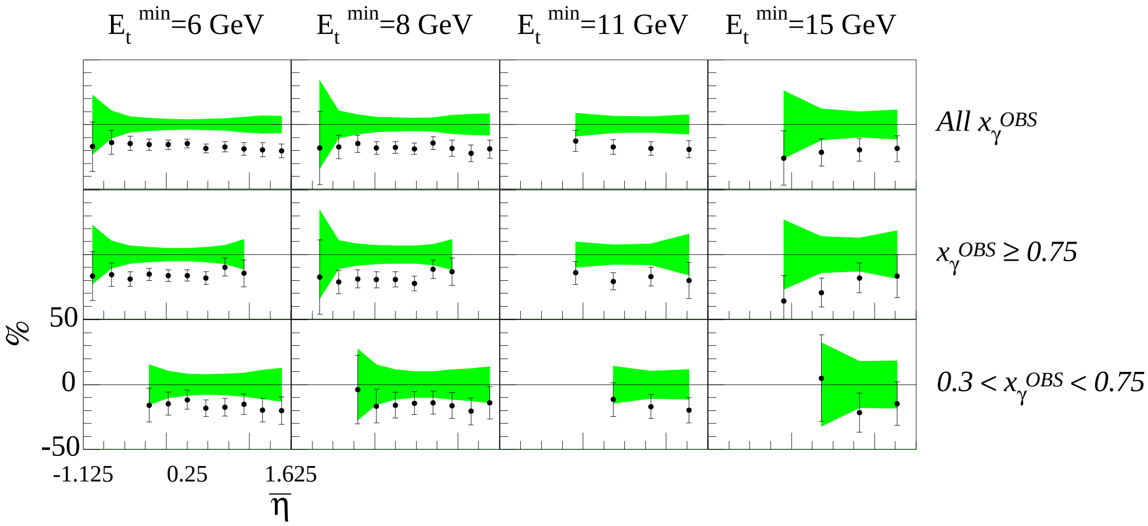

Figure 6.23: *Percentage effect on the KTCLUS cross sections of scaling E_T^{jet} by -5% and y_{JB} by -3% in the data. The error bars indicate the statistical error on these points and the shaded band indicates the statistical error on the central analysis*

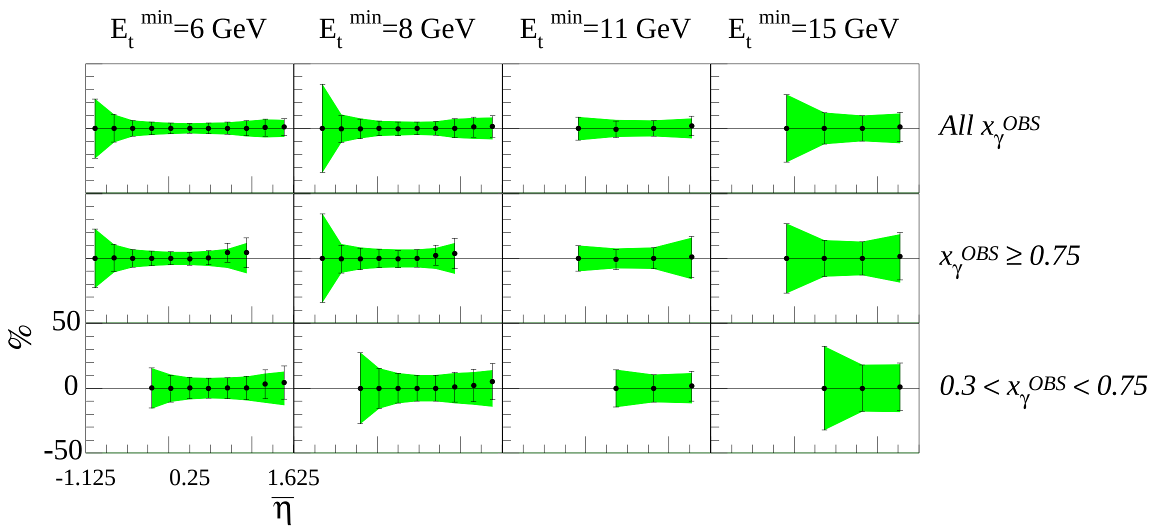

Figure 6.24: *The percentage effect on the KTCLUS cross sections of scaling down the energies for the* BCAL(RCAL) *by 6(2.5)%, in the Monte Carlo and rerunning the trigger. The error bars indicate the statistical error on these points and the shaded band indicates the statistical error on the central analysis*

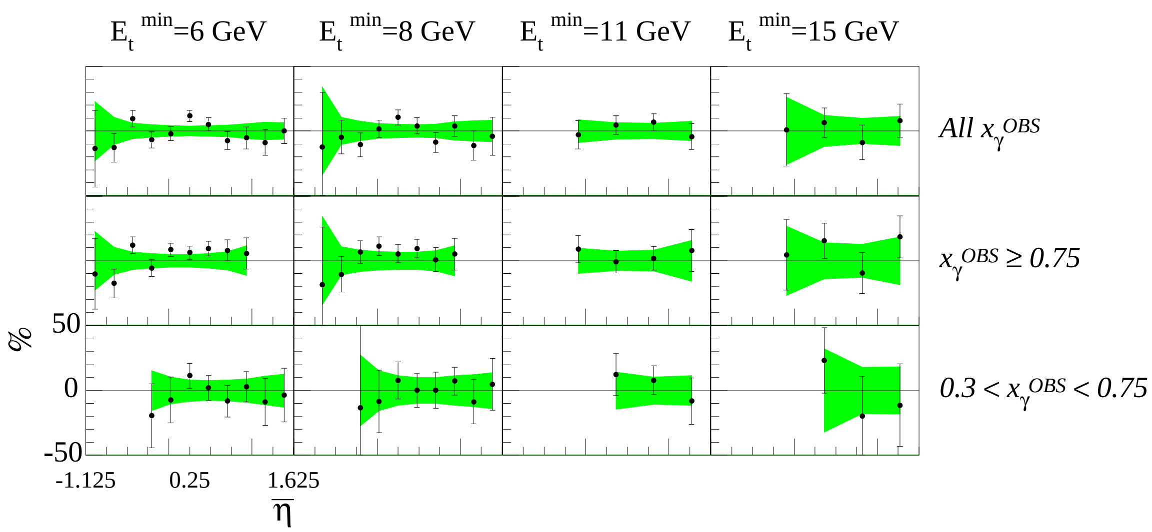

Figure 6.25: *Percentage difference between the PYTHIA KTCLUS hadronic cross section, and the 'measured' PYTHIA cross section unfolded using HERWIG. The error bars indicate the statistical error on these points and the shaded band indicates the statistical error on the central analysis*

the events in this area with small y is slightly changed.

In addition to the checks described above, where the procedure for extracting the cross section from the data was varied, a check on the overall approach was made by using the standard procedure to unfold a cross section from the reconstructed PYTHIA sample after the detector simulation. This was then compared to the true hadronic cross section from PYTHIA. Figure 6.25 shows that the difference between the true and extracted cross sections are of the same order as the statistical errors on the central analysis. The fluctuations seen can be attributed to the lower statistics in the PYTHIA sample compared to the data. This is a check on the effect of migrations between bins. Another approach to checking this bin-by-bin method is to use a matrix unfolding method. This has been done [40, 96] and produced a result that was completely consistent with the bin by bin unfolding method used here.

6.8 Summary of the Measurement

In total 12 cross sections, $d\sigma/d\bar{\eta}$, have been measured in the kinematic region defined by equations 3.22. Four for direct($x_\gamma^{OBS} \geq 0.75$) events, four for resolved ($0.3 < x_\gamma^{OBS} < 0.75$) events, and 4 for the whole x_γ^{OBS} range, where x_γ^{OBS} is calculated using E_T^{CORjet} and $y_{_{Cor}}$. These being for cuts on the minimum corrected jet transverse energy of $E_T^{min} = 6$, 8, 11 and 15 GeV. These cross sections have been measured for the jet algorithms KTCLUS, PUCELL, and EUCELL, and corrected for detector acceptance. The cross sections are measured in bins of $\bar{\eta}$ of constant width. The bin width used does however vary between the different x_γ^{OBS} regions and minimum E_T^{jet} cuts. The statistical errors on the measured points include those from the data as well as those from the Monte Carlo used for the acceptance correction. Of the systematic errors, those arising from the calorimeter energy scale and the associated uncertainty in its response to jets are largest and are also highly correlated with $\bar{\eta}$. This is termed the principal correlated error on each cross section. The background contributions to the measured cross sections have been assessed and found to be very small. Therefore they have not been subtracted.

Chapter 7

Results

In this chapter the measured cross sections will be discussed with a view to the physics conclusions that can be drawn. In addition a comparison with an earlier measurement of the $E_T^{min} = 6$ GeV, $x_\gamma^{OBS} \geq 0.75$ cross section is made. Tables containing all the results are given in appendix B.

7.1 Comparison of the Jet Algorithms

Figure 7.1 shows the results for all three jet algorithms for the whole range of $x_\gamma^{OBS}$and for $E_T^{min} = 6$, 8, 11 and 15 GeV. The overall dependence of the cross section on E_T^{min} is examined in section 7.2. Looking first at the results for $E_T^{min} = 6$ GeV (figure 7.1(a)), one sees that the cross section is almost linear up to $\bar{\eta} \approx 0.25$, where it levels off. The first thing to notice when comparing the cross sections for the different jet finders is that the two cone algorithms PUCELL and EUCELL give significantly different results. The plateau in the forward region lies around 60% higher for EUCELL than for PUCELL. This shows how large the scope for differences is within the Snowmass Convention. Therefore, if one wants to interpret a jet cross section in a sensible way, simply describing a jet finder as a cone algorithm is not enough, rather it is necessary to define clearly exactly how the algorithm operates. The cluster algorithm KTCLUS has a totaly independent

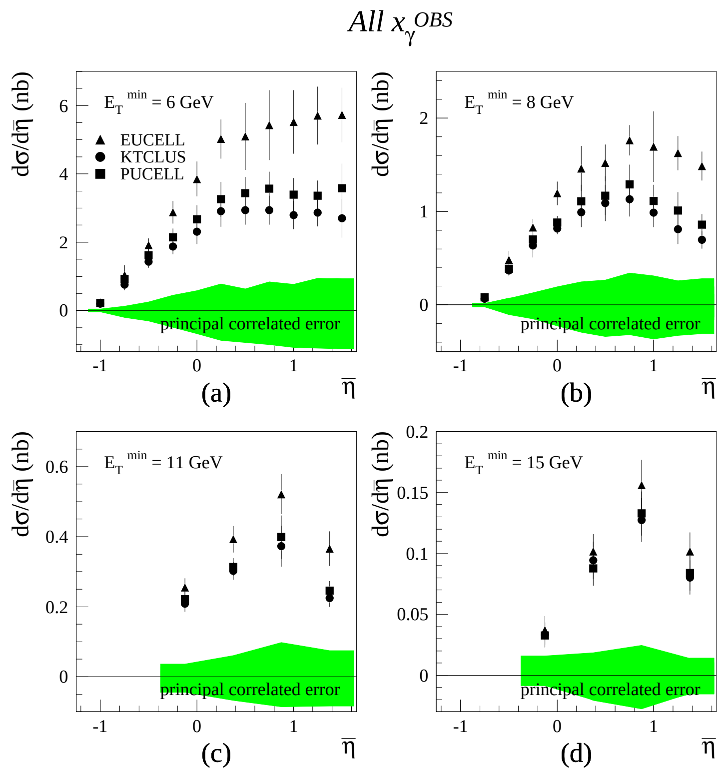

Figure 7.1: *The measured cross sections $d\sigma/d\bar{\eta}$ for the full range of x_γ^{OBS} and the four different E_T^{min} cuts, and all three jet algorithms used in this analysis. The error bars are the combined systematic and statistical errors, excluding the principal correlated uncertainties. The shaded band gives the maximum principal correlated error at each point.*

operation to the cone algorithms. The results it produces are however comparable. In particular the KTCLUS results are very similar to those for PUCELL, though around 20% lower.

The differences described above can be traced back to the precluster phase of the algorithms. While EUCELL can combine objects into a precluster that are as much as two cone radii appart, PUCELL only clusters things that are separated by a maximum of one cone radius. Here the effective radius in PUCELL is actually raised a little due to the merging of jets in the final stage of the algorithm. Therefore EUCELL can combine more transverse energy into its jets, which means that more jets are above the E_T^{min} threshhold, and hence the cross section is larger. At every step of KTCLUS objects with a maximum separation of unity can be combined. This is not directly comparable to the preclustering of a cone algorithm, however it seems entirely plausible that it should lead to a similar behaviour to preclustering with cone radius 1. Hence the the similarity between the results for KTCLUS and PUCELL (with cone radius 1) is understandable.

The variation of the cross sections for the different jet algorithms by almost a factor 2 makes it clear that jets are not fundamental objects, but rather a characteristic of the final state that are defined by the algorithm used to find them. Never the less all the cross sections have a similar form, and the results for KTCLUS and PUCELL are similar in magnitude, though they use different approaches to define the jets. Therefore jets are not simply artifacts of the algorithm applied, but real objects that can be detected and measured in a variety of ways.

Looking at the cross sections shown in figure 7.1(a), (b), (c) and (d) one sees that the differences between the results for the different jet algorithms become smaller as E_T^{min} rises. For $\bar{\eta} \approx 1$ the relative difference between EUCELL and PUCELL falls from around 64% for $E_T^{min} = 6$ GeV to around 15% for E_T^{min}= 15 GeV. This shows that measurements at higher transverse energies depend less on the exact jet definition. However, they also require a much greater data sample and can no longer reach the lowest values of x_γ^{OBS} and x_p^{OBS}. This convergence of the results of the different algorithms at higher E_T^{jet} is expected since jets, in general, become narrower as their transverse energy increases (see section 4.6.4 and [94]), and hence the differences in preclustering become less significant. The fall off in the forward region of $\bar{\eta}$ apparent in the higher E_T^{min} cross sections is a result of the raised transverse energy threshold limiting the minimum x_γ^{OBS} attainable.

Figures 7.2 and 7.3 show the results for the $0.75 \leq x_\gamma^{OBS}$ and $0.3 < x_\gamma^{OBS} < 0.75$ regions respectively. The cross section for $x_\gamma^{OBS} \geq 0.75$ and $E_T^{min} = 6$ GeV shows a rise up to $\bar{\eta} \approx 0.25$ where it starts to fall off. This fall off is a direct result of the x_γ^{OBS} cut. The reader is referred to section 7.2 for a discussion of the evolution of the cross sections with E_T^{min}. Once again there are significant differences between the results for the different jet finders which become smaller as E_T^{min} increases.

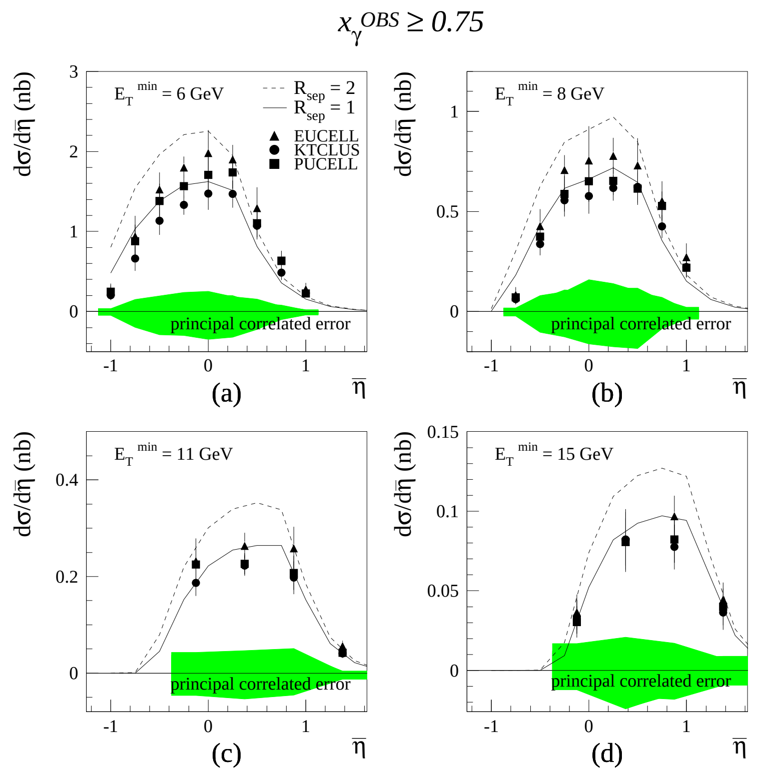

Figure 7.2: *The measured cross sections $d\sigma/d\bar{\eta}$ for the range $0.75 \leq x_\gamma^{OBS}$ and the four different E_T^{min} cuts, and all three jet algorithms used in this analysis. The error bars are the combined systematic and statistical errors. The shaded band gives the maximum principal correlated error at each point. The solid (dashed) line is the result of a NLO calculation with R_{sep}=1 (2).*

The differences seen are however smaller than for the all x_γ^{OBS}cross sections. This is because events with high x_γ^{OBS} contain no significant photon remnant and the jets are therefore in a relatively clean environment, and also because jets in direct photon events are generally narrower in shape than those from resolved photon interactions [94].

The resolved photoproduction cross section for $E_T^{min} = 6$ GeV (figure 7.3(a)) rises from around 0.8 nb at $\bar{\eta} = -0.25$ to a maximum value at $\bar{\eta} = 0$, followed by a decrease back to 0.2 nb by $\bar{\eta} = 1.5$. The EUCELL jet cross sections are again systematically higher than the PUCELL cross sections which are once more slightly above those for KTCLUS. The separation between EUCELL and the other two jet algorithms is larger than in the direct case - a factor of two at the lowest E_T^{min} values - but again becomes less significant at higher E_T^{min}. The cross sections for

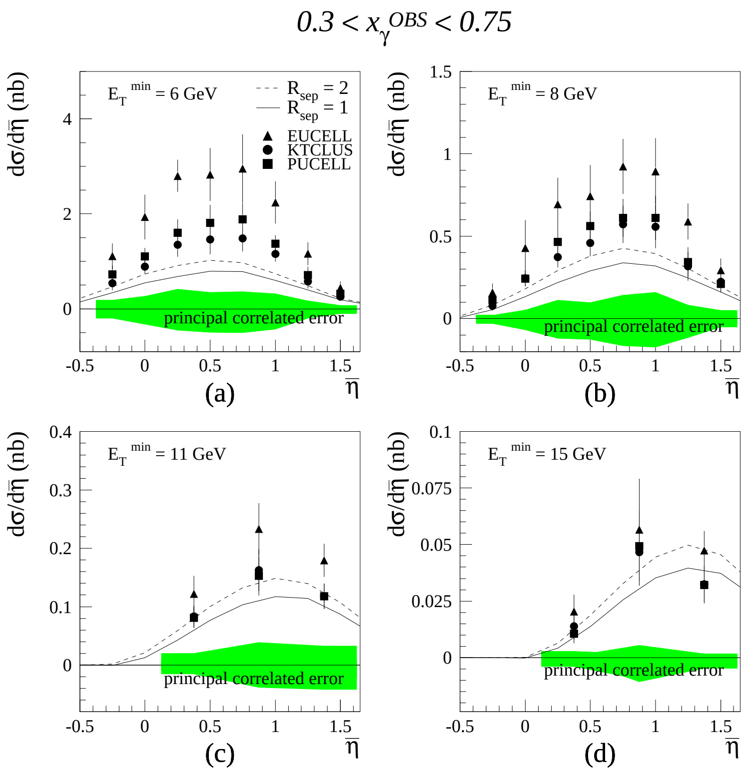

Figure 7.3: *The measured cross sections $d\sigma/d\bar{\eta}$ for the range 0.3< x_γ^{OBS} <0.75 and the four different E_T^{min} cuts, and all three jet algorithms used in this analysis. The error bars are the combined systematic and statistical errors, excluding the principal correlated uncertainties. The shaded band gives the maximum principal correlated error at each point. The solid (dashed) line is the result of a NLO calculation with R_{sep}=1 (2).*

0.3< x_γ^{OBS} <0.75 fall off to both sides because of the x_γ^{OBS} limits. The differences between the three jet algorithms here are similar to those in the all x_γ^{OBS} cross sections.

Also shown on figures 7.2 and 7.3 are curves for NLO calculations from Klasen and Kramer [46] with R_{sep}= 1 and R_{sep}= 2. For further discussion of these see section 7.3.

7.2 Dependence on the Jet Transverse Energy

In figures 7.1, 7.2 and 7.3 it can been seen that in general the cross section falls sharply with rising E_T^{min}, and that the phase space in $\bar{\eta}$ becomes ever narrower.

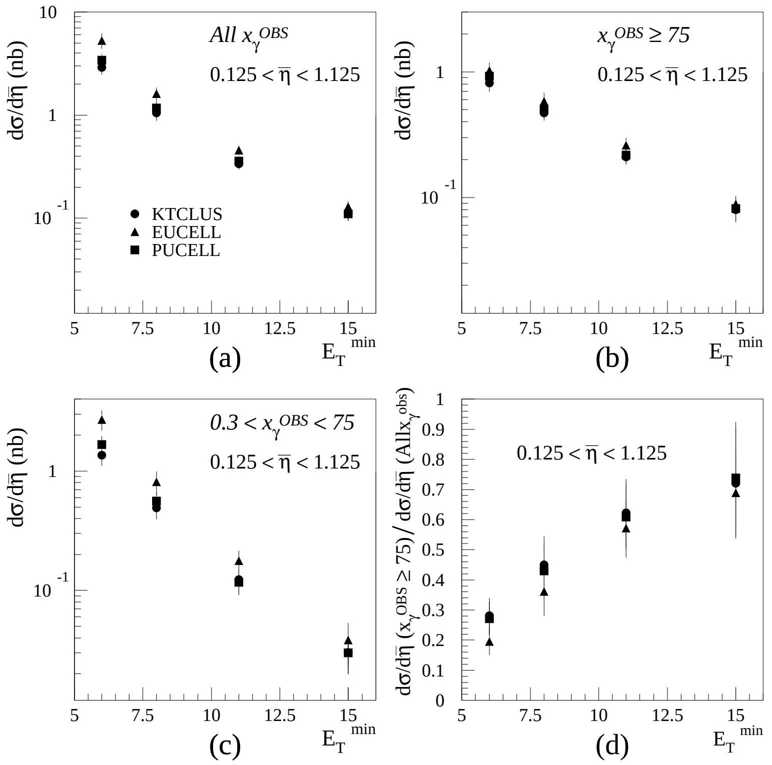

Figure 7.4: *The evolution of the cross sections with E_T^{min}: $d\sigma/d\bar{\eta}$ for 0.125< $\bar{\eta}$ <1.125, for the KTCLUS, EUCELL, and PUCELL as a function of E_T^{min} for (a) all x_γ^{OBS} (b) 0.75$\leq x_\gamma^{OBS}$ and (c) 0.3< x_γ^{OBS} <0.75. (d) shows the ratio of the cross sections for 0.75$\leq x_\gamma^{OBS}$ and all x_γ^{OBS}. The error bars represent the combined systematic and statistical uncertainty, excluding the principal correlated uncertainties.*

The minimum $\bar{\eta}$ reached rises from around -1 at $E_T^{min} = 6$ GeV, to around 0 for E_T^{min}=15 GeV. Also the peak in the cross section occurs at gradually larger values of $\bar{\eta}$. These effects are due to kinematic reasons, particularly the cuts on y, as can be seen from figure 6.7.

The chosen binning is so constructed that for all cross sections and all E_T^{min} thresholds it is possible to calculate the cross section for $0.125 < \bar{\eta} < 1.125$ by averaging the measured points in this $\bar{\eta}$ range. As this covers a large part of all the cross sections it is then possible to compare the evolution of the cross sections with E_T^{min}. Figure 7.4(a) shows $d\sigma/d\bar{\eta}$ for $0.125 < \bar{\eta} < 1.125$ as a function of E_T^{min} for the whole x_γ^{OBS} region. Here one sees once again that the differences between the jet algorithms becomes smaller as E_T^{min} rises. This naturally means that the cross section falls with different strengths for the different jet algorithms.

For KTCLUS it goes as approximately $d\sigma/d\bar{\eta} \propto (E_T^{min})^{-3.5}$.

Figure 7.4(b) and (c) show the E_T^{min} dependence of the cross sections in the high and low x_γ^{OBS} regions respectively. At around $d\sigma/d\bar{\eta} \propto (E_T^{min})^{-2.7}$ for KTCLUS, the fall off in the $x_\gamma^{OBS}\geq 0.75$ cross section with increasing E_T^{min} is significantly less steep than for full event sample. Conversely the fall of in the $0.3< x_\gamma^{OBS} <0.75$ region is the steepest at something like $d\sigma/d\bar{\eta} \propto (E_T^{min})^{-4.18}$ for KTCLUS. Comparing figure 7.4(b) and (c) it can be seen that whereas for E_T^{min}=6 GeV the resolved cross section is clearly higher than the direct, by E_T^{min}= 15 GeV the situation is reversed. This is consistent with expectations since at smaller x_γ^{OBS} there is less energy available to produce jets. In addition resolved photon subprocesses have an angular dependence which means that relatively more partons are produced at small angles to the beam axis [45] in the dijet centre of mass system. Both these things lead to the dominance of direct photon events at higher transverse momenta. This is shown directly in figure 7.4(d) where the ratio of the $x_\gamma^{OBS}\geq 0.75$ and all x_γ^{OBS} cross sections for $0.125 < \bar{\eta} < 1.125$ is given. It can be seen that at E_T^{min}=15 GeV the direct photon processes account for around 70% of the total cross section, and only around 25% at E_T^{min}= 6 GeV.

7.3 Comparison with NLO Calculations

In this section comparisons of the measured cross sections to NLO perturbative QCD calculations are presented. The main advantage of NLO calculations over LO is a much reduced scale dependence (see section 2.8). However they only include the first step of parton showering and no hadronisation. In addition NLO calculations make no provision for MI, and for this reason comparisons are only made after applying x_γ^{OBS} cuts to exclude the region most affected by underlying events.

Before making any comparisons, the constraints on the out going partons applied in the calculations should be discussed. Since jets may be accompanied by other soft gluons (outside the jets), there is a potential problem when the two jets have the same E_T^{jet}. The infrared singularity associated with summing the soft gluon contributions is usually cancelled by the singularity coming from the one-loop contribution. For two jets with the same E_T^{jet} some of the phase space for the soft gluon terms is restricted and an incomplete cancellation may occur in some calculations. As a consequence Klasen and Kramer [46] have allowed the second jet to have an E_T^{jet} as low as 1 GeV below the E_T^{min} threshold, which they apply to the higher E_T^{jet} jet. This has the drawback that the cross section is then sensitive to changes in the value used for this lower cut on the second jet. Harris and Owens [47] have applied a low cutoff on the energy of the very soft gluons and found that the dependence of the cross sections on the value of the low energy cutoff used is much less than the quoted errors on the data. These different approaches account for the differences between the theory curves shown later.

The size of the differences between the cross sections for the different jet finders have a direct effect on the comparison with pQCD calculations. As was indicated in section 3.3, it is again necessary to have a more precise definition of the jets than the simplest Snowmass convention. In section 3.3 the use of the R_{sep} parameter was given as one possible solution to the problem. Figures 7.2 and 7.3 include curves for NLO QCD calculations from Klasen and Kramer [46] using $R_{sep} = 1$ (solid curve) and $R_{sep} = 2$ (dashed curve). In these calculations the NLO GRV [53] parton distributions for the photon and the CTEQ3M [100] parton distributions for the proton are employed.

Looking first at the lowest E_T^{min}= 6 GeV cross section for the high x_γ^{OBS} region (shown in figure 7.2(a)) it can be seen that the differences between the different jet finders used in the experiment and those between the calculations for different values for R_{sep} are similar. The calculation with R_{sep}= 1 is very similar to the results for PUCELL and KTCLUS, while EUCELL lies a little below R_{sep}= 2, as should be the case (see section 3.3). The PUCELL and KTCLUS cross sections remain in good agreement with the NLO curve calculated with $R_{sep} = 1$ for all $\bar{\eta}$

and for all E_T^{min} thresholds. The only exception is in bins at the most negative values of $\bar{\eta}$ in the lower E_T^{min} cross sections, where the trend is for the calculation to lie above the data. Though the separation between EUCELL, PUCELL and KTCLUS cross sections becomes smaller at higher E_T^{jet}, the separation between the two theory curves remains significant.

In the 0.3< x_γ^{OBS} <0.75 region the differences between the curves with different R_{sep} again show the same trend as the data, with the $R_{sep} = 2$ curves being higher than those for $R_{sep} = 1$. However the differences between the different jet algorithms are larger than the differences for the different R_{sep} values. Here one must take into account that in the calculation there are no MI. When comparing the magnitude of the cross sections it can be seen that for $E_T^{min} = 6$ GeV and 8 GeV, the NLO QCD curves lie significantly below the data. For higher E_T^{min} values the calculations are broadly consistent with the data. This behaviour is consistent with MI, parton shower, and hadronisation effects becoming less important as E_T^{jet} increases.

Since the differences in the theory curves can not be due to the QCD structure of hadronic jets, these figures confirm that even when comparing measurements to calculations with no parton showering or hadronisation it is necessary to match the jet definitions used in the calculations to those used in the experiment. The above discussion leads to the conclusion that for NLO calculations R_{sep} can be used to achieve this matching, and eliminate a lot of the uncertainty when making such comparisons. It is however only a fix at NLO and does not generalise to higher order calculations.

In Figures 7.5 and 7.6 the KTCLUS jet cross sections are shown again, with Klasen and Kramer's NLO QCD calculations (with $R_{sep} = 1$) employing two different parton distribution functions for the photon - namely those of NLO GRV(solid curves [53]) and GS (dashed curves [52]). It can be seen that the agreement is in general good for both distribution functions, except in the two lowest E_T^{jet} regions of the resolved cross section (figure 7.6(a) and (b)) where the QCD calculations

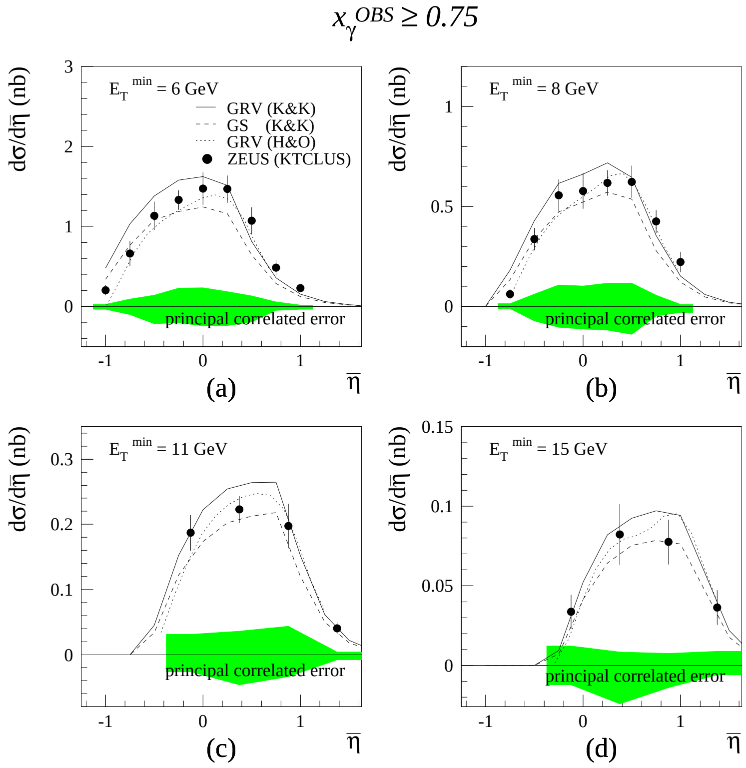

Figure 7.5: *The cross sections $d\sigma/d\bar{\eta}$ measured using KTCLUS for the range $0.75 \leq x_\gamma^{OBS}$ and the four different E_T^{min} cuts. The error bars are the combined systematic and statistical errors, excluding the principal correlated uncertainties which are shown in the shaded band. The data are compared to NLO QCD calculations from Klasen and Kramer, for two different photon parton distributions, GRV and GS, and from Harris and Owens using GRV (see text). All three calculations use $R_{sep} = 1$.*

are significantly below the data. Perhaps surprisingly, the difference between the photon parton distributions is largest in the direct photoproduction region. This is due to differences between the quark distributions in the photon for $x_\gamma > 0.8$, where they are poorly constrained by F_2^γ data. These differences persist at high E_T^{jet}. Also shown in figures 7.5 and 7.6 is a NLO QCD calculation (again with $R_{sep} = 1$) from Harris and Owens using NLO GRV $\overline{\mathrm{MS}}$ for the photon, and NLO CTEQ4 $\overline{\mathrm{MS}}$ for the proton. At high x_γ^{OBS} there is again good agreement with the measurements, but at low x_γ^{OBS} the disagreement in the two lowest E_T^{jet} regions is larger than for Klasen and Kramer's calculations. This disagreement persists to some extent in the third ($E_T^{min} =$ 11 GeV) low x_γ^{OBS} cross section.

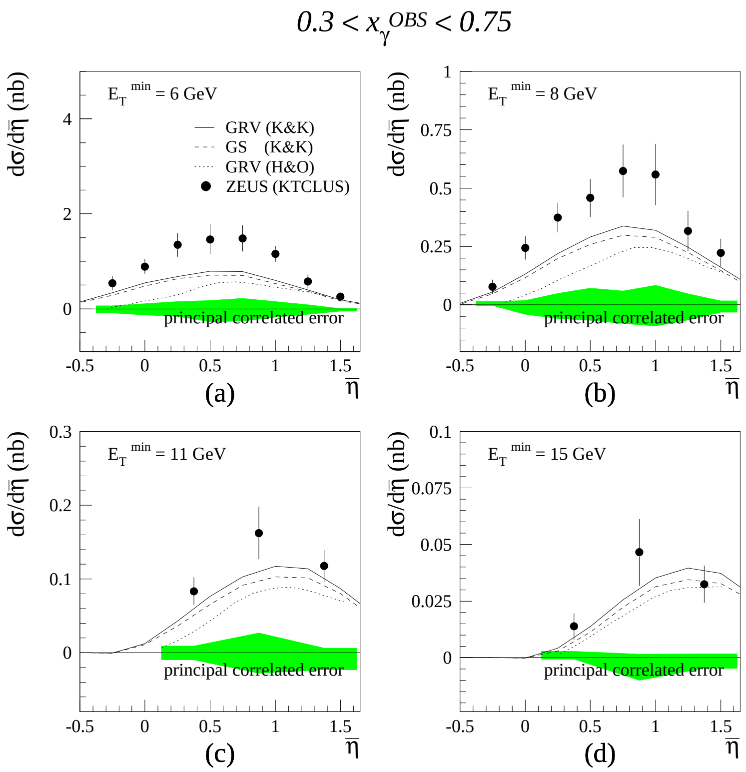

Figure 7.6: *The cross sections $d\sigma/d\bar{\eta}$ measure using KTCLUS for the range 0.3< x_γ^{OBS} <0.75 and the four different E_T^{min} cuts. The error bars are the combined systematic and statistical errors, excluding the principal correlated uncertainties which are shown in the shaded band. The data are compared to NLO QCD calculations from Klasen and Kramer, for two different photon parton distributions, GRV and GS, and from Harris and Owens using GRV (see text). All three calculations use R_{sep} = 1.*

7.3.1 Comparison with Predictions from HERWIG

The cross section without cuts on x_γ^{OBS} includes x_γ^{OBS} values down to 0.05, the lowest value allowed by the other kinematic cuts. At the lower values of x_γ^{OBS}, the jet profiles in section 4.6.4 and the x_γ^{OBS} distributions shown in figure 4.4 indicate discrepancies between the data and the MC simulations. Nevertheless, this cross section remains interesting as its shape is less biased by kinematic cuts than the cross sections in restricted ranges of x_γ^{OBS}. Here the shape is compared to predictions from the HERWIG Monte Carlo simulation. As explained in chapter 4 this program includes models for MI, parton showering and hadronisation, but its predictions have a large scale dependence due to the fact that it includes only LO matrix elements.

Figure 7.7 shows the dijet cross section for E_T^{min}= 6 GeV for the whole x_γ^{OBS} range compared to various predictions from HERWIG for different photon structure functions, and CTEQ3(LO) for the proton. While the simulation can describe the shape of the cross section, these predictions fail to describe the overall normalisation requiring an ad hoc multiplicative scale factor of about 1.8 to agree with the data. This factor was determined by considering the region $\bar{\eta}< 0$ where all the photon parton distribution function parameterisations give similar results. A factor of this magnitude is not unreasonable given the scale dependence of the MC (see section 4.3).

The solid curve in figure 7.7 gives the prediction for GRV(LO) for the photon. It gives the best description of the data over the whole $\bar{\eta}$ range. Using this structure function but not including the simulation of MI results in the dashed curve. It shows a stronger fall off in the forward region than the curve with MI, and thus is less consistent with the data. Also shown for this structure function is the curve for events generated with direct photons. As expected these events lie mainly in the rear direction. To estimate the contributions from VMD photons the GRV pion parton distribution function [101] was used to model the photon structure. The result of this is shown as the dashed curve labelled VMD. The figure shows that the VMD contribution rises towards larger $\bar{\eta}$ though it is small throughout the kinematic region studied here. The sum of direct and VMD photon events alone cannot describe the cross section found in the experiment, therefore anomalous photon events make up a major part of these cross sections.

Without MI, HERWIG with the LAC1 photon parton distribution function gives a very similar prediction to the GRV without MI, though it rises a little forward of $\bar{\eta}$=1. With MI the prediction rises very strongly and is excluded by the data. This drastic difference arises because of the large soft gluon content in LAC1 which leads to a higher number of partonic interactions per event. Given that the data is generally described better when MI are included (see chapter 4, [61, 62]), a small gluon content to the photon is favoured. The DG and GS parton distribution

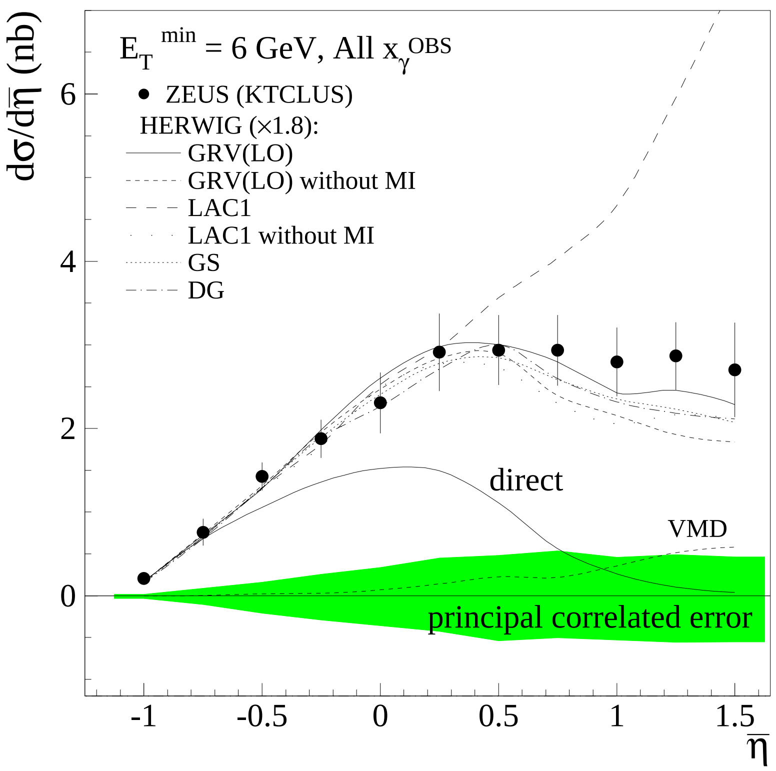

Figure 7.7: *The cross section $d\sigma/d\bar{\eta}$ measured using KTCLUS for the full range of x_γ^{OBS} and E_T^{min}=6 GeV, compared to the expectations of various HERWIG MC simulations (see text). The error bars represent the combined systematic and statistical uncertainty, excluding the principal correlated uncertainties which are shown in the shaded band.*

functions, where the gluon fraction is smaller than in GRV, lead to predictions that lie below the GRV curve, which cannot be excluded by this measurement. It should also be noted that the effect of MI is a strong function of the choice of $\hat{p}_{tmin}$ [63]. With the value of $\hat{p}_{tmin}$ = 2.5 GeV used here, the data favour the GRV parton distribution with MI.

As the predictions obviously depend strongly on the inclusion or not of MI, any conclusions drawn about the photon structure are also dependent on the assumptions of the model used to generate the MI. The measurement itself is however relatively independent of these assumptions, and could be confronted with any other model. In addition the cross section covers regions in which MI have little effect (high x_γ^{OBS}, low $\bar{\eta}$, high E_T^{jet}), and these regions could in principle be used to investigate the photon structure with more certainty. However the errors on the

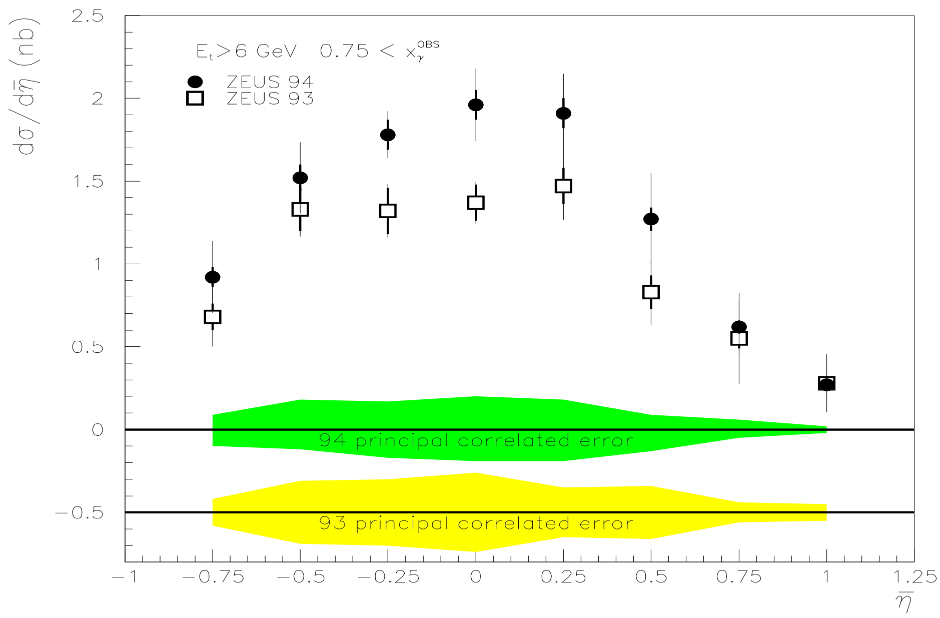

Figure 7.8: *Comparison of Zeus '93 and '94 dijet cross sections. The thin (thick) error bars represent the systematic (statistical) uncertainty.*

measurement, and the similarities between the various predictions in this region mean that no conclusion can be drawn from figure 7.7. In the regions where the impact of MI is larger than a change in the parton distribution function (low x_γ^{OBS}, large $\bar{\eta}$, low E_T^{jet}), this measurement could be used to confront different models for the QCD dynamics of high energy photon proton interactions.

7.4 Comparison with the '93 Measurement

The Measurement of the $x_\gamma^{OBS} \geq 0.75$ cross section for $E_T^{min} = 6$ GeV using the EUCELL jet finder should be directly comparable to the same measurement made using the '93 ZEUS data [54]. However a large discrepancy ($\sim 28\%$) between the two is seen, as shown in figure 7.8. In order to track down and identify the causes of this difference a number of factors were investigated. It was found that the main causes of the discrepancy are:

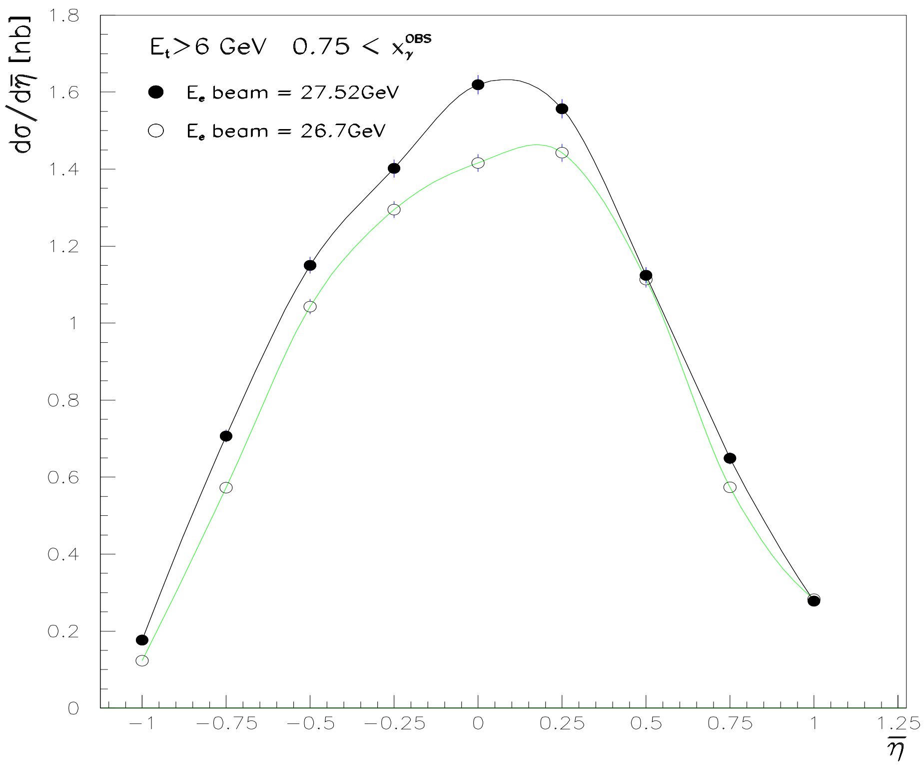

Figure 7.9: *Effect on the cross section of different electron/positron beam energies in HERA between '93 and '94 as predicted by HERWIG. The errors are purely statistical.*

1. Firstly the way in which the calorimeter energy scale correction was implemented was different. For the '93 measurement the E_T^{jet} and $y_{_{JB}}$ were scaled up by 5% in the data, and the average of the unscaled and scaled result for each bin was taken. The method used in this analysis is explained in section 6.1. If the '94 measurement is treated in the same way, in this respect, as the '93 measurement, it produces a result around 11% lower than the standard '94 cross section.

2. During the 1994 data taking the positron beam had an energy of 27.52 GeV, whereas during 1993 the electron beam was of 26.7 GeV. NLO Calculations show a $\sim$ 3% effect due to this difference [87], and Monte Carlo predictions show an effect of between around 4% and 10% depending on the generator used. Figure 7.9 shows the effect as predicted by HERWIG. The general effect predicted by both Monte Carlo and NLO calculations is that the central

and rear regions of the cross section are raised, while the forward region is lowered. The total estimated effect is $\sim 5\%$ in the peak.

3. The Monte Carlo versions used to extract the cross section were different in ‘93 and described the data less well. When the old version of the Monte Carlo (HERWIG 5.7 instead of 5.8) is used to calculate the acceptance and other corrections the cross section is around 5% lower

4. In the ’93 analysis the results of extracting the cross section with HERWIG and PYTHIA were averaged. This again results in a few percent reduction in the central cross section.

These effects combined reduce the discrepancy between ’93 and ’94 from $\sim 30\%$ to less then 10%. This can be considered insignificant given the size of the errors on both measurements, and that there are other small differences in the method used to extract the cross section not mentioned above.

Chapter 8

Summary and Conclusions

In low Q^2 electron proton collisions the electron beam can be considered as providing a source of almost real photons which interact with partons in the proton. Hard partonic photon proton interactions (photoproduction) result in final states containing jets. At leading order two processes are responsible for jet photoproduction. The photon may either interact in a point like way (direct) or first fluctuate into a hadronic state (resolved). Thus photoproduction may be used to study the structures of both the proton and the photon. At higher orders the distinction between direct and resolved processes is not so clear. The average pseudorapidity of the jets in the final state of these events is directly related to the boost between the $\gamma - p$ centre of mass system and the lab frame, and hence to x_γ and x_p, the fractions of the photon and proton momenta entering the hard sub process. Therefore jet cross sections measured as a function of the average η^{jet} should be sensitive to the parton distributions inside the photon and proton.

In the analysis described in this thesis dijet photoproduction in positron proton collisions was studied using a data sample collected in 1994 with the ZEUS detector at HERA. The data sample has an integrated luminosity of 2.7pb^{-1}. Using this data sample photoproduced dijet cross sections $d\sigma/d\bar{\eta}$ have been measured with three different jet algorithms: KTCLUS, EUCELL and PUCELL, where $\bar{\eta}$ is the average pseudorapidity of the two highest transverse energy jets in an event. EUCELL and PUCELL are both Snowmass cone algorithms, whereas KTCLUS is a cluster algorithm. No attempt was made to correct back to a parton level cross section as any such correction would be highly model dependent. The cross sections presented here are measured at the hadron level by using Monte Carlo simulations to correct for the detector acceptance. Consequently they can be used to confront the predictions of any model for the hard subprocess and the production of the hadronic jets.

Photoproduction events were selected by requiring that the scattered positron was not detected in the uranium calorimeter. This corresponds to a maximum Q^2 of $\sim$ 4 GeV^2, and an average of $\sim$ 10^{-3} GeV^2. In defining the kinematic regions in which the cross sections were measured x_γ^{OBS}, the fraction of the photon momentum involved in the production of the two highest transverse energy jets in an event, was used to provide an experimental definition of direct and resolved photoproduction that is valid to all orders. Cross sections were measured for the whole range of x_γ^{OBS}, and for $0.75 \leq x_\gamma^{OBS}$ (direct) and $0.3 < x_\gamma^{OBS} <0.75$ (resolved), and for E_T^{min}= 6, 8, 11, and 15 GeV. E_T^{min} is the minimum transverse energy of the jets used. A cut of $|\Delta\eta| < 0.5$ was placed on the two jets to reduce the sensitivity of the cross sections to the angular distribution of the jets, and increase the correlation between $\bar{\eta}$ and x_γ and x_p. In addition only events with $0.2< y <0.8$ were used to reduce the contamination from DIS and beam gas interactions. In photoproduction y is effectively the fraction of the positron momentum carried by the interacting photon.

Previously a measurement of $d\sigma/d\bar{\eta}$ for E_T^{min}= 6 GeV and $x_\gamma^{OBS}\geq0.75$ and $x_\gamma^{OBS}< 0.75$ was made with data collected using the ZEUS detector in 1993. The measurement presented in this thesis uses much higher statistics, an improved calorimeter calibration, and Monte Carlo simulations that give a significantly better description of the data. The improved statistics meant that it was possible to make the measurement for the higher E_T^{min} thresholds and thus investigate the

E_T dependence of the cross sections. It also made it possible to place the cut at x_γ^{OBS}=0.3 on the resolved cross section to reject the region where there are significant discrepancies between the data and the Monte Carlo. Comparing the results of this analysis to the '93 measurement for E_T^{min}= GeV and $x_\gamma^{OBS}\geq$0.75 it was found that the increase in the energy of the electron/positron beam from 26.7 GeV to 27.5 GeV raises the cross section. Some Monte Carlo predictions suggest that this shift is as much as 10% in the centre of the cross section.

The measured cross sections vary by up to a factor of two when different cone or clustering algorithms are used for the definition of jets. The trend is for EUCELL cross sections to lie significantly higher than those of PUCELL, which in turn are slightly higher than those of KTCLUS. Particularly significant is that the results for EUCELL and PUCELL, which are nominally the same type of algorithm, differ by up to ~60%, while KTCLUS which uses a completely independent approach agrees reasonably well with PUCELL. Therefore to interpret jet cross sections in any sensible way it is necessary to define clearly exactly how the jet algorithm operates. As the E_T^{min} of the cross section rises the differences between the results for the different jet algorithms become smaller, and thus the sensitivity to the exact jet definition is reduced. However, in the cross sections measured here, differences are still present in the highest transverse energy (E_T^{min}= 15 GeV) cross sections. Increasing the E_T^{min} threshold has the drawback that it is no longer possible to access the lowest values of x_γ and x_p.

The cross section as a whole falls steeply as E_T^{min} is increased. Due to kinematic reasons it also becomes narrower in $\bar{\eta}$, and the peak falls further forward. The direct photon component of the cross section displays a significantly flatter dependence on E_T^{min} than the complete sample, and while it constitutes only around 1/4 of the cross section at E_T^{min}= 6 GeV, by E_T^{min}= 15 GeV it clearly dominates over the resolved. This is due to the higher x_γ^{OBS} which results in more energy being available for the production of the jets, and also to differences in the angular distributions of the outgoing partons from the dominant direct and resolved subprocesses.

When the photon fluctuates into a hadronic state it is possible that more than one partonic scatter may occur between the photon and the proton. Monte Carlo models which include such multiparton interactions (MI) describe the jet profiles and the distributions of the various kinematic variables seen in the data better than those which only simulate one hard scatter per photon proton collision. However there is still a deficit in the Monte Carlo at low y, low E_T^{jet}, and low x_γ^{OBS} in the forward region. As mentioned above, the effect of this deficit on the resolved cross section is largely dealt with by applying the cut at $x_\gamma^{OBS} = 0.3$.

It is found that Monte Carlo simulations both with and without multiparton interactions are capable of describing the $\bar{\eta}$ dependence of the cross section when no x_γ^{OBS} cuts are applied. In particular the prediction of HERWIG with MI using the GRV parameterisation for the parton distributions in the photon is slightly favoured. With the model for MI used here, a higher gluon content at small x_γ, like LAC1, is not consistent with the data. In the region of high x_γ^{OBS}, high E_T^{jet} and low $\bar{\eta}$ MI play virtually no role, so that here, if only in a restricted x_γ range, this measurement could be used to make relatively model independent statements about the photon structure. In the other extreme, i.e. small x_γ^{OBS}, low E_T^{jet} and large $\bar{\eta}$, it could be used to test different models for multiparton interactions.

As mentioned earlier, the magnitude of the measured cross section depends to a significant extent on the jet algorithm used. Therefore, if one wishes to compare NLO calculations to the data, it is necessary to match the theoretical and experimental jet definitions. The method for doing this presented in this thesis was to introduce the parameter R_{sep}. It was seen that, using values of R_{sep} determined by considering exactly how each algorithm works, the variations seen in the data could be reproduced in the calculations.

Comparison of the direct photon cross sections ($x_\gamma^{OBS} \geq 0.75$) with NLO QCD calculations shows good agreement in both shape and magnitude over a wide range of E_T^{jet} and η^{jet}. The NLO calculations also display a sensitivity to the photon structure at large x_γ. Calculations for the resolved photon cross sections in the region $0.3 < x_\gamma^{OBS} < 0.75$, which include jets with 6 GeV< E_T^{jet} < 11 GeV are found to lie below the data. However, for higher jet energies there is agreement. It is possible that the discrepancy between the calculations and the data at low x_γ^{OBS} and low E_T^{jet} is due to the calculations not including MI.

The NLO calculations include all $2 \to 2$ and $2 \to 3$ LO and NLO diagrams, and use parameterisations of the parton distributions of the proton and photon which use the DGLAP evolution equations. The general agreement between the measured and calculated cross sections shows that we have a good understanding of the photoproduction of jets, and that the current models for the structure of the photon are reasonable. It also means that, in the areas where the agreement between this measurement and the calculations is good, this data could be used together with other measurments, such as F_2^γ or F_2^p, to constrain the parton distributions in the photon and proton.

The uncertainty on the cross sections measured in this analysis is dominated by the systematic errors, particularly those associated with the energy scale of the calorimeter. Therefore a more precise measurement is only possible with a much improved Monte Carlo simulation, and a significant reduction in this uncertainty in the calorimeter calibration. An enlargement in the size of the data sample could be used to measure cross sections with even higher jet transverse energies. The reason for doing this would be to reduce the influence of non perturbative effects such as hadronisation, and to become less sensitive to the exact jet definition. However, as has already been pointed out, raising the E_T^{jet} threshold limits the sensitivity of the cross section to the structure of the proton and photon at low values of x_γ and x_p.

Appendix A

Extraction of the EUCELL and PUCELL Cross Sections

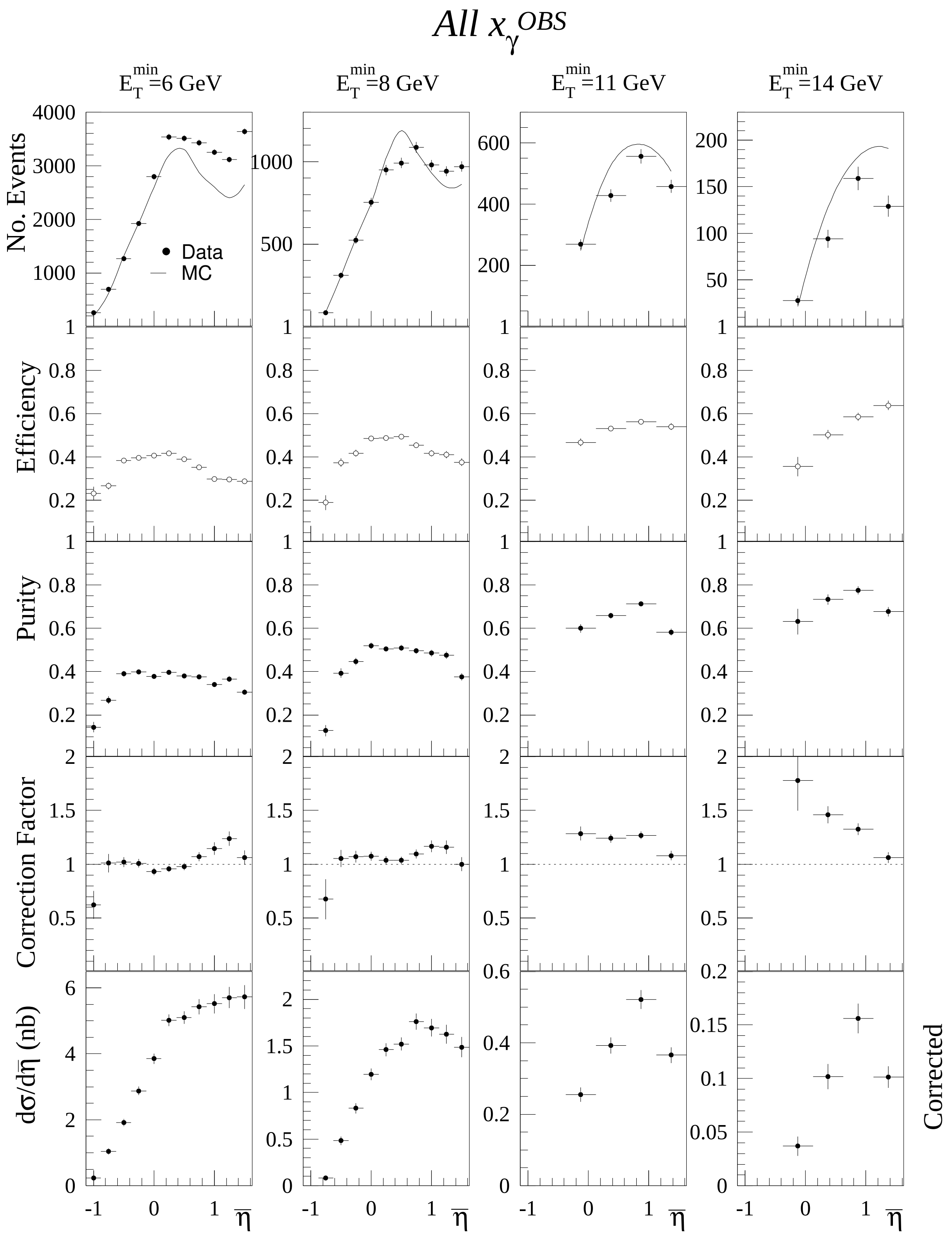

Figure A.1: *The unfolding of the cross sections for EUCELL with HERWIG, for the complete x_γ^{OBS} range*

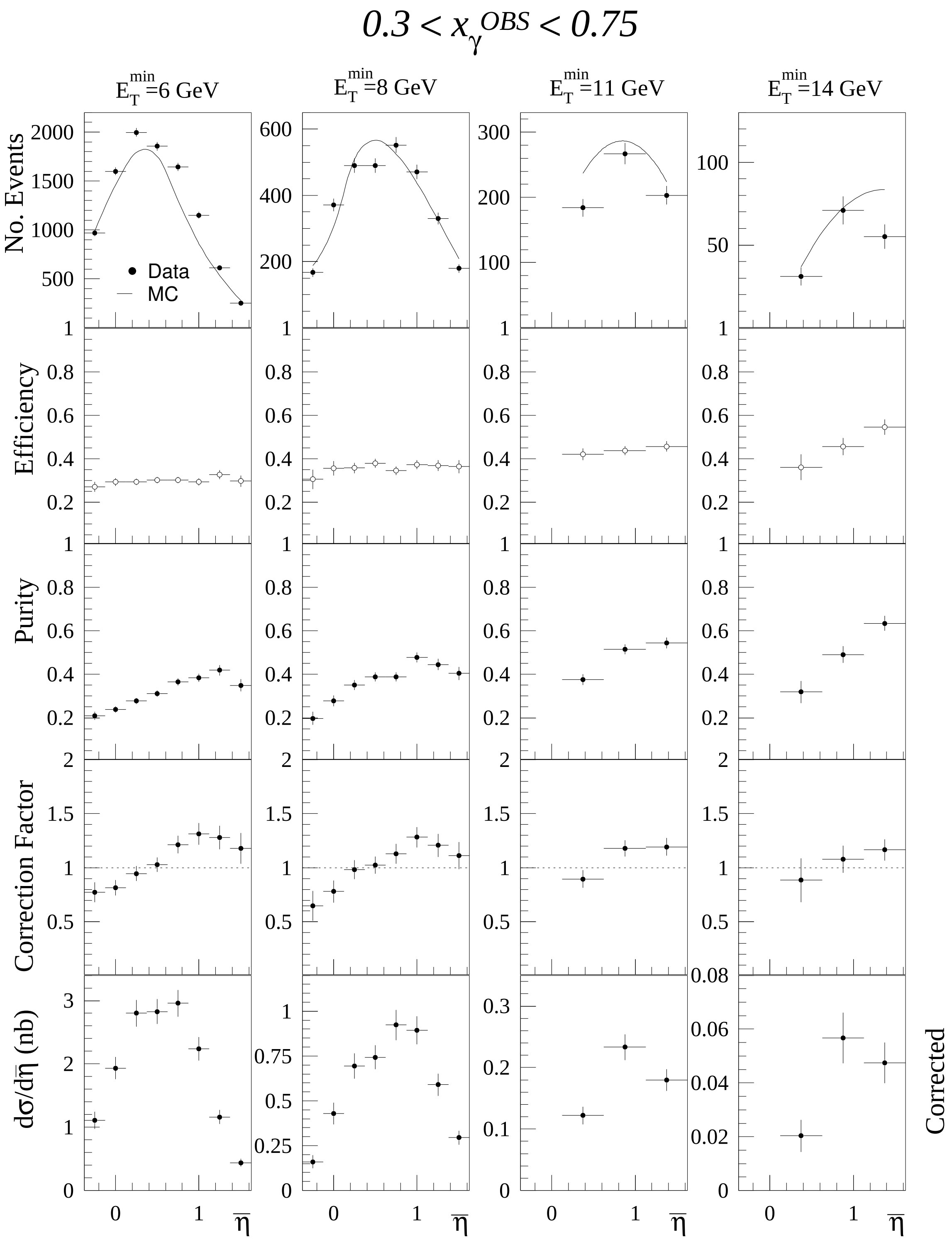

Figure A.2: *The unfolding of the cross sections for EUCELL with HERWIG, for resolved events.* $0.3 < x_\gamma^{OBS} < 0.75$

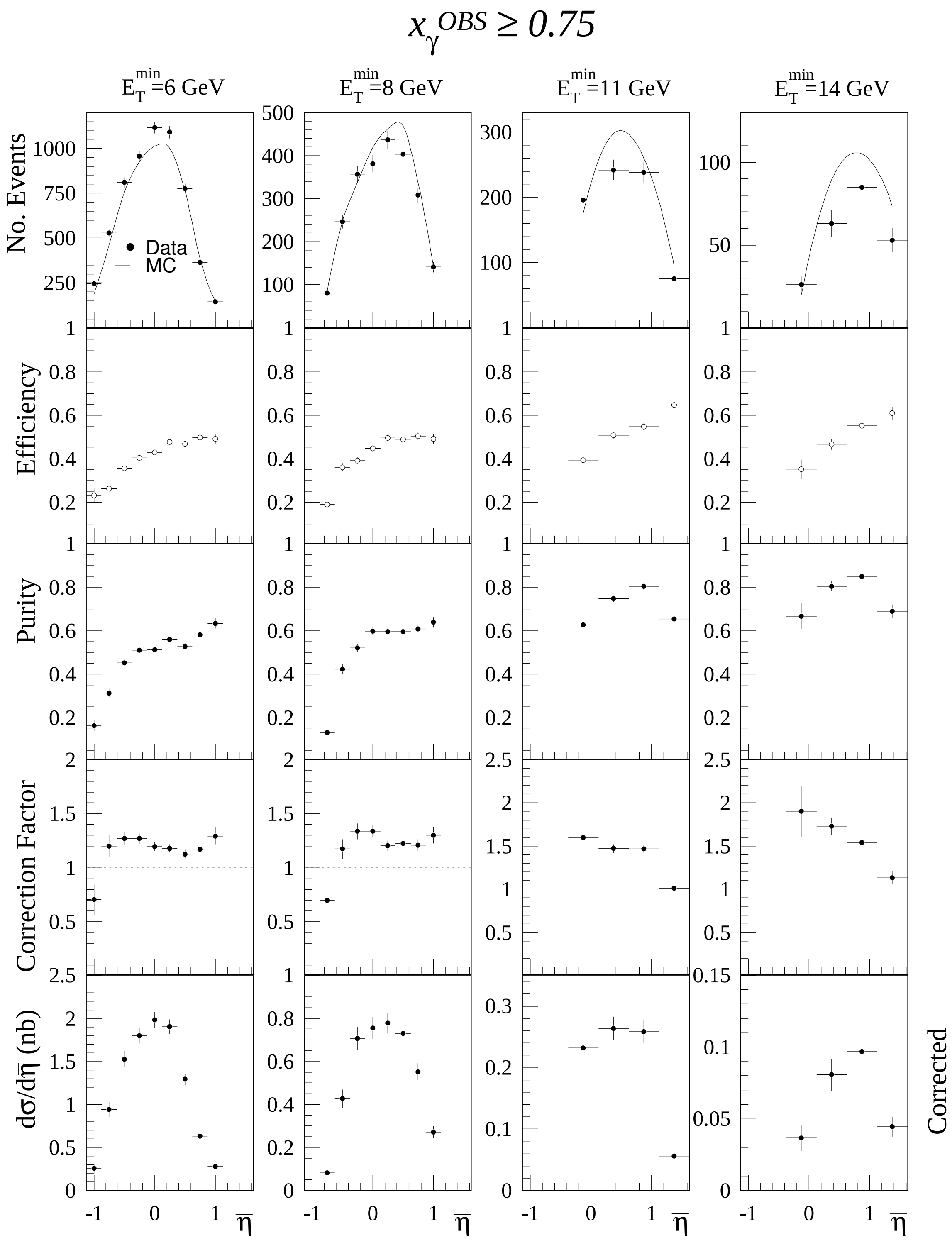

Figure A.3: *The unfolding of the cross sections for EUCELL with HERWIG, for direct events.* $x_\gamma^{OBS} \geq 0.75$

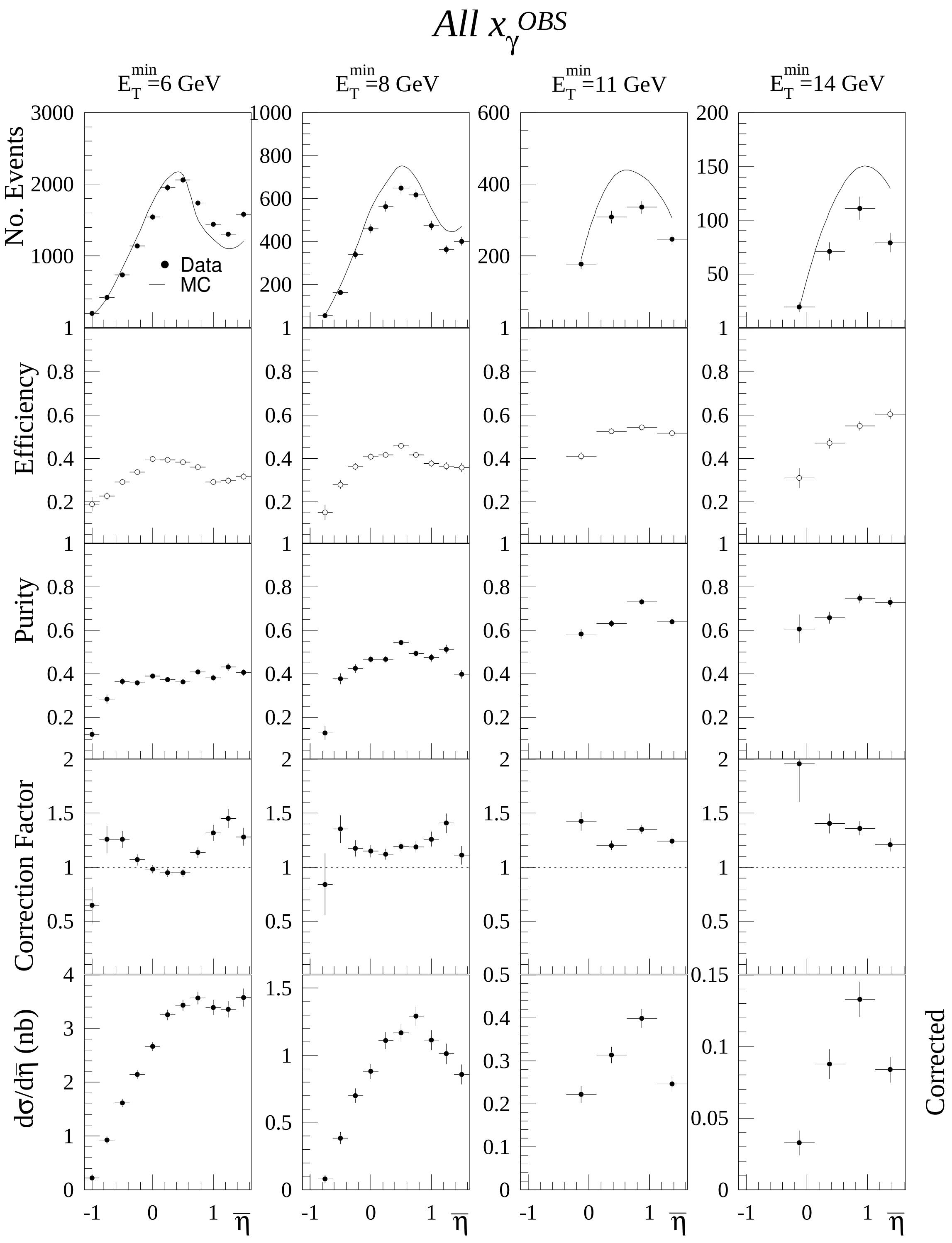

Figure A.4: *The unfolding of the cross sections for PUCELL with HERWIG, for the complete x_γ^{OBS} range*

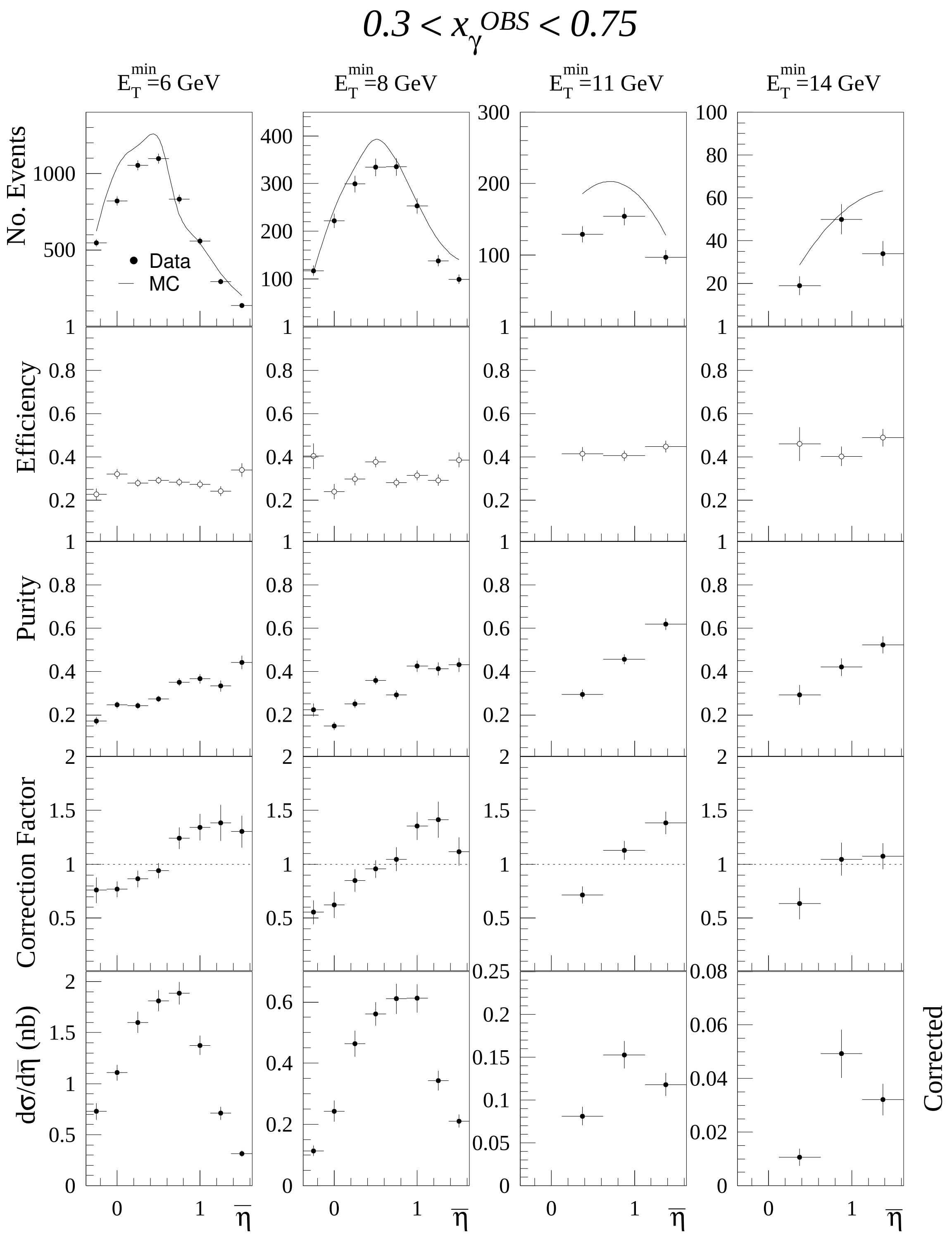

Figure A.5: *The unfolding of the cross sections for PUCELL with HERWIG, for resolved events.* $0.3 < x_\gamma^{OBS} < 0.75$

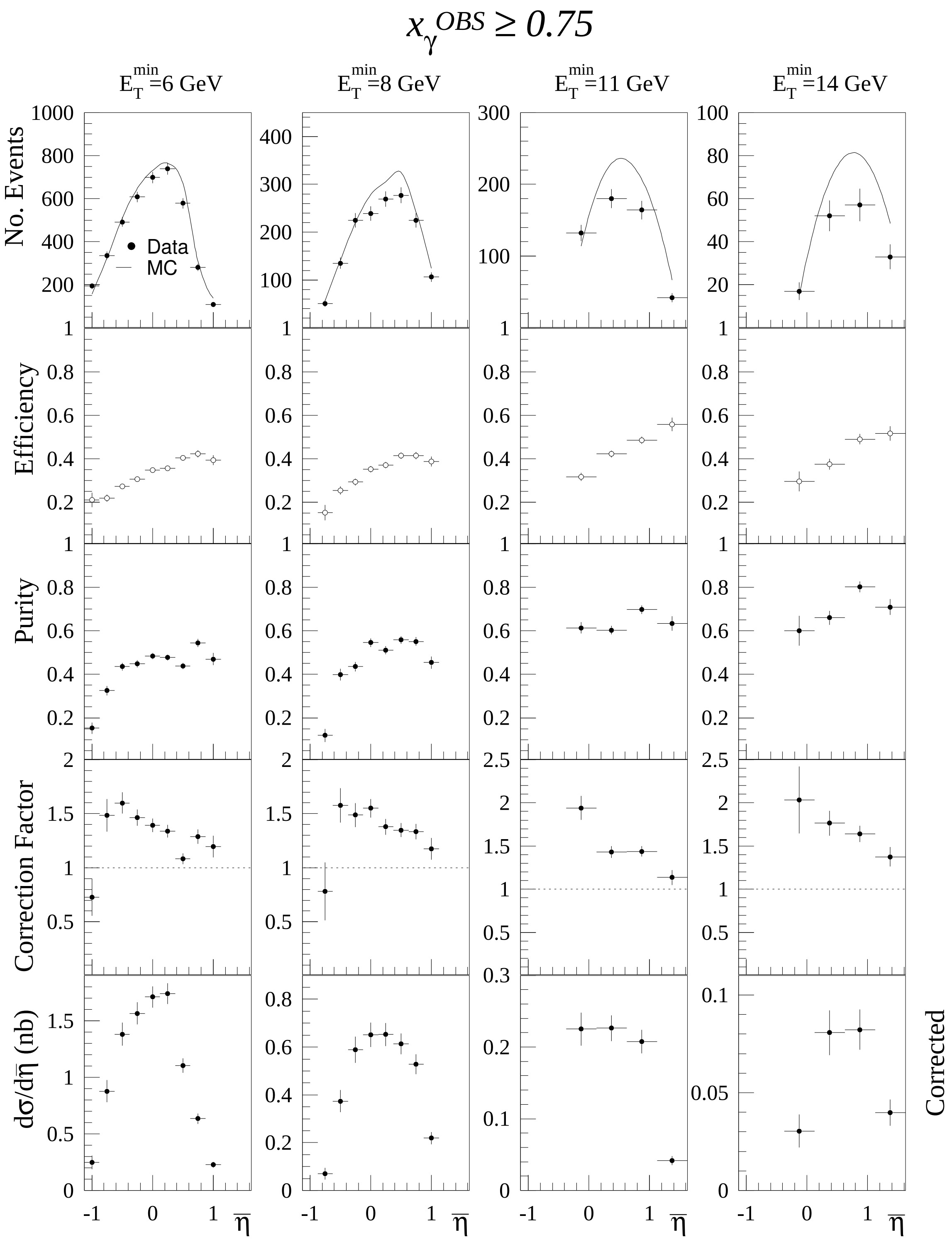

Figure A.6: *The unfolding of the cross sections for PUCELL with HERWIG, for direct events.* $x_\gamma^{OBS} \geq 0.75$

Appendix B

Tables of Results

$\bar{\eta}$	$\frac{d\sigma}{d\bar{\eta}}$ [nb]	stat. [nb]	syst. [nb]	corrl. syst. [nb]		DIS [%]
$E_T^{min} > 6$ GeV						
-1.000	0.21	0.05	0.06	+ 0.02	-0.04	15
-0.750	0.76	0.08	0.14	+ 0.09	-0.11	10
-0.500	1.43	0.09	0.14	+ 0.16	-0.21	5
-0.250	1.88	0.09	0.21	+ 0.26	-0.29	2
0.000	2.31	0.10	0.35	+ 0.34	-0.36	3
0.250	2.91	0.11	0.45	+ 0.45	-0.42	1
0.500	2.94	0.12	0.40	+ 0.48	-0.54	1
0.750	2.93	0.14	0.40	+ 0.54	-0.50	1
1.000	2.80	0.16	0.38	+ 0.46	-0.53	1
1.250	2.87	0.19	0.36	+ 0.49	-0.56	1
1.500	2.70	0.17	0.54	+ 0.47	-0.55	0
$E_T^{min} > 8$ GeV						
-0.750	0.06	0.02	0.02	+ 0.01	-0.01	9
-0.500	0.37	0.04	0.05	+ 0.04	-0.06	7
-0.250	0.64	0.05	0.12	+ 0.07	-0.09	4
0.000	0.82	0.05	0.04	+ 0.10	-0.15	1
0.250	0.99	0.05	0.15	+ 0.12	-0.18	2
0.500	1.09	0.06	0.18	+ 0.12	-0.20	1
0.750	1.13	0.06	0.17	+ 0.13	-0.16	1
1.000	0.99	0.07	0.14	+ 0.14	-0.18	1
1.250	0.81	0.06	0.15	+ 0.11	-0.18	1
1.500	0.69	0.06	0.07	+ 0.11	-0.13	1
$E_T^{min} > 11$ GeV						
-0.125	0.21	0.02	0.01	+ 0.02	-0.03	1
0.375	0.30	0.02	0.02	+ 0.04	-0.05	1
0.875	0.37	0.02	0.05	+ 0.07	-0.07	1
1.375	0.22	0.02	0.02	+ 0.03	-0.04	1
$E_T^{min} > 15$ GeV						
-0.125	0.033	0.009	0.005	+ 0.013	-0.009	0
0.375	0.094	0.012	0.010	+ 0.012	-0.020	0
0.875	0.127	0.013	0.013	+ 0.005	-0.025	0
1.375	0.080	0.009	0.011	+ 0.014	-0.015	3

Table B.1: *The cross sections for KTCLUS for the whole x_γ^{OBS} range.*

$\bar{\eta}$	$\frac{d\sigma}{d\bar{\eta}}$ [nb]	stat. [nb]	syst. [nb]	corrl. syst. [nb]		DIS [%]
$E_T^{min} > 6$ GeV						
-1.000	0.21	0.05	0.04	+ 0.03	-0.03	10
-0.750	0.66	0.07	0.14	+ 0.09	-0.10	6
-0.500	1.13	0.08	0.16	+ 0.14	-0.21	0
-0.250	1.33	0.07	0.10	+ 0.23	-0.20	0
0.000	1.47	0.08	0.19	+ 0.23	-0.24	0
0.250	1.47	0.07	0.15	+ 0.19	-0.24	0
0.500	1.07	0.06	0.16	+ 0.13	-0.19	0
0.750	0.49	0.04	0.08	+ 0.06	-0.05	0
1.000	0.23	0.03	0.04	+ 0.02	-0.03	0
$E_T^{min} > 8$ GeV						
-0.750	0.06	0.02	0.02	+ 0.01	-0.01	6
-0.500	0.34	0.04	0.04	+ 0.06	-0.07	1
-0.250	0.56	0.05	0.07	+ 0.11	-0.10	0
0.000	0.58	0.04	0.08	+ 0.10	-0.11	0
0.250	0.62	0.04	0.05	+ 0.12	-0.12	0
0.500	0.62	0.04	0.07	+ 0.12	-0.14	0
0.750	0.43	0.03	0.05	+ 0.06	-0.05	0
1.000	0.22	0.03	0.04	+ 0.01	-0.03	0
$E_T^{min} > 11$ GeV						
-0.125	0.19	0.02	0.02	+ 0.03	-0.03	0
0.375	0.22	0.02	0.01	+ 0.04	-0.05	0
0.875	0.20	0.02	0.03	+ 0.04	-0.03	0
1.375	0.04	0.01	0.01	+ 0.00	-0.01	5
$E_T^{min} > 15$ GeV						
-0.125	0.034	0.009	0.006	+ 0.012	-0.012	0
0.375	0.082	0.011	0.015	+ 0.008	-0.024	0
0.875	0.078	0.010	0.010	+ 0.008	-0.014	0
1.375	0.036	0.007	0.009	+ 0.009	-0.006	8

Table B.2: *The cross sections for KTCLUS for 0.75* $\leq x_\gamma^{OBS}$

$\bar{\eta}$	$\frac{d\sigma}{d\bar{\eta}}$ [nb]	stat. [nb]	syst. [nb]	corrl. syst. [nb]		DIS [%]
$E_T^{min} > 6$ GeV						
-0.250	0.54	0.08	0.12	+ 0.06	-0.09	5
0.000	0.89	0.09	0.13	+ 0.11	-0.13	4
0.250	1.35	0.11	0.22	+ 0.15	-0.16	2
0.500	1.46	0.11	0.29	+ 0.17	-0.27	1
0.750	1.48	0.12	0.25	+ 0.22	-0.26	1
1.000	1.16	0.11	0.13	+ 0.15	-0.18	0
1.250	0.58	0.06	0.14	+ 0.08	-0.11	0
1.500	0.26	0.03	0.06	+ 0.00	-0.05	0
$E_T^{min} > 8$ GeV						
-0.250	0.08	0.02	0.02	+ 0.01	0.00	8
0.000	0.24	0.04	0.03	+ 0.02	-0.04	3
0.250	0.37	0.04	0.05	+ 0.05	-0.06	3
0.500	0.46	0.05	0.07	+ 0.07	-0.07	2
0.750	0.57	0.06	0.10	+ 0.06	-0.08	2
1.000	0.56	0.07	0.11	+ 0.08	-0.09	0
1.250	0.32	0.04	0.08	+ 0.05	-0.07	0
1.500	0.22	0.03	0.05	+ 0.02	-0.03	0
$E_T^{min} > 11$ GeV						
0.375	0.08	0.01	0.01	+ 0.01	-0.01	2
0.875	0.16	0.02	0.03	+ 0.03	-0.03	2
1.375	0.12	0.01	0.02	+ 0.01	-0.02	0
$E_T^{min} > 15$ GeV						
0.375	0.014	0.004	0.004	+ 0.003	0.001	0
0.875	0.047	0.008	0.012	+ 0.001	-0.010	0
1.375	0.032	0.006	0.006	+ 0.002	-0.005	0

Table B.3: *The cross sections for KTCLUS for* $0.3 \leq x_\gamma^{OBS} \leq 0.75$.

$\bar{\eta}$	$\frac{d\sigma}{d\bar{\eta}}$ [nb]	stat. [nb]	syst. [nb]	corrl. syst. [nb]		DIS [%]
$E_T^{min} > 6$ GeV						
-1.000	0.24	0.05	0.07	+ 0.05	-0.04	14
-0.750	1.04	0.10	0.27	+ 0.13	-0.20	9
-0.500	1.91	0.10	0.16	+ 0.26	-0.30	5
-0.250	2.88	0.13	0.31	+ 0.44	-0.49	2
0.000	3.85	0.15	0.49	+ 0.58	-0.67	2
0.250	5.02	0.18	0.54	+ 0.78	-0.87	1
0.500	5.10	0.19	0.96	+ 0.64	-0.93	1
0.750	5.43	0.24	1.00	+ 0.84	-1.00	1
1.000	5.52	0.29	0.88	+ 0.77	-1.08	1
1.250	5.71	0.32	0.78	+ 0.95	-1.10	1
1.500	5.72	0.36	0.72	+ 0.93	-1.12	0
$E_T^{min} > 8$ GeV						
-0.750	0.08	0.02	0.03	+ 0.02	-0.02	6
-0.500	0.48	0.05	0.08	+ 0.07	-0.10	9
-0.250	0.83	0.06	0.07	+ 0.13	-0.15	4
0.000	1.19	0.06	0.11	+ 0.19	-0.22	2
0.250	1.46	0.07	0.23	+ 0.25	-0.29	1
0.500	1.52	0.07	0.18	+ 0.26	-0.34	1
0.750	1.76	0.09	0.14	+ 0.34	-0.32	1
1.000	1.69	0.10	0.37	+ 0.31	-0.37	1
1.250	1.63	0.10	0.15	+ 0.26	-0.33	0
1.500	1.49	0.11	0.11	+ 0.28	-0.31	1
$E_T^{min} > 11$ GeV						
-0.125	0.26	0.02	0.02	+ 0.04	-0.04	1
0.375	0.39	0.02	0.03	+ 0.06	-0.07	3
0.875	0.52	0.03	0.05	+ 0.10	-0.09	0
1.375	0.37	0.02	0.04	+ 0.07	-0.08	1
$E_T^{min} > 15$ GeV						
-0.125	0.037	0.009	0.007	+ 0.016	-0.004	0
0.375	0.102	0.012	0.008	+ 0.018	-0.021	0
0.875	0.156	0.014	0.015	+ 0.025	-0.027	0
1.375	0.102	0.010	0.012	+ 0.014	-0.015	2

Table B.4: *The cross sections for EUCELL for the whole x_γ^{OBS} range*

$\bar{\eta}$	$\frac{d\sigma}{d\bar{\eta}}$ [nb]	stat. [nb]	syst. [nb]	corrl. syst. [nb]		DIS [%]
$E_T^{min} > 6$ GeV						
-1.000	0.26	0.05	0.07	+ 0.04	-0.05	12
-0.750	0.94	0.09	0.24	+ 0.15	-0.20	6
-0.500	1.53	0.09	0.19	+ 0.19	-0.29	1
-0.250	1.80	0.09	0.10	+ 0.24	-0.30	0
0.000	1.98	0.09	0.27	+ 0.25	-0.35	0
0.250	1.90	0.08	0.16	+ 0.19	-0.32	0
0.500	1.29	0.07	0.25	+ 0.16	-0.23	0
0.750	0.63	0.04	0.12	+ 0.07	-0.10	0
1.000	0.28	0.03	0.08	+ 0.02	-0.04	0
$E_T^{min} > 8$ GeV						
-0.750	0.08	0.02	0.03	+ 0.02	-0.02	3
-0.500	0.43	0.04	0.07	+ 0.08	-0.10	2
-0.250	0.71	0.05	0.05	+ 0.10	-0.13	1
0.000	0.75	0.05	0.16	+ 0.16	-0.16	0
0.250	0.78	0.05	0.08	+ 0.14	-0.18	0
0.500	0.73	0.05	0.13	+ 0.10	-0.18	0
0.750	0.55	0.04	0.09	+ 0.06	-0.09	0
1.000	0.27	0.03	0.06	+ 0.02	-0.04	0
$E_T^{min} > 11$ GeV						
-0.125	0.23	0.02	0.04	+ 0.04	-0.05	0
0.375	0.26	0.02	0.02	+ 0.05	-0.05	0
0.875	0.26	0.02	0.04	+ 0.05	-0.05	0
1.375	0.06	0.01	0.01	+ 0.00	-0.01	4
$E_T^{min} > 15$ GeV						
-0.125	0.037	0.009	0.006	+ 0.017	-0.008	0
0.375	0.081	0.011	0.010	+ 0.021	-0.017	0
0.875	0.097	0.011	0.006	+ 0.017	-0.018	0
1.375	0.045	0.007	0.008	+ 0.008	-0.009	5

Table B.5: *The cross sections for EUCELL for $0.75 \leq x_\gamma^{OBS}$.*

$\bar{\eta}$	$\frac{d\sigma}{d\bar{\eta}}$ [nb]	stat. [nb]	syst. [nb]	corrl. syst. [nb]		DIS [%]
$E_T^{min} > 6$ GeV						
-0.250	1.11	0.14	0.23	+ 0.18	-0.20	4
0.000	1.93	0.18	0.44	+ 0.27	-0.33	2
0.250	2.80	0.21	0.26	+ 0.41	-0.45	1
0.500	2.83	0.20	0.52	+ 0.34	-0.50	1
0.750	2.96	0.21	0.69	+ 0.36	-0.50	1
1.000	2.24	0.18	0.41	+ 0.31	-0.43	0
1.250	1.16	0.11	0.21	+ 0.17	-0.20	0
1.500	0.44	0.06	0.13	+ 0.07	-0.10	0
$E_T^{min} > 8$ GeV						
-0.250	0.16	0.04	0.04	+ 0.02	-0.03	10
0.000	0.43	0.06	0.16	+ 0.05	-0.07	4
0.250	0.69	0.07	0.14	+ 0.11	-0.12	2
0.500	0.74	0.07	0.18	+ 0.10	-0.13	2
0.750	0.92	0.08	0.14	+ 0.14	-0.16	1
1.000	0.89	0.08	0.19	+ 0.16	-0.17	0
1.250	0.59	0.06	0.09	+ 0.08	-0.11	0
1.500	0.29	0.04	0.06	+ 0.05	-0.05	0
$E_T^{min} > 11$ GeV						
0.375	0.12	0.01	0.03	+ 0.02	-0.02	6
0.875	0.23	0.02	0.04	+ 0.04	-0.04	1
1.375	0.18	0.02	0.02	+ 0.03	-0.04	0
$E_T^{min} > 15$ GeV						
0.375	0.020	0.006	0.005	+-0.001	-0.004	0
0.875	0.057	0.009	0.020	+ 0.005	-0.010	0
1.375	0.047	0.008	0.004	+ 0.002	-0.003	0

Table B.6: *The cross sections for EUCELL for $0.3 \leq x_\gamma^{OBS} \leq 0.75$.*

$\bar{\eta}$	$\frac{d\sigma}{d\bar{\eta}}$ [nb]	stat. [nb]	syst. [nb]	corrl. syst. [nb]		DIS [%]
$E_T^{min} > 6$ GeV						
-1.000	0.22	0.04	0.06	+ 0.03	-0.04	15
-0.750	0.93	0.07	0.17	+ 0.08	-0.13	10
-0.500	1.62	0.08	0.16	+ 0.18	-0.24	5
-0.250	2.15	0.08	0.24	+ 0.24	-0.33	2
0.000	2.67	0.08	0.41	+ 0.30	-0.41	3
0.250	3.25	0.09	0.50	+ 0.44	-0.47	1
0.500	3.43	0.10	0.47	+ 0.45	-0.63	1
0.750	3.57	0.12	0.49	+ 0.54	-0.61	1
1.000	3.39	0.14	0.46	+ 0.55	-0.64	1
1.250	3.36	0.15	0.42	+ 0.59	-0.66	1
1.500	3.58	0.17	0.71	+ 0.70	-0.73	0
$E_T^{min} > 8$ GeV						
-0.750	0.08	0.03	0.02	+ 0.01	-0.01	9
-0.500	0.39	0.04	0.05	+ 0.07	-0.07	7
-0.250	0.70	0.05	0.13	+ 0.09	-0.10	4
0.000	0.88	0.06	0.04	+ 0.11	-0.16	1
0.250	1.11	0.06	0.16	+ 0.16	-0.20	2
0.500	1.17	0.06	0.20	+ 0.16	-0.22	1
0.750	1.29	0.07	0.20	+ 0.16	-0.18	1
1.000	1.11	0.07	0.16	+ 0.16	-0.20	1
1.250	1.01	0.08	0.18	+ 0.14	-0.22	1
1.500	0.86	0.07	0.09	+ 0.20	-0.16	1
$E_T^{min} > 11$ GeV						
-0.125	0.22	0.02	0.02	+ 0.03	-0.03	1
0.375	0.31	0.02	0.02	+ 0.04	-0.05	1
0.875	0.40	0.02	0.06	+ 0.08	-0.07	1
1.375	0.25	0.02	0.02	+ 0.03	-0.05	1
$E_T^{min} > 15$ GeV						
-0.125	0.033	0.009	0.005	+ 0.011	-0.008	0
0.375	0.088	0.010	0.009	+ 0.011	-0.019	0
0.875	0.133	0.012	0.013	+ 0.005	-0.026	0
1.375	0.084	0.009	0.011	+ 0.010	-0.016	3

Table B.7: *The cross sections for PUCELL for the whole x_γ^{OBS} range.*

$\bar{\eta}$	$\frac{d\sigma}{d\bar{\eta}}$ [nb]	stat. [nb]	syst. [nb]	corrl. syst. [nb]		DIS [%]
$E_T^{min} > 6$ GeV						
-1.000	0.25	0.06	0.05	+ 0.03	-0.04	10
-0.750	0.88	0.10	0.18	+ 0.10	-0.14	6
-0.500	1.38	0.10	0.19	+ 0.14	-0.26	0
-0.250	1.56	0.10	0.11	+ 0.18	-0.24	0
0.000	1.71	0.09	0.22	+ 0.20	-0.28	0
0.250	1.74	0.09	0.18	+ 0.20	-0.28	0
0.500	1.10	0.06	0.16	+ 0.10	-0.20	0
0.750	0.63	0.05	0.11	+ 0.08	-0.06	0
1.000	0.23	0.03	0.04	+ 0.02	-0.03	0
$E_T^{min} > 8$ GeV						
-0.750	0.07	0.03	0.02	+ 0.02	-0.01	6
-0.500	0.37	0.05	0.05	+ 0.07	-0.08	1
-0.250	0.59	0.06	0.07	+ 0.07	-0.11	0
0.000	0.65	0.05	0.09	+ 0.12	-0.13	0
0.250	0.65	0.05	0.05	+ 0.12	-0.13	0
0.500	0.61	0.04	0.07	+ 0.10	-0.14	0
0.750	0.53	0.04	0.06	+ 0.07	-0.06	0
1.000	0.22	0.03	0.04	+ 0.01	-0.03	0
$E_T^{min} > 11$ GeV						
-0.125	0.23	0.02	0.02	+ 0.04	-0.03	0
0.375	0.23	0.02	0.01	+ 0.04	-0.05	0
0.875	0.21	0.02	0.03	+ 0.05	-0.04	0
1.375	0.04	0.01	0.01	+ 0.00	-0.01	5
$E_T^{min} > 15$ GeV						
-0.125	0.030	0.008	0.005	+ 0.011	-0.011	0
0.375	0.081	0.012	0.015	+ 0.008	-0.024	0
0.875	0.082	0.010	0.010	+ 0.008	-0.015	0
1.375	0.040	0.007	0.009	+ 0.009	-0.007	8

Table B.8: *The cross sections for PUCELL for $0.75 \leq x_\gamma^{OBS}$.*

$\bar{\eta}$	$\frac{d\sigma}{d\bar{\eta}}$ [nb]	stat. [nb]	syst. [nb]	corrl. syst. [nb]		DIS [%]
$E_T^{min} > 6$ GeV						
-0.250	0.73	0.08	0.17	+ 0.08	-0.12	5
0.000	1.11	0.08	0.16	+ 0.12	-0.16	4
0.250	1.60	0.10	0.27	+ 0.21	-0.19	2
0.500	1.81	0.10	0.36	+ 0.25	-0.33	1
0.750	1.89	0.11	0.32	+ 0.28	-0.33	1
1.000	1.37	0.09	0.15	+ 0.18	-0.21	0
1.250	0.71	0.07	0.17	+ 0.10	-0.14	0
1.500	0.31	0.03	0.08	+ 0.04	-0.06	0
$E_T^{min} > 8$ GeV						
-0.250	0.11	0.02	0.03	+ 0.02	0.00	8
0.000	0.24	0.03	0.03	+ 0.01	-0.04	3
0.250	0.46	0.04	0.06	+ 0.05	-0.07	3
0.500	0.56	0.04	0.08	+ 0.08	-0.08	2
0.750	0.61	0.05	0.10	+ 0.06	-0.09	2
1.000	0.61	0.05	0.12	+ 0.09	-0.10	0
1.250	0.34	0.03	0.08	+ 0.04	-0.07	0
1.500	0.21	0.02	0.05	+ 0.02	-0.03	0
$E_T^{min} > 11$ GeV						
0.375	0.08	0.01	0.01	+ 0.01	-0.01	2
0.875	0.15	0.02	0.03	+ 0.03	-0.03	2
1.375	0.12	0.01	0.02	+ 0.01	-0.02	0
$E_T^{min} > 15$ GeV						
0.375	0.011	0.003	0.003	+ 0.002	0.001	0
0.875	0.049	0.009	0.013	+-0.002	-0.011	0
1.375	0.032	0.006	0.005	+ 0.002	-0.005	0

Table B.9: *The cross sections for PUCELL for $0.3 \leq x_\gamma^{OBS} \leq 0.75$.*

Bibliography

[1] ZEUS Collab., “ZEUS, A detector for HERA”, PRC 87-02, September 1987

[2] K. Piotrzkowski, M. Zachara,
“Determination of the ZEUS Luminosity in ’93” ZEUS-Note 94-167.

[3] K. Piotrzkowski and M. Zachara,
“Determination of the ZEUS Luminosity in 1994”, ZEUS-Note 95-138.

[4] ZEUS Collab., Uwe Holm edt.,
“ZEUS - A detector for HERA. Status report 1993”

[5] N. Harnew et al., “The Technique of z Coordinate Determination using a Time Difference Measurement for the ZEUS Central Tracking Detector”, ZEUS-Note 89-038.

[6] N. Dyce, K. Long, J. Shulman,
“The CTD Reconstruction Program User’s Guide”, ZEUS-Note 94-011.

[7] T. Tymieniecka, “On Neutrons in Uranium- Scintillator Calorimeters”, DESY 91-012.

[8] J. del Peso and E. Ros, “Fast Simulation of Electromagnetic Showers in the ZEUS Calorimeter”, DESY 91-005.

[9] Marc de Kamps, “Changes and extensions of the calorimeter reconstruction programme” ZEUS-Note 94-014.

[10] The ZEUS Calorimeter Group, "Response of a Uranium-Scintillator Calorimeter to Electrons, Pions and Protons in the Momentum Range 0.5-10 GeV/c", DESY 89-149.

[11] U. Behrens et al., "Calibration of the Forward and Rear ZEUS Calorimeter using Cosmic Ray Muons.", DESY 93-121.

[12] The ZEUS Calorimeter Group, "Test of the ZEUS Forward Calorimeter Prototype", DESY 89-128.

[13] The ZEUS Luminosity Group,
"First Measurements of HERA Luminosity by ZEUS Lumi Monitor", DESY 92-066.

[14] The ZEUS Data Acquisition Group, "ZEUS Contributions to the Real-Time 93 Conference", Vancouver, Canada. DESY 93-091.

[15] R. Brun, " ZEBRA - Reference Manual", Program Library Q100/Q101, CERN 1991.

[16] S. Fisher & P. Palazzi, The ADAMO data system, RAL (1990)

[17] ZEUS Collab., M. Derrick et al., *Phys. Rev. Lett.* **75** (1995) 1006-1011.

[18] H1 Collab., S. Aid et al., *Phys. Lett.* B **397** (1996) 319.

[19] R. P. Feynman, *Phys. Rev. Lett.* **23** (1969) 1415

[20] M. Gell-Mann, Phys. Lett. **8** (1964) 214
G. Zweig, CERN-8192/TH 401 (1964)
G. Zweig, CERN-8419/TH 412 (1964).

[21] B. R. Martin, G. Shaw, "Particle Physics", Wiley 1992.

[22] R.K. Ellis, W. J. Stirling, B. R. Webber,
'QCD and Collider Physics', Cambridge, (1996)

[23] C.G. Callan, D. Gross, *Phys. Rev. Lett.* **23** (1969) 1957

[24] A. Bodek et al., *Phys. Rev.* D **20** (1979) 1471

[25] JD. Bjorken, *Phys. Rev.* B **179** (1969) 1547

[26] D.H. Perkins, "Introduction to High energy Physics", Addison Wesley, (1987).

[27] R. Brandelik et al., *Phys. Lett.* B **97** (1980) 453
S.-L. Wu, Phys. Rep. **107** (1984) 59.

[28] ZEUS-F_2(1992), Zeus Collab., M.Derrick et al. *Phys. Lett.* B **316** (1993) 412
H1-F_2 (1992), H1 Collab., I Abt et al., *Nucl. Phys.* B **407** (1993) 515.

[29] V. Gribov, E. M. Levin, M. G. Ryskin, Phys.Rep. **100** (1983) 1.

[30] G. Altarelli, G. Parisi, *Nucl. Phys.* B **126** (1977) 298

[31] Y. Balitzki, L. N. Lipatov, Sov.J.Nucl.Phys. **28** (1978) 822
E. A. Kuraev, L. N. Lipatov, V. S. Fadin, Sov. Phys. JETP **44** (1976) 443, Sov. Phys. JETP **45** (1977) 199.

[32] A. De Rújula et al., *Phys. Rev.* D **10** (1974) 1649

[33] V. Gribov, L.N. Lipatov, Sov. J. Nucl. Phys **15** (1972) 438
Y.L. Dokshitzer, Sov. Phys. JETP **46** (1977) 641.

[34] L.N. Hand, *Phys. Lett.* B **129** (1963) 1834
S.D Drell, J.D. Walecka, Ann. Phys. (NY), **28** (1964) 18
F.J. Gilman, *Phys. Rev.* B **4** (1972) 123

[35] B. Burow, "A Measurement of the Total Photon-Proton Cross section in the centre of mass range 167 to 194 GeV" DESY F35D-94-01.

[36] C.F. Weizsäcker, Z. Phys. **88** (1934) 612
E.J. Williams, Proc. Roy. Soc. London A bf 139 (1933) 163
E.J. Williams, Phys. Rev. **45**, (1934) 729
For a recent treatment for HERA experiments see S. Frixone, M.L. Mangano, P.Nason, G.Ridolfi, *Phys. Lett.* B **319** (1993) 339.

[37] G.A. Schuler, T. Sjöstrand, 'The hadronic Properties of the photon in γ p interactions', CERN-TH 6718/92 (1992).
G.A. Schuler, T. Sjöstrand, 'Towards a Complete Description of High-Energy Photoproduction', CERN-TH 6796/93 (1993).

[38] E. Witten, *Nucl. Phys.* B **120** (1977) 189.

[39] J.J. Sakurai and D. Schildknecht, *Phys. Lett.* B **41** (1972) 489

[40] L. Feld, Ph.D. thesis BONN-IR-96-17, Bonn University, December 1996.

[41] ZEUS Collab., M. Derrick et al., 'Study of the Photon Remnant in Resolved Photoproduction at HERA', *Phys. Lett.* B **354** (163-177) 1995.

[42] V. Del Duca, "An Introduction to the Perturbative QCD Pomeron and to Jet Physics at Large Rapidities" DESY 95-023.

[43] M. Drees, F. Halzen, *Phys. Rev. Lett.* **61** (1988) 275
M. Drees, R.M. Godbole, *Phys. Rev.* D **39** (1989) 169

[44] T. Tymieniecka, A. F. Zarnecki, DESY 92-137.

[45] ZEUS Collab., M. Derrick et al., *Phys. Lett.* B **384** (1996) 401

[46] M. Klasen and G. Kramer, *Z. Phys.* C **72** (1996) 107-122
M. Klasen and G. Kramer, *Z. Phys.* C **76** (1997) 67-74.

[47] H. Baer, J. Ohnemus, and J. F. Owens, *Phys. Rev.* D **40** (1989) 2844
B. W. Harris, J. F. Owens, 'Photoproduction of Jets at NLO', To appear in proceedings of the 1996 Meeting of the American Physical Society, Division of Particles and Fields (DPF 96), Minneapolis, Minnesota, 10-15 Aug 1996,
B. W. Harris, J. F. Owens, *Phys. Rev.* D **56** (1997) 4007-4016.

[48] P. Aurenche, L. Bourhis, M. Fontannaz, J. Ph. Guillet, 'Dijet cross section in photoproduction at HERA', Proceedings of the HERA Workshops 95/96.

[49] H. Abramowicz, K. Charchula, M. Krawczyk, A. Levy, U. Maor, Int. J. Mod. Phys. A **8** (1993) 1005

[50] M. Drees, K. Grassie, *Z. Phys.* C **28** (1985) 451.

[51] H. Abramowicz, K. Charcula, A. Levy, DESY Report 91-069 (1991)
H. Abramowicz, K. Charcula, A. Levy, *Phys. Lett.* B **269** (1991) 456

[52] L. E. Gordon, J. K. Storrow, *Z. Phys.* C **56** (1992) 307.
L. E. Gordon, J. K. Storrow, *Phys. Lett.* B **291** (1992) 320

[53] M. Glück, E. Reya, A. Vogt, *Phys. Rev.* D **46** (1992) 1973.
M. Glück, E. Reya, A. Vogt, *Phys. Rev.* D **45** (1992) 3986

[54] ZEUS Collab., 'Dijet Cross Sections in Photoproduction at HERA', *Phys. Lett.* B **348** (1995) 665-680.
J.M. Butterworth, R.G. Feild, L.Feld, L. Sinclair ZEUS-Note 95-010

[55] H1 Collab., T. Ahmed et al., 'Single Inclusive Parton Cross Sections in photoproduction and the Photon structure', *Nucl. Phys.* B **445** (1995) 195.

[56] J.R. Forshaw, R.G. Roberts, *Phys. Lett.* B **319** (1993) 539.

[57] M. Drees, R.M. Godbole, 'Measuring the parton content of the photon at the DESY ep collider HERA', *Phys. Rev.* D **39** (1989) 169.

[58] T. Sjöstrand, M. v. Zijl, 'A multiple-interaction model for the event structure in hadron collisions', *Phys. Rev.* D **36** (1987) 2019
G. A. Schuler and T. Sjöstrand, Phys. Lett. B300 (1993) 169;
Nucl. Phys. Bbf 407 (1993) 539

[59] ZEUS Collaboration, 'Global Event Properties in Hard Photoproduction at HERA', Int.Europhys.Conf on HEP, Brussels, 1995, paper 0380.

[60] M. Erdmann, 'The Partonic Structure of the Photon: Photoproduction at the Lepton-Proton Collider HERA', DESY 96-090

[61] H1 Collab., S. Aid et al., Z. Phys. C**70** (1996) 17.

[62] J. M. Butterworth and J. R. Forshaw, J. Phys. G**19** (1993) 1657.

[63] J. M. Butterworth, J. R. Forshaw and M. H. Seymour, Z. Phys. C72 (1996) 637

[64] ZEUS Collab., M. Derrick et al., *Phys. Lett.* B **322** (1994) 287.

[65] F. Jaquet, A. Blondel, Proceedings of the study of an ep-facility for Europe, DESY 79-48 (1979) 391

[66] M. H. Seymour, 'Jets in QCD', CERN-TH/95-176.

[67] J. Huth et al., Proc. of the 1990 DPF Summer Study on High Energy Physics, Snowmass, Colorado, edited by E. L. Berger World Scientific, Singapore, (1992) p.134.

[68] P. d. Jong, 'Status of the Uranium Calorimeter Reconstruction Software', ZEUS-Note 92-019.

[69] W. T. Giele and W. B. Kilgore,*Phys. Rev.* D **55** (1997) 7183;
M. H. Seymour, 'Jet Shapes in Hadron Collisions', RAL-97-026.
W. B. Kilgore, 'Next to Leading Order Three Jet Production at Hadron Colliders', To appear in the proceedings of XXXIInd Rencontres de Moriond, Les Arcs, France, 22-29 March 1997.

[70] P. J. Bussey, EUCELL, ZEUS Phantom library.

[71] S. Catani, Y. L. Dokshitzer, M. H. Seymour, B. R. Webber, *Nucl. Phys.* B **406** (1993) 187.

[72] M. H. Seymour, private correspondence.

[73] S. D. Ellis, Z. Kunszt, D. E. Soper, *Phys. Rev. Lett.* **69** (1992) 3615.

[74] J. M. Butterworth, L. Feld, M. Klasen, G. Kramer, 'Matching Experimental and Theoretical Jet Definitions for Photoproduction at HERA', Proceedings of the HERA Workshop 95/96

[75] H1 Collab., T. Ahmed et al., 'Hard Scattering in gamma-p interactions', *Phys. Lett.* B **297** (1992) 205.

[76] H1 Collab., I. Abt et al., 'Measurement of Inclusive Jet Cross Sections in Photoproduction at HERA', *Phys. Lett.* B **314** (1993) 436.

[77] ZEUS Collab., M. Derrick et al., 'Observation of hard scattering in photoproduction at HERA', *Phys. Lett.* B **297** (1992) 404.

[78] ZEUS Collab., M. Derrick et al., 'Observation of direct processes in photoproduction at HERA', *Phys. Lett.* B **322** (1994) 287.

[79] ZEUS Collab., M. Derrick et al., 'Inclusive Jet Differential Cross Sections in Photoproduction at HERA', *Phys. Lett.* B **342** (1995) 417.

[80] K. Desch, 'Jet-Produktion in hochenergetischen Photon-Proton-Kollisionen bei HERA', Dissertation, BONN-IR-95-13, 1995.

[81] ZEUS Collab., M. Derrick et al., *Phys. Lett.* B **348** (1995) 665.
ZEUS Collab., M. Derrick et al., *Phys. Lett.* B **384** (1996) 401-413.

[82] J. R. Forshaw and R. G. Roberts, *Phys. Lett.* B **319** (1993) 539.

[83] HERWIG 5.8/5.7; G. Marchesini, B.R. Webber, G. Abbiendi, I.G. Knowles, M.H. Seymour and L. Stanco, Comp. Phys. Comm. bf 67 (1992) 465.
(For specific versions http://surya11.cern.ch/users/seymour/herwig/)

[84] J. R. Forshaw, J. K. Storrow, 'Photon-induced minijets', *Phys. Rev.* D **46** (1992) 4955.

[85] J. M. Butterworth, J. R. Forshaw, M. H. Seymour, 'Multiparton Interactions in Photoproduction at HERA', CERN-TH/95-82.

[86] H.-U. Bengtsson and T. Sjöstrand, Comp. Phys. Comm. bf 46 (1987) 43.
T. Sjöstrand, CERN-TH.6488/92.
(For specific versions http://thep.lu.se/tf2/staff/torbjorn/Pythia.html)

[87] M. Klasen, Private communication

[88] GEANT, Program Library Q123, CERN 1993.

[89] H. Plothow-Besch, 'PDFLIB: a library of all available parton density functions of the nucleon, the pion and the photon and the corresponding alpha(s) calculations', Comp.Phys.Comm. **75** (1993) 396-416.

[90] A. Martin, W.J. Stirling and R.G. Roberts, RAL preprint RAL-94-055 (1994)

[91] M. Vreeswijk, PhD. Thesis (University of Amsterdam, 1996)

[92] J. Repond, "Jet energy Corrections', Zeus-Note 96-133.

[93] F. Pelucchi, S. Schlenstedt, J.H. Vossebeld Zeus-Note 96-104.

[94] C. Glasman, J. Terron, 'Measurement of Jet Shapes in Photoproduction at HERA', ZEUS-96-126

[95] ZEUS Collab., M. Derrick et al., *Z. Phys.* C **72** (1996) 399.

[96] L. Feld, R. L. Saunders, J. M. Butterworth, "Measurement of Dijet Cross Sections in Photoproduction at HERA", ZEUS-Note 97-057.

[97] A.Kwiatkowski, H. Spiesberger, H. J. Möring, Physics at HERA Vol.3 DESY 1992 1294

[98] G. Ingelman, Physics at HERA Vol.3 DESY 1992 1366

[99] L. Lönnblad,Comp. Phys. Comm. **71** (1992) 15

[100] CTEQ Collab., J. Botts et al., *Phys. Lett.* B **304** (1993) 159;
CTEQ Collab., H.L. Lai et al., *Phys. Rev.* D **51** (1995) 4763.

[101] M. Glück, E. Reya and A. Vogt, *Z. Phys.* C **53** (1992) 651.